APPLIED COMPUTATIONAL ELECTROMAGNETICS SOCIETY JOURNAL

March 2021
Vol. 36 No. 3
ISSN 1054-4887

The ACES Journal is abstracted in INSPEC, in Engineering Index, DTIC, Science Citation Index Expanded, the Research Alert, and to Current Contents/Engineering, Computing & Technology.

The illustrations on the front cover have been obtained from the research groups at the Department of Electrical Engineering, The University of Mississippi.

MARCH 2021 REVIEWERS

Maximilian James Arpaio
Mehmet Belen
You Chen
Thippesha D.
Zaheer Ahmed Dayo
Oguzhan Demiryurek
Ayman Elboushi
Mang He
Taha Imeci
Matteo Lodi
Jagadish M.
Hemant Magadum
Dhirgham Naji
Abbas Omar
Antonio Orlandi
James Quinlan
R. S. Suriavel Rao
Sobhan Roshani
Avisankar Roy
Ramesh S.
Stefano Selleri
Sellakkutti Suganthi
Thomas Søndergaard
Tomasz Szczegielniak
Irfan Ullah
Wei-Chung Weng
Salah Yahya
Xingqiu Yuan
Yujuan Zhao

THE APPLIED COMPUTATIONAL ELECTROMAGNETICS SOCIETY JOURNAL

Vol. 36 No. 3 March 2021

TABLE OF CONTENTS

DNA Hybridization Detection based on Plasmonic Photonic Crystal Fiber

Mohammad Y. Azab [1], Abed M. Nasr [1], S. S. A. Obayya [1,*] and Mohamed Farhat O. Hameed [1,2,3, *]

[1] Faculty of Engineering, Mansoura University
Mansoura, Egypt, Mansoura, 35516, Egypt

[2] Centre for Photonics and Smart Materials
Zewail City of Science and Technology, October Gardens, 6th of October City, Giza 12578, Egypt
sobayya@zewailcity.edu.eg

[3] Nanotechnology and Nanoelectronics Engineering Program
Zewail City of Science and Technology, October Gardens, 6th of October City, Giza 12578, Egypt
mfarahat@zewailcity.edu.eg

Abstract ─ A novel design of surface plasmon (SP) photonic crystal fiber (PCF) for DNA hybridization detection is proposed and analyzed. The suggested biosensor relies on plasmonic D-shaped PCF configuration. Accordingly, the core guided mode in the silica core is coupled with the SP mode near the plasmonic layer. The resonance wavelength is sensitive to the DNA hybridization process. Therefore, the suggested bio-sensor is studied to maximize the DNA hybridization detection sensitivity by adjusting the structural geometrical parameters. The numerical results are obtained using full vectorial finite element method with perfectly matched layer boundary condition and non-uniform meshing capabilities. The reported D-shaped PCF offers high wavelength sensitivity of 405.4 nm/RIU with a corresponding amplitude sensitivity of 5.65 RIU^{-1}. Consequently, the applications based on DNA classification can be potentially implemented by the reported biosensor.

Index Terms ─ D-shaped fiber, DNA hybridization, photonic crystal fiber, plasmonic biosensor.

I. INTRODUCTION

Photonic crystal fiber (PCF) [1] is one of the most reliable designs in the field of waveguides and optical sensors. PCFs are characterized by their high field confinement, low attenuation loss, high effective mode area and high design flexibility. Further, adding a plasmonic material to the PCF structure allows the coupling between the core guided modes and the surface plasmon (SP) modes. The coupling takes place when the real parts of the effective indices of the core and SP modes are the same. The plasmonic PCFs have been widely used for Glucose level monitoring [2] and cancer early detection [3]. However, it will be used in the current manuscript for DNA hybridization detection which has become of great importance. Through the DNA hybridization process, the single stranded DNA (ssDNA) is transformed into double stranded DNA (dsDNA) when the two complement ssDNA sequences are merged together. To detect the hybridization process, two techniques can be used, namely label free and label-based. The label based mechanism requires a complex handling for the liquid along with labeling procedure with a long assay time. Therefore, the label-free procedure is highly needed for monitoring bimolecular interaction in real time without the labeling process. A slot-waveguide biosensor based on label-free mechanism for detecting DNA hybridization has been suggested with sensitivity of 856 nm/RIU and a corresponding detection-limit of 1.43×10^{-6} RIU [4]. In addition, Yin *et al.* [5] have investigated a thin-core fiber based modal interferometer DNA sensor. Such a sensor is based on layer-by-layer self-assembly where a sensitivity of 0.27 nm/matched-base has been obtained at a concentration of 1 mM. Further, an interferometric reflectance imaging sensor has been suggested to quantify the mass density for DNA [6]. Furthermore, a sensitivity of 893.5 nm/RIU has been achieved using a horizontal slot waveguide biosensor with a ring resonator arrangement [7]. However, the analysis of the proposed designs in [4, 7] does not study the whole system with the suggested micro-ring resonator. Moreover, a microfiber Bragg grating (mFBG) was presented as a sensing probe for DNA hybridization detection with a surrounding refractive index (SRI) resolution up to 2.6×10^{-5} RIU [8]. Additionally, an in-line fiber Michelson interferometer based optofluidic biosensor was proposed for the detection of DNA hybridization with a detection limit of 5 nano-Mole (nM)

Submitted On: May 10, 2020
Accepted On: February 6, 2021
https://doi.org/10.47037/2020.ACES.J.360301

[9]. Further, a microfiber Bragg grating (mFBG) based reflective fiber-optic biosensor has been investigated in [10] for DNA hybridization detection using layer-by-layer self-assembly technology. Recently, PCF biosensor has been proposed with plasmonic rod for the detection of DNA hybridization with a sensitivity of 94.59 nm/RIU [11]. In addition, Kaye *et al.* [12] have used a localized SPR (LSPR) coupled fiber-optic (FO) nano-probe for the detection of DNA hybridization and DNA concentrations with detection limit of 10 fM. Moreover, a highly sensitive hybrid plasmonic slot-waveguide (HPSW) biosensor based on silicon-on-insulator was proposed by Hameed *et al*. [13] for DNA hybridization detection. Such a sensor [13] is characterized by sensitivity of 1890.4 nm/RIU and a detection-limit of 2.65×10^{-6} RIU. However, the HSPW has a complex structure for fabrication.

In this paper, a D-shaped PCF biosensor is presented and analyzed for detecting DNA hybridization process. The proposed design achieves wavelength and amplitude sensitivities of 405.4 nm/RIU and 5.65 RIU^{-1}, respectively. Further, the suggested D-shape design has the advantage of fabrication simplicity with higher sensitivity than 94.59 nm/RIU of that presented in [11]. Further, the reported sensor relies on the widely fabricated hexagonal PCF with a great capability for applications based on DNA classification.

II. NUMERICAL TECHNIQUE

In this study, full vectorial finite element method (FVFEM) [14, 15] is used for the modal analysis of the suggested DNA biosensor. Based on Maxwell's equations, the following magnetic field based vector wave equation can be expressed as:

$$\nabla \times (\varepsilon^{-1} \nabla \times \mathrm{H}) - \omega^2 \mu_0 \mathrm{H} = 0, \qquad (1)$$

where μ_0 is the free space permeability and ω is the angular frequency. In addition, $\varepsilon = \varepsilon_0 \varepsilon_r$ is the waveguide material permittivity where ε_r is the relative permittivity and ε_0 is the free space permittivity. By applying the standard finite element method to the wave equation, the following eigenvalue equation can be obtained:

$$[\mathrm{K}]\{\mathrm{H}\} - \beta^2[\mathrm{M}]\{\mathrm{H}\} = \{0\}, \qquad (2)$$

where [H] is the global magnetic field vector, [M] and [K] are the global mass and stiffness matrices, β is the propagation constant and $\{0\}$ is the null vector. By solving the eigenvalue equation, the eigenvalue β and the wave vector H can be determined. Moreover, the propagation constant β for a specific mode is used to calculate the effective index via $n_{eff} = \beta/k$, given that k is the wavenumber of free space. In this study, the FVFEM is used via Comsol Multiphysics 5.4 software package [16]. Through the modal analysis of the suggested biosensor, non-uniform meshing is used with minimum element size of $1.12 \times 10^{-4}\ \mu m$. Further, 399217 degrees of freedom are employed to maximize the calculation accuracy and save the computation cost. An AMD dual-core computer processor at 2.9 GHz with 8.0 GB RAM and 64-bit operating system has been used to run the software with an average runtime of 120 seconds/run.

III. DESIGN CONSIDERATIONS AND NUMERICAL RESULTS

To justify our choice of the D-shape configuration, a complete ring–shaped PCF biosensor design will be first considered as shown in Fig. 1 (a). The sensor is based on one ring of hexagonal lattice PCF with a solid core and silica background material. The proposed PCF biosensor has air holes diameter d and a hole pitch Λ while the silver layer has a thickness t. An additional air hole of diameter $d_s = 0.3d$ is also added at a distance $d_y = 0.65\ \Lambda$ below the center to enhance the biosensor sensitivity. It may be seen from Fig. 1 (a) that the silver layer is deposited on the outer surface of the PCF followed by a linker layer which attracts the DNA strands. The linker layer consists of silane with 1 nm thickness and 1.42 index of refraction. Further, the DNA strands are added after the linker layer. According to [4], the thickness of the DNA layer before (ssDNA) and after (dsDNA) the hybridization process is the same value of 8 nm. Moreover, the refractive indices of the ssDNA and dsDNA layers are equal to 1.456 and 1.53, respectively. Further a water layer of refractive index 1.33 is added where the DNA strands are inserted. Additionally, the computational domain is truncated by using PML layer.

The relative permittivity of silica glass ε_s is dependent on the wavelength λ in μm via [11]:

$$\varepsilon_s = 1 + \frac{B_1\lambda^2}{\lambda^2 - C_1} + \frac{B_2\lambda^2}{\lambda^2 - C_2} + \frac{B_3\lambda^2}{\lambda^2 - C_3}, \qquad (3)$$

where the constants B_3, B_2 and B_1 have values of 0.8974794, 0.4079426 and 0.6961663, respectively. On the other hand, C_3, C_2 and C_1 are equal to 97.9340025 μm^2, 0.0135120631 μm^2 and 0.00467914826 μm^2, respectively. Additionally, the relative permittivity of the silver can be obtained using the following Drude-Lorentz model [17]:

$$\varepsilon_{Ag} = 1 - \frac{\Omega_p^2}{\omega(\omega - i\Gamma_0)} + \sum_{j=1}^{k} \frac{f_j \omega_p^2}{\left(\omega_j^2 - \omega^2\right) + i\omega\Gamma_j}, \qquad (4)$$

where ω_p is the plasma frequency, k is the number of oscillators with frequency ω_j, strength f_j, and lifetime $1/\Gamma_j$, while $\Omega_p = \sqrt{f_0}\omega_p$ is the plasma frequency associated with intraband transitions with oscillator strength f_0 and damping constant Γ_0.

Figure 1 (b) shows the wavelength dependence of the real parts of the effective index of the transverse magnetic (TM) SP mode and the TM core guided mode. Additionally, the confinement loss for the quasi TM core guided mode is also presented in Fig. 1 (b). The study is carried out at $\Lambda = 1.2$ μm, $d = 0.56$ μm, $t = 70$ nm and

ssDNA layer with index of refraction of 1.456. The inset of Fig. 1 (b) shows that at $\lambda = 700$ nm away from the coupling wavelength, the quasi TM core guided mode has a good confinement to the core region. Accordingly, the real parts of the effective index of both the core guided and the SP modes are away from each other and no coupling occurs. On the other hand, at $\lambda = 745$ nm, the real parts of the effective index of both the quasi TM core guided mode and SP mode are the same. As a result, the power transfer to the SP mode from the core mode is maximum where the quasi TM core guided mode is less confined in the core region as shown in the inset of Fig. 1 (b).

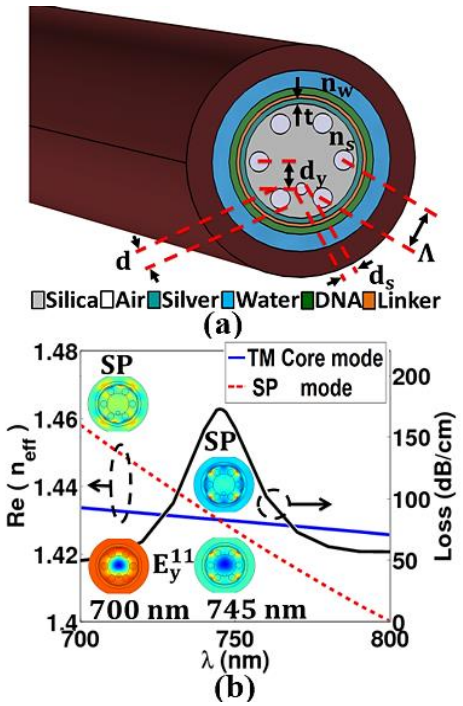

Fig. 1. (a) 3D schematic diagram of ring shaped DNA SPR PCF biosensor, and (b) Effective indices of the main component of the SP mode and the quasi TM core mode along with the confinement losses of the TM core mode as a function of the wavelength at $n_{DNA} = 1.456$. The inset shows field plots of the SP mode and the fundamental components of the quasi TM core mode at wavelengths of 700 nm and 745 nm.

The sensitivity of the suggested DNA sensor to the degree of hybridization is tested via the interrogation methods for both the wavelength and amplitude. The wavelength sensitivity can be calculated via the change in the resonance wavelength for the two DNA cases (n=1.456 for ssDNA and n=1.53 for dsDNA) [4] as follows [2]:

$$S_\lambda = \partial\lambda_0(n_{DNA})/\partial n_{DNA}\,, \quad \text{nm/RIU} \qquad (5)$$

where λ_0 is the resonance wavelength for a specific DNA refractive index n_{DNA}. Additionally, the amplitude sensitivity (RIU^{-1}) can be obtained using the following equation [2]:

$$S_A = -\frac{\partial\alpha(\lambda, n_{DNA})/(\partial n_{DNA})}{\alpha(\lambda, n_{DNA})}\,, \qquad (6)$$

where $\alpha(\lambda, n_{DNA})$ is the confinement loss of the core guided mode as a function of the DNA refractive index n_{DNA} and wavelength λ. Unfortunately, the numerical study results in very low wavelength and amplitude sensitivities of 13.5 nm/RIU and 0.33 RIU^{-1}, respectively. Accordingly, to enhance the sensitivity of the DNA biosensor, a horizontal etching is applied on the PCF to obtain a D-shaped SPR PCF as shown in Fig. 2 (a). The D-shape is obtained by removing two rows of the air holes via horizontal etching. The core region is obtained by introducing a solid silica rod instead of a capillary in the central region. The proposed PCF structure has a hexagonal lattice with air holes diameter d and a hole pitch Λ as presented in Fig. 2 (a). Further, a silver layer of thickness t is deposited on the etched surface which serves as a plasmonic material. Additionally, a layer of silane with thickness 1 nm and refractive index of 1.42 is added above the silver as a linker layer for DNA strands.

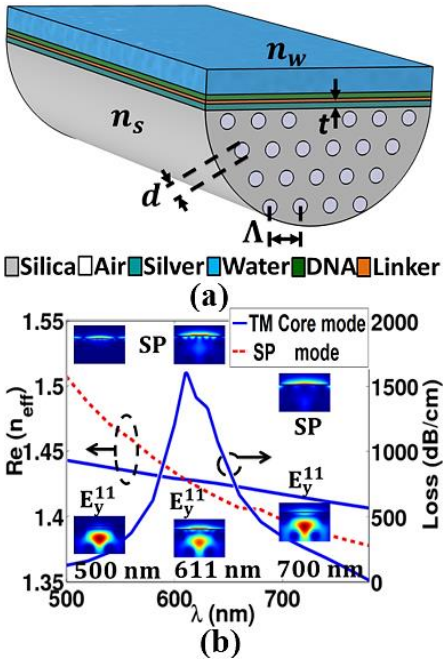

Fig. 2. (a) 3D schematic diagram of D-shaped DNA SPR PCF biosensor, and (b) effective indices of the main component of the SP mode and the quasi TM core mode along with the confinement losses of the TM core mode as a function of the wavelength at $n_{DNA} = 1.456$. The inset shows field plots of the SP mode and the fundamental components of the quasi TM core mode at wavelengths of 500 nm, 611 nm and 700 nm.

It is worth noting that the thickness of the DNA layer before and after the hybridization process has the same value of 7 nm [4]. Additionally, the DNA layer is surrounded by a water of refractive index 1.33. The modal analysis is performed on a computational domain of rectangular shape having a width 11.04 μm and a height 9.05 μm with a PML boundary condition. Further, minimum element size of 0.000232 μm and 305113 degrees of freedom are used to describe the used non uniform mesh. Due to the horizontal etching of the plasmonic D-shaped PCF, only TM modes are considered in the following study. The dependency of the real parts of the effective indices of the SP mode and the TM core guided mode along with the confinement loss for the quasi wavelength dependent TM core guided mode are presented in Fig. 2 (b). This investigation is performed at $\Lambda = 1.2\ \mu m$, $d = 0.6\ \mu m$, $t = 70\ nm$ with a ssDNA layer of refractive index 1.456. The field plots in the inset of Fig. 2 (b) clarify that away from the coupling wavelength (500 nm and 700 nm), the TM core guided mode is well confined to the core region where no coupling is obtained between the core guided mode and the SP mode. However, at the coupling wavelength of 611 nm, both the SP mode and the TM core guided mode have the same effective index. Accordingly, the confinement loss has its maximum value at the coupling wavelength of 611 nm. The suggested D-shaped DNA biosensor's sensitivity is optimized by controlling the structural geometrical parameters such as the hole pitch Λ, the air holes diameter d and the silver layer thickness t. First, the hole pitch is considered with the following values: 1.2 µm, 1.3 µm and 1.4 µm while the air hole diameter and the silver thickness are kept constant at 0.6 µm and 70 nm, respectively. Figure 3 represents the wavelength dependence of the loss spectra along with the amplitude sensitivity for ssDNA and dsDNA at different hole pitch values. It can be realized from Fig. 3 (a) that at $\Lambda = 1.2$ µm, the coupling wavelength is found at 611 nm for the ssDNA ($n_{DNA} = 1.456$), while the dsDNA case ($n_{DNA} = 1.53$) has a resonance wavelength of 630 nm. The resultant shift in the wavelength is equal to 19 nm and the corresponding wavelength sensitivity is 256.75 nm/RIU. In addition, the amplitude sensitivity for the same Λ is equal to 5.66 RIU^{-1} as shown in Fig. 3 (d). At $\Lambda = 1.3$ µm, the resonance wavelength has a blue shift to 602 nm and 617 nm for the ssDNA and dsDNA, respectively. Accordingly, Figs. 3 (b) and (e) show that both the amplitude and wavelength sensitivities are decreased to 5.06 RIU^{-1} and 202.70 nm/RIU, respectively. When $\Lambda = 1.4$ µm is used, the resonance wavelengths have further blue shifts as may be seen from Fig. 3 (c) to 593 nm and 610 nm for ssDNA and dsDNA, respectively. Figures 3 (c) and (f) reveal that the corresponding amplitude and wavelength sensitivities are equal to 5.79 RIU^{-1} and 229.72 nm/RIU, respectively. Therefore, the hole pitch will be kept constant at 1.2 µm with high sensitivity of 256.75 nm/RIU in the subsequent simulations. The same study is carried out for silver layer thickness with three values of 60 nm, 70 nm and 80 nm while the air holes diameter and hole pitch are fixed at 0.6 μm and 1.2 μm, respectively. Figure 4 shows the amplitude sensitivity and confinement loss as a function of the wavelength for different silver layer thicknesses. Figure 4 (a) and shows that at $t = 60$ nm, the resonance occurs at λ=611 nm and 627 nm, respectively. Consequently, the obtained S_A and S_λ are equal to 7.71 RIU^{-1} and 216.21 nm/RIU, respectively. At a silver layer thickness of 70 nm, the resonance wavelength has the same value for ssDNA (611 nm) and a slight increase for dsDNA (630 nm).

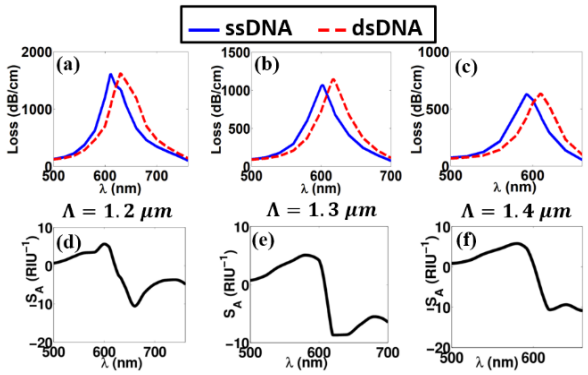

Fig. 3. Confinement losses for the quasi TM core mode and amplitude sensitivity as a function of the wavelength for ssDNA and dsDNA layers at different values of Λ.

Therefore, an increase in the wavelength sensitivity to 256.75 nm/RIU is realized while the obtained S_A is reduced to 5.66 RIU^{-1} as may be seen from Figs. 4 (b) and (e). Further, Fig. 4 (c) reveals that the resonance wavelengths are similar to that of 60 nm at a silver thickness of 80 nm. As a result, the obtained wavelength sensitivity has the same value of 216.21 nm/RIU while a further decrease in the amplitude sensitivity to 3.6 RIU^{-1} is obtained as shown in Fig. 4 (f). The next study is concerned with the diameter of the air holes with values of 0.52 μm, 0.56 μm and 0.60 μm, where the hole pitch and silver layer thickness are kept constant at 1.2 μm and 70 nm, respectively. It may be seen from Fig. 5 (a) that at $d = 0.52\ \mu m$, the coupling occurs at wavelengths of 609 nm and 636 nm for ssDNA ($n_d = 1.456$) and dsDNA ($n_d = 1.53$), respectively. Therefore, the corresponding amplitude and wavelength sensitivities are equal to 7.69 RIU^{-1} and 364.68 nm/RIU, respectively as observed from Figs. 5 (a), (d). It may be also observed from Fig. 5 (b) that using air holes diameter of 0.56 μm could shift the resonance wavelengths to 610 nm and 640 nm for ssDNA ($n_d = 1.456$) and dsDNA ($n_d = 1.53$), respectively. Accordingly, a high wavelength sensitivity of 405.4 nm/RIU is obtained while a slight decrease in

the amplitude sensitivity to 5.62 RIU^{-1} is realized from Figs. 5 (b) and (e). When the air holes diameter is increased to 0.6 μm, the resonance is obtained at 611 nm for ssDNA and 630 nm for dsDNA. The corresponding wavelength sensitivity is decreased to 256.75 nm/RIU while the amplitude sensitivity is nearly the same.

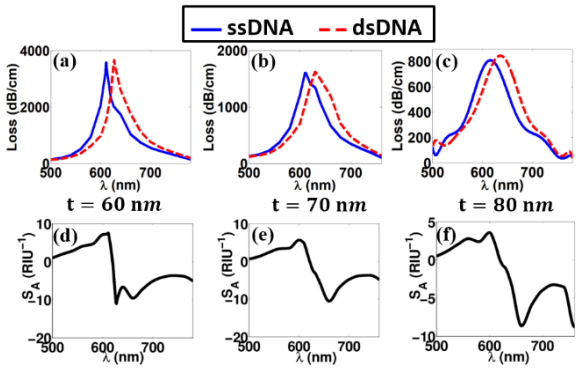

Fig. 4. Confinement losses for the quasi TM core mode and amplitude sensitivity as a function of the wavelength for ssDNA and dsDNA layers at different values of silver layer thickness t.

The suggested D-shaped PCF DNA biosensor is based on silica glass hexagonal lattice which can be fabricated using the well-known stake and draw method [18] where the air holes can be arranged with high accuracy. Additionally, the D-shaped configuration can be accomplished via fiber polish where splicing is applied for long PCF between two single-mode fibers. Then, the spliced fiber is fixed by using a pair of fiber holders. Additionally, the polishing length and depth is accurately controlled by a computer program. Moreover, the silver nano-layer can be obtained using thermal evaporation, sputtering technique and wet-chemistry technique [3]. Further, surface roughness can be minimized via employing chemical vapor deposition (CVD) technique [1]. It is worth noting that slot waveguides biosensors [4, 7, 13] have complex structures with very small geometrical parameters and different layers of different materials. In addition, the coupling to the slot waveguide with a photonic strip-slot waveguide is needed which suffers from undesired back-reflection. Further, mode conversion may occur at the coupling interface which decreases the biosensor sensitivity [19]. In addition, the design in Ref. [11] is based on gold nanowires infiltration which is considered also of high complexity. Further, the technique used in calculating the sensitivity in the slot waveguide designs is based on obtaining the shift in the resonance wavelength via the difference in the effective index of the fundamental core mode. On the other hand, the design of Ref. [11] and the current design are based on obtaining the actual shift in the resonance peek of the confinement loss. Accordingly, the current design uses a more applicable and accurate technique. Moreover, the actual shift in the resonance wavelength for the current design (30 nm) is far higher than any of the preceding designs. Therefore, the sensitivity value of the current design has more reality than those of the other designs.

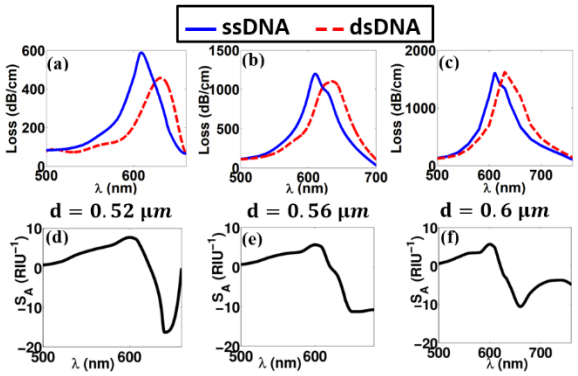

Fig. 5. Confinement losses for the quasi TM core mode and amplitude sensitivity as a function of the wavelength for ssDNA and dsDNA layers at different values of d.

IV. CONCLUSION

An innovative structure of SPR PCF biosensor for DNA hybridization detection is proposed and analyzed. The reported design is based on D-shaped configuration with high amplitude and wavelength sensitivities of 5.65 RIU^{-1} and 405.4 nm/RIU, respectively. Further, the suggested DNA biosensor has advantage in terms of simplicity for the fabrication process. Therefore, the applications based on DNA classification can be potentially implemented by the proposed biosensor with simple and efficient label free technique.

REFERENCES

[1] P. J. Sazio, A. Amezcua-Correa, C. E. Finlayson, J. R. Hayes, T. J. Scheidemantel, N. F. Baril, B. R. Jackson, D. J. Won, Zhang, F. Margine, E. R. V. Gopalan, V. H. Crespi, and J. V. Badding, "Micro-structured optical fibers as high-pressure micro-fluidic reactors," *Science*, vol. 311, no. 5767, pp. 1583-1586, Mar. 2006.

[2] M. Y. Azab, M. F. O. Hameed, and S. S. A. Obayya, "Multi-functional optical sensor based on plasmonic photonic liquid crystal fibers," *Opt. Quant. Electron.*, vol. 49, no. 2, pp. 1-17, Jan. 2017.

[3] A. A. Rifat, R. Ahmed, A. K. Yetisen, H. Butt, A. Sabouri, G. A. Mahdiraji, S. H. Yun, and F. R. M. Adikan, "Photonic crystal fiber based plasmonic sensors," *Sensor. Actuator. B Chem.*, vol. 243, pp. 311-325, May 2017.

[4] T. Dar, J. Homola, B. M. A. Rahman, and M. Rajarajan, "Label-free slot-waveguide biosensor for the detection of DNA hybridization," *Applied*

Optics, vol. 51, no. 34, pp. 8195-8202, Nov. 2012.

[5] M. J. Yin, C. Wu, L. Y. Shao, W. K. E. Chan, A. P. Zhang, C. Lu, and H. Y. Tam, "Label-free, disposable fiber-optic biosensors for DNA hybridization detection," *Analyst*, vol. 138, no. 4, pp. 1988-1994, Jan. 2013.

[6] S. Ahn, D. S. Freedman, X. Zhang, and M. S. Unlü, "High-throughput label-free detection of DNA hybridization and mismatch discrimination using interferometric reflectance imaging sensor," *Methods in Molecular Biology*, vol. 1039, pp. 181-200, July 2013.

[7] C. Viphavakit, M. Komodromos, C. Themistos, W. S. Mohammed, K. Kalli, and B. M. A. Rahman, "Optimization of a horizontal slot waveguide biosensor to detect DNA hybridization," *Applied Optics*, vol. 54, no. 15, pp. 4881-4888, May 2015.

[8] Y. Cao, T. Guo, X. Wang, D. Sun, Y. Ran, X. Feng, and B. O. Guan, "Resolution-improved in situ DNA hybridization detection based on microwave photonic interrogation," *Opt. Express*, vol. 23, no. 21, pp. 27061-27070, Oct. 2015.

[9] R. Gao, D. F. Lu, J. Cheng, Y. Jiang, L. Jiang, J. D. Xu, and Z. M. Qi, "Fiber optofluidic biosensor for the label-free detection of DNA hybridization and methylation based on an in-line tunable mode coupler," *Biosensors and Bioelectronics*, vol. 15, no. 86, pp. 321-329, Dec. 2016.

[10] D. Sun, T. Guo, and B. O. Guan, "Label-free detection of DNA hybridization using a reflective microfiber Bragg grating biosensor with self-assembly technique," *Journal of Lightwave Technology*, vol. 35, no. 16, pp. 3354-3359, Aug. 2017.

[11] M. Y. Azab, M. F. O. Hameed, A. M. Nasr, and S. S. A. Obayya, "Label free detection for DNA hybridization using surface plasmon photonic crystal fiber biosensor," *Optical and Quantum Electronics*, vol. 50, no. 68, pp. 1-13, Jan. 2018.

[12] S. Kaye, Z. Zeng, M. Sanders, K. Chittur, P. M. Koelle, R. Lindquist, U. Manne, Y. Lin, and J. Wei, "Label-free detection of DNA hybridization with a compact LSPR-based fiber-optic sensor," *Analyst*, vol. 142, pp. 1974-1981, Apr. 2017.

[13] M. F. O. Hameed, A. S. Saadeldin, E. M. A. Elkaramany, and S. S. A. Obayya, "Label-free highly sensitive hybrid plasmonic biosensor for the detection of DNA hybridization," *Journal of Lightwave Technology*, vol. 35, no. 22, pp. 4851-4858, Nov. 2017.

[14] S. S. A. Obayya, B. M. A. Rahman, and H. A. El-Mikati, "New full-vectorial numerically efficient propagation algorithm based on the finite element method," *Journal of Lightwave Technology*, vol. 18, no. 3, pp. 409-415, Mar. 2000.

[15] S. S. A. Obayya, B. M. A. Rahman, K. T. V. Grattan, and H. A. El-Mikati, "Full vectorial finite-element-based imaginary distance beam propagation solution of complex modes in optical waveguides," *Journal of Lightwave Technology*, vol. 20, no. 6, pp. 1054-1060, June 2002.

[16] COMSOL Multiphysics® [Online] Available: http://www.comsol.com. COMSOL AB, Stockholm, Sweden"

[17] A. D. Rakic, A. B. Djurisic, J. M. Elazar, and M. L. Majewski, "Optical properties of metallic films for vertical-cavity optoelectronic devices," *Applied Optics*, vol. 37, no. 22, pp. 5271-5283, Aug. 1998.

[18] P. Russell, "Photonic crystal fibers," *Science*, vol. 299, no. 5605, pp. 358-362, Jan. 2003.

[19] V. M. N. Passaro and M. La-Notte, "Optimizing SOI slot waveguide fabrication tolerances and strip-slot coupling for very efficient optical sensing," *Sensors*, vol. 12, no. 3, pp. 2436-2455, Feb. 2012.

An Efficient Rotationally Symmetric Approach for the Design of Sparse Conformal Arrays in Wide Angle Scanning

Pengfei Gu*, Zhenhong Fan, Dazhi Ding, and Rushan Chen

Department of Communication Engineering, Nanjing University of Science and Technology, Nanjing, China
*pengfeigu@njust.edu.cn

Abstract ─ This paper addresses a novel rotationally symmetric technique with multiple constraints for sparse conformal array synthesis. The purpose is to synthesis a sparse optimal common element positions on the conformal surface varying multiple patterns of wide angle scanning with the behavior of low sidelobe levels (SLL). The conformal surface aperture is partitioned into several rotationally symmetric sections. The element positions and element numbers of only one section need to be optimized, which contribute to the reduction of optimizing variables and computation resources. We formulate the synthesis problem as a constrained optimization problem, which takes the peak sidelobe level (PSLL) as the fitness function, and sets the total number of array elements, the minimum spacing between two adjacent elements to form multiple constraints. The Brain Storm Optimization (BSO) is further exploited into the synthesis problem with multiple constraints. A set of representative numerical examples are presented to assess the advantages and effectiveness of the proposed method.

Index Terms ─ Conformal sparse array, rotational symmetry, wide angle scanning.

I. INTRODUCTION

Differ from the synthesis of sparse planar arrays, conformal antenna arrays show unparalleled advantages of reduced aerodynamic drag, saved space, and wide-angle coverage for applications in aircraft, missiles, naval ships and high-speed vehicles. With the wide application of array antennas in radar communication and electronic system, the number of array elements and corresponding complexity increase greatly, which cause great challenges to the limited platform space, the weight and cost of conformal array antennas.

Many stochastic optimization methods have been presented for the synthesis of sparse linear and planar arrays, such as genetic algorithm (GA) [1], [2], differential evolution (DE) [3], [4] algorithm, Particle swarm optimization (PSO) algorithm [5]. Recently, a series of synthesis techniques based on the sparse signal recovery theory of Bayesian compressive sampling (BCS) method [6], [7] and non-iterative approach named matrix pencil method (MPM) [8]-[10] are presented for the reconstruction of sparse arrays with desired pattern synthesis. Despite its success and efficiency, there are still many challenges for the synthesis and optimization of conformal sparse arrays. The inherent nonlinearity and non-planar directional anisotropy of conformal carrier surface lead to the inadaptability of the direct array pattern multiplication in the synthesis process. Most linear or planar array synthesis methods cannot be directly applied to the design of sparse conformal arrays.

Recently, many techniques of GA [11], [12], PSO [13]-[15], DE [16] and others [17], [18] have been extended to the synthesis of sparse conformal arrays. However, a relatively new global optimization method: Brain Storm Optimization (BSO), hasn't yet been applied in antenna and electromagnetic applications. Brain Storm Optimization (BSO), which was developed in 2011 by Shi, is a swarm intelligence optimization algorithm inspired by the collective behaviour of human beings in solving problems [19]. The application of BSO in different fields has shown to be successful [20]-[23]. But there is relatively few correlational research work for the design of sparse conformal arrays. To above stochastic or global optimization methods, they may fall into local optima and turn out to be relatively time-consuming when optimizing large arrays with various variables of positions, excitations and even the number of elements. Moreover, it may only fit for the sparse synthesis of one fixed or shaped-beam pattern. When applied to the case of reconfigurable multiple-patterns, it also has the problem that cannot guarantee the same best distribution varying multiple-patterns in wide-angle scanning. It is a technical difficulty and challenge to realize fast optimization of sparse conformal arrays, which considers the influence of conformal carrier-surface shape and element distribution on array behavior in wide angle scanning. How to effectively reduce the number of optimization variables is much more important.

Conformal array antennas are usually mounted onto a cylindrical, spherical, conical, or some other smoothly curved surfaces due to aerodynamic or hydrodynamic requirements [24], [25]. The characteristic of rotational

Submitted On: October 12, 2020
Accepted On: February 1, 2021

https://doi.org/10.47037/2020.ACES.J.360302

symmetry can be also found in the carrier such as the hemisphere, cylindrical, the cone and so on. The rotational symmetry characteristic [26] was firstly exploited into the optimization of thinned wideband planar arrays with the reduction of computational complexity and suppression of peak sidelobe level (PSLL). But it hasn't been found there are some researches of rotational symmetry technique for the optimization of large sparse conformal arrays.

In the study, an effective and general approach is developed for the fast synthesis of sparse conformal array capable of radiating desired patterns varying scanning angles. The rotationally symmetry technique is exploited to accelerate the sparse conformal array synthesis process with the reduction of optimization variable number and computational complexity. The BSO algorithm is utilized to further improve radiation performance in wide-angle scanning by optimizing array element distributions. The constraint on the minimum element spacing and multiple-pattern performance is made to ensure finding the common best sparse element positions.

The framework of the paper is organized in the following manner. In Section II, the problem formulation and the theory of the synthesis of sparse conformal arrays is presented. Numerical examples of sparse conformal array optimization demonstrate the validity of the proposed method in Section III. Finally, Section IV concludes the paper.

II. THEORY AND FORMULATION

A. Conformal array model

Consider a conformal array of N elements located arbitrarily on a carrier surface as shown in Fig. 1, the total far field $F(\theta,\phi)$ of conformal phased arrays along the direction (θ,ϕ) in the global coordinate system can be expressed as below:

$$F^i(\theta,\phi)=\sum_{n=1}^{N}\omega_n^i E_n(\theta,\phi)\exp(jk\mathbf{r}_n\mathbf{u}), \qquad (1)$$

where $k=2\pi/\lambda$ denotes the wave number, N is the total array element number. ω_n^i represents the complex excitation coefficient of the i^{th} direction for the n^{th} element, $\mathbf{r}_n=(x_n,y_n,z_n)$ is the location vector in the global coordinate system and $E_n(\theta,\phi)$ represents the n^{th} vector pattern along the wave propagation direction $\mathbf{u}$. $\mathbf{u}=[\sin\theta\cos\phi,\sin\theta\sin\phi,\cos\theta]^T$ is the unit vector in the spherical coordinate system.

Since each element on the carrier surface has its own position and orientation, it is more convenient to first consider the field of each element in their own coordinate system and then transform the field back to the global coordinate system. The coordinate transformation is exploited to superimpose all elements' components at the far field $F(\theta,\phi)$ in the global coordinate system (x, y, z):

$$F(\theta,\phi)=\sum_{n=1}^{N}\omega_n Z_n^T E_n'(\theta_n',\phi_n')\exp(jk\mathbf{r}_n\mathbf{u}), \qquad (2)$$

where Z_n^T is the transform matrix form the local coordinate system of the nth element to the global coordinate system, and $E_n'(\theta_n',\phi_n')$ represents the vector pattern in the local coordinate system. More details can be referred to [12] and [18].

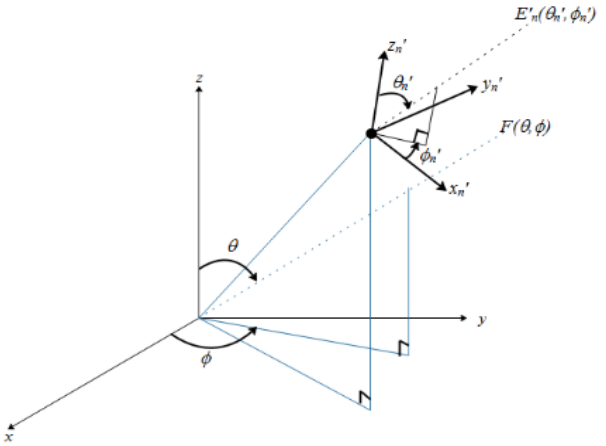

Fig. 1. Global and local coordinate system.

B. The synthesis procedure of sparse conformal array

In the paper, we aim to design an effective synthesis method to redesign an optimal array distribution of sparse conformal array while maintaining the performance of desired low SLL and a constraint on the minimum element spacing of avoiding adjacent elements too close, which further avoids the intersection of two actual array units. Moreover, the sparse distribution of array elements and minimum element-spacing constraint contribute to larger spacing between units than that of uniform array, which slightly reduces the mutual coupling of array elements. The multi-objective optimizing model can be formed as:

$$\begin{cases} SLL=\max\left((F^i(\theta,\phi)\notin Mainbeam\right), & i=1,\cdots,T \\ \Delta r_{mn}\ge d_{target}, & m,n\in[1,N] \text{ and } m\ne n \end{cases}, \qquad (3)$$

where SLL represents the maximum sidelobe level of the total array pattern $F(\theta,\phi)$ and Δr_{mn} is the distance of the mth and nth array element. To avoid too close condition of adjacent elements, the minimum target element spacing of d_{target} is taken into account of the sparse conformal array optimizing procedure.

Benefit from the conformal rotational symmetric technique, the element positions in only one-partitioned region is required to be optimized by the proposed synthesis method, which contributes to the effectively

reduction of optimization variables and computation complexity on large conformal arrays. The detailed introduction of 8-part truncated cone conformal array is illustrated in Fig. 2, where the rotational symmetric is partitioned into the whole structure with 8 parts ($\Delta\phi = 2\pi / Q{=}2\pi / 8$). Two optimizable variables of ($r \le r_q \le R, 0 \le \phi_q \le \Delta\phi$) are extracted from the geometry configuration, where r_q represents the radius of the truncated cone conformal surface and ϕ_q is the angle coverage of per-sector region. The coordinate of array elements along the z-sub coordinate can be got as below:

$$z_q = \frac{R - r_q}{R - r} \cdot h . \tag{4}$$

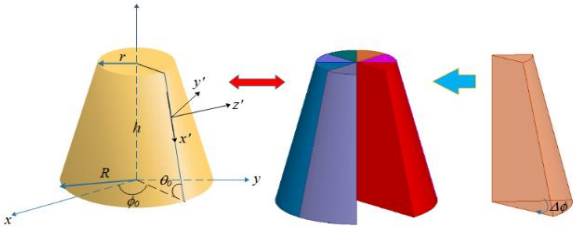

Fig. 2. Detailed division of truncated conformal array with 8 rotational symmetric parts.

The element position (x_q, y_q, z_q) can be easily got by the way above. It also fits for the cone conformal array. But for the hemisphere conformal array in Fig. 3, each array element distribution in the pie-shaped wedge can be simplistically expressed as two optimizable variables of ($r_q = R$, $0 \le \phi_q \le \Delta\phi$, $0 \le \theta_q \le \pi/2$). Depending on the characteristic of conformal rotational symmetry and proposed hybrid BSO wide-angle scanning multiple-pattern synthesis method, the extension to the effective synthesis of large or ultra-large scale sparse conformal arrays becomes feasible with the reduction of optimization variable number and computation complexity to some degree.

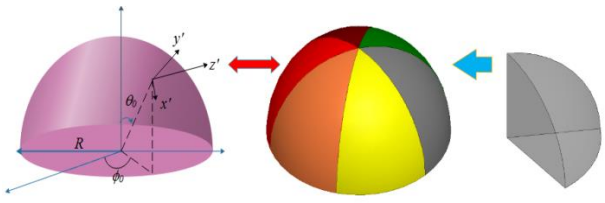

Fig. 3. Geometry of the rotationally symmetric hemisphere conformal array.

To ensure the constraint of minimum element spacing d_{target}, limits on the interval scope of r_q and ϕ_q for each array element location in the pie-shaped optimized slice are firstly considered. Meanwhile, the neighbored elements in the neighbored slice are also considered to avoid placing two elements too close together. The planform of array elements on the rotational symmetrical carrier surface is shown as Fig. 4.

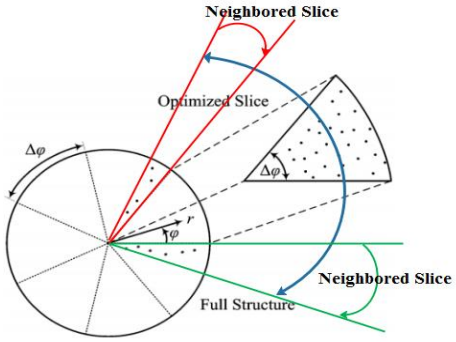

Fig. 4. Consideration of element spacing.

By using the constraints of minimum number of array elements, the minimum spacing between two adjacent elements and the optimizable SLLl in wide-angle scanning, the fitness function can be formulated as below:

$$f_{fit} = a\left|\left[\max(SLL_t) - PSLL\right]\right| + b\left|(d_{target} - \min(d_{target}, d_{\min}))\right|, \quad t = 1, \cdots, T , \tag{5}$$

where $SLL_t\,(t = 1, \cdots, T)$ is the actual maximum sidelobe level of the t^{th} pattern for the conformal sparse array in wide-angle scanning and *PSLL* represents the desired minimum sidelobe level. The constraint on the synthesis of sparse conformal array varying multiple-patterns is addressed by the proposed method. $d_{\min}$ is the minimum element spacing of the optimized sparse conformal array. A criterion is built by the fitness function of Eq. (5), which aims at constraining on the minimum spacing $d_{\min}$ among conformal array elements and suppressing the *SLL* of multiple patterns to the desired index.

For the design and optimization of sparse conformal arrays, the variable parameters of r_q and ϕ_q $(q = 1, \cdots, N_Q)$ for each element can be generated by the BSO method in each population and updated generation. The entire sparse conformal array is reconstructed by symmetrically rotating optimized conformal array element position in one part of *Q*-folds. The multi-objective optimizing model of Eq. (3) and fitness function of Eq. (5) is incorporated into a hybrid reformulation as:

$$\begin{cases} \min\left(N_Q\right) \\ SLL = \max\left((F^i(\theta,\phi) \notin Mainbeam\right), \quad i = 1, \cdots, T , \\ \Delta r_{mn} \ge d_{target}, \quad 1 \le m, n \le N,\ m \ne n, N = N_Q \cdot Q \end{cases} \tag{6}$$

where N_Q represents the element number of pie-optimized slice. *SLL* is a relatively worst extraction from the performance of maximum SLL within multiple-patterns in wide-angle coverage. The BSO is exploited

to optimize conformal designs to obtain deferent performance characteristics of conformal array far-field radiation patterns with fewer elements. It improves the probability of finding a solution by organizing ideas generated from a diverse group of individuals in the brainstorming process. It mainly contains three operations and a typical brainstorming process with optimizing steps is given as Fig. 5. For more information of BSO, the reader can refer to the reference [23].

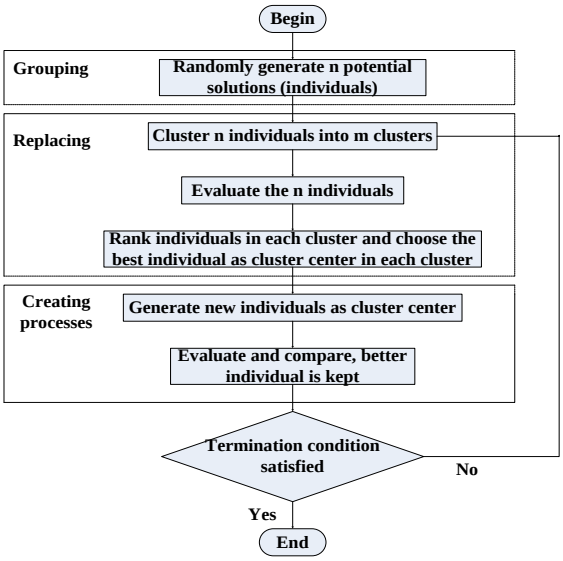

Fig. 5. Flowchart of the BSO algorithm.

The sparse ratio [9], [10] is defined as γ to account for the element saving of sparse conformal array compared with original conformal array:

$$\gamma = \frac{N - N'}{N} \times 100\%, \tag{7}$$

where N' is the number of optimized sparse conformal array antenna elements and N is the number of the original conformal uniform array element number with half-wavelength interval.

III. NUMERICAL RESULTS

In order to evaluate the efficiency and performance of the proposed method, several representative examples are studied for the synthesis of sparse conformal arrays in the section. All of synthesis examples are executed on a Sugon computing server of Intel Purley X745-G30 with 2TB RAM. d_{target} of all numerical examples are set as 0.5λ.

As the first synthesis examples, an effective design of a sparse hemisphere conformal array is presented by the proposed method. The initial λ/2 uniform spacing conformal array is composed of 7 circular ring sub-arrays distributed on the hemisphere carrier surface with 118 elements in all, see Fig. 6.

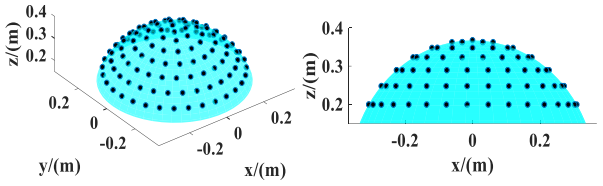

Fig. 6. (a) Uniform hemisphere array. (b) Left view of uniform hemisphere array.

The radius of the hemisphere is 3λ corresponding to the free wavelength at 2.45GHz. All elements are given uniform excitations. The hemisphere geometry is rotationally partitioned into 6 symmetric conformal regions. The optimized synthesis per region is designed to have N_Q array elements with $2N_Q$ optimizable variables, whose element of one symmetric part is restricted on the carrier surface region of ($r_q = 3\lambda$, $0 \le \phi_q \le 2\pi/6$, $0 \le \theta_q \le \pi/2$). The topmost unit remains motionless. The desired SLL is set as -25dB and iterative optimizing steps is set as 500 to ensure full convergence. d_{target} is 0.5λ. The design objective is to realize low SLL with fewer elements by only optimizing array distribution without excitations. Eventually, the optimized conformal sparse array reaches SLL of -25.45dB with a minimum element spacing of 0.51λ. The optimization time is 0.32 hour. The total element number of optimized array is 91 with sparse ratio γ of 23%. The optimized conformal sparse element locations are shown in Fig. 7 (a) and its top view is given in Fig. 7 (b). The array factor of optimized sparse conformal array is shown in Fig. 8 (a). The cut plane ϕ=26° of optimized sparse conformal array has the peak SLL of -25.45dB as in Fig. 8 (b). Compared E-plane pattern between initial uniform conformal array (SLL=-17.3dB) and sparse array (SLL=-27.8dB) is given in Fig. 8 (c). The PSLL of optimized sparse conformal array is far less than that of the initial uniform one. The proposed method can be also combined with the optimization of element excitations, not only positions, to realize lower SLL.

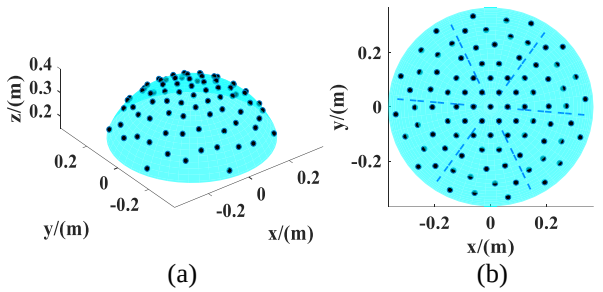

Fig. 7. (a) Sparse hemisphere array. (b) Planform of sparse hemisphere array.

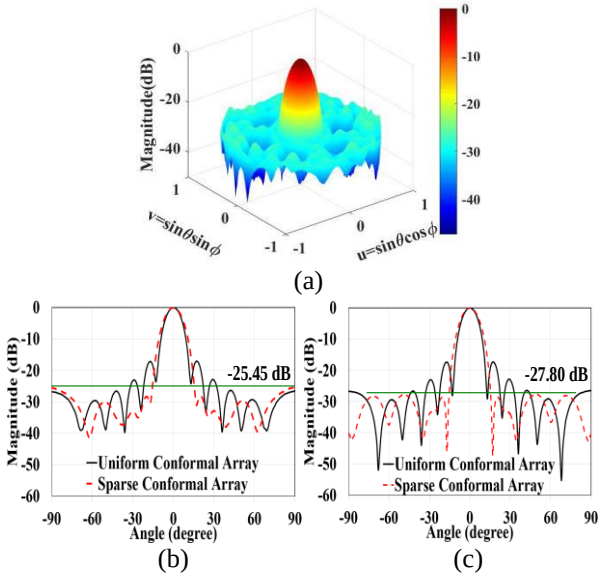

Fig. 8. (a) Optimized pattern. (b) Cut pattern ϕ=26˚ of sparse hemisphere array. (c) E-plane pattern of sparse hemisphere array.

Moreover, we vary the sector number Q to discuss relevant influences on the performance of synthesized patterns for sparse conformal array. The same array configuration is used. Though, the number of optimized sparse array remains nearly constant, different Q brings about different optimizable element number for one sector. Detailed performances of conformal synthesized patterns with different sectors are shown in Table 1, where the PSLL, and total number N are given. It is interesting to note that different sector numbers cause different effects on the radiation property of sparse conformal array. Though more sectors directly reduce the optimizing dimension of conformal array, but it is not linearly related to the better radiation performance. The top view of sparse conformal array element distribution with rotational sectors of Q=5 and Q=8 is respectively shown in Figs. 9 (a) and (b). The 3D pattern of optimized sparse conformal array with Q=8 is shown in Fig. 10 (a). E-plane pattern and cut-plane (ϕ=138˚) pattern of synthesized sparse conformal array is compared with uniform conformal array in Fig. 10 (b), where the PSLL is marked with green line as -26.53 dB in ϕ=138˚.

Table1: Investigation of rotational sector number

Sector Number Q	Element Number of Each Sector	Total Number N'	PSLL (dB)
5	18	91	–24.46
6	15	91	–25.45
7	13	92	–24.25
8	11	89	–26.53
9	10	91	–26.41

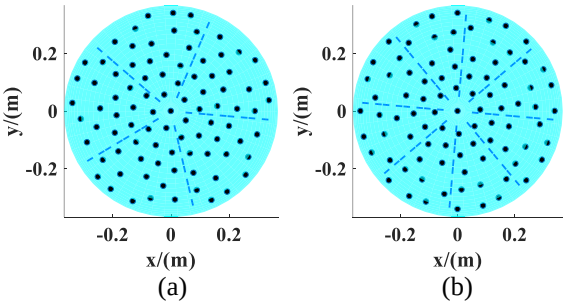

Fig. 9. (a) Element distribution with Q=5. (b) Element distribution with Q=8.

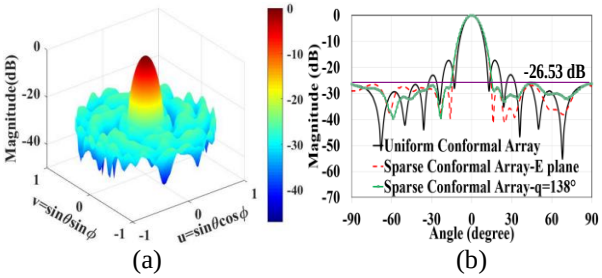

Fig. 10. (a) Optimized pattern. (b) Cut pattern ϕ=138˚ and E-plane pattern of sparse hemisphere array.

Table 2: Investigation of sparse ratio

Total Number N'	Sparse Ratio γ (%)	PSLL (dB)
55	53.4	–27.09
67	43.2	–28.34
73	38.1	–29.91
91	23	–26.60

To further verify the influence of different sparse ratios γ on the performance of synthesized sparse conformal pattern, the array number varies from 55 to 91 with the same initial conformal array geometry of the first numerical example. The rotational sector Q is fixed as 6. The radiation behaviors of synthesized sparse array with different sectors are shown in Table 2, where PSLL, sparse ratio γ and total number N are listed. Though the sparse conformal array allows to have more freedom of element distributions to improve array performance, but not the less element number the better radiation behavior. The optimized sparse conformal array (N'=73) has the best performance of SLL=-29.91dB with sparse ratio of 38.1%, where its E-plane pattern and top view of element layout is respectively shown in Figs. 11 (a) and (b). Then, with the increasing of reduced elements, the radiation behavior of SLL will be raised from -29.91dB to -27.09dB. The E-plane and H-plane pattern of the conformal sparse array ($N' = 55$) is presented in Figs. 12 (a) and (b) respectively, its corresponding top view of element distribution is shown in Fig. 12 (c).

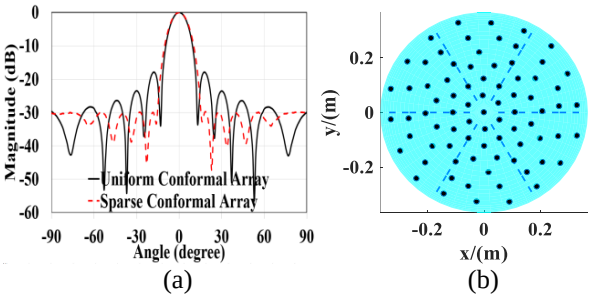

Fig. 11. (a) Synthesized E-plane pattern of sparse hemisphere array. (b) Element distribution with N=73.

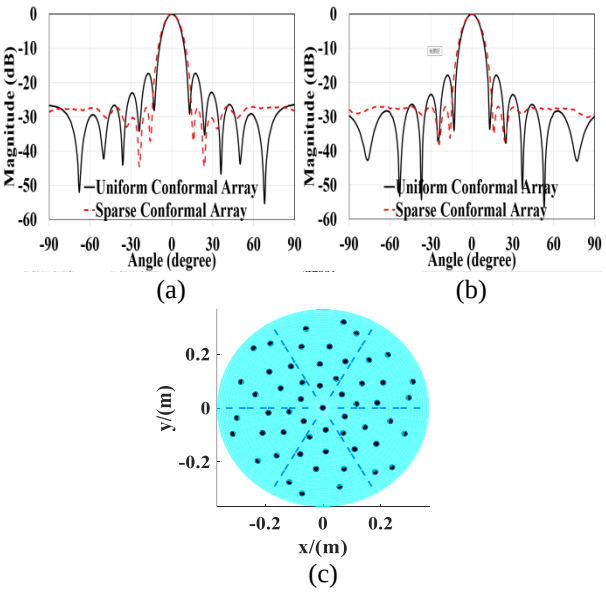

Fig. 12. (a) Synthesized pattern of E-plane for sparse hemisphere array. (b) Synthesized pattern of H-plane for sparse hemisphere array. (c) Element layout with N=55.

Moreover, the comparison behaviors of synthesized patterns with other presented approaches of NSGAII [11] and PSOGA [14] are compared in Table 3. The proposed method has better performance of lower SLL in different sparse ratio conditions compared with the synthesized results optimized by NSGAII and PSOGA.

Table 3: Comparison between SLL of the hemisphere array with different sparse ratio

Number *N'*	**Sparse Ratio γ (%)**	**NSGAII [11]**	**PSOGSA [14]**
55	53.4	-20.1	-24.8
67	43.2	-20.4	-25.1
73	38.1	-21.1	-25.5
91	23.0	-21.6	-26.1

Moreover, the proposed method is further exploited to the synthesis of sparse conformal arrays in wide angle scanning. For the initial λ/2 uniform spacing conformal array, the equivalent antenna number on the hemisphere surface is 265 with nine circular subarrays; see Fig. 13. The radius of the hemisphere is 6λ corresponding to the free wavelength at 2.45GHz. All elements are initially given uniform excitations.

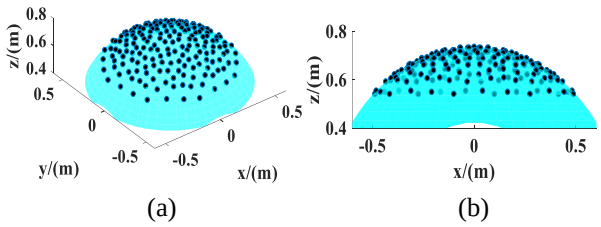

Fig. 13. (a) Uniform hemisphere array. (b) Left view of uniform hemisphere array.

The optimized design of sparse conformal array is selected to divide into 8 symmetric conformal regions with N_Q elements and $2N_Q$ optimizable variables per part. The topmost unit remains motionless. The elements in the fold are limited to the region defined by ($r_q = 3\lambda$, $0 \le \phi_q \le 2\pi/6$, $0 \le \theta_q \le \pi/2$). The scanning angle θ covers from 0˚ to 60˚ with 15˚–uniform space and φ is fixed to be 0˚. The desired SLL is set to be -20dB. Firstly, the optimizable excitations of sparse conformal elements all set to be one. The sparse array reaches the SLL of -20.0dB with a minimum element spacing of 0.51λ within the scanning angle from 0˚ to 45˚ upon 500 iterative optimizing steps, but the SLL of the synthesized sparse conformal array is –18.19 dB in the larger scanning angle of 60˚. The total element number of optimized array is 185. The sparse ratio γ is 30.2%. The optimization requires nearly 1.18 hour.

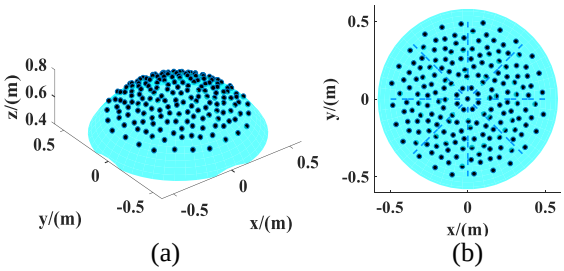

Fig. 14. (a) Sparse hemisphere array. (b) Top view of sparse conformal hemisphere array.

The optimized conformal sparse element locations are shown in Fig. 14 (a) and its top view is given in Fig. 14 (b). The synthesized sparse conformal patterns of equal excitations in different scanning angle are compared with the patterns of initial uniform array in Fig. 15. The black lines are the main cut pattern of uniform array in different

angle scanning and the lines with the cross symbol represent main cut pattern of sparse conformal array in different angle scanning.

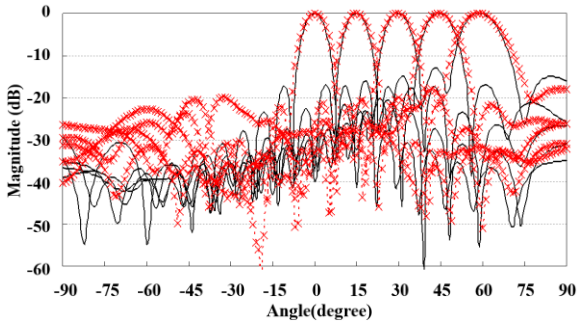

Fig. 15. Comparison of synthesized sparse conformal patterns of equal excitations with the initial uniform conformal array.

To further reduce the sidelobe level, the amplitude excitations of sparse conformal array elements are exploited into the optimizing procedure of the rotational symmetry BSO method. The synthesized sparse conformal patterns of optimized excitations in different angle scanning are presented in Fig. 16. The synthesized results of uniform array with equal excitations, sparse conformal array with equal excitations and optimized excitations are detailed-compared in Table 4. It can be seen that the sparse conformal array with the further optimization of excitations have better performance of the SLL under -25dB in wide angle scanning.

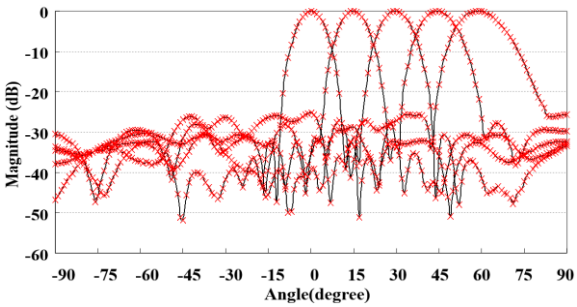

Fig. 16. Synthesized sparse conformal patterns of optimized excitations.

Table 4: Comparison between SLL of the hemisphere array in wide angle scanning

Scanning Angle (θ,ϕ)	**Uniform Array (dB)**	**Sparse Array1 (dB)**	**Sparse Array2 (dB)**
(0˚, 0˚)	-17.24	-22.15	-32.04
(15˚, 0˚)	-17.56	-21.46	-30.96
(30˚, 0˚)	-16.05	-20.64	-30.21
(45˚, 0˚)	-14.81	-20.05	-27.71
(60˚, 0˚)	-12.84	-18.19	-25.67

Moreover, we vary the d_{target} to investigate the relationship between sparse ratio and sparse conformal array performance in wide-angle scanning. The d_{target} varies from 0.45λ to 0.7λ. The minimum element space constraint of d_{target} directly influences the sparse ratio of reconstructed array when fixed aperture. The larger the element space, the higher the sparse ratio. Detailed radiation performance varying d_{target} is shown in Table 5. It is not entirely true that the more elements, the better the radiation behavior such as d_{target}=0.45λ and d_{target}=0.5λ. However, smaller spacing and more elements may make it easier to achieve lower SLL in larger scanning angle, e.g., 60˚. With the further increase of d_{target} from 0.5λ to 0.7λ, the sparse ratio rises to 42.3%. But, the SLL behavior is getting worse especially in larger scanning angle, whose SLL is only -13.76dB in (60˚, 0˚)-scanning angle with d_{target}=0.7λ. The sparse array distribution with d_{target}=0.7λ and its top view is shown in Figs. 17 (a) and (b). The synthesized pattern of sparse array in different angle scanning is shown in Fig. 18 (a) and its 3D pattern in 0˚ and 60˚ is presented in Figs. 18 (b) and (c), respectively.

Table 5: SLL comparison of sparse array varying d_{target} in wide angle scanning

d_{target} **(λ)**	0.45	0.5	0.6	0.7
Sparse Ratio γ **(%)**	24.1	30.2	36.2	42.3
(0˚, 0˚)	-21.36	-22.15	-21.02	-19.39
(15˚, 0˚)	-20.87	-21.46	-20.31	-18.77
(30˚, 0˚)	-20.16	-20.64	-19.24	-16.56
(45˚, 0˚)	-19.78	-20.05	-18.48	-14.98
(60˚, 0˚)	-18.96	-18.19	-17.25	-13.76

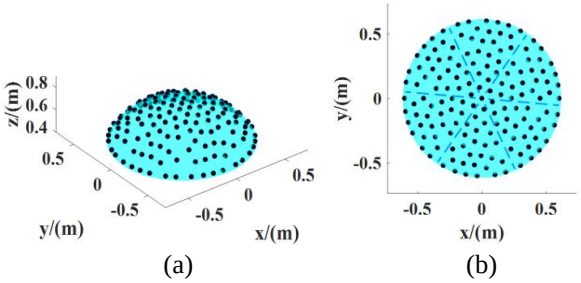

(a) (b)

Fig. 17. (a) Sparse conformal array of d_{target}=0.7λ. (b) Top view of reconstructed sparse conformal array.

With the synthesized sparse conformal array distribution Fig. 14 of above multiple-pattern optimizing numerical example, the reference flat-top pattern of [9] is formed as the desired objective to be optimized and designed by the proposed method. The SLL within the coverage of $\theta \in [-90^{\circ}, -30^{\circ}]$ and $[30^{\circ}, 90^{\circ}]$ is set as

-30dB, the normalized Gain of synthesized conformal pattern fluctuates no more than 1dB up or down in the coverage angle of $\theta \in [-15^{\circ}, 15^{\circ}]$. The synthesized flat-top pattern of sparse conformal array is presented in Fig. 19 with 400 iterative optimizing steps. The optimized *SLL* in the designated region is -29.83 dB, which is close to the expected value of -30dB. The performance of the designed pattern in the fluctuant zone also meets the desired requirement, which is in the range of ± 0.95dB.

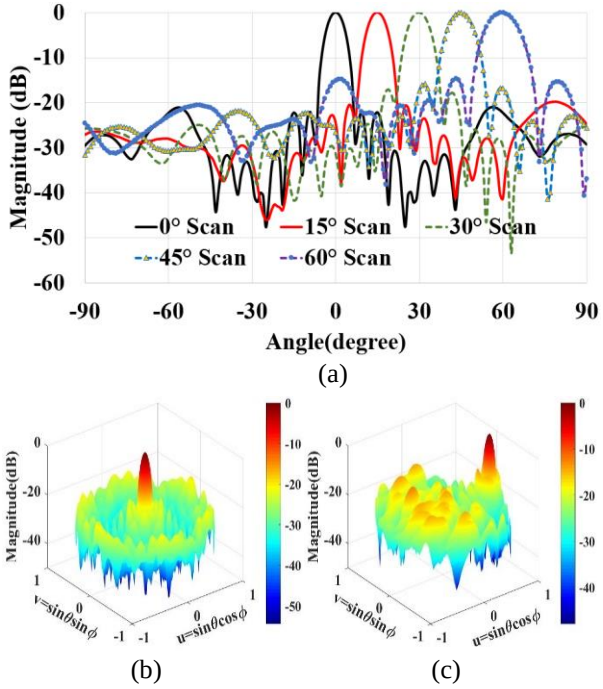

(a) (b) (c)

Fig. 18. (a) synthesized pattern of different scanning angle under d_{target}=0.7λ. (b) 3D pattern of direction 0˚. (c) 3D pattern of direction 60˚.

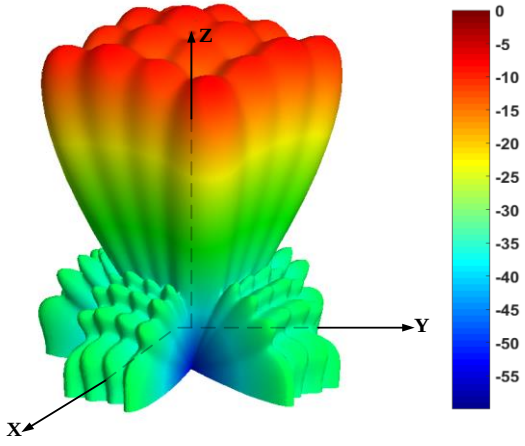

(a)

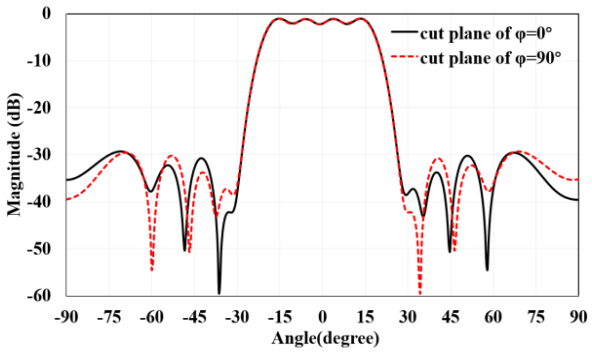

(b)

Fig. 19. Synthesized shaped-beam pattern of sparse conformal array: (a) 3D view of flat-top pattern; (b) different cut plane patterns.

IV. CONCLUSION

A novel hybrid rotationally symmetric sparse conformal array design techniques is introduced in the paper to find the solutions under multiple constraints. Exploiting rotational symmetry not only provides a way to simplify optimal designs, but also accelerate the optimization of larger conformal arrays in the same computing resources. The problem size is reduced by only optimizing element distributions in a small conformal slice of the carrier surface aperture. Numerical results indicate that the proposed method can design sparse conformal arrays with lower sidelobe levels and suppresses grating lobes in wide angle scanning. In addition, we investigate the effects of sparse ratio on synthesized patterns. Further works will take account of the mutual coupling effects on actual conformal array elements into the synthesis and optimizing procedure of large sparse conformal arrays.

ACKNOWLEDGMENT

This work is founded by Natural Science Foundation of China 62001228, 61771246, 61731001, National Key Laboratory Foundation of China under Grant 6142411203108.

REFERENCES

[1] K. Chen, Z. S. He, and C. L. Han, "A modified real GA for the sparse linear array synthesis with multiple constraints," *IEEE Trans. Antennas Propag.*, vol. 54, no. 7, pp. 2169-2173, July 2006.

[2] K. Chen, X. Yun, Z. He, and C. Han, "Synthesis of sparse planar arrays using modified real genetic algorithm," *IEEE Trans. Antennas Propag.*, vol. 55, no. 4, pp. 1067-1073, Apr. 2007.

[3] S. K. Goudos, K. Siakavara, T. Samaras, Elias E. Vafiadis, and J. N. Sahalos, "Sparse linear array

synthesis with multiple constraints using differential evolution with strategy adaptation," *IEEE Antennas Wireless Propag. Lett*., vol. 10, pp. 670-673, July 2011.

[4] H. Liu, H. W. Zhao, W. M. Li, and B. Liu, "Synthesis of sparse planar arrays using matrix mapping and differential evolution," *IEEE Antennas Wireless Propag. Lett*., vol. 15, pp. 1905-1908, Mar. 2016.

[5] K. V. Deligkaris, Z. D. Zaharis, D. G. Kampitaki, S. K. Goudos, I. T.Rekanos, and M. N. Spasos, "Thinned planar array design using Boolean PSO with velocity mutation," *IEEE Trans. Mag*., vol. 45, no. 3, pp. 1490-1493, Mar. 2009.

[6] G. Oliveri, M. Carlin, and A. Massa, "Complex-weight sparse linear array synthesis by Bayesian compressive sampling," *IEEE Trans. Antennas Propag*., vol. 60, no. 5, pp. 2309-2325, May 2012.

[7] G. Oliveri and A. Massa, "Bayesian compressive sampling for pattern synthesis with maximally sparse non-uniform linear arrays," *IEEE Trans. Antennas Propag*., vol. 59, no. 2, pp. 467-481, Feb. 2011.

[8] Y. H. Liu, Q. H. Liu, and Z. P. Nie, "Reducing the number of elements in multiple-pattern linear arrays by the extended matrix pencil methods," *IEEE Trans. Antennas Propag*., vol. 62, no. 2, pp. 652-660, Feb. 2014.

[9] P. F. Gu, G. Wang, Z. H. Fan, and R. S. Chen, "Efficient unitary matrix pencil method for synthesising wideband frequency patterns of sparse linear arrays," *IET Microwaves Antennas and Propagation*, vol. 12, pp. 1871-1876, May 2018.

[10] P. F. Gu, G. Wang, Z. H. Fan, and R. S. Chen, "An efficient approach for the synthesis of large sparse planar array," *IEEE Transactions on Antennas and Propagation*, vol. 67, no. 12, pp. 7320-7330, Aug. 2019.

[11] J. O. Yang, Q. R. Yuan, F. Yang, H. J. Zhou, and Z. P. Nie, "Synthesis of conformal phased array with improved NSGA-II algorithm," *IEEE Trans. Antennas Propag*., vol. 57, no. 12, pp. 4006-4009, June 2009.

[12] M. A. N. Fakher, "Pattern synthesis for a conformal array antenna mounted on a paraboloid reflector using genetic algorithms," *Applied Computational Electromagnetics Society Journal*, vol. 30, no. 2, pp. 230-236, Feb. 2015.

[13] Y. Y. Bai, S. Xiao, C. Liu, and B. Z. Wang, "A hybrid IWO/PSO algorithm for pattern synthesis of conformal phased arrays," *IEEE Trans. Antennas Propag*., vol. 61, no. 4, pp. 2328-2332, Apr. 2012.

[14] B. Sun, C. Liu, Y. Liu, X. Wu, Y. Li, and X. Wang, "Conformal array pattern synthesis and activated elements selection strategy based on PSOGSA algorithm," *Int. J. Antennas Propag*., vol. 6, pp. 1-11, June 2015.

[15] H. L. Li, Y. C. Jiang, Y. Ding, J. Tian, and J. J. Zhou, "Low-sidelobe pattern synthesis for sparse conformal arrays based on PSO-SOCP optimization," *IEEE Access*, vol. 6, pp. 77429-77439, Nov. 2018.

[16] J. L. Guo and J. Y. Li, "Pattern synthesis of conformal array antenna in the presence of platform using differential evolution algorithm," *IEEE Trans Antennas Propag*., vol. 57, no. 9, pp. 2615-2621, Sep. 2009.

[17] T. K. Vo Dai, T. Nguyen, and O. Kilic, "A non-focal Rotman lens design to support cylindrically conformal array antenna," *Applied Computational Electromagnetics Society Journal*, vol. 33, no. 2, pp. 240-243, Feb. 2018.

[18] Z. Li, L. Tan, X. Kang, J. Su, Q. Guo, Y. Yang, and J. Wang, "A novel wideband end-fire conformal antenna array mounted on a dielectric cone," *Applied Computational Electromagnetics Society Journal*, vol. 31, no. 8, pp. 959-966, Aug. 2016.

[19] Y. Shi, "Brain storm optimization algorithm," in *Advances in Swarm Intelligence*, Y. Tan, Y. Shi, Y. Chai, and G. Wang, Eds., Berlin, Heidelberg: Springer Berlin Heidelberg, pp. 303-309, 2011.

[20] C. Sun, H. Duan, and Y. Shi, "Optimal satellite formation reconfiguration based on closed-loop brain storm optimization," *IEEE Computational Intelligence Magazine*, vol. 8, no. 4, pp. 39-51, Nov. 2013.

[21] Z. Xu, X. F. Li, X. T. Meng, and Y. T. Liu, "A distributed brain storm optimization for numerical optimization and graph planarization," *IEEE Access*, vol. 7, pp. 39770-39781, Apr. 2019.

[22] Y. X. Jiang, X. Chen, F. C. Zheng, T. D. Niyato, and X. H. You, "Brain storm optimization-based edge caching in fog radio access networks," *IEEE Transactions on Vehicular Technology*, 2021, early access.

[23] A. Aldhafeeri and Y. R. Samii, "Brain storm optimization for electromagnetic applications: Continuous and discrete," *IEEE Trans. Antennas Propag*., vol. 67, no. 40, pp. 2710-2722, Jan. 2019.

[24] V. Pierro, V. Galdi, G. Castaldi, I. M. Pinto, and L. B. Felsen, "Radiation properties of planar antenna arrays based on certain categories of aperiodic tilings," *IEEE Trans. Antennas Propag*., vol. 53, no. 2, pp. 635-644, Feb. 2005.

[25] A. F. Morabito and P. G. Nicolaci, "Optimal synthesis of shaped beams through concentric ring isophoric sparse arrays," *IEEE Antennas Wireless Propag. Lett*., vol. 16, pp. 979-982, Apr. 2017.

[26] M. D. Gregory, F. A. Namin, and D. H. Werner, "Exploiting rotational symmetry for the design of ultra-wideband planar phased array layouts," *IEEE*

Trans. Antennas Propag., vol. 61, no. 1, pp. 176-184, Jan. 2013.

Pengfei Gu was born in Nanjing, China. He received the B.S. and Ph.D. degrees in Electromagnetic Field and Microwave Technique from the School of Electrical Engineering and Optical Technique, Nanjing University of Science and Technology, Nanjing, China, in 2012 and 2019 respectively. He is currently pursuing post-doctoral in Electronic and Communication Engineering at Nanjing University of Science and Technology. His research interests are antennas, array optimizations, array sparse and computational electromagnetics.

Zhenhong Fan was born in Jiangsu, China, in 1978. He received the M.Sc. and Ph.D. degrees in Electromagnetic Field and Microwave Technique from the Nanjing University of Science and Technology (NJUST), Nanjing, China, in 2003 and 2007, respectively. In 2006, he was a Research Assistant with the Center of wireless Communication, City University of Hong Kong. He is currently a Professor of Electronic Engineering with NJUST. He is the author or a coauthor of over 50 technical articles. His current research interests include computational electromagnetics, and electromagnetic scattering and radiation.

Dazhi Ding received the B.Sc. and Ph.D. degrees in Electromagnetic Field and Microwave Technique from Nanjing University of Science and Technology (NJUST), Nanjing, China, in 2002 and 2007, respectively.

During 2005, he was with the Center of wireless Communication in the City University of Hong Kong, Kowloon, as a Research Assistant. He joined the Department of Electrical Engineering, Nanjing University of Science and Technology (NJUST), Nanjing, China, where he became a Lecturer in 2007. In 2014, he was promoted to Full Professor in NJUST. He was appointed Head of the Department of Communication Engineering, NJUST in September 2014. He is the author or coauthor of over 30 technical papers. His current research interests include computational electromagnetics, electromagnetic scattering and radiation. He has authored or coauthored more than 80 papers. He is the recipient of the Foundation for China Excellent Young Investigators presented by the National Science Foundation (NSF) of China in 2015.

Rushan Chen received the B.Sc. and M.Sc. degrees from the Department of Radio Engineering, Southeast University, China, in 1987 and 1990, respectively, and the Ph.D. degree from the Department of Electronic Engineering, City University of Hong Kong, in 2001.

He joined the Department of Electrical Engineering, Nanjing University of Science and Technology (NJUST), China, where he became a Teaching Assistant in 1990 and a Lecturer in 1992. Since September 1996, he has been a Visiting Scholar with the Department of Electronic Engineering, City University of Hong Kong, first as Research Associate, then as a Senior Research Associate in July 1997, a Research Fellow in April 1998, and a Senior Research Fellow in 1999. From June to September 1999, he was also a Visiting Scholar at Montreal University, Canada. In September 1999, he was promoted to Full Professor and Associate Director of the Microwave and Communication Research Center in NJUST, and in 2007, he was appointed as the Head of the Department of Communication Engineering, NJUST. He was appointed as the Dean in the School of Communication and Information Engineering, Nanjing Post and Communications University in 2009. And in 2011 he was appointed as Vice Dean of the School of Electrical Engineering and Optical Technique, NJUST. Currently, he is a principal investigator of more than 10 national projects. His research interests mainly include computational electromagnetics, microwave integrated circuit and nonlinear theory, smart antenna in communications and radar engineering, microwave material and measurement, RF-integrated circuits, etc. He has authored or coauthored more than 260 papers, including over 180 papers in international journals.

Analysis for Scattering of Non-homogeneous Medium by Time Domain Volume Shooting and Bouncing Rays

Jun Li, Huaguang Bao, and Dazhi Ding

School of Electronic and Optical Engineering
Nanjing University of Science and Technology, Nanjing, Jiangsu Province 210094, China
hgbao@nujst.edu.cn

Abstract ─ In order to evaluate scattering from hypersonic vehicles covered with the plasma efficiently, time domain volume shooting and bouncing rays (TDVSBR) is first introduced in this paper. The new method is applied to solve the transient electromagnetic scattering from complex targets, which combines with non-homogeneous dielectric and perfect electric conducting (PEC) bodies. To simplify the problem, objects are discretized into tetrahedrons with different electromagnetic parameters. Then the reflection and transmission coefficients can be obtained by using theory of electromagnetic waves propagation in lossy medium. After that, we simulate the reflection and transmission of rays in different media. At last, the scattered fields or radiation are solved by the last exiting ray from the target. Compared with frequency-domain methods, time-domain methods can obtain the wideband RCS efficiently. Several numerical results are given to demonstrate the high efficiency and accuracy of this proposed scheme.

Index Terms ─ Non-homogeneous dielectric, time domain, Volume Shooting and Bouncing Rays (VSBR).

I. INTRODUCTION

In recent years, with the application of short pulse ultra wideband (UWB) communication in target recognition and remote sensing, electromagnetic (EM) time domain analysis method has received more and more attention. All kinds of numerical methods in computational EM have been widely used in various fields. Especially, the time-domain high frequency approximation methods have attracted more and more attention in the scattering analysis of electrically large structures.

With the rapid development of computer technology, the simulation capability of full-wave methods have been improved greatly. But it is also tedious to solve scattering of large electrical structures with full-wave methods [1-3]. Therefore, it is significant for seeking a superior-efficiency method to analyze the scattering from electrically large structures. Moreover, high frequency approximation methods fulfill the requirements in this project. In fact, with the increasing electrically size of the target, mutual coupling effects between elements have been reduced gradually. Therefore, the results of the high frequency approximation methods are more and more close to results of full wave numerical methods. Above all, high frequency approximation methods have crucial values in engineering application for the rapid analysis of EM scattering of electrically large targets. Time-domain full wave methods include the Finite Difference Time Domain (FDTD) [4-6], the Time Domain Finite Element Method (FETD) [7,8], and the Time Domain Integral Equation Method (TDIE) [9,10], etc. One of the advantages for the above time domain numerical method is that accurate EM simulation results can be obtained from the targets with complex shapes and materials. However, the above methods also have their own defects [11]. For example, the cumulative error of time stepping, the truncation error of spatial sampling and the numerical error of the radiation boundary condition. Meanwhile, time-domain full wave methods mentioned above have a common fatal defect: when the electric size of the scattering/radiation target is large, they all have a great demand on computer memory and are time-consuming. In contrast, the time domain high frequency approximation methods are the best effective way to solve the above issues. Compared with time-domain full wave methods, the advantages of time-domain high frequency approximation methods are remarkable. They cost less computing memory but have fast computing speed. According to different situations, time domain high frequency approximation methods can also combine with time domain full wave methods [12,13]. At present, it is common to analyze perfect electrically conducting (PEC) and homogeneous medium through high frequency approximation methods. For PEC or homogeneous medium, we usually use Physical Optics (PO) or Shooting and Bouncing Rays (SBR) to analyze the scattering or radiation of targets [14-16]. For non-homogeneous medium, such as plasma, the plasma sheath is equivalent to layered homogeneous dielectric in high frequency approximation methods

Submitted On: May 6, 2020
Accepted On: December 6, 2020
https://doi.org/10.47037/2020.ACES.J.360303

[17,18]. Obtaining the reflection coefficient of plasma sheath by recursion formulas. However, if the situation is complicated that the speed of hypersonic vehicles reached more than 10 Mach. Then the aircraft sheath electron obvious change causes dielectric constant change irregularly. Time domain full wave methods cannot solve hypersonic vehicles efficiently. As a result, we urgently need a new method to solve this problem.

In this paper, a novel method is proposed to analyze the scattering of objects, which are combined with non-homogeneous medium and PEC bodies. When the rays are propagating in non-homogeneous medium, they transmit and reflect on the interface of different medium. After multiple reflection and refraction, the rays leave objects and finally the far field integration is calculated by the principle of Physical Optics. The paper is organized as follows. Section II contains EM computing formulas of TDVSBR in detail. In Section III. numerical examples demonstrating the accuracy and efficiency of the method are presented. In Section IV, we conclude the advantages of the new method in solving the scattering of non-homogeneous dielectric and metal mixed target.

II. THEORY AND FORMULATION

A. Shooting and Bouncing Ray (VSBR) modeling framework involving dielectrics and perfect conductors

The main task of the spread of wave in dielectrics in an SBR based approach is to calculate the reflected and transmitted waves at material interfaces. In most case, the wave will generate nonuniform wave when wave transmitted between the nonuniform lossy medium. It means the directions of constant phase and amplitude plane of the wave are not identical, and there is an angle $0 \le \rho \le \pi/2$ between them (for uniform wave ρ=0). Similar to [19], the scenario to investigate is shown in Fig. 1, where a nonuniform wave propagates from medium 1 to medium 2. The complex propagation vector γ can be generally represented as $\gamma=\alpha+j\beta$ with α represents the amplitude vector and β represents the phase vector. In [20], the relevant work of solving the reflection and transmission coefficients of the nonuiform wave propagates in the nonuiform medium is presented.

The propagation vector in medium i can be express in real-angle form as:

$$\begin{aligned}\gamma_i=&\alpha_i\left(\sin\varsigma_i\hat{e}_x+\cos\varsigma_i\hat{e}_z\right)\\&+j\beta_i\left(\sin\xi_i\hat{e}_x+\cos\xi_i\hat{e}_z\right)\end{aligned}, \tag{1}$$

where $\varsigma_i=\xi_i+\rho_i$ and $i=1,2$.

The intrinsic propagation constant of medium i is only determined by the properties of material, which can be expressed by:

$$\begin{aligned}\gamma_{0i}&=\alpha_{0i}+j\beta_{0i}=jk_0\sqrt{\varepsilon_{ri}\mu_{ri}}\\&=\frac{\omega}{c}\sqrt{|\varepsilon_{ri}||\mu_{ri}|}\left(\sin\sigma+j\cos\sigma\right)\end{aligned}, \tag{2}$$

where $\alpha_{0i}=\frac{\sqrt{\varepsilon_{ri}\mu_{ri}}}{c}sin\sigma$, $\beta_{0i}=\frac{\sqrt{\varepsilon_{ri}\mu_{ri}}}{c}cos\sigma$.

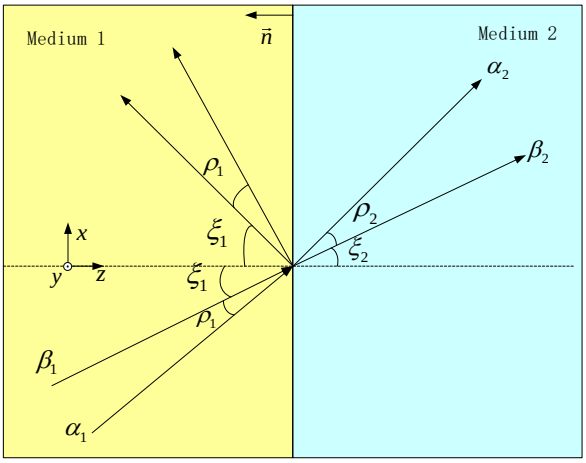

Fig. 1. Angles and directions to describe the wave propagation at the transition of two lossy media.

According to phase continuity at the interface of the two media and the law of Snell, we can obtain:

$$\begin{aligned}\alpha_1=&\sqrt{\frac{\beta_{01}^2-\alpha_{01}^2}{2}}\\&\cdot\sqrt{\sqrt{1+\left(\frac{2\alpha_{01}\beta_{01}}{\left(\beta_{01}^2-\alpha_{01}^2\right)\cos\rho_1}\right)^2}-1}\end{aligned}, \tag{3}$$

$$\begin{aligned}\beta_1=&\sqrt{\frac{\beta_{01}^2-\alpha_{01}^2}{2}}\\&\cdot\sqrt{\sqrt{1+\left(\frac{2\alpha_{01}\beta_{01}}{\left(\beta_{01}^2-\alpha_{01}^2\right)\cos\rho_1}\right)^2}+1}\end{aligned}. \tag{4}$$

By defining:

$$\gamma_{1t}=\alpha_1\sin\varsigma_1+j\beta_1\sin\xi_1. \tag{5}$$

We can obtain:

$$\alpha_2=\sqrt{\frac{1}{2}\left(\left|\gamma_{1t}\right|^2+\mathrm{Re}\left(\gamma_{02}^2\right)+\left|\gamma_{1t}^2-\gamma_{02}^2\right|\right)}, \tag{6}$$

$$\beta_2=\sqrt{\frac{1}{2}\left(\left|\gamma_{1t}\right|^2-\mathrm{Re}\left(\gamma_{02}^2\right)+\left|\gamma_{1t}^2-\gamma_{02}^2\right|\right)}. \tag{7}$$

For TE polarization, we obtain:

$$R_{TE}=\frac{\mu_2A_1-\mu_1A_2}{\mu_2A_1+\mu_1A_2}, \tag{8}$$

$$T_{TE} = \frac{2\mu_2 A_1}{\mu_2 A_1 + \mu_1 A_2}, \tag{9}$$

where $A_1 = \alpha_1 \cos\varsigma_1 + j\beta_1 \cos\xi_1$ and $A_2 = \alpha_2 \cos\varsigma_2 + j\beta_2 \cos\xi_2$.

R represents the reflection coefficient and T represents the transmission coefficient. From the expression, there is no relationship between the reflection coefficient and the frequency of incident wave. So is the transmission coefficient.

In the same way, for TM polarization, we obtain:

$$R_{TM} = \frac{-\varepsilon_2 A_1 + \varepsilon_1 A_2}{\varepsilon_2 A_1 + \varepsilon_1 A_2}, \tag{10}$$

$$T_{TM} = \frac{2\varepsilon_2 A_1}{\varepsilon_2 A_1 + \varepsilon_1 A_2}. \tag{11}$$

According to reflection and transmission coefficient, we can achieve the reflection and transmission field. To calculate the scattered far field, we not only need the equivalent electric currents, but also need the equivalent magnetic currents. According to the Stratton-Chu formula, we deduce the scattered far field of physical optics. The scattered far field is obtained by accumulation of the electric current and the magnetic current contributions.

B. Calculation of broadband RCS

When the rays comes from the air into the medium, the total field on the surface is as followed:

$$\vec{E} = \vec{E}^i + \vec{E}^r, \tag{12}$$

$$\vec{H} = \vec{H}^i + \vec{H}^r. \tag{13}$$

$\vec{E}$ and $\vec{H}$ represent the total electric and magnetic field on the surface of the object respectively. *i* represent the incident and *r* represent the reflection. The far field is obtained by solving the current and magnetic current on the surface of the medium.

$\vec{E}^i\left(\vec{r}',t\right)$ is the time series of the incident electric field when it intersects with the target at the last time:

$$\vec{E}^i\left(\vec{r}',t\right) = \vec{e}_0^i\left(\vec{r}',t\right)s(t), \tag{14}$$

where $s(t)$ represents the incident pulse. It is known from the Fourier transform that the frequency domain multiplication corresponds to the convolution of the time domain:

$$\vec{E}_J^s(\vec{r},t) = \frac{1}{4\pi rc}\hat{s}\times\int_s \hat{s}\times\left\{\hat{n}\times\left[\begin{array}{l} k_i\times\vec{e}_0^i\left(\vec{r}',t\right) \\ +k_s\times\left(\overline{\overline{R}}(t)*\vec{e}_0^i\left(\vec{r}',t\right)\right)\end{array}\right]\right\} \times\frac{\partial}{\partial t}s\left(t-t_d\right)ds, \tag{15}$$

$$\vec{E}_M^s(\vec{r},t) = -\frac{1}{4\pi rc}\hat{s}\times\int_s \hat{n}\times\left[\begin{array}{l}\vec{e}_0^i\left(\vec{r}',t\right) \\ +\left(\overline{\overline{R}}(t)*\vec{e}_0^i\left(\vec{r}',t\right)\right)\end{array}\right]\frac{\partial}{\partial t}s\left(t-t_d\right)ds, \tag{16}$$

$$\vec{E}^s(\vec{r},t) = \vec{E}_J^s(\vec{r},t) + \vec{E}_M^s(\vec{r},t), \tag{17}$$

where Z_0 represents the wave impedance of free space, $\vec{r}$ is the position vector of the observation point and $\vec{r}'$ is position vector of any element of the target surface. *r* represents the distance from surface element to observation point, $\hat{n}$ is the unit normal vector of the surface element. $t_d = \left(\hat{i}\cdot\vec{r}_0 - \hat{s}\cdot\vec{r}'\right)/c$ represents the time delay. The time domain response sequence is transformed by discrete Fourier transform, and the corresponding frequency response sequence can be obtained. Finally, we will obtain the broadband RCS, after the frequency domain response sequence is divided by the frequency domain sequence of the incident pulse signal.

When the rays emitted from the medium into the air, the total field on the surface is as followed:

$$\vec{E} = \vec{E}^t, \tag{18}$$

$$\vec{H} = \vec{H}^t, \tag{19}$$

$$\vec{H}^t = \frac{1}{Z_0}\left(k_t\times\vec{E}^t\right), \tag{20}$$

where k_t represents the direction of transmission of rays.

$\vec{E}^i\left(\vec{r}',t\right)$ represents the time series of the transmission electric field out of the target:

$$\vec{E}^t\left(\vec{r}',t\right) = \vec{e}_0^t\left(\vec{r}',t\right)s(t), \tag{21}$$

$$\vec{E}_J^s(\vec{r},t) = \frac{1}{4\pi rc}\hat{s}\times\int_s \hat{s}\times\left\{\hat{n}\times\left[k_t\times\vec{e}_0^{\,t}\left(\vec{r}',t\right)\right]\right\} \cdot\frac{\partial}{\partial t}s\left(t-t_d\right)ds, \tag{22}$$

$$\vec{E}_M^s(\vec{r},t) = -\frac{1}{4\pi rc}\hat{s}\times\int_s \hat{n}\times\vec{e}_0^{\,t}\left(\vec{r}',t\right)\frac{\partial}{\partial t}s\left(t-t_d\right)ds, \tag{23}$$

$$\vec{E}^s(\vec{r},t) = \vec{E}_J^s(\vec{r},t) + \vec{E}_M^s(\vec{r},t). \tag{24}$$

III. NUMERICAL RESULTS

The first example and the second example are carried out on the computer of Intel(R) Core(TM)2 Quad CPU Q9500 equipped with 8GB RAM at 2.83GHz and the edition of FEKO is 7.0. TDVSBR and FDVSBR are coded by FORTRAN. This is a big cube which is made up of 8 smaller cubes and the length of each small cube is 0.2m in Fig. 2. When the frequency is 3 GHz, the relative dielectric constant and electrical conductivity of

the dark cubes are respectively $\varepsilon_r = 0.95$, $\sigma = 0.067$. The light cubes are $\varepsilon_r = 0.8$, $\sigma = 0.085$. The permeability μ_r of them are (1.0,0). The center frequency of the incident pulse is $f_0 = 2$ GHz, and the effective frequency band of the calculation is $1 \sim 3$ GHz. The direction of incidence of the pulse is $\theta = 45°$, $\varphi = 0°$.

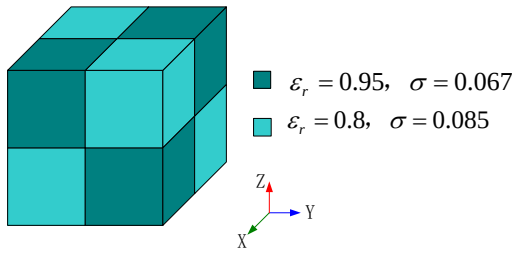

Fig. 2. Non-homogeneous medium cubes.

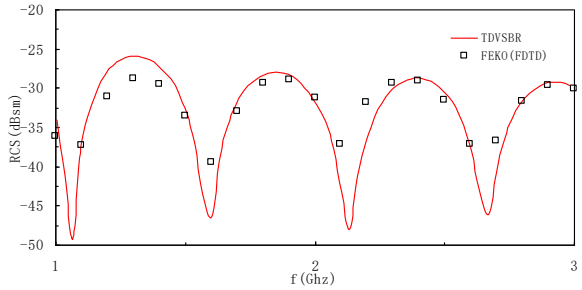

Fig. 3. Broadband monostatic RCS(VV) of non-homogeneous medium cube.

Table 1: The efficiency of different methods

	TDVSBR	**FEKO(FDTD)**
Time(s)	5	1282
Memory (MB)	4.8	191

The result of TDVSBR and FEKO make a good agreement in Fig. 3. Table 1 shows that the time of FEKO(FDTD) is about 256 times slower than TDVSBR in first example. TDVSBR has great advantages than FEKO(FDTD).

The second example shows a complex mixed target of rectangular metal cavity (6m*6m*10m) and non-homogeneous dielectric (3m*3m*2m) in Fig. 4. Dielectric parameters and permeability of the light purple rectangular are $\varepsilon_r = 4$, $\sigma = 0.033$ and deep purple rectangular are $\varepsilon_r = 5$, $\sigma = 0.0825$. $\theta = 15°, \varphi = 0°$ is the incidence direction and observation direction.

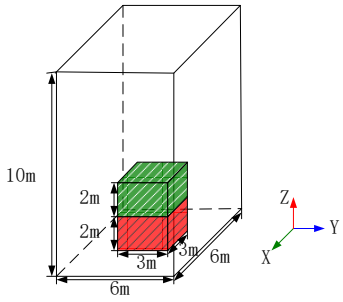

Fig. 4. A complex mixed target of rectangular metal cavity and non-homogeneous dielectric.

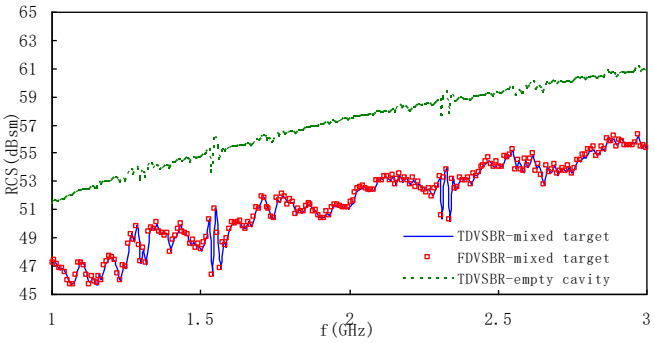

Fig. 5. The broadband monostatic RCS(vv) of empty cavity and the combined target.

In Fig. 5, the RCS of combined target is higher than the empty cavity and the gap reaches more than 10dB. Because of the electric size of the target is too large, we need to use subdivision technique to increase the efficiency of the new method. We use the corresponding gird of 300MHz to fit the shape of the mixed target, and subdivide the gird 3 times through the subdivision technique. The time-consuming of TDVSBR is 198s, and the memory of it is about 10 MB.

The third example is shown in Fig. 6, It calculates the broadband RCS of a metal warhead at a height of 30km and a speed of 10 Maher. The radius of warhead is 0.1m and the length is 0.2m. The plasma sheath radius of the ionized plasma is 0.4m and the length is 0.6m. the central frequency of the incident pulse is $f_0 = 6$ GHz, and the effective frequency band of the calculation is from 3 to 12GHz. The direction of incidence of the pulse is $\theta = 90°$, $\varphi = 0°$. In this method, we consume the relative dielectric constant and electrical conductivity are constant at center frequency of the interested frequency band. When the dispersion effect is obvious, this method has its disadvantages.

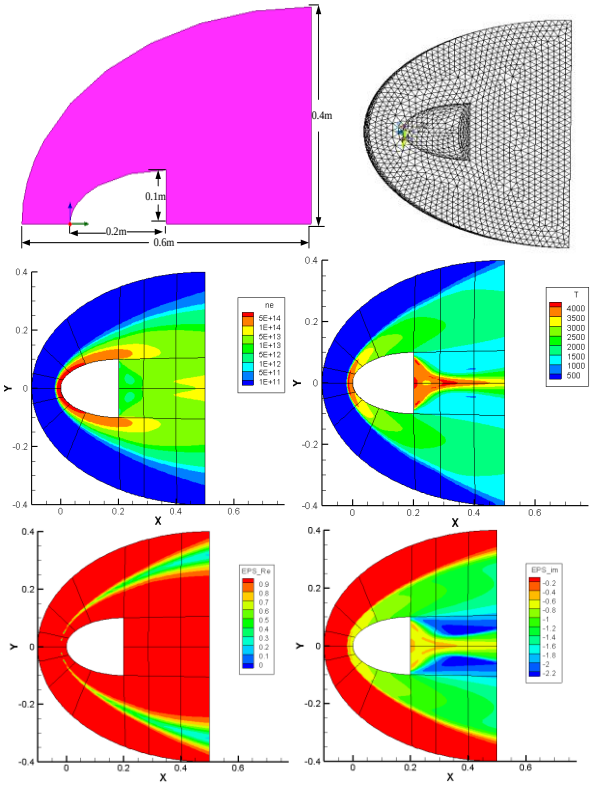

Fig. 6. The model of plasma sheath.

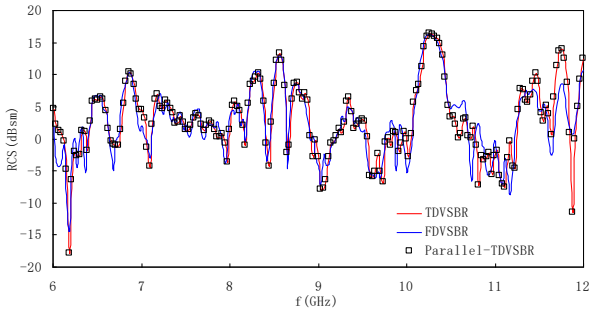

Fig. 7. Broadband monostatic RCS(vv) of plasma sheath.

In Fig. 7, the result of TDVSBR and FDVSBR are in good agreement. We do not consider the despersion of the plasma in TDVSBR. Strictly writing, the despersion of the plasma has effect on the way of the propagation of the rays. If ways have always change with the time. Then TDVSBR has to trace the path of the rays at every point of time. It must time-consuming and we do not accept this TDVSBR. Therefore, we weaken the influence of despersion on plasma. In our work, ε_r, μ_r and σ of dielectric are fixed value. The value of three parameters are selected at the center frequency. In FDVSBR, ε_r, μ_r and σ of dielectric in plasma sheath change with the frequency of the incident. However, in TDVSBR, when the frequency of the incident is changing, ε_r, μ_r and σ of dielectric in plasma sheath are fixed. When the band of incident is not wide, ε_r, μ_r and σ of dielectric in plasma sheath have little impact on RCS at different frequency of the incident. ε_r, μ_r have influence on the way of the ray. If the way of the ray changes at different frequencies of incident, TDVSBR would time-consuming and lose the its advantage. For convenience, we fix ε_r, μ_r and σ of dielectric in plasma sheath at different frequencies of incident.

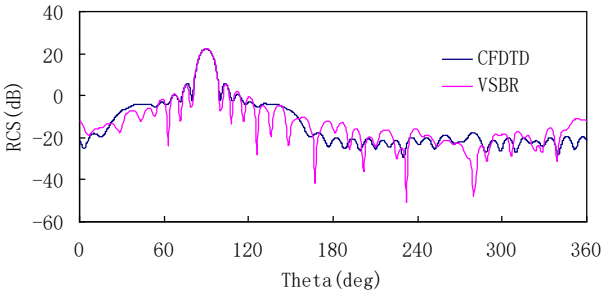

Fig. 8. Bistatic RCS(vv) of plasma sheath at 3GHz.

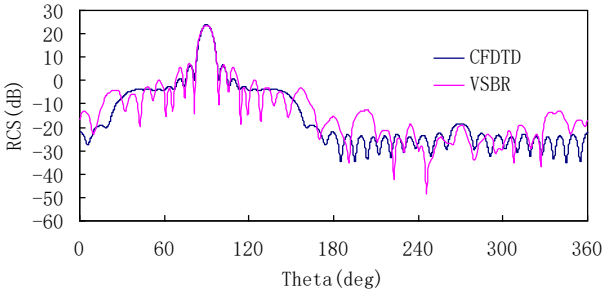

Fig. 9. Bistatic RCS(vv) of plasma sheath at 3.5GHz.

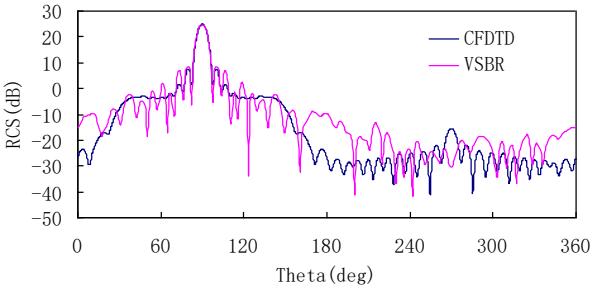

Fig. 10. Bistatic RCS(vv) of plasma sheath at 4GHz.

In Fig. 8, Fig. 9 and Fig. 10, observation range is $\varphi = 0°$, $\theta = 0 \sim 360°$. The results of CFDTD and TDVSBR are in good agreement. ε_r, μ_r and σ of plasma has little effect on the scattering, therefore we

use TDVSBR to evaluate the the scattering of plasma.

As shown in Fig. 11, the time domain response of CFDTD and TDVSBR has a good agreement at the observation point (100m,0,0). In order to simulate electromagnetic characteristics of plasma sheath conveniently, researchers commonly use different medium to simulate plasma sheath.

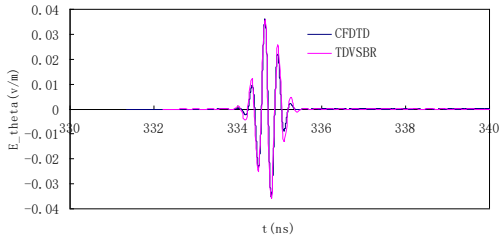

Fig. 11. The time domain response of plasma sheath at (100m,0,0).

As shown in Table 2, TDVSBR has great advantages than full wave methods in analyze of electrical large plasma sheath. TDVSBR costs less memory and has higher computing speed than CFDTD.

Table 2: The comparison of computational efficiency between the CFDTD method and TDVSBR method, and the two methods are used on a single CPU code

	TDVSBR	**CFDTD**
Time(h)	0.24	80
Memory(G)	1.2	30

IV. CONCLUSION

A novel high frequency approximation method based on SBR to calculate the scattering of non-homogeneous dielectric and metal mixed target is presented. According to the time and memory consumption, the new method is more efficient than accurate method, and the accuracy of the new method is acceptable. An important breakthrough of the new method in high approximation method is to calculate the non-homogeneous dielectric and metal mixed target, especially the complex target, such as hypersonic vehicle.

ACKNOWLEDGMENT

This work was supported in part by Natural Science Foundation of 61931021, 61890541, National Key Lab of Science and Technology on space microwave under Grant 2018SSFNKLSMT-06, and Grant HTKJ2020KL504012, by the Fundamental Research Funds for the Central Universities No. 30918011202.

REFERENCES

[1] L. Wang, M. Wang, K. Zhang, W. Cui, H. Zheng, and E. Li, "Three-dimensional spherical-shaped UPML for FDTD with cubic lattices," *Applied Computational Electromagnetics Society Journal*, vol. 34, no. 3, pp. 425-433, 2019.

[2] J. Cao, R. S. Chen, Y. L. Hu, and S. F. Tao, "A higher order Nyström scheme for marching-on-in-time solution of time-domain integral equation," *IEEE Trans. Antennas Propagat.*, vol. 63, pp. 2762-2767, 2015.

[3] Y. L. Hu and R. S. Chen, "Analysis of scattering from composite conducting dispersive dielectric objects by Time-domain volume-surface integral equation," *IEEE Trans. Antennas Propagat.*, vol. 64, pp. 1984-1989, 2016.

[4] J. G. Maloney, G. S. Smith, and W. R. Scott, "Accurate computation of the radiation from simple antennas using the finite-difference time-domain method," *IEEE Trans. Antennas Propagat.*, vol. 38, pp. 1059-1068, 1990.

[1] H. Bao and R. Chen, "An efficient domain decomposition parallel scheme for leapfrog ADI-FDTD method," *IEEE Trans. Antennas Propagat.*, vol. 65, pp. 1490-1494, 2017.

[5] Z. Sun, L. Shi, Y. Zhou, B. Yang, and W. Jiang, "FDTD evaluation of LEMP considering the lossy dispersive ground," *Applied Computational Electromagnetics Society Journal*, vol. 33, no. 1, pp. 4-17, 2018.

[6] M. Dong, J. Chen, and A. Zhang, "A convolutional perfectly matched layer (CPML) for the fourth-order one-step leapfrog HIE-FDTD method," *Applied Computational Electromagnetics Society Journal*, vol. 33, no. 1, pp. 1-6, 2018.

[7] Z. Lou and J.-M. Jin, "Modeling and simulation of broad-band antennas using the time-domain finite element method," *IEEE Trans. Antennas Propagat.*, vol. 53, pp. 4099-4110, 2005.

[8] Y. L. Hu and R. S. Chen, "Hybridization of curvilinear time-domain integral equation and time-domain optical methods for electromagnetic scattering analysis," *IEEE Trans. Antennas Propagat.*, vol. 46, pp. 318-324, 1998.

[9] S. P. Walker and C. Y. Leung, "Parallel computation of time-domain integral equation analyses of electromagnetic scattering and RCS," *IEEE Trans. Antennas Propagat.*, vol. 45, pp. 614-619, 1997.

[10] X. Zhou and T. J. Cui, "A closed-form representation of time-domain far fields based on physical optics," *IEEE Trans. Antennas Propagat.*, vol. 11, pp. 965-968, 2012.

[11] A. Altintas and P. Russer, "Time-domain equivalent edge currents for transient scattering," *IEEE Trans. Antennas Propag*., vol. 49, pp. 602-606, 2001.
[12] L. X. Yang, D. B. Ge, and B. Wei, "Time-domain physical-optics method for transient scattering analysis," *The 2006 4th Asia-Pacific Conference on Environmental Electromagnetics*, Dalian, China, pp. 861-864, 2006.
[13] A. Boag and C. Letrou, "Multilevel fast physical optics algorithm for radiation from non-planar apertures," *IEEE Trans. Antennas Propag*., vol. 53, pp. 2064-2072, 2005.
[14] C. Pienaar, J. W. Odendaal, J. C. Smit, J. Joubert, and J. E. Cilliers, "RCS results for an electrically large realistic model airframe," *Applied Computational Electromagnetics Society Journal*, vol. 45, pp. 87-90, 2018.
[15] D. Shi, X. Tang, C. Wang, M. Zhao, and Y. Gao, "A GPU implementation of a shooting and bouncing ray tracing method for radio wave propagation," *Applied Computational Electromagnetics Society Journal*, vol. 32, pp. 614-620, 2017.
[16] W. Wong and D Cheng, "High-frequency scattering from a conducting cylinder with an inhomogeneous plasma sheath," *IEEE Trans. Antennas Propag*., vol. 17, pp. 208-215, 1969.
[17] S. H. Liu and L. X. Guo, "Analyzing the electromagnetic scattering characteristics for 3-D inhomogeneous plasma sheath based on PO method," *IEEE Transactions on Plasma Science*, vol. 44, pp. 2838-2843, 2016.
[18] R. Radcliff and C. Balanis, "Modified propagation constants for nonuniform plane wave transmission through conducting media," *IEEE Trans. Geosci. Remote Sens*., vol. 20, pp. 408-411, 1982.
[19] J. Roy, "New results for the effective propagation constants of nonuniform plane waves at the planar interface of two lossy media," *IEEE Trans. Antennas Propag*., vol. 51, no. 6, pp. 1206-1215, 2003.
[20] R. Brem and T. F. Eibert, "A shooting and bouncing ray (SBR) modeling framework involving dielectrics and perfect conductors," *IEEE Trans. Antennas Propag*., vol. 63, no. 8, pp. 3599-3609, 2003.

Jun Li was born in Taizhou, China. He received the B.S. degree in Optical Engineering from the School of Electrical Engineering and Optical Technique, Zijin College of Nanjing University of Science and Technology, Nanjing, China, in 2013. He is currently pursuing his Ph.D. degree in Electronic Engineering at Nanjing University of Science and Technology. The interest of his research are antennas, high frequency method and computational electromagnetics.

Huaguang Bao received the B.S. and Ph.D. degrees in Electromagnetic Field and Microwave Technique from Nanjing University of Science and Technology (NUST), Nanjing, China, in 2011 and 2017, respectively. In 2017, he was a Post-Doctoral Scholar with the Computational Electromagnetics and Antennas Research Laboratory, Department of Electrical Engineering, Pennsylvania State University, University Park, PA, USA. He is currently an Associate Professor with the Electronic Engineering of NJUST. His research interests include semiconductor simulation, RF-integrated circuits, and computational electromagnetics.

Dazhi Ding was born in Jiangsu, China, in 1979. He received the B.S. and Ph.D. degrees in Electromagnetic Field and Microwave Technique from Nanjing University of Science and Technology (NUST), Nanjing, China, in 2002 and 2007, respectively. During 2005, he was with the Center of Wireless Communication in the City University of Hong Kong, Kowloon, as a Research Assistant. He is currently an Associate Professor with the Electronic Engineering of NJUST. He is the author or co-author of over 30 technical papers. His current research interests include computational electromagnetics, electromagnetic scattering, and radiation.

Neural-Network-Based Multiobjective Optimizer for Dual-Band Circularly Polarized Antenna

Tarek Sallam [1,2], Ahmed M. Attiya [3], and Nada Abd El-Latif [3]

[1] Faculty of Electronic and Information Engineering
Huaiyin Institute of Technology, Huai'an 223002, Jiangsu, China

[2] Faculty of Engineering at Shoubra, Benha University, Cairo, Egypt
tarek.sallam@feng.bu.edu.eg

[3] Microwave Engineering Dept., Electronics Research Institute (ERI), Cairo, Egypt
attiya@eri.sci.eg

Abstract ─ A multiobjective optimization (MOO) technique for a dual-band circularly polarized antenna by using neural networks (NNs) is introduced in this paper. In particular, the optimum antenna dimensions are computed by modeling the problem as a multilayer feed-forward neural network (FFNN), which is two-stage trained with I/O pairs. The FFNN is chosen because of its characteristic of accurate approximation and good generalization. The data for FFNN training is obtained by using HFSS EM simulator by varying different geometrical parameters of the antenna. A two strip-loaded circular aperture antenna is utilized to demonstrate the optimization technique. The target dual bands are 835–865 MHz and 2.3–2.35 GHz.

Index Terms ─ Circularly polarized antenna, feed-forward neural networks, multiobjective optimization.

I. INTRODUCTION

Design of multiband single-fed circularly polarized antenna represents a complicated problem due to the requirements of obtaining matching properties combined with two equal orthogonal fields and phase shift of $\pm\pi/2$. For a single band circular polarized printed antenna, these conditions can be obtained by using symmetric shape structure like square or circular loaded by diagonal perturbations. By controlling the area of these perturbations compared to the total are of the printed antenna, it would be possible to generate two equal orthogonal modes along the printed antenna with the required phase shift [1, 2]. The design of these antenna configurations can be formulated analytically by using cavity model [1]. However, for the case of multiband single-fed circularly polarized antenna the problem becomes more complicated and cannot be directly represented in a simple cavity model. On the other hand, numerical simulation tools can be used to simulate different configurations to obtain the corresponding properties for these configurations but these numerical tools cannot be used directly to design for specific properties. Thus, it is required to combine machining learning tools with numerical simulation tools to introduce appropriate design for such complicated problems, which cannot be formulated in simple analytical models [3–6].

Solving multiobjective optimization problems (MOPs) with traditional optimization methods has been found to be difficult because these methods often require many complex computations and the common way in this case is to reduce the set of objectives into a single objective and handle it accordingly. On the other hand, artificial intelligence (AI) techniques have proved to be good alternatives so they are now widely utilized in solving MOPs. One of these techniques is Neural Networks (NNs). NNs [7] model biological neural systems. They have been applied to many real-world problems, as a data analysis tool to map nonlinear relationships between process inputs and outputs, especially in classification and pattern recognition. In addition, NNs have been applied to problems in optimization and linear programming. While NNs are developed from the field of AI and brain modeling, they can also be considered as function approximation tools, which learn the relationship between independent variables and dependent variables, much like regression or other more traditional approaches. The principal difference between NNs and statistical approaches is that NNs make no assumptions about the statistical distribution or properties of the data, and therefore NNs tend to be more useful in practical situations. NNs are also an inherently nonlinear approach giving them more accuracy when modeling complex data patterns. Moreover, when closed form solutions do not exist and trial-and-error methods are the only approaches to solving the problem (like the problem at hand). By

Submitted On: October 18, 2020
Accepted On: January 27, 2021

https://doi.org/10.47037/2020.ACES.J.360304

training an NN one can use it to predict solutions to the problem. These properties make NNs gaining a huge momentum in the field of RF and microwave modeling and design [8–14] mainly because of its generalization capability, nonlinear property, massive parallelism, adaptive learning capability, fast convergence rates, insensitivity to uncertainty, and VLSI implementations. Recently, NNs have been applied successfully to the field of RFID technology such as ranging [15], signal modeling [16], positioning [17], and sensing [18].

In [19], a dual-band circularly polarized RFID reader antenna is designed by using ramped convergence particle swarm optimization (RCPSO). This algorithm uses a multi-start approach to break down the optimization problem by considering only a subset of antenna dimensions at a time, hence overcoming the curse of dimensionality and premature convergence of classical PSO. However, this requires large execution time (about 10 hours for PSO and ~50 hours for RCPSO).

Motivated by the inherent advantages of NNs, this paper presents a feed-forward neural network (FFNN)-based multiobjective optimization (MOO) approach to design a dual-band circularly polarized antenna. NNs typically adopt two steps: training and recalling. The network is first trained with known input–output pattern pairs; although a large training pattern set may be required for network training, it can be implemented separately. After training, it can be used directly to replace the complex system dynamics. In this paper, the FFNN is trained on data generated by the HFSS simulator by varying the antenna dimensions. There are two stages of training/recalling.

II. FFNN ARCHITECTURE

A NN consists of a set of processing units, called nodes or neurons, connected by weighted arcs, where the weights represent the strength of connections. The nodes are organized into layers [7]. Nodes in the input layer called input nodes, accept input from the outside world and nodes in the output layer, called output nodes, generate output to the outside world. Nodes in the input layer are used to distribute inputs only and do not serve any processing or computational function. Nodes in layers between the input layer and the output layer called hidden nodes, and these layers are called hidden layers.

NNs can be of several kinds of architecture. They can contain one or more hidden layers of neurons and may have feedback connections or not. The NN architecture constructed for our purpose here is multilayer perceptron (MLP) network. The networks are of feed-forward ones in which the signals always propagate from the input to the output layer without any feedback connections. In addition to the MLP, there are other NN structures [7] used for antennas, for example, radial basis function (RBF) networks and self-organizing map (SOM) networks [20]. A list of applications of NNs for antennas and arrays is given in [21], along with the type of network structure used and the advantage/ disadvantage of application.

Figure 1 shows a FFNN of only two hidden layers. However, more hidden layers can be added. In each neuron (node), the scalar input z is transmitted through a connection that multiplies its strength by the scalar weight w, to form the product wz, again a scalar. This product may be added to a scalar bias b (much like a weight, except that it has a constant input of 1) to form the final argument of an activation function f. The most frequently used activation function is the sigmoid function.

An NN is trained to represent an unknown mapping by employing a training set (a collection of paired input and desired output vectors observed from the unknown mapping). The purpose in training a NN is to determine the values of the elements in the weight matrix **W** so that the NN can closely represent the unknown mapping. The training of a NN is accomplished by the following steps:

(1) Mapping input vectors from the training set by the current version of the NN to their computed output vectors.
(2) Comparing the computed output vectors with their respective desired output vectors in the training set, and then.
(3) Adjusting the values of the components of **W** so as to reduce any differences between the computed and desired output vectors.

After a number of training iterations, the connectivity weights and node biases of the NN converges to a set of values that minimizes the differences between the computed and desired output vectors, and the NN organizes itself internally to construct a model to represent the unknown mapping from the input space to the output space. Thus, any new input vector presented to an appropriately trained NN yields an output vector similar to the one that would have been given by the actual mapping.

In this kind of network, learning process is done by error back-propagation (BP) learning rule in which the weights between the connections are adjusted such that the mean square error (MSE) between the targets and the inputs of the training set is returned back through the layers of neural units and eventually minimized as the performance of the neural system is maximized.

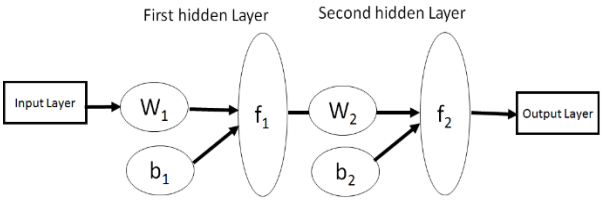

Fig. 1. The structure of FFNN

III. FFNN APPLICATION TO DESIGN A SINGLE-FED DUAL-BAND CIRCULARLY POLARIZED ANTENNA

As an example for utilizing FFNN in antenna design, the design of a single-fed multiband circularly polarized antenna is presented in this section. The proposed antenna is designed for multiband RFID reader system operating at two frequency bands; 835–865 MHz and 2.31–2.35 GHz, specifically. The required reflection coefficient of the antenna at these bands should be less than –10 dB and the corresponding axial ratio should be less than 3dB. The initial geometry of the proposed antenna is shown in Fig. 2. It is composed of a circular aperture in the ground plane of a grounded dielectric slab. The thickness of the substrate is $t = 1.6$ mm. The substrate is FR4 material with a dielectric constant $\varepsilon_r = 4.6$ and loss tangent $\tan\delta = 0.02$. The effective dielectric constant on the circular aperture can be approximated as $\varepsilon_{re} \approx (\varepsilon_r + 1)/2$. For this effective dielectric constant, the radius of a circular aperture which would be resonant at the center frequency of the lower band; 850 MHz, can be obtained approximately as $R = 46$ mm. This approximation is based on the assumption that the field distribution in this case is the dominant TE_{11} mode field distribution along a circular aperture of radius R [24]. This aperture is printed on a square substrate of length $L = 108$ mm. Two arbitrary conducting strips are printed on the other side of the dielectric slab. One of these two conducting strips are used as a feeding strip to the circular aperture while the other strip is a parasitic one which is used to introduce the required perturbation to obtain circular polarization.

It should be noted that, the position of the feeding strip is chosen to be near the center of the aperture to increase the coupling effect between the TE_{11} mode in the circular aperture and the feeding polygon. On the other hand, the parasitic strip is located near the edge of the circular aperture and nearly parallel to the feeding strip to introduce a small coupling with the excited TE_{11} mode in the circular aperture. This small coupling represents the required perturbation to introduce the required circular polarization. Each strip is a polygon composed of four corners. For each polygon, the *xy* coordinates of three corners are variable while the fourth corner is fixed constant. In addition, the two corners of the polygon at the feeding edge of the substrate have a constant value of *x* which corresponds to the *x* position of this edge. Thus, the total number of variables in this case for the two strips is ten variables. These ten variables can be used introduce infinite configurations for these two strips while keeping their starting positions at the feeding edge. The limits of these variables are chosen such that the two strips would lie within the dimensions of the substrate as well as the two strips should not be intersecting. Assuming that the center of the circular aperture is located at $x = 0$ and $y = 0$, the starting *xy* coordinates of the two strips would be as presented in Table 1.

Table 1: Initial values of the corners of the two strips

Corner No.	Strip#1 (Feeding Strip)		Strip#2 (Parasitic Strip)	
	x (mm)	*y* (mm)	*x* (mm)	*y* (mm)
1	54 (Fixed)	–18 (Fixed)	54 (Fixed)	49 (Fixed)
2	–32	–18	–35	42
3	8	–11	–30	40
4	54 (Fixed)	–10	54 (Fixed)	46

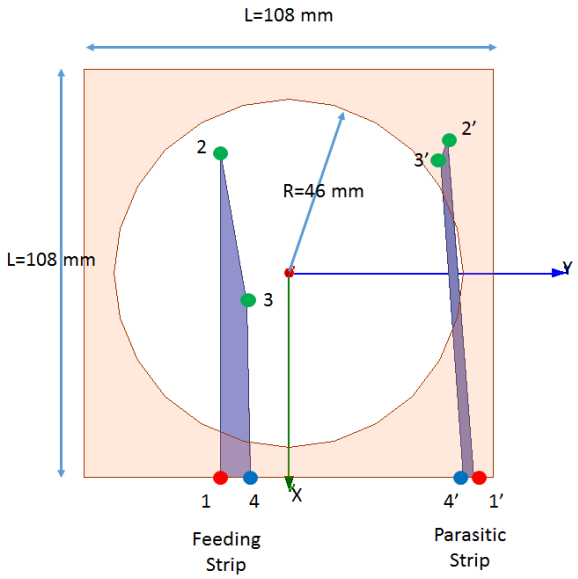

Fig. 2. Initial geometry of the proposed circular aperture antenna with its feeding and parasitic strips. The center of the antenna is located at the origin. The corners of the feeding strip and the parasitic strip are numbered from 1 to 4. The positions of the first corner for both the feeding and the parasitic strips are fixed and marked with red marker. The *x*-positions of the fourth corner for both the feeding and the parasitic strips are fixed while the *y*-positions are variable. These points are marked with blue marker. The second and the third corners for both strips are variable for both *x* and *y*. The points are marked in green. The initial values for these corners are presented in Table 1.

These variable parameters are presented as a variable vector **D** of ten elements which are $[x_2, y_2, x_3, y_3, y_4, x_{2\prime}, y_{2\prime}, x_{3\prime}, y_{3\prime}, y_{4\prime}]$ The initial values of these variable parameters according to Table 1 are: $\mathbf{D} = [-32, -18, 8, -11, -10, -35, 42, -30, 40, 46]^T$.

Figure 3 shows the results of this initial design

obtained by using HFSS. It can be noted that the resonance of this initial design is nearly around 750 MHz while the reflection coefficient of the antenna 2.35 GHz is only about –3dB. On the other hand, the axial ratio is greater than 8 dB in the two bands.

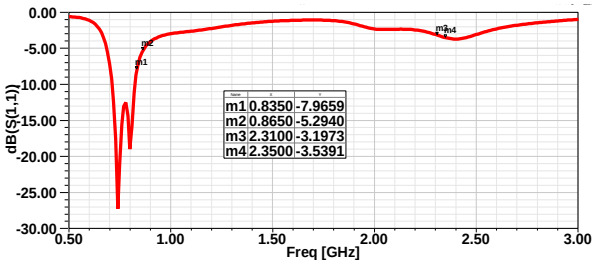

(a)

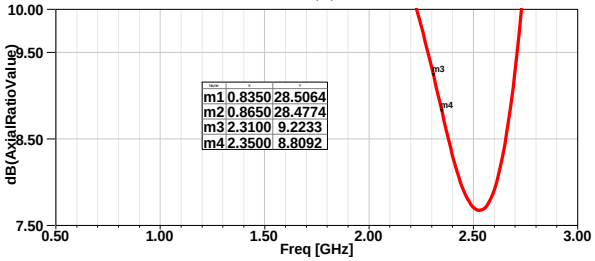

(b)

Fig. 3. Simulation results for the proposed antenna with initial parameters of the two strips: (a) reflection coefficient of the antenna, and (b) axial ratio of the radiation pattern in the broadside direction.

IV. THE FFNN-BASED MOO MODEL

One of the applications of NNs is *optimization*, where the aim is to find the optimal values of parameters in an optimization problem [22]. In this paper, The FFNN-based MOO model is used in a reverse way (inverse modeling) in which design variables are derived from objectives [23], where the input layer of the FFNN represents the objectives and the output layer represents the parameters to be optimized. Figure 4 shows the general FFNN-based model for solving MOPs.

Figure 5 shows the FFNN-based MOO model for the design of RFID reader antenna. Here, we have two objectives, the reflection coefficient ($|S_{11}|$) and axial ratio (AR). Thus, the input objective vector is [$|\mathbf{S_{11}}|$ | **AR**], where the vector $|\mathbf{S_{11}}|$ represents the linear-scale (to be in the range [0,1] suitable for NN training) values of $|S_{11}|$ in the target two bands, while the vector **AR** contains the linear-scale values of *AR* in both bands (normalized by its norm to unify the input parameter space). The target two bands are 835–865 MHz and 2.31–2.35 GHz. The frequency step is taken as 0.01 GHz, so we have 9 values for both $|\mathbf{S_{11}}|$ and **AR** (4 in lower band and 5 in the higher band). Therefore, the dimension of the input vector is 18 with the input layer of the FFNN having 18 neurons.

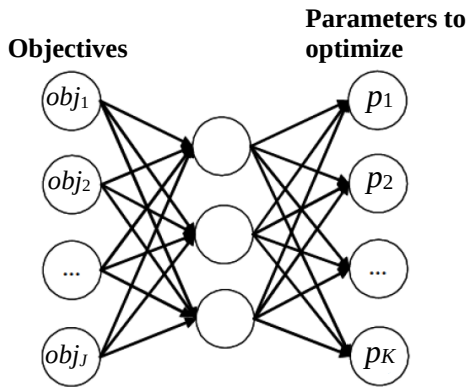

Fig. 4. The general FFNN-based MOO model.

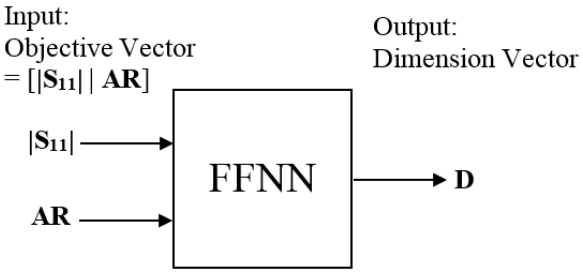

Fig. 5. The FFNN-based MOO model for the design of the proposed antenna.

To design a symmetric FFNN it is preferred to reduce the number of variables dimensions of the antenna to be nine instead of ten. This can be obtained by fixing any one of these variables. Thus, in the present analysis, the *y* position of the third corner of the first strip is fixed at –11 mm. It should be noted that this is an arbitrary choice and other choices are also possible. Thus, the remaining variables to be optimized would be nine variables. The output from FFNN in this case is the vector $\mathbf{D}'$ of the nine antenna variables. It should be noted that, each variable in the vector $\mathbf{D}'$ is normalized by using its minimum and maximum values to be in the range [0,1] for FFNN training. In this way, the size of the output layer of the FFNN is 9 neurons. The initial absolute value of the vector **D** in this case is $|\mathbf{D}| = [32,18,8,10,35,42,30,40,46]^T$.

Thus, the size of any training pattern will be 27, 18 inputs and 9 outputs. After many experimental simulation trials, it is found that three hidden layers with 10, 15, and 20 neurons, provide the best accuracy. Based on the above analysis, the final FFNN model is 18:10:15:20:9. The training patterns are extracted from the HFSS simulator by varying the nine dimensions of antenna along two stages of training/recalling. In either stage, 80% of total training patterns is randomly chosen for training and remaining 20% for validation.

The FFNN is trained using BP algorithm, which is implemented in C++. In the recalling, the trained FFNN is given the desired input vector, which contains the desired values of $|S_{11}|$ and *AR* over dual-band, to output the corresponding antenna dimensions. The recalling is also implemented by C++.

V. RESULTS AND DISCUSSIONS

A. Stage1 training/recalling

In the first stage of FFNN training/recalling, only one dimension is varied between its minimum and maximum values with a certain step, while all other dimensions are kept constant at their default values. The vectors of minimum, maximum absolute values are $|\mathbf{D}_{min,stg1}| = [27,13,3,5,30,37,25,35,41]^T$ and $|\mathbf{D}_{max,stg1}| = [37,23,13,10,40,47,35,45,51]^T$, respectively, with ten steps from the minimum to the maximum value for each variable. In this way, we have a total of 99 training patterns. The final MSE is 0.000891 after 500,000 iterations. The total training time is about 15 min. After the training, the FFNN is recalled and the output dimensions were $|\mathbf{D}_{stg1}| = [29.58,31.53, 7.7,10,38,24.87, 33.43,24.87,48.13]^T$. Then, these output dimensions are simulated in HFSS and the simulations results are shown in Fig. 6. Compared to the antenna with default dimensions (before optimization) shown in Fig. 3, it can be noted that the performances of $|S_{11}|$ and *AR* have been improved in both bands after the first stage of optimization. However, $|S_{11}|$ has a better performance in lower band than in higher band, and vice versa for *AR*.

B. Stage2 training/recalling

In the second stage of FFNN training/recalling, the training data is generated by HFSS by simulating 100 different sets of dimensions (100 training patterns). In order to exploit the results of stage1, the dimensions in this stage are randomly generated *around* the output dimensions from stage1 $\mathbf{D}_{stg1}$ using normal distribution keeping them as *means* and using a constant variance of 5 for all dimensions. In this case, The vectors of min and max dimensions are $\mathbf{D}_{min,stg2} = \mathbf{D}_{stg1} - \mathbf{5}$ and $\mathbf{D}_{max,stg2} = \mathbf{D}_{stg1} + \mathbf{5}$, where **5** is a vector with all elements are equal 5. The final MSE is 0.000015 after 500,000 iterations. The total training time is about 20 min. After the training, the FFNN is recalled and the output dimensions were $\mathbf{D}_{stg2} = \mathbf{D}_{final}$ = [26.26, 37, 12.89, 14.92, 33, 23.41, 37.55, 18.41, 48.89]. The corresponding final values of the corners of the two strips are presented in Table 2. The final configuration is simulated by using HFSS and the simulations results are shown in Fig. 7.

Compared to stage1 in Fig. 6, it can be noted from Fig. 7 that $|S_{11}|$ and *AR* have overall better results in target bands with much improvement in UHF band for both of them. $|S_{11}|$ has still better performance in UHF band than in SHF, but for AR, the performances in both bands now become almost equal with a deeper notch in UHF band. In addition, it can be seen from Fig. 7 that after the second stage of optimization, $|S_{11}|$ and *AR* are beneath –10 dB and 3 dB, respectively, in both bands of interest, allowing the final optimized antenna to be considered as a universal RFID reader antenna.

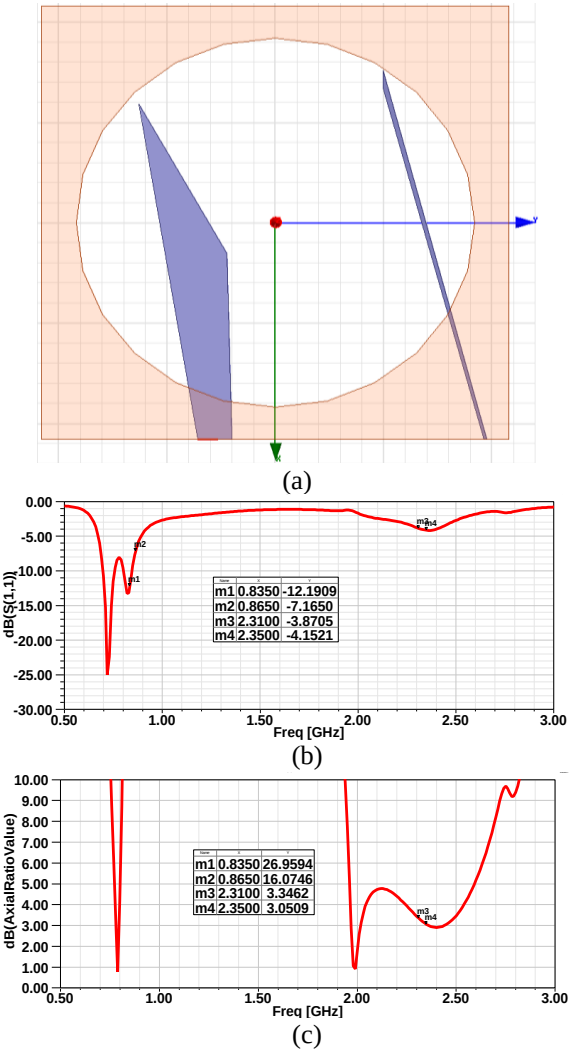

Fig. 6. The output from stage1 training/recalling: (a) geometry of the antenna, (b) reflection coefficient of the antenna, and (c) axial ratio.

Table 2: Final values of the corners of the two strips

Corner No.	Strip#1 (Feeding Strip)		Strip#2 (Parasitic Strip)	
	x (mm)	*y* (mm)	*x* (mm)	*y* (mm)
1	54 (Fixed)	–18 (Fixed)	54 (Fixed)	49 (Fixed)
2	–26.26	–37	–33	23.41
3	12.89	–11 (Fixed)	–37.55	18.41
4	54 (Fixed)	–14.92	54 (Fixed)	48.89

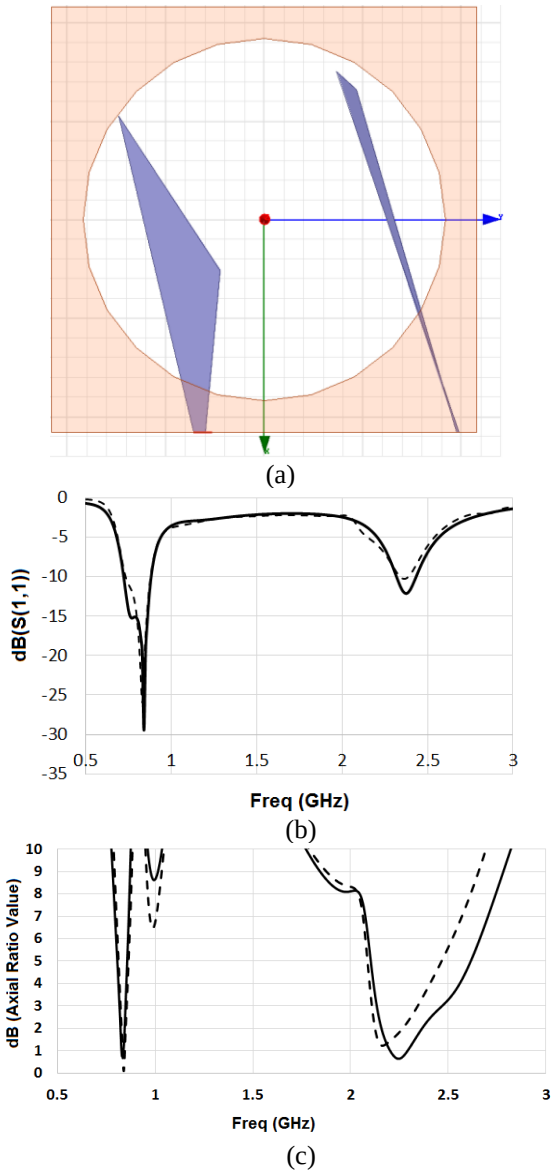

Fig. 7. The output (final) from stage2 training/recalling: (a) geometry of the antenna, (b) reflection coefficient of the antenna, and (c) axial ratio. Solid line by using HFSS and dashed line by using CST.

To verify the obtained result, the same structure with its final dimensions is simulated by using CST. Figure 7 shows a comparison between the results of the HFSS (solid line) and CST (dashed line) simulations. Good agreements between the results of the two simulation techniques are obtained for both the reflection coefficient and the axial ratio of the designed antenna structure with its final dimensions.

VI. CONCLUSION

A dual band circularly polarized antenna is presented in this paper. The proposed antenna is composed of a circular aperture on a grounded dielectric slab. This circular aperture is fed by a feeding strip and perturbed by another parasitic strip to introduce circular polarization. The shape and dimensions of these two strips are optimized by using a NN-based MOO model. Each strip has four corners. Each corner has two variables; x and y positions. Thus, the total number of variables is sixteen. To make the starting point of each strip fixed at the edge of the substrate, the starting corners for the two strips are fixed. Thus, four variable are assumed to be constant. In addition, the last corner at each strip is assumed to be located on the edge of the substrate. Thus, the x values for the last corners on the two strips are also constant. Thus, the remaining number of variables is ten. The notable benefits of the proposed NN model are simplicity and accurate determination of the characteristic parameters of the antenna. The NN model is accurate enough to yield the parameters of the antenna thus eliminating the long time consuming process of determination various design parameters using costly software packages. A distinct advantage of neural model computation is that after proper training, a NN completely bypasses the repeated use of complex iterative processes for new cases presented to it. The total training time was just about 35 min. The optimized design is compact and exhibits less than –10 dB $|S_{11}|$ and 3 dB *AR* in both bands making it practically ideal dual-band circularly polarized RFID reader antenna.

REFERENCES

[1] J. R. James and P. S. Hall, *Handbook of Microstrip Antennas*. IET, 1989.

[2] S. S. Gao, Q. Luo, and F. Zhu, *Circularly Polarized Antennas*. John Wiley & Sons, 2013.

[3] C. Wang, J. Li, A. Zhang, W. T. Joines, and Q. H. Liu, "Dual-band capacitively loaded annular-ring slot antenna for dual-sense circular polarization," *Journal of Electromagnetic Waves and Applications*, vol. 31, no. 9, pp. 867-878, 2017.

[4] K. M. Mak, H. W. Lai, K. M. Luk, and C. H. Chan, "Circularly polarized patch antenna for future 5G mobile phones," *IEEE Access*, vol. 2, pp. 1521-1529, 2014.

[5] H. Yang, Y. Fan, X. Liu, and M. M. Tentzeris, "Single-fed dual-band circularly polarized patch antenna with wide 3-dB axial ratio beamwidth for CNSS applications," *2019 IEEE MTT-S International Wireless Symposium (IWS)*, pp. 1-3, 2019.

[6] K.-L. Lau, K.-M. Luk, and K.-F. Lee, "Design of a circularly-polarized vertical patch antenna," *IEEE Transactions on Antennas and Propagation*, vol. 54, no. 4, pp. 1332-1335, Apr. 2006.

[7] S. Haykin, *Neural Network: A Comprehensive Foundation*. Upper Saddle River, NJ, USA: Prentice-Hall, 1999.

[8] Q. J. Zhang and K. C. Gupta, *Neural Networks for RF and Microwave Design*. Boston, MA: Artech House, 2000.

[9] T. Sallam, A. B. Abdel-Rahman, M. Alghoniemy, and Z. Kawasaki, "A novel approach to the recovery of aperture distribution of phased arrays with single RF channel using neural networks," *2014 Asia-Pacific Microwave Conference*, Sendai, Japan, pp. 879-881, 2014.

[10] T. Sallam, A. B. Abdel-Rahman, M. Alghoniemy, Z. Kawasaki, and T. Ushio, "A Neural-network-based beamformer for phased array weather radar," *IEEE Transactions on Geoscience and Remote Sensing*, vol. 54, no. 9, pp. 5095-5104, Sept. 2016.

[11] L. Liu, Z. Guan, G. Shen, P. Zhao, and G. Wang, "Parameters extraction for equivalent circuit model based on artificial intelligence," *2019 IEEE International Conference on Computational Electromagnetics (ICCEM)*, Shanghai, China, pp. 1-3, 2019.

[12] L. Yuan, X. Yang, C. Wang, and B. Wang, "Multibranch artificial neural network modeling for inverse estimation of antenna array directivity," *IEEE Transactions on Antennas and Propagation*, vol. 68, no. 6, pp. 4417-4427, June 2020.

[13] S. Rani and J. S. Sivia, "Design and development of virtual instrument for fault diagnosis in fractal antenna array," *Int. J. RF Microw. Comput. Aided Eng.*, vol. 30, no. 1, 2020.

[14] S. Dutta, B. Basu, and F. A. Talukdar, "Cascaded neural network based small array synthesis with robustness to noise," *Int. J. RF Microw. Comput. Aided Eng.*, vol. 31, no. 1, 2021.

[15] M. Agatonovic, E. Di Giampaolo, P. Tognolatti, and B. Milovanovic, "Artificial neural networks for ranging of passive UHF RFID tags," *2013 11th International Conference on Telecommunications in Modern Satellite, Cable and Broadcasting Services (TELSIKS)*, Nis, pp. 505-508, 2013.

[16] Z. Chen and C. Wang, "Modeling RFID signal distribution based on neural network combined with continuous ant colony optimization," *Neurocomputing*, vol. 123, pp. 354-361, 2014.

[17] J. Wang, W. Wei, W. Wang, and R. Li, "RFID hybrid positioning method of phased array antenna based on neural network," *IEEE Access*, vol. 6, pp. 74953-74960, 2018.

[18] S. Jeong, M. M. Tentzeris, and S. Kim, "Machine learning approach for wirelessly powered RFID-based backscattering sensor system," *IEEE Journal of Radio Frequency Identification*, vol. 4, no. 3, pp. 186-194, Sept. 2020.

[19] S. Kibria, M. T. Islam, and B. Yatim, "New compact dual-band circularly polarized universal RFID reader antenna using ramped convergence particle swarm optimization," *IEEE Transactions on Antennas and Propagation*, vol. 62, no. 5, pp. 2795-2801, May 2014.

[20] C. G. Christodoulou and M. Georgiopoulos, *Applications of Neural Networks in Electromagnetics*. Artech House, Boston, 2001.

[21] C. G. Christodoulou and A. Patnaik, "Neural networks for antennas," *In Modern Antenna Handbook*, C. A. Balanis (Ed.), pp. 1625-1657, 2008.

[22] A. P. Engelbrecht, *Computational Intelligence: An Introduction*. John Wiley & Sons, 2007.

[23] K. Kobayashi, M. Miki, and T. Hiroyasu, "Mechanism of multi-objective genetic algorithm for maintaining the solution diversity using neural network," *In Lecture Notes in Computer Science*, vol. 4403, pp. 216-226, 2007.

[24] C. A. Balanis, *Antenna Theory: Analysis and Design*. 3rd Ed., John Wiley & Sons. Inc, 2005.

A Low Complex Modified Grey Wolf Optimization Model for OFDM Peak Power Reduction

R. S. Suriavel Rao [1], R. Menaka [2], and R. Alexciyaa Winslet [3]

[1] Department of Electronics and Communication Engineering
Dhanalakshmi Srinivasan College of Engineering, Coimbatore, India
suriavelraors@gmail.com

[2] Department of Electronics and Communication Engineering
Chennai Institute of Technology

[3] Department of Electronics and Communication Engineering
Karunya Institute of Technology and Sciences, Coimbatore, India

Abstract **–** Orthogonal frequency division multiplexing (OFDM) or multicarrier modulation is an essential signal processing technique in new generation wireless gadgets owing to its potential to support fast and spectrally efficient transmission. One of the major limitations of OFDM systems is the peak-to-average power ratio (PAPR) of transmit data. In this article, a novel meta heuristic algorithm called modified grey wolf optimizer is used to boost the computing performance of subcarrier phase factor search in the undisputed partial transmit sequence method. The proposed modified grey wolf optimizer (mGWO) has a balancing between exploration and exploitation phases while searching for peak power carriers and brings out a nearly optimal performance but with less number of iterations. The objective is to propose low complex computing algorithm without compromising the output quality. The simulation results of proposed mGWO-PTS model assure improvements around 20 to 25 percent from that of the comparative counterparts such as GWO-PTS, PSO-PTS, and etc.

Index Terms **–** BER, modified grey wolf optimizer, OFDM, PAPR.

I. INTRODUCTION

In the state of the art of wireless technology Orthogonal Frequency Division Multiplexing (OFDM) technique is a substantial signal processing algorithm due to its high speed compatibility, robustness to noise and appreciable spectral efficiency. One of the major limitations to employ OFDM in systems is the peak to average power ratio (PAPR) of the transmitted subcarriers. In this article, a novel modified Grey Wolf Optimizer (mGWO) is proposed to perform the phase factor search within the popular Partial Transmit Sequence technique such that the results are promising with low complex computations. Unlike any other search algorithm, the modified grey wolf optimizer rearranges the balancing between exploration and exploitation in searching of the best solution and brings out an optimal performance that has been generally achieved in many of its previous counterparts. The main goal of this proposed scheme is to achieve low complexity and a better PAPR minimization with a near or sub optimal data rate delivery across users. The results have proved that the modified grey wolf optimization algorithm used in phase factor search process yields improved performance than other combinations of PTS optimization algorithms.

Orthogonal Frequency Division Multiplexing is a widely used multi carrier modulation scheme by which data is loaded over multiple narrow sub carriers so that frequency diversity is achieved along with frequency flat fading to sub carriers. This provides spectral efficiency over single carrier transmission. Every subcarrier is modulated using one of the digital modulation schemes such as QPSK, 16QAM, and etc. at a low data rate. The choice of orthogonal sub carriers facilitates frequency flat fading thereby the noise impact is minimized to a larger extent. Thus, the SNR of transmit signal increases which ensures little noise filtering process at the receiver end. OFDM is established on the very familiar technique called Frequency Division Multiplexing (FDM). In FDM different users are allotted separate dedicated frequency channels. Each channel in FDM is detached from the other user bands by a frequency guard band to avoid inter carrier interference (ICI) between adjacent channels. Idle channels lead to spectrum wastage in case of FDM. The OFDM scheme differs from conventional FDM in many interrelated ways which are as mentioned below:

- Different subcarriers convey the different data blocks.
- Subcarriers are symmetrical to each other.

Submitted On: October 27, 2020
Accepted On: January 18, 2021

https://doi.org/10.47037/2020.ACES.J.360305

- Guard bands are added to every subcarrier to confine the channel in order to eliminate spectral leakage which causes Inter-Symbol Interference (ISI).
- Spectra are used efficiently by allowing overlap across successive sub channels or sub carriers.
- System is protected against co-channel interference and parasitic noise.
- Addition of Cyclic Prefix (CP) eliminates inter-symbol interference and inter carrier interference.
- It uses IFFT to enforce multicarrier modulation.
- Cancels any channel which is affected by frequency selective fading.
- Each sub-channel has low data rate so that the symbol duration is large thereby frequency flat fading occurs.

II. THE PEAK TO AVERAGE POWER RATIO

The channel variations in an Orthogonal Frequency Division Multiplexing signals may experience higher peak power values in the time field as several number of subcarriers are involved. These subcarriers are created using the famous Inverse Fast Fourier transform (IFFT) scheme. In a wireless transmitter one of the major challenges is to have linear power amplification. If power peaking occurs among subcarriers cross over distortion is induced. This is nothing but noise addition leading to distort the amplitude of the modulated carriers and hence data is lost. Another point is that PAPR leads to voltage surge to a considerable extent in the uplink which affects the constraint of battery power control in a mobile or portable device.

As it is mentioned earlier the PAPR is mathematically expressed as:

$$PAPR_{db} = 10\ log\left(\frac{max\ [x(t)x^*(t)]}{E\ [x(t)x^*(t)]}\right), \quad (1)$$

where, the component $\left(\frac{max\ [x(t)x^*(t)]}{E\ [x(t)x^*(t)]}\right)$ represents the peak to mean power ratio of an instantaneous OFDM signal $x(t)$. In general, an OFDM symbol contains complex tones which are evenly spaced in the frequency domain in orthogonal multiples of $x(t) = e^{j2\pi ft}$.

At period $t = T$, the signal's peak value,

$$max[x(t)x^*(t)] = max\left[e^{j2\pi ft}e^{-j2\pi ft}\right] = max[e^0] = 1. \quad (2)$$

The signal's mean squared value,

$$E[x(t)x^*(t)] = E(e^{j2\pi ft}e^{-j2\pi ft}) = 1. \quad (3)$$

Using results of equations (1) and (2) the resultant PAPR is 0 dB. This means there is no peaking of power or it means that the peak power equals average power and hence no noise. Similar to the above equations, an OFDM signal is also expressed by including all the complex tones which are evenly spaced in the frequency domain as $x(t) = e^{j2\pi ft}$. It is well known that the time domain representation of OFDM signal is done by summing K complex tones spaced apart by 90 degrees from each other. The following equation defines it as a simple function $x(t)$ in terms of amplitude a_k and complex phase $e^{\frac{j2\pi kt}{T}}$:

$$x(t) = \sum_0^{K-1} a_k e^{\frac{j2\pi kt}{T}}. \quad (4)$$

To make it simple, let us assume $a_k = 1$ for any k value. In this case, the signal's peak value is:

$$\begin{aligned} &max[x(t)x^*(t)] \\ &= max\left[\sum_{k=0}^{K-1} a_k \left(e^{\frac{j2\pi kt}{T}}\right) \sum_{k=0}^{K-1} a_k{}^* \left(e^{\frac{-j2\pi kt}{T}}\right)\right] \\ &= max\left[a_k a_k{}^* \sum_{k=0}^{K-1}\sum_{k=0}^{K-1} e^{\frac{j2\pi kt}{T}} e^{\frac{-j2\pi kt}{T}}\right] = 1. \end{aligned} \quad (5)$$

The signal's mean square value is,

$$\begin{aligned} E[x(t)x^*(t)] &= E\left[\sum_{k=0}^{K-1} a_k\ e^{\frac{j2\pi kt}{T}} \sum_{k=0}^{K-1} a_k{}^* \left(e^{\frac{-j2\pi kt}{T}}\right)\right], \\ &= E\left[a_k\ a_k{}^* \sum_{k=0}^{K-1}\sum_{k=0}^{K-1} e^{\frac{j2\pi kt}{T}} e^{\frac{-j2\pi kt}{T}}\right] = 1. \end{aligned} \quad (6)$$

Thus, if the subcarriers are modulated using same type of modulation, the PAPR is 0 dB, making the transmission noise free. It is important to notice that the IFFT operation is responsible to produce orthogonal subcarriers. Each subcarrier is loaded with a set of data by a suitable modulation scheme, for which an adaptive modulation or bit loading or power allocation scheme is employed. As it is known modulation is the process of converting a low frequency information bearing signal into a high frequency signal. Equation (6) is nothing but the autocorrelation of signal x(t). The Fourier transform of autocorrelation of x(t) gives out the Welch power spectral density which means the power distribution across a given frequency band. Welch spectrum helps an user to identify the signal strength of each subcarrier. At receiver end, Welch spectrum is used to provide the channel state information (CSI) which means the channel variations due to fading as it is a mobile wireless channel. In channel estimation process there are three approaches involved. A part of the CSI shall be sent back to the transmitter from receiver and vice versa so that it becomes a semi blind approach. In blind approach, no CSI is used. In data aided approach a cyclic redundancy check (CRC) or side information (SI) is used for signal detection and estimation at the receiver.

III. METAHEURISTICS IN MODIFIED GREY WOLF ALGORITHM

In recent years, the swarm intelligence model of animals is preferred for multi objective combinatorial optimization. The grey wolf algorithm is preferred as one of the most encouraging problem solving technique for encountering real time big data applications having large

number of computations. The joint effort among fish, birds, flies and herd of animals to look for food and survival by planning a wise structure is known as swarm intelligence (SI). In order to handle nonlinear and combinatorial optimization problems, a huge amount of computing is needed. This results in system complexity and increased processing time to find out the best minima or maxima of a local or global search. There are numerous computing models developed by mimicking the swarm intelligence of various living organisms such as insect, wolf, bumble bees, winged animals, birds, fish, bat, fruit fly, fire fly, dragon fly, whales and etc. The Particle Swarm Optimization (PSO), Ant Colony Optimization (ACO), Firefly Algorithm (FFA), Artificial Bee Colony (ABC) algorithm, Spider Monkey Optimizer (SMO), Whale Optimization (WO), African Buffalo Optimization (ABO), and Grey Wolf Optimizer (GWO) are some of the popular swarm intelligent algorithms which had proved that they are capable of solving industrial and research related optimization problems.

In the process of attaining computational intelligence, it is interesting to note that the choice of any search and optimization algorithm results in a similar statistical performance as proposed by the No Free Lunch (NFL) theorem. This theorem states that no free lunch is possible without a cost. The quality of any search problem has its cost. As the quality grows up the computations do grow. The Grey Wolf Optimizer (GWO) depends on administration and progression approach to hunt a prey. GWO algorithm is a new addendum to the group of swarm insight based metaheuristics. In the group of swarm intelligence based computing, GWO is the main approach which depends on a team coordinated hunting behaviour. The GWO calculation is a straight forward population based calculation which reproduces the authority and social conduct of the grey wolves to prey.

IV. RELATED WORKS

Article [1] uses a new swarm intelligence named the fireworks algorithm (FWA) to reduce PAPR while achieving a low computational complexity in MIMO-OFDM system. It reduces the phase factor search complexity of PTS algorithm while maintaining the desired PAPR optimization accuracy. Paper [2] projects innumerable algorithms to cut down the computational complexity along with PAPR. This is achieved by inculcating partial transmit sequences (PTS) method, variable to variable crossover in Cuckoo search algorithm (CSA) and also a combination of two methods. Thus, providing a better PAPR function than GA-PTS with adjacent partition and with pseudo-random partition. Study from [3] reveals an efficient PTS approach on particle swarm optimization to attain reduced PAPR and computational complexity wherein the proposed method expeditiously searches for the optimum combination of section rotation factors to decrease the procedural complexness.

Paper [4] deals with solution for rigorous hunt over the entire phase search which lead to high computing complexity. A less optimum PTS method is demonstrated upon the self-adaptive multi-population differential evolution algorithm (SAMDE) to find high quality resolutions with low computational cost by acquiring each sub-population of individuals over consequent generations.

Research in [5] applies SLM with ABC algorithm in PAPR reduction of MIMO-OFDM System. Also, artificial bee colony (ABC) algorithm, Modified ABC and parallel ABC (P-ABC) for SLM scheme are proposed which gives better PAPR reduction performance with less complexity. This proposed algorithm is giving better PAPR reduction and bit error rate (BER) performances with less complexity.

Article [6] samples various Algorithms on PAPR Reduction in OFDM System. Lately a sub optimal scheme which is based on artificial bee colony (ABC) algorithm is projected to hunt the better phase factors which also offer efficient PAPR reduction in OFDM system with less complexity. Information regarding optimal phase set is transmitted as side information which reduces the overall bandwidth efficiency. This problem is solved in paper [7] by adjoining PTS and GA in mapping scheme. Thus, leads to lower computations, increases the effective searching of function parameters and reduces the number of searches, to find the optimum phase factors. Though wavelet packet modulation has a merit of flexibility and modular implementation capability, it sustains high PAPR which extends signal distortion.

A new technique on biogeography based optimization is enhanced to a better level named generalized oppositional biogeography based optimization is exploited in the OFDM system to reduce PAPR and PTS searching complexity. By combining these two techniques in [8] the result exceeded the original algorithm prospects. In article [9], another PTS scheme has been developed so as to descent the PAPR by choosing the ideal stage factor by means of a versatile ABC optimization process. It can diminish the computational involution for bigger PTS sub blocks and offers lower PAPR in the meantime. Bat algorithm, when used for optimization the of sub-carrier phase it suffers from local optimum and low convergence accuracy. In paper [10] the velocity formula is updated so as to achieve convergence speed and speed while nullifying premature convergence. By implementing this improved algorithm in CO-OFDM PAPR is reduced by 5.48 dB and also searching ability and accuracy is amplified. The suggested algorithmic rule enhances the Peak to Average Power Reduction than using other selective mapping algorithms, Genetic and Quantum evolutionary.

Moreover, the suggested algorithmic rule meets faster than the quantum evolutionary and genetic algorithms. PTS selection is highly complex and the Computational Complexity is huge when all the subcarriers are transmitted in the OFDM system. Paper [11] applies a novel method named PTS selection, a modified chaos clone shuffled frog leaping algorithm (MCCSFLA), it's based on the chaos theory. This algorithm can converge to the global optimum, achieves better PAPR reduction, and converges faster. The impact of OFDM IFFT/FFT computational complexity in [12] is treated well with new approaches in the FPGA implementation context.

V. PROPOSED MGWO-PTS MODEL

The block diagram of the proposed model using mGWO-PTS is shown in Fig. 1. Grey Wolf belongs to the family of Canidae forming the apex position in the family of predators. Grey wolves almost live in a pack of size from 5 to 12 on an average.

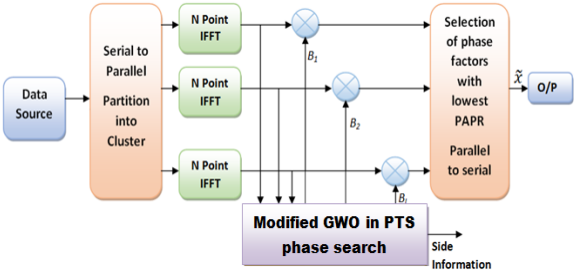

Fig. 1. Block diagram of the proposed model using mGWO-PTS.

The pack has alpha, beta, delta and omega wolves. Alpha leads the pack whereas others follow it. The betas are either female or male. Either the male or female can be the most effective nominee in the Alpha level, by the other case if the one in every alpha wolf are attacked terribly or passes away. The beta conveys alpha's command throughout the pack and it offers the feedback to an alpha wolf. The last out ranking grey wolf is omega. The Omega represents the character of the whipping boy The Omegas constantly resist all the opposite commanding wolves. The final wolves are also allowed to eat.

They must appear the form of Omega and is not a very important individual inside pack, it is determined that total pack face in internal fighting issues other case of missing the omega. It will often exhibit brutality and annoyance of all the wolves by the Omega. It always satisfies the complete maintenance and packing the dominance structure. In few conditions the omega will additionally be acting like baby sitters in the pack. A typical hunting scenario is shown in Fig. 2.

The behavior of grey wolves is categorized as follows.

- Sensing, Chasing, Tracking, and Approaching the prey.
- Encircling, Provoking, Pursuing the prey until it stops moving.
- Attacking and killing the prey.

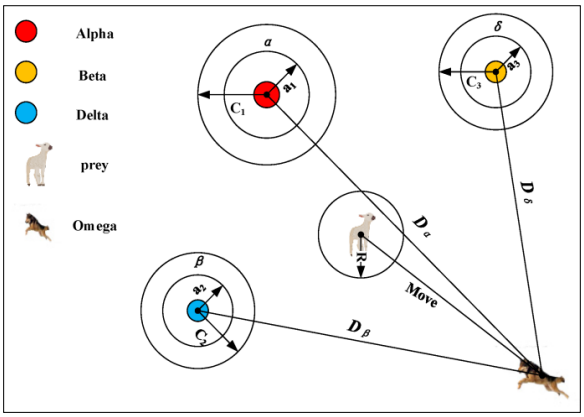

Fig. 2. Grey wolves hunting scheme (source: https://www.google.com).

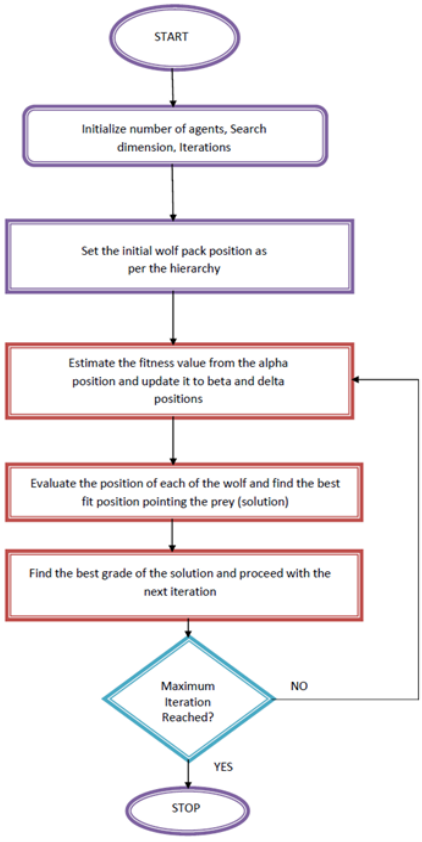

Fig. 3. Flow chart of mGWO algorithm.

Figure 3 clearly illustrates the sequential process flow of the modified GWO algorithm. As it is verified from the literature studies, the convergence of mGWO is faster and efficient compared to its former version the grey wolf algorithm. In this case, the exploration takes 70 percent effort whereas exploitation phase consumes 25 percent search effort, resulting in a non linear search. The proposed algorithm exhibits appreciable global convergence by avoiding local minima.

Equation (7) describes the linear search model of conventional grey wolf optimizer model in which both the exploration and exploitation phases of finding the minimum phase value occupy 50 percent effort respectively:

$$a = 2\left(1 - \frac{t}{T}\right). \quad (7)$$

From equation (8) it is evident that a squared search function is introduced by which the exploration of prey (solution) needs almost 70 percent search iterations just to locate the prey; and remaining 30 percent search effort is spent to zero in to the prey (solution):

$$a = 2\left(1 - \frac{t^2}{T^2}\right). \quad (8)$$

VI. RESULTS AND DISCUSSION

This section presents several results in support of the proposed method to find the minimum PAPR values with fast convergence.

Figure 4 illustrates the proposed mGWO tool box in which an optimum value of 0.998 is obtained with merely 200 iterations.

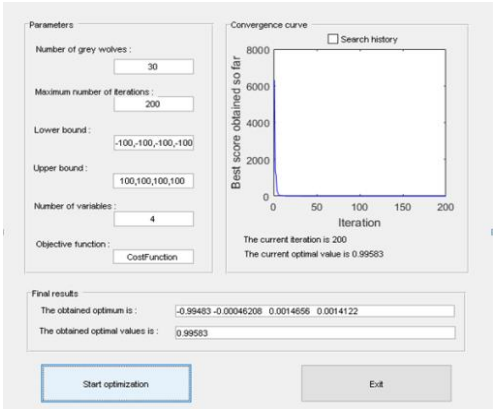

Fig. 4. Performance of mGWO at 200 iterations.

Figure 5 illustrates that the proposed mGWO converges to the minimum value with 280 iterations whereas conventional GWO takes 330 iterations. This ensures that the proposed mGWO saves computations by 15%.

Figure 6 compares the peak power reduction capacity of proposed method and other conventional methods. Proposed mGWO-OFDM exhibits low peak to average power at a low SNR of 14 dB.

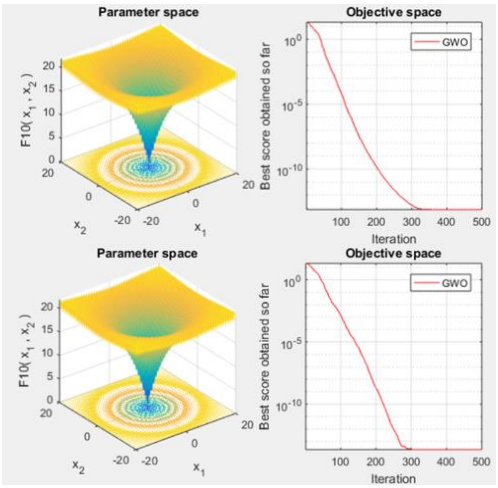

Fig. 5. GWO versus mGWO for 500 iterations.

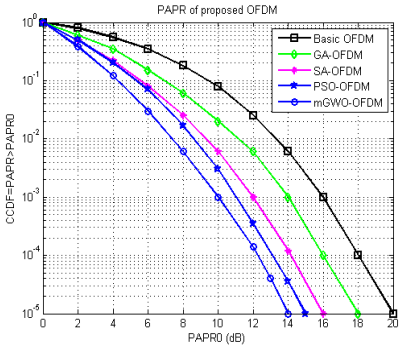

Fig. 6. PAPR of proposed method.

Figure 7 portrays the BER performance of proposed PTS based PAPR reduction by using proposed mGWO. At the lowest SNR of 10 dB, the proposed scheme exhibits a lowest BER of 10^{-5} whereas the error increases significantly in all other methods. The detailed BER pattern at SNR of 10 dB is depicted in Fig. 8.

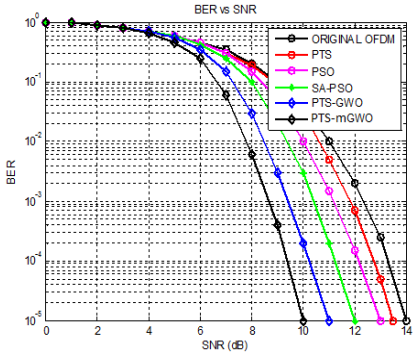

Fig. 7. BER performance of proposed PTS-mGWO.

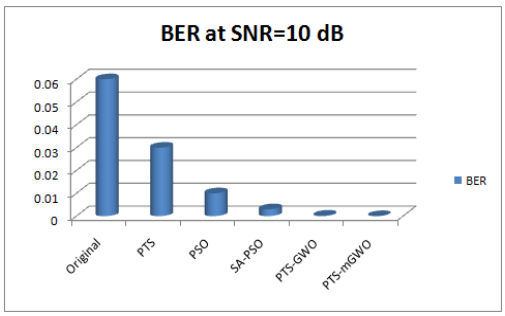

Fig. 8. BER performance of PTS-mGWO at SNR=10dB.

VII. CONCLUSION

The proposed work gives a better output for OFDM optimization and reduced PAPR values by the PTS method using the modified grey wolf algorithm. The modified GWO gets an earlier convergence when compared to the original GWO and also a reduced complexity is obtained in the results.

ACKNOWLEDGMENT

This article is neither financially supported nor sponsored by any government or non-government agencies.

REFERENCES

[1] L. Amhaimar, S. Ahyoud, A. Elyaakoubi, A. Kaabal, K. Attari, and A. Asselman, "PAPR reduction using fireworks search optimization algorithm in MIMO-OFDM systems," *Journal of Electrical and Computer Engineering*, vol. 2018, pp. 1-11, 2018.

[2] P. Krishna and R. Naraiah, "Modified Cuckoo search algorithm for PAPR reduction in OFDM," *International Journal of Pure and Applied Mathematics*, vol. 120, no. 6, pp. 223-231, 2018.

[3] M. H. Aghdam and A. A. Sharifi, "PAPR reduction in OFDM systems: An efficient PTS approach based on particle swarm optimization," *ICT Express*, vol. 5, no. 3, pp. 178-181, 2019.

[4] H. Ait-Saadi, J. Chouinard, and A. Guessoum, "A PAPR reduction for OFDM signals based on self-adaptive multipopulation DE algorithm," *International Journal of Electrical and Computer Engineering*, vol. 7, no. 5, pp. 2651-2660, 2017.

[5] R. Andraju, M. V. Lakshmi, and K. R. L. Reddy, "PAPR Reduction of MIMO-OFDM system using SLM with ABC algorithm," *IOSR Journal of Electronics and Communication Engineering*, vol. 12, no. 4, pp. 1-9, 2017.

[6] A. Joshi and D. S. Saini, "GA-PTS using novel mapping scheme for PAPR reduction of OFDM signals without SI," *Wireless Personal Communications*, vol. 92, no. 2, pp. 639-651, 2017.

[7] N. Taspinar and Y. T. Moskurt, "PAPR reduction using genetic algorithm in lifting-based wavelet packet modulation systems," *Turkish Journal of Electrical engineering and Computer Sciences*, vol. 24, no. 1, pp. 184-195, 2016.

[8] S. K. Goudos, "A novel generalized oppositional bio-geography based optimization algorithm: Application to peak to average power ratio reduction in OFDM systems," *Open Mathematics*, vol. 14, no. 1, pp. 705-722, 2016.

[9] V. Maddala and R. R. Katta, "Adaptive ABC algorithm based PTS scheme for PAPR reduction in MIMO-OFDM," *International Journal of Intelligent Engineering Systems*, vol. 10, no. 2, pp. 48-57, 2017.

[10] L. Jian-Fei, W. Shao-Ying, Z. Xiang-Ye, L. Jia, W. Meng-Jun, "PAPR reduction method for CO-OFDM system based on improved bat algorithm," *Acta Photonica Sinica*, vol. 45, no. 10, ID: 1006001, 2016.

[11] J. Zhou, E. Dutkiewicz, R. P. Liu, X. Huang, G. Fang, and Y. Liu, "A modified shuffled frog leaping algorithm for PAPR reduction in OFDM systems," *IEEE Transactions on Broadcasting*, vol. 61, no. 4, pp. 698-709, 2015.

[12] Md. A. Hossain, I. Elshafiey, and M. A. S. Alkanhal, "Real-time implementation of UWB-OFDM SAR imaging system using shared memory based FPGA," *Applied Computational Electromagnetics Society*, vol. 29, no. 11, pp. 895-903, 2014.

R. S. Suriavel Rao received Ph.D. degree in Information and Communication Engineering from Anna University Chennai. He received both Bachelor and Master Degrees in Electronics and Communication Engineering from M.S. University and Anna University respectively. He is currently serving in the capacity of Professor cum Research Consultant. He has expertise in ASIC design, Antenna and Communication system design as well. Currently he is working on IoT, AI, Deep/Machine learning techniques, and data science. He has vast quantity of teaching and research experiences. His areas of interest are OFDM optimization, WiMax technology, IoT, SoC Design, 5G Wireless Technology.

R. Menaka obtained her Ph.D. degree in Information and Communication Engineering from Anna University Chennai. She received Bachelor degree in Electronics and Communication Engineering from Madras University and Masters degree in Applied Electronics from College of Engineering, Guindy (Anna University). She is presently working as Professor in the Department of ECE, Chennai Institute of Technology. She has around 20 years of teaching experience. Her area of Interest includes Mobile Ad hoc Networks, Wireless Networks and Image & Signal Processing.

R. Alexciyaa Winslet received B.Tech. degree in Electronics and Communication Engineering from Karunya Institute of Technology and Sciences, Coimbatore. She is currently a Post Graduate Student with specialization in VLSI Design at Karunya Institute of Technology and Sciences. Her areas of interest include OFDM system optimization, IC Design using Verilog Coding, and fabrication.

Analysis and Design of an Efficient and Novel MIMO Antenna for 5G Smart Phones Using FDTD and FEM

Raees M. Asif [1], Abdul Aziz [1], M. Amjad [1], Majid N. Akhtar [2], A. Baqir [3], and M. Nawaz Abbasi [1]

[1] Faculty of Engineering & Technology
The Islamia University of Bahawalpur, Bahawalpur, 63100, Pakistan
raees.asif@mnsuet.edu.pk, abdul.aziz@iub.edu.pk, muhammad.amjad@iub.edu.pk, nawaz.abbasi@iub.edu.pk

[2] Department of Physics
MNS University of Engineering & Technology, Multan, 66000, Pakistan
majidniazakhtar@mnsuet.edu.pk

[3] Department of Electrical and Computer Engineering
COMSATS University Islamabad, Sahiwal Campus, Sahiwal, 57000, Pakistan
abuzar@cuisahiwal.edu.pk

Abstract ─ A novel and compact antenna element is analyzed and designed to achieve an efficient 4x4 MIMO antenna for a mobile phone at 3.5 GHz band for 5G communication. FTDT and FEM techniques are used to analyze and compare modeling accuracy of the proposed MIMO antenna. It has achieved a minimum isolation of 19.7dB between two antennas with radiation efficiency of 86%. The improved isolation and efficiency for the proposed MIMO antenna has been achieved without any decoupling structure between antennas, instead larger separation between elements due to compact size of the proposed element facilitated to achieve good performance. Pattern diversity is also achieved by arranging adjacent asymmetric antennas in reverse direction with each other. The envelope correlation coefficient (ECC) is less than 0.002 and Channel Capacity loss (CCL) is also less than 0.4 bps/Hz in the whole frequency band (3.36-3.66 GHz), which is suitable for 5G MIMO systems.

Index Terms ─ Channel Capacity Loss (CCL), Envelope Correlation Coefficient (ECC), Finite Difference Time Domain (FDTD), Finite Element Method (FEM), Multi-Input Multi-Output (MIMO).

I. INTRODUCTION

The aspiration of high speed data transmission rate for smart phones is increasing exponentially. 5G wireless communication system is a consequent telecommunication standard that may achieve data rates up to tens of gigabits/second [1-2]. Such high data rates may be achieved by using multi-input multi-output (MIMO) system with multiple isolated antennas in a mobile phone [3-10]. These multiple antennas may transmit and receive data simultaneously on a single radio frequency channel. MIMO uses multiple path propagation at the same time that ensures the reliability and higher data transmission rate without using extra bandwidth.

Quality of signal transmission can be enhanced if higher isolation is achieved between MIMO antennas of a portable communication device. The mutual coupling among antenna elements causes poor isolation and reduced efficiency [3]. Design of highly efficient MIMO antenna with better isolation and improved bandwidth within a mobile phone is a challenging issue due to common ground of MIMO antenna system.

Several techniques have been reported recently to reduce mutual coupling between antenna elements of a MIMO system. Some popular techniques are: orthogonal arrangement [4-6], neutralization line [7], diagonal arrangement [8, 9], protruded ground plane [10], common grounding branch [11, 12], balanced open slot [13], metamaterial structure [14] and defected ground [15, 16, 17]. However, all these techniques may reduce the coupling between MIMO antenna elements at the cost of reduced efficiency.

Analysis and design of an efficient and compact multi-input and multi-output (MIMO) antenna element is presented for 5G smart phones. FDTD and FEM techniques are used to analyze and compare modeling accuracy of the 4x4 MIMO antenna. Better isolation and bandwidth enhancement is achieved by the novel MIMO antenna system. A minimum isolation of 19.7dB has been achieved between antenna elements without using

Submitted On: September 21, 2020
Accepted On: January 20, 2021
https://doi.org/10.47037/2020.ACES.J.360306

any decoupling structure.

II. MIMO ANTENNA GEOMETRY

Geometry of the proposed novel antenna elements array is shown in the Fig. 1. All dimensions of parameters are in millimeters. Similar to the modern smart phones, the horizontal system substrate has dimensions of 75×150×0.8 mm^3 and it is connected with two vertical substrates on longer sides of the system substrate. The dimension of each vertical substrate is 0.8×150×6 mm^3. All the four antennas are printed on both sides of vertical substrate as shown in Fig. 1. The material for both system and vertical substrate is FR-4 with ε_r = 4.4 and loss tangent = 0.02 and the material for ground and printed patch elements is copper annealed with thickness of 0.035 mm.

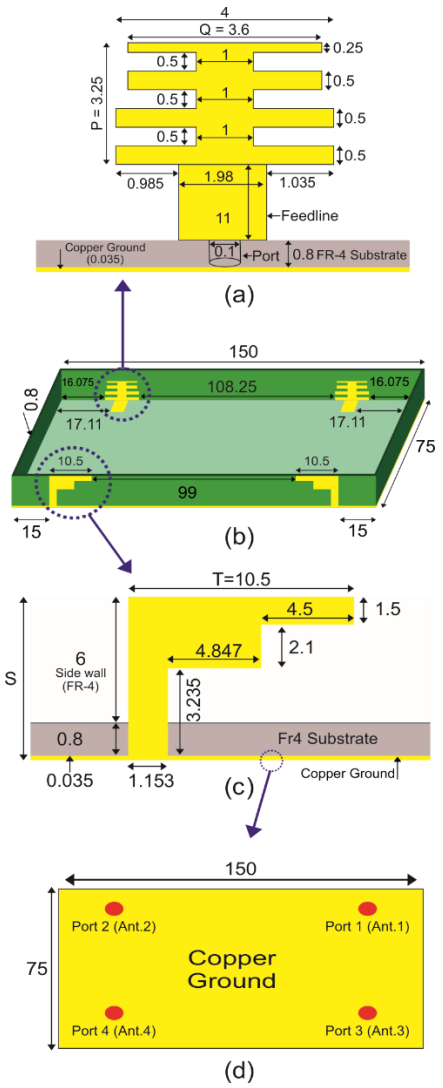

Fig. 1. Proposed structure of MIMO antenna: (a) Yagi-Uda shaped element, (b) complete structure of MIMO antenna, (c) staircase element, and (d) copper ground.

Each antenna consists of a Yagi-Uda shaped element (connected with microstrip feed) on front side of the vertical substrate and a staircase element (connected with ground) on backside of Yagi-Uda shaped element. Each of the microstrip feed line is excited with a 50 Ω coaxial probe. Yagi-Uda shaped element is used to reduce antenna size due to multiple current paths available in Yagi-Uda shaped element. It helps to increase electrical length while keeping the antenna size compact. Asymmetric staircase element is used to concentrate current density on one side of the patch antenna that helps to increase effective spacing and hence isolation between two adjacent antennas arranged in reverse direction. Such reverse arrangement of adjacent asymmetric elements also helped to achieve pattern diversity. The reason for higher isolation and pattern diversity is explained in next section.

III. ANALYSIS OF MIMO ANTENNA

A. Computational analysis using FDTD and FEM

Computational analysis of 4x4 MIMO antenna is performed using two different computational analysis techniques in CST Microwave Studio, first technique is FDTD (Finite Difference Time Domain) of time domain solver while the other technique is FEM (Finite Element Method) of frequency domain solver. FDTD is used with Perfect Boundary Approximations (PBA) on a hexahedral grid while FEM is used on a tetrahedral grid with open boundary conditions.

S-parameters for FDTD computational analysis are shown in Fig. 2. It can be seen that all the reflection coefficients ($S_{11}, S_{22}, S_{33}, S_{44}$) are less than -10 dB (2:1 VSWR), which ensures acceptable impedance matching from 3.33 to 3.66 GHz, while transmission coefficients depicts the minimum isolation of 19.7 dB at 3.5GHz. Due to evenness and simplicity, the analysis has been made by considering only following transmission coefficients: $S_{21} = S_{12,}$, $S_{31} = S_{13}$ and $S_{41} = S_{14}$. It can be seen that all the transmission coefficients are less than the required standard of at least -15 dB without any decoupling network. The isolation is achieved due to larger effective spacing between compact elements. It is the reason, due to which maximum isolation of greater than 29 dB is achieved between antenna 1&4, as they are diagonally placed. So, the proposed MIMO antenna is best suited for smartphones used for 5G applications.

To verify modeling accuracy of the proposed MIMO antenna, it is also analyzed using FEM technique. S-parameters for FEM technique are shown in Fig. 3. It can be seen that the impedance bandwidth and isolation between MIMO antennas are almost similar to those achieved through FDTD technique. A very little deviation in impedance matching and a frequency shift is ignorable due to a minor convergence error in any of the computational techniques. Therefor the proposed MIMO antenna model may be used to achieve required isolation

and impedance bandwidth performance.

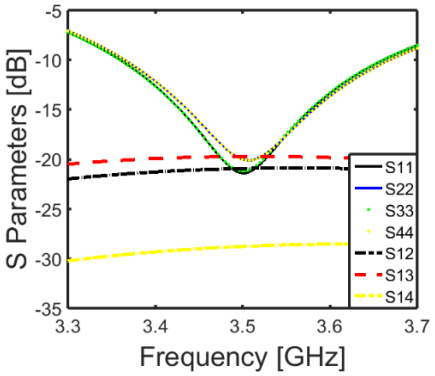

Fig. 2. S-parameters for the 4x4 MIMO antenna using FDTD.

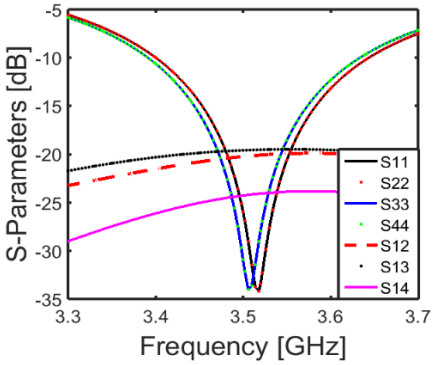

Fig. 3. S-parameters for the 4x4 MIMO antenna using FEM.

B. Parametric analysis

In parametric analysis, some computational aspects of the proposed design are presented. It may help to perceive in-depth understanding about modeling issues of the critical parameters, which are used to optimize the proposed MIMO antenna patch elements.

The parametric analysis for P and Q dimensions of Yagi-Uda shaped element for return loss are shown in Figs. 4 and 5, respectively. It can be seen that the resonance curve shifts from right to left with increase in P, while impedance matching at 3.5 GHz is better for optimized value of P=3.25 mm. In a similar way the resonance curve shifts from right to left with increase in Q, however, return loss also increases with increase in Q. The optimized value of Q=3 mm is selected to have moderate return loss at 3.5 GHz.

Similar parametric curves for T and S dimensions of staircase element are shown in Figs. 6 and 7, respectively. It can be seen that resonance curve shifts again from right to left while return loss decreases with increase in value of T. The return loss is minimum at optimum value of T=10.5 mm. It can also be seen that the S dimension has very important role in impedance matching and the return loss decreases with increase in S at 3.5 GHz.

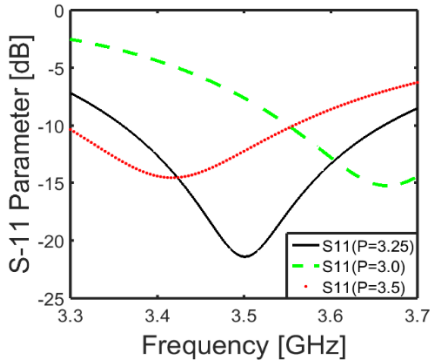

Fig. 4. Parametric analysis of dimension P for return loss.

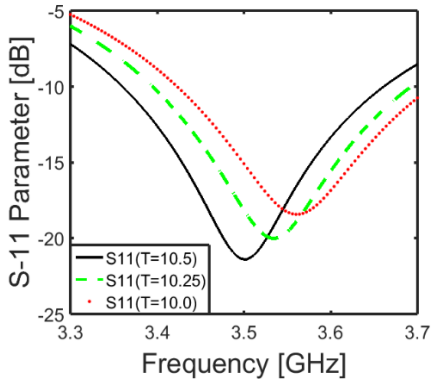

Fig. 6. Parametric analysis of dimension T for return loss.

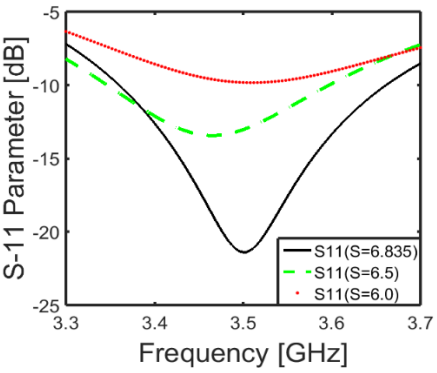

Fig. 7. Parametric analysis of dimension S for return loss.

C. Surface current analysis

Surface current distributions at 3.5GHz on all the four antennas when Antenna-1 is excited and remaining ports are matched with 50Ω load are shown in Fig. 8 (a). The isolation between MIMO antennas is evident from the maximum current distribution on Antenna-1

while minimum current distribution on remaining three antennas. For Antenna 1 in Fig. 8 (b), it can be seen that the density of current distribution is higher on left side of the Yagi-Uda and staircase elements. As arrangement of Antenna-2 on the same edge is kept in reverse direction to that of Antenna-1, so if it is excited then surface current density for Antenna-2 elements will be higher on right side of the Yagi-Uda and staircase elements of Antenna-2. This will increase the effective spacing and hence isolation between the antenna elements on the same edge. Similar arrangement for Antenna-3 and Antenna-4 on the other edge causes similar higher isolation between the two antennas. There is already enough separation of 75mm (greater than λo/2) between the two edges, so all the four antennas have enough isolation (greater than 19.7 dB). So, the larger effective spacing among antennas is the key reason for higher isolation between MIMO antennas.

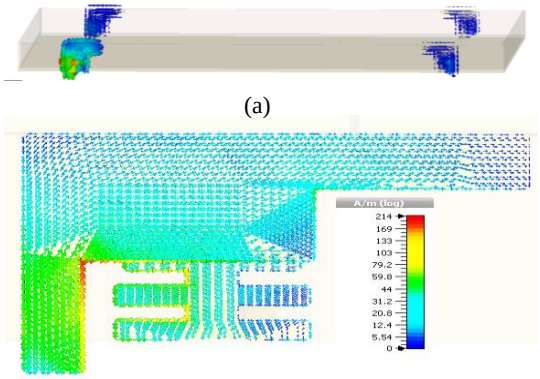

Fig. 8. Surface current distribution analysis: (a) current on all antennas, and (b) current on Antenna 1.

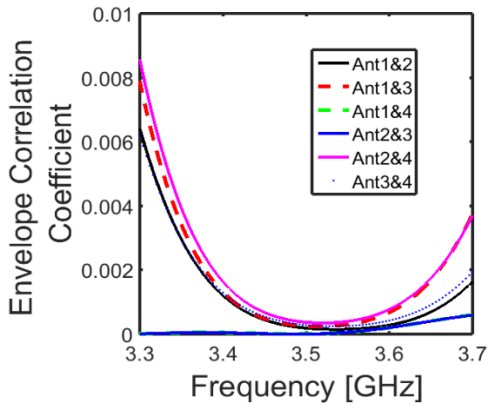

Fig. 9. Envelope Correlation Coefficient (ECC) between antennas of the 4x4 MIMO antenna system.

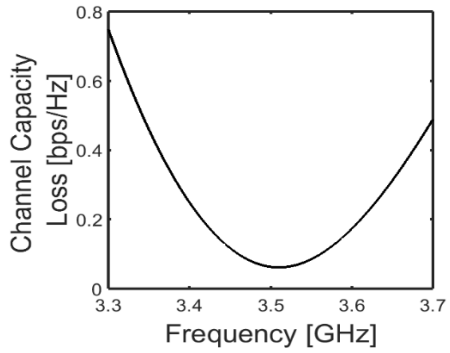

Fig. 10. Channel Capacity Loss (CCL) of the 4x4 MIMO antenna system.

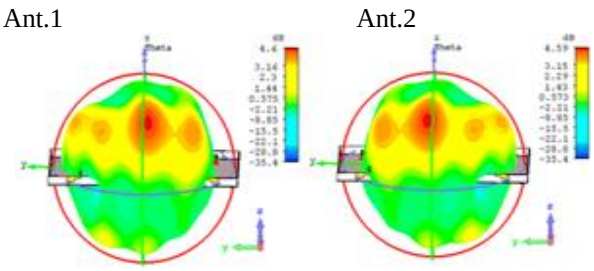

Fig. 11. 3D radiation patterns: (a) Antenna-1 and (b) Antenna-2.

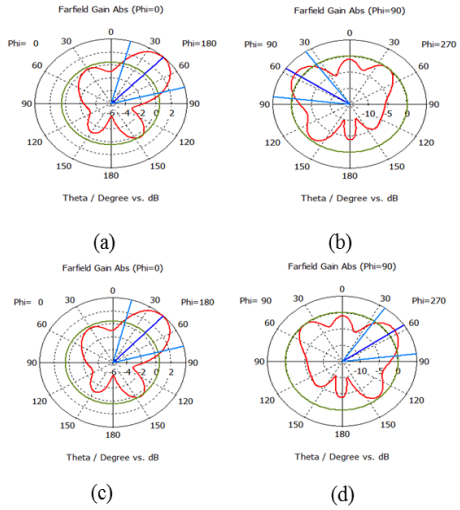

Fig. 12. 2D radiation patterns: (a) Antenna-1, xz-plane; (b) Antenna-1, yz-plane; (c) Antenna-2, xz-plane; (d) Antenna-2, yz-plane.

D. Diversity analysis for gain and radiation pattern

Channel Capacity Loss (CCL) and Envelope Correlation Coefficient (ECC) are used to evaluate gain diversity performance of the proposed MIMO antenna. ECC is plotted in Fig. 9, it can be seen that ECC is less

than 0.002 in the desired frequency band of 3.33-3.66 GHz. ECC between antenna 1&4 and antenna 2&3 is almost zero as they are diagonally placed.

Channel capacity loss (CCL) of the MIMO antenna is calculated by using following equations:

$$C_{loss} = -Log_2 \det(\varphi^R), \quad (1)$$

$$\varphi^R = \begin{bmatrix} \rho_{11} & \rho_{12} \\ \rho_{21} & \rho_{22} \end{bmatrix}, \quad (2)$$

$$\rho_{ii} = 1 - \left(|S_{ii}|^2 + |S_{ij}|^2\right), \quad (3)$$

$$\rho_{ij} = -\left|S_{ii}^* S_{ij} + S_{ji}^* S_{ij}\right|. \quad (4)$$

The value of CCL is also below 0.4 bps/Hz in the desired frequency band as shown in Fig. 10. As the values of ECC and CCL are below than the required standard limits for a 4x4 MIMO antenna system, so the proposed MIMO antenna has decent gain diversity performance.

Radiation patterns for adjacent antennas, Antenna-1 and Antenna-2, are shown in Figs. 11 and 12. All the antennas have achieved similar gain performance and peak gain for each antenna is 4.6 dBi as shown in Fig. 13, for Antenna-1, while the radiation efficiency of each antenna varies from 81 to 86% in the desired frequency band. However, it can be seen that the radiation beam of Antenna-2 is directed towards opposite direction to that of Antenna-1 due to reverse arrangement of both asymmetric antennas with respect to each other. Such radiation patterns verify that the pattern diversity is also achieved.

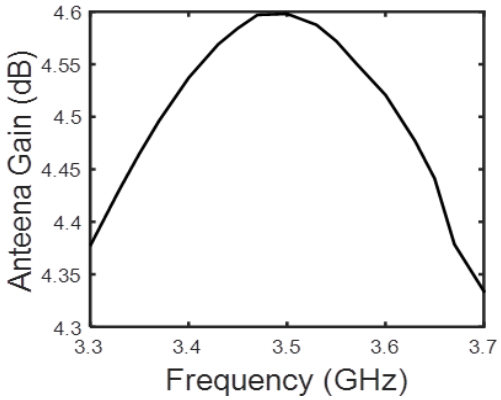

Fig. 13. Gain performance for Antenna-1 of the MIMO antenna system.

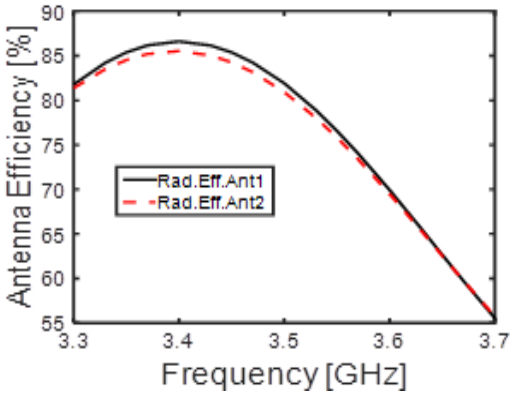

Fig. 14. Radiation Efficiency for Antenna-1&2 of the MIMO antenna system.

IV. COMPARISON WITH PREVIOUS WORKS

The performance of the proposed MIMO antenna is compared with previous recent works in Table 1 to highlight significance of the proposed antenna. It can be seen that the proposed MIMO antenna has achieved comparable performance with improved isolation greater than 19.7 dB, radiation efficiency up to 86%, total efficiency up to 77% and -10dB impedance bandwidth of 300 MHz without any decoupling structure between compact size (71.1mm^2) antennas. Therefore, the proposed MIMO antenna system is a suitable potential player for future 5G MIMO smart phone applications.

V. CONCLUSION

This work has been proposed a 4×4 efficient MIMO antenna system at 3.5 GHz frequency band (3.36–3.66 for 5G smart phone applications. The proposed model is analyzed using FDTD and FEM to verify its modeling accuracy. The adjacent antennas are arranged in reverse direction to achieve higher isolation with suitable gain and pattern diversity. Higher isolation (> 19 dB) has been achieved without any decoupling structure between antennas. The proposed MIMO antenna has also achieved radiation efficiency up to 86% and low value of ECC (< 0.02). The Channel capacity loss (CCL) of the proposed 4×4 MIMO antenna system has also been calculated and it is less than 0.4 bits/Hz in the desired frequency band. Therefore, the proposed MIMO antenna system is a suitable potential candidate unit for massive MIMO system in future.

Table 1: Comparison with previous recent works

Ref.	BW (GHz)	Isolation (dB)	ECC	TE (%)	Antenna Element Size (mm^2)	Isolation Technique	Antenna Array
[5]	3.4-3.6 (-6dB)	> 20	< 0.06	< 74	12×7	Orthogonal arrangement	4×4
[6]	3.4-3.6 (-6dB)	> 12	< 0.15	< 40	26×3	Neutralization line	4×4
[9]	3.4-3.6 (-10dB)	> 17	< 0.1	< 73	9.4×7	Common grounding branch	4×4
[10]	3.4-3.6 (-10dB)	> 10	< 0.2	< 70	17×5	Protruded ground plane	8×8
[11]	3.4-3.6 (-10dB) 4.8–5.0 (-10dB)	> 17	< 0.03	< 67	10×7	Common grounding branch	4×4
[12]	3.4-3.6 (-6dB) 4.8–5.0 (-6dB)	> 12	< 0.02	< 80	3.9×17.7	Linear + diagonal arrangement	4×4
This work	3.36-3.66 (-10dB)	> 20	< 0.002	< 77	10.5×6.835	Reverse + diagonal arrangement	4×4

REFERENCES

[1] J. G. Andrews, S. Buzzi, W. C, Stephen V. Hanly, A. Lozano, A. C. K. Soong, and J. C. Zhang, "What will 5G be?," *IEEE Journal on Selected Areas in Communications*, vol. 32, no. 6, pp. 1065-1082, June 2014.

[2] Nokia white paper: '5G deployment below 6 GHz'. Available at https://resources.ext.nokia.com/asset/201315, accessed Aug. 2017.

[3] M. Abdullah, Y.L. Ban, K. Kang, M.-Y. Li, and M. Amin, "Compact four-port MIMO antenna system at 3.5 GHz," *IEEE 2nd Advanced Information Technology, Electronic and Automation Control Conference (IAEAC)*, Mar. 26, 2017.

[4] A. A. Ibrahim, J. Machac, and R. M. Shubair, "UWB MIMO antenna for high speed wireless applications," *Applied Computational Electromagnetic Society Journal*, vol. 34, no. 9, pp. 1294-1299, Sept. 2019.

[5] H. T. Chattha, "4-Port 2-element MIMO antenna for 5G portable applications," *IEEE Access*, Special Section on Antenna and Propagation for 5G and Beyond, June 27, 2019.

[6] L. Sun, H. Feng, Y. Li, and Z. Zhang, "Compact 5G MIMO mobile phone antennas with tightly-arranged orthogonal mode pairs," *IEEE Transactions on Antennas and Propagation*, vol. 66, no. 11, pp. 6364-6369, Nov. 2018.

[7] S.-C. Chen, M.-K. Wu, C.-W. Chiang, and M.-S. Lin, "3.5-GHz four-element MIMO antenna system for 5G laptops with a large screen-to-body ratio," *Journal of Electromagnetic Waves and Applications*, vol. 34, pp. 1195-1209, Nov. 2019.

[8] A. Zhao and Z. Ren, "Size reduction of self-isolated MIMO antenna system for 5G mobile phone applications," *IEEE Antennas and Wireless Propagation Letters*, vol. 18, no. 1, pp. 152-156, Jan. 2019.

[9] Z. Ren, A. Zhao, and S. Wu, "MIMO antenna with compact decoupled antenna pairs for 5G Mobile terminals," *IEEE Antennas and Wireless Propagation Letters*, vol. 18, no. 7, pp. 1367-1371, July 2019.

[10] Y.-L. Ban, C. Li, C.-Y.-D. Sim, G. Wu, and K.-L. Wong, "4G/5G multiple antennas for future multi-mode smartphone applications," *IEEE Access*, vol. 4, pp. 2981-2988, June 2016.

[11] Z. Ren and A. Zhao, "Dual-band MIMO antenna with compact self-decoupled antenna pairs for 5G mobile applications," *IEEE Access*, vol 7, pp. 82288-82296, June 2019.

[12] W. Zhang, Z. Weng, and L. Wang, "Design of a dual-band MIMO antenna for 5G smartphone application," *IEEE International Workshop on Antenna Technology (IWAT)*, Mar. 2018.

[13] Y. Li, C.-Y.-D. Sim, Y. Luo, and G. Yang, "High-isolation 3.5-GHz 8-antenna MIMO array using balanced open slot antenna element for 5G smartphones," *IEEE Transactions on Antennas & Propagation*, vol. 67, pp. 3820-3830, June 2019.

[14] J. Jiang, Y. Xia, and Y. Li, "High isolated X-band MIMO array using novel wheel-like metamaterial decoupling structure," *Applied Computational Electromagnetic Society Journal*, vol. 34, no. 12,

pp. 1829-1836, Dec. 2019.

[15] H. Alsaif, M. Usman, M. T. Chughtai, and J. Nasir, "Cross polarized 2×2 UWB-MIMO antenna system for 5G wireless applications," *Progress in Electromagnetics Research*, vol. 76, pp. 157-166, Dec. 2018.

[16] M. Yang, Y. F. Sun, and T. Q. Liao, "Multi-mode narrow-frame antenna for 4G/5G metal rimmed mobile phones," *Applied Computational Electromagnetic Society Journal*, vol. 35, no. 8, Aug. 2020.

[17] J. Su, Z. Dai, J. Du, J. Yu, Z. Chen, and Z. Li, "A compact dual band MIMO antenna for 5G mobile communication," *Applied Computational Electromagnetic Society Journal*, vol. 34, no. 11, pp. 1731-1738, Nov. 2019.

Broadband, Beam-Steering Asymmetric Stacked Microstrip Phased Array with Enhanced Front-to-Back Ratio

Melih Türk [1] and Fikret Tokan [2]

[1] The Scientific and Technological Research Council of Turkey, Gebze, 41470, Kocaeli, Turkey
melih.turk@tubitak.gov.tr

[2] Department of Electronics and Communications Engineering, Faculty of Electrical and Electronics
Yildiz Technical University, Istanbul, Turkey
ftokan@yildiz.edu.tr

Abstract — The backward radiation is a critical problem that may cause breakdown of the front-end circuits that are integrated behind the antenna. Thus, antennas having high Front to Back Ratio (FBR) are required. For phased arrays, the back lobe suppression is required for all scanning angles at all frequencies of the band. In this work, a stacked patch linear array with asymmetric configuration is proposed. It is capable of scanning the beam in $\pm 40^{o}$ with less than 1.34 dB scanning loss. Due to the usage of probe-fed stacked patches as the antenna elements, impedance matching in 8-10 GHz is achieved. More than 30 dB FBR is obtained for broadside radiation. It is above 20 dB when the beam is steered to $\theta = 40^{o}$. This is valid for all frequencies of the band. A prototype is fabricated and measured. Higher than 38 dB FBR is observed. With its broadband, high FBR and low scanning loss, the proposed asymmetrical stacked patch phased array is suitable as radar and base station antenna.

Index Terms — Back-lobe suppression, front to back ratio, linear phased array, stacked patch, wideband antenna.

I. INTRODUCTION

Microstrip antenna arrays are popular solutions for wide beam scanning function that is essential in radar, electronic warfare and communication systems. Wide frequency coverage, ease of fabrication and conformity are key parameters for the success of these systems. Among feeding structures, probe-fed solution is widely used due to its robust nature and impedance matching performance [1]. However, narrow band characteristic of a microstrip antenna is a major drawback for wide band applications. There has been considerable interest towards designing wideband microstrip antennas to be used in phased arrays for wide beam scanning. It is proved that thick laminates with low dielectric constant is likely to give the largest bandwidth responses and good surface wave efficiencies [2]. Many designs consisting of different geometries have been introduced in literature [3]. A probe fed stacked square patch slotted wideband microstrip antenna is presented [4-5]. An asymmetrical complementary split ring resonator (CSRR) loaded stacked microstrip patch antenna is introduced for broadband applications in [6]. The shape of the patch is formed into a rose leaf and fed with a capacitive coupled rectangular feed in [7]. With the rose leaf structure, impedance bandwidth performance of the antenna is increased up to 69%. Stacked patch antennas have been implemented in low temperature cofired ceramic (LTCC), as well [8-10]. Array examples of stacked patches are also presented [11-14]. In order to obtain broadband characteristic, a patch array is arranged as a three stacked structure consisting of one radiation patch and two parasitic patches [11]. An array configuration of 16 element 45^{o} polarized stacked patches in LTCC is designed for fifth-generation (5G) applications [12]. A 16-element linear polarized stacked patch array and its feeding network is demonstrated for Ku-band applications [13]. A phased array consisting of 32 circularly polarized stacked patch antennas is used to enhance the bandwidth characteristics of commercial drones [14].

Mutual coupling effect between antenna elements is a critical issue in the design of microstrip arrays. This effect may lead to impedance mismatch, decrease in gain, increase in side lobe level (SLL) and occurrence of scanning blindness [15]. Electromagnetic bandgap (EBG) structures that create a photonic crystal to suppress the surface-wave propagation were developed to eliminate mutual coupling and prevent the degradation in radiation performance of the array [16-18].

Defected ground structures (DGS) have been proposed to improve mutual coupling between patch elements [15, 19]. The effect of DGS on coupling characteristics is observed by means of a two element microstrip array and the positive impact of the DGS on mutual coupling is investigated in [19]. However,

Submitted On: October 26, 2020
Accepted On: January 24, 2021
https://doi.org/10.47037/2020.ACES.J.360307

existence of DGS resulted in higher back lobe level of the array pattern. The backward radiation is a critical problem that may cause breakdown of the front-end circuits that are integrated behind the antenna. Besides, the back lobe radiation results in multipath signal propagation that may lead to error in differential positioning systems. The coverage capacity of a base station antenna may also be affected due to the overlapping areas between adjacent sectors [20-21]. Various techniques such as ground plane edge shaping, using a semi-transparent ground plane or isolated soft surface structure and optimizing reflector shape have been applied for the suppression of back lobes in literature [21-26]. [21-25] have been specifically applied to microstrip antennas. Besides, some antennas are introduced as candidates with high FBR values. These include circularly polarized antenna [27], short microstrip leaky-wave antenna [28] and substrate integrated waveguide slot antenna [29]. Various antenna array structures also proposed for improving FBR in broad frequency band [30-32]. A suppressed back-lobe substrate-integrated waveguide slot array antenna is presented for X-band [30]. In [31] a microstrip antenna array with DGS structure is proposed for back lobe reduction. In [32], a mode superposed microstrip patch antenna with bandgap structures is introduced to improve the FBR.

In the above mentioned works, the back radiation is investigated for the radiation of the antenna in broadside direction. However, for a phased array, back lobe generation is observed for all scanning angles. On this ground, in this work, we proposed an asymmetric array structure as an advantageous solution for the broadband phased arrays with concerns in particular wide-scan ranging with suppressed back lobe characteristics, compactness and suitable for simple manufacturing process. The dimensions of asymmetric array structure are investigated by a parametric analysis of substrate size. The proposed stacked patch asymmetric phased array architecture is applied to X-band. With a linear array consisting of 8-elements, $\pm 40^{o}$ beam scanning is observed with less than 1.34 dB scanning loss in the whole 8-10 GHz frequency band. FBR is observed above 30 dB for broadside radiation. Up to $\pm 40^{o}$, the back lobe is suppressed more than 20 dB.

The structure of stacked microstrip antenna and its radiation characteristics are introduced in Section II. Also, its radiation performance is compared with that of traditional microstrip antenna. In Section III, an asymmetrical phased array consisting of stacked patches is demonstrated and its back lobe suppression is observed in terms of scanning angle. In Section IV, experimental verification of the fabricated array prototype is given. Finally, Section VI concludes the paper.

II. DESIGN OF WIDEBAND MICROSTRIP ANTENNA

Stacked structure consists of a ground plane at the bottom layer. A dielectric layer with the radiating patch element is placed above the ground plane. A stacked layer and a parasitic patch are planted as the top layer. The structure of the stacked patch antenna is shown in Fig. 1 together with its design parameters. The stacked patch antenna is fed by a coaxial line whose impedance is $50\ \Omega$. The lower patch is etched on a Rogers 4003C substrate ($\tan\delta = 0.0027$ at 10 GHz) with 35 μm copper thickness, whereas the upper patch is etched on foam ($\tan\delta \cong 0.001$ at 10 GHz) to reduce loss due to surface waves and widen the bandwidth of the antenna. The main beam radiation of the antenna is orthogonal to x-y plane. All dimensions of the stacked patch antenna are listed in Table 1.

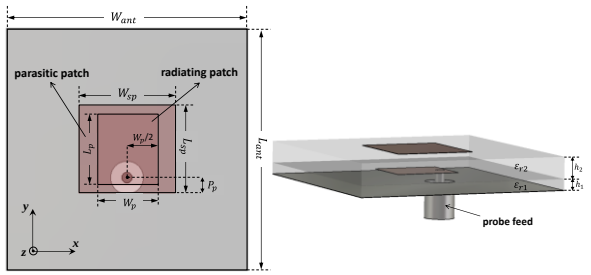

(a) (b)

Fig. 1. Stacked patch antenna: (a) top view; (b) lateral view.

Table 1: Broadband stacked patch antenna dimensions

Parameter	Dimension
ε_{r1}	3.38
ε_{r2}	1.07
W_{ant}	30 mm
L_{ant}	30 mm
W_{sp}	12 mm
L_{sp}	11 mm
W_p	7.5 mm
$\boldsymbol{P_p}$	**2 mm**
L_p	9 mm
h_1	1.52 mm
h_2	3 mm

The numerical analysis of the designed antennas in the paper is accomplished with a three dimensional (3D) full-wave electromagnetic solver, CST Microwave Studio [33]. To demonstrate the superior performance of the stacked patch, results are compared with that of an ordinary patch antenna whose dimensions and material is exactly same with the radiating patch and lower substrate of the stacked patch antenna. Thus, the size and material

details for this structure can also be found in Table 1. In Fig. 2 (a), reflection coefficient variations of the ordinary patch and stacked patch antennas are given as the function of frequency. The bandwidth of the patch antenna covers a 320 MHz band between 8.28-8.6 GHz. The S_{11} variation of the stacked patch antenna is lower than -10 dB for the whole band of interest. This figure clearly demonstrates the broadband characteristic of the stacked structure. The gain and total efficiency variation of the antennas are given in Fig. 2 (b) and Fig. 2 (c), respectively. More than 1 dB gain enhancement and total efficiency above 90% is obtained with the stacked structure in the whole 8-10 GHz band.

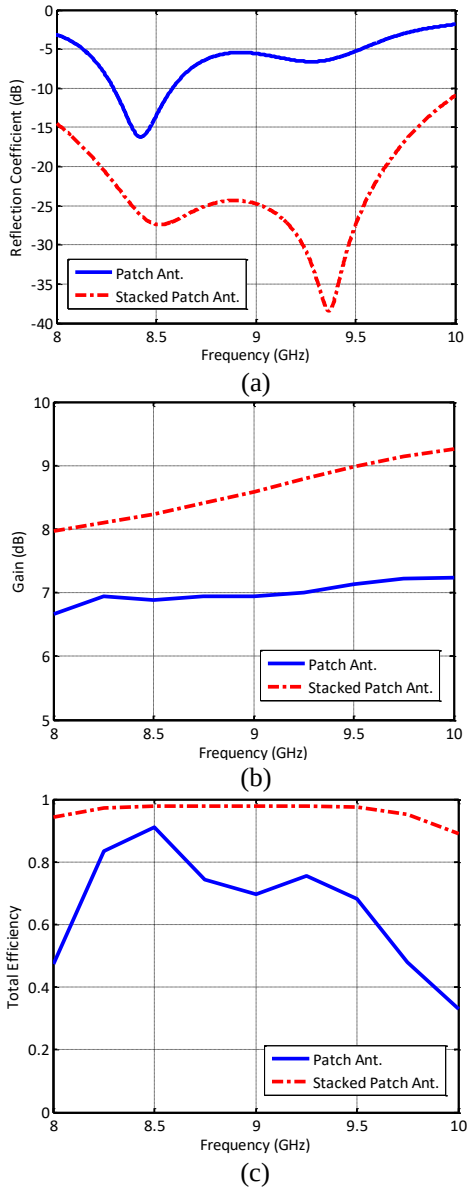

Fig. 2. Performance comparison of stacked patch antenna and ordinary patch antenna: (a) reflection coefficient; (b) gain; (c) total efficiency.

The simulated co-polarized gain patterns are given in Fig. 3 in E- and H-planes at 8 GHz, 9 GHz and 10 GHz. The main beam radiation is observed along z-axis. Shape of the pattern does not change significantly in $\emptyset = 0$ plane. On the hand, the beam in $\emptyset = 90^0$ plane narrows with increasing frequency.

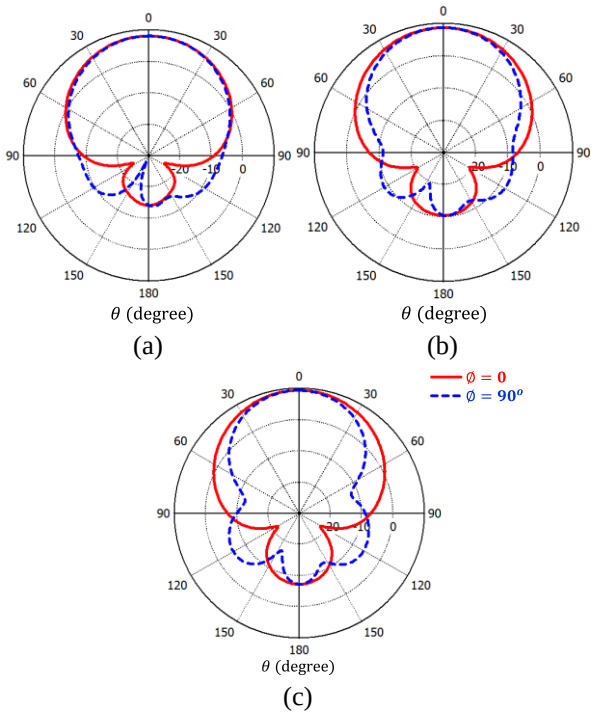

Fig. 3. Gain patterns of stacked patch antenna: (a) 8 GHz, (b) 9 GHz, and (c) 10 GHz.

III. X-BAND PHASED ARRAY DESIGN

Phased arrays are capable of electronically scanning the beam in a predefined angular range with predefined beam characteristics by adjusting the excitation phase and amplitude of the antenna elements. The level of mutual coupling between antenna elements is related with the relative positions of the elements. The dominant surface wave mode couples more strongly compared to other modes in the E-plane. Since the amount of coupling varies with different scan angles, the input impedance of the array will vary with the scanning angle, as well.

In radar applications, planar phased array topologies capable of scanning the space in a single plane are widely required. Automotive radars that scan the horizontal plane within the $\pm 30^o$ scanning angle can be given as an example. In this section, two demonstrations for the linear phased array are given. They both use stacked patch antenna elements and scan the beam in $\pm 40^o$ scanning angle with low scanning loss. The major difference between two examples is their structure. One of them has patch antenna elements placed to the substrate with equal distance from the edges. In the

other one, the patch is placed with unequal distances from the edges. We call this one as asymmetric structure. Asymmetrical structure of the array improves the radiation characteristics of the array, especially reduces the back lobe radiation. Suppression of the back lobe is a critical issue in radars, since its existence may deteriorate the front end circuit of the radar.

A. X-Band linear phased array design

Two linear phased arrays consisting of wide-band stacked patch antenna elements are demonstrated in this section. Stacked patch antenna radiation characteristics are given in Section 2. The distance between antenna elements d, is calculated with $d_{max} = \lambda_c/(1 + |\sin\theta|)$ to avoid grating lobe generation. Here, θ is the beam scanning angle. By setting $\theta = 40^o$, d is determined as $20\,mm$ which is smaller than half wavelength at the lowest frequency of the band. Symmetric and asymmetric stacked patch phased array structures are given in Fig. 4. The lower patch is etched on Rogers 4003C substrate ($\varepsilon_{r1} = 3.38$) and the upper patch is etched on foam ($\varepsilon_{r2} = 1.07$). The patches of the array given in Fig. 4 (a) have been centered to the substrate of the array. To reduce diffraction effect, the substrate size of the array is increased as given in Fig. 4 (b).

Front to back ratio of the asymmetric antenna array structure is investigated by a parametric analysis of substrate size. During this study each parameter (W_1,W_2) is varied alone while the other one is held fixed. The influence of the variables W_1 and W_2 in the antenna array back lobe radiation is summarized in Table 2 and Table 3. It is clear from these tables that highest FBR values are obtained for W_1 to W_2 ratio of 2:1 at the whole operation frequency band.

Table 2: The FBR variations with W_2 when W_1 value is fixed to 13.5 mm

FBR (dB)		W_2 (mm)				
		13.5	20	27	33.5	40.5
W_1 = 13.5 (mm)	8 GHz	17.4	20.3	26.7	19.9	16.8
	9 GHz	17.9	20	24.8	18.6	18
	10 GHz	16.7	19	23.7	18.5	18

Table 3: The FBR variations with W_1 when W_2 value is fixed to 13.5 mm

FBR (dB)		W_1 (mm)				
		13.5	20	27	33.5	40.5
W_2 = 13.5(mm)	8 GHz	17.4	20.2	28.3	23.9	18.4
	9 GHz	17.9	20.7	34	22.2	20
	10 GHz	16.7	18.7	36.2	21.5	18.8

As a result, backward radiation is suppressed. The patches of the asymmetric structure are located 2:1 ratio from the lateral sides of the array. Also, wider spacing is left at the right and left edges of array. The dimensions of the two structures are listed in Table 4.

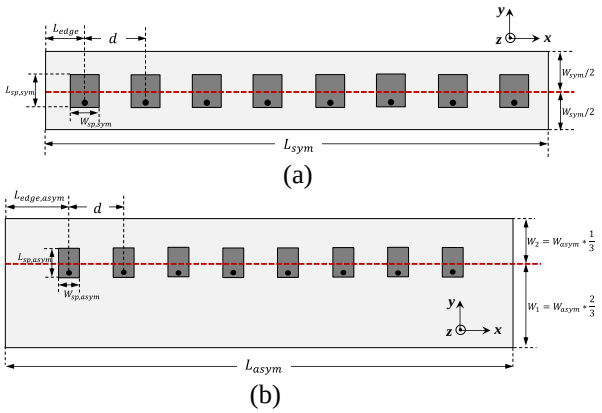

Fig. 4. Stacked microstrip phased array: (a) symmetric; (b) asymmetric configuration.

Table 4: Broadband stacked microstrip phased array dimensions

Symmetric Configuration		Asymmetric Configuration	
Parameter	**Dimension(mm)**	**Parameter**	**Dimension(mm)**
W_{sym}	27	W_{asym}	40.5
L_{sym}	168	L_{asym}	190
d	20	d	20
L_{edge}	14	$L_{edge,asym}$	25
$W_{sp,sym}$	12	$W_{sp,asym}$	12
$L_{sp,sym}$	11	$L_{sp,asym}$	11

B. Simulation results

The array factor (AF) of an N-element linear array placed along *x*-axis can be expressed as:

$$AF = \sum_{n=1}^{N} e^{j(n-1)\psi}, \quad (1)$$

where, $\psi = kdsin\theta cos\emptyset + \beta$. Here, d is the distance between antenna elements, θ is the beam scanning angle and k is the free space wavenumber. The excitation phases of the antenna elements of the linear array are calculated by using $\beta = -kdsin\theta cos\emptyset$ formula since the antenna elements are placed along *x*-axis. It should be noted that the beam of the array is scanning in the x-z plane, thus $\emptyset = 0$ in this plane.

Non-uniform amplitude distribution is preferred to obtain lower namely, -30 dB side lobe levels. Corresponding Dolph-Chebyshev amplitude values are listed in Table 5. The overall size of the symmetrical phased array is $27mm \times 168\,mm$. On the other hand, asymmetrical phased array has $40.5mm \times 190mm$ real estate area.

Active reflection coefficient, Γ_{m} defines the ratio of reflected power when all the antenna elements are simultaneously excited. It can be calculated by Eq. (2) for unequal phase and amplitude excitations:

$$\Gamma_{\mathrm{m}}(\theta) = \sum_{n=1}^{N} S_{mn}\, e^{-jknd\sin\theta}, \quad (2)$$

where $k = 2\pi/\lambda$, m is the index indicating the mth array element and S_{mn} is the transmission coefficient from

port n to port m. The mutual coupling between antenna elements is considered in this equation. Active S-parameters of the symmetric and asymmetric 8 element phased arrays when the beam is steered to $\theta = 40^o$ are given in Fig. 5. Higher values of reflection coefficient are observed for the elements in the middle of the array. $S_{active,j}$ is lower than -10 dB for all j values except $j = 4$. Although $S_{active,4}$ reaches approximately to -9 dB at the lowest frequency of the band for symmetric structure and at the highest frequency of the band for asymmetric structure, its level is still acceptable.

Table 5: Dolph-Chebychev function amplitude values for the linear array

Amplitude #	Value
A_1	0.2622
A_2	0.5187
A_3	0.812
A_4	1
A_5	1
A_6	0.812
A_7	0.5187
A_8	0.2622

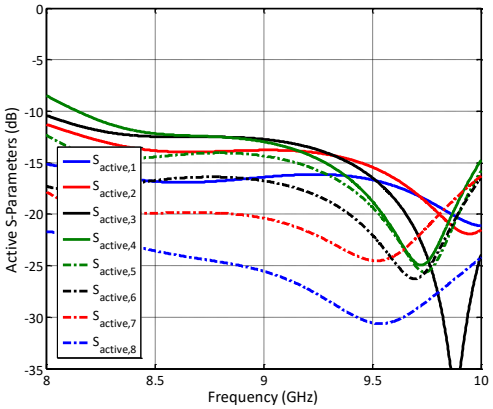

(a)

(b)

Fig. 5. Simulated active S-parameters of a 8-element stacked microstrip phased array radiating to $\theta = 40^o$: (a) symmetric; (b) asymmetric configuration.

Reducing back lobe radiation is critical for radar and base station antenna arrays. Back lobe radiation can be suppressed by using a low back lobe antenna. To increase the subscriber capacity, FBR is expected to be more than 20 dB [26]. The radiation patterns of the symmetrical and asymmetrical arrays at 8 GHz are given in Fig. 6 (a) and Fig. 6 (b), respectively. The patterns are demonstrated up to 40^oscanning angle. The amplitude of array element excitations is listed in Table 5, whereas their relative phases are listed in Appendix I.

For the symmetric stacked patch phased array, 17.14 dB FBR is observed at broadside direction at 8GHz. It decreases to 14.06 dB when the beam is steered to 40^o. The scanning loss for steering the beam to 40^o is 0.54 dB. For the asymmetric structure, FBR is more than 30 dB for broadside radiation and 20.1 dB for 40^oscanning. There is almost no scanning loss for this structure. These figures clearly demonstrate the positive effect of asymmetric placement of the patches on the FBR. Similar conclusions are observed for the patterns at 9 and 10 GHz in Fig. 7 and Fig. 8, respectively. By altering the dimensions of substrate of the array, FBR is increased above 20 dB for all scanning angles at all frequencies. The scanning loss of symmetric structure for steering the beam to 40^o at 9 and 10 GHz are 0.9 dB and 2.19 dB, respectively. It is 0.1 dB and 1.34 dB for the asymmetric structure. Thus, asymmetric structure has positive effect on the scanning loss, as well.

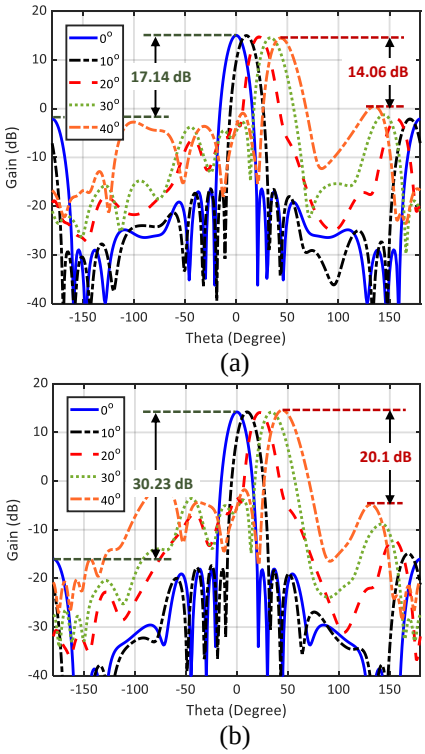

(a)

(b)

Fig. 6. Scanning performance of phased arrays at 8 GHz: (a) symmetric; (b) asymmetric array.

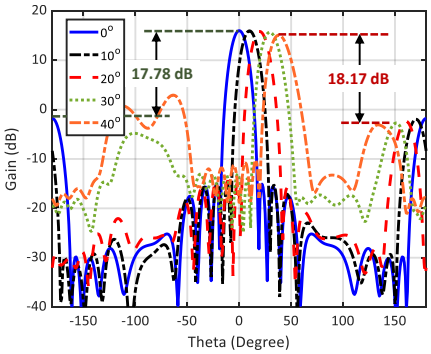

(a)

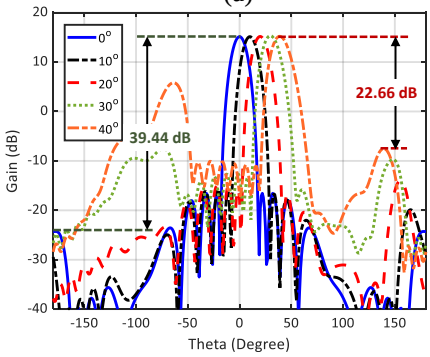

(b)

Fig. 7. Scanning performance of phased arrays at 9 GHz: (a) symmetric; (b) asymmetric array.

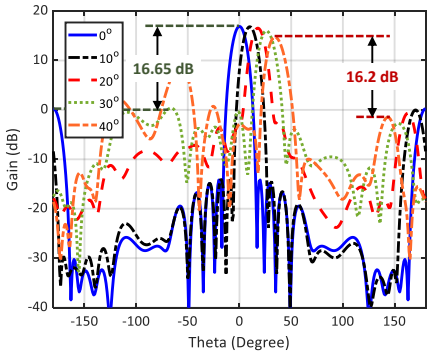

(a)

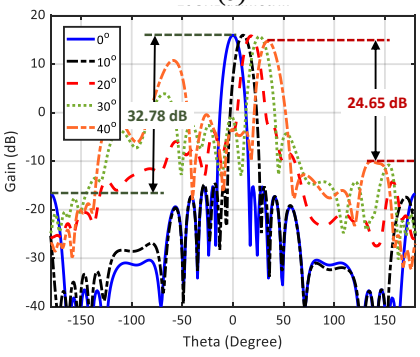

(b)

Fig. 8. Scanning performance of phased arrays at 10 GHz: (a) symmetric; (b) asymmetric array.

IV. EXPERIMENTAL CHARACTERIZATION AND ANALYSIS

For the easy fabrication, a radome layer is added to the array as the top layer. It is Rogers 5880 substrate ($\tan\delta = 0.0009$ at 10 GHz) with 0.254 mm thickness. The dielectric constant of the radome substrate is $\varepsilon_r = 2.2$. The parasitic patches are positioned to the bottom side of the radome as shown in Fig.9 (a). Foam with 3mm thickness is placed under this layer. Below foam layer, there are radiating patches on Rogers 4003C substrate as shown in Fig. 9 (b). By gluing these layers, the asymmetric stacked patch array is constructed. The side view of the fabricated prototype is shown in Fig. 9 (c). SMA connectors that operate up to 18 GHz are soldered to the radiating patches.

(a)

(b)

(c)

Fig. 9. Layers of the asymmetric stacked patch array prototype: (a) bottom view of Rogers 5880 radome layer; (b) top view of Rogers 4003C substrate; (c) side view of the stacked patch array. Foam with 3mm thickness is placed between these two layers.

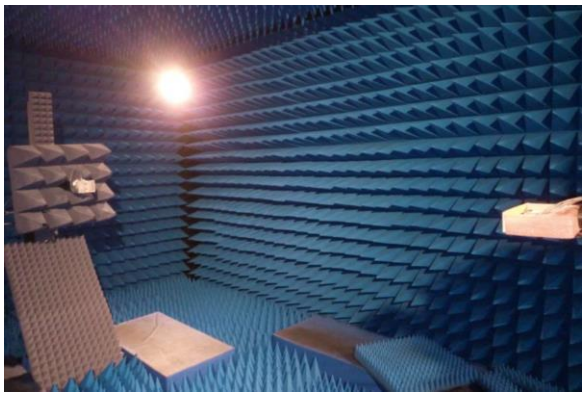

Fig. 10. Measurement setup of the asymmetric stacked patch array in the anechoic chamber.

1×8 RF divider is used for the amplitude excitations of the antenna elements. Fabricated asymmetric stacked patch array is measured in an anechoic chamber. The measurements are performed with 1° resolution at $\phi = 0°$ plane between $-180^o \leq \theta \leq 180^o$. Measurement setup of the array is shown in Fig. 10. The array is measured for the broadside radiation.

Measured active S-parameters of the 8-element asymmetric stacked microstrip phased array is given in Fig. 11 for the case when the array is radiating to $\theta = 0^o$. Ripples are observed in the active S-parameter curves due to the external reflections in the measurement setup. Although existence of ripples is clearly observed, the characteristics of these parameters exhibit similar characteristics with the simulated ones. Measured active S-Parameters show good impedance matching performance within 8-10 GHz band.

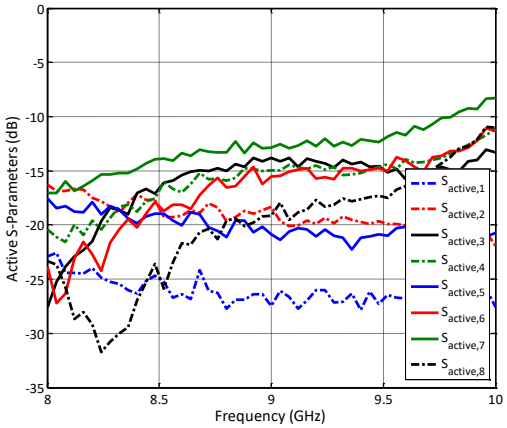

Fig. 11. Measured active S-parameters of the 8-element asymmetric phased array radiating to $\theta = 0^o$.

Table 6: Comparison of proposed structure with references

Reference	Technique	Frequency	FBR improvement (dB)
[30]	Planar choke	9.45-10.30 GHz	>20 dB
[31]	Partial ground and DGS	9.1 GHz	> 6 dB
[32]	EBG structure as a reflector	4.90-5.42 GHz	> 5 dB
Present paper	Asymmetric structure	8-10 GHz	> 20 dB

Measured and simulated normalized co- and cross-pol radiation patterns for broadside radiation are given in Fig.12. Uniform amplitude excitations are used. The simulated and measured patterns are in a good agreement. FBR of 42.06 dB, 45.3 dB and 38.72 dB are observed for the measured patterns of 8 GHz, 9 GHz and 10 GHz, respectively. The peak gain is measured as 10.25 dBi, 12.364 dBi and 10.93 dBi. Effectiveness of using asymmetric structure is clearly observed in the co-pol patterns of simulated and measured array. Table 6 shows the comparisons of our proposed array structure with several published works. These results show that the prosed asymmetric structure improves FBR better than the techniques of previous works in broad frequency band [30-32].

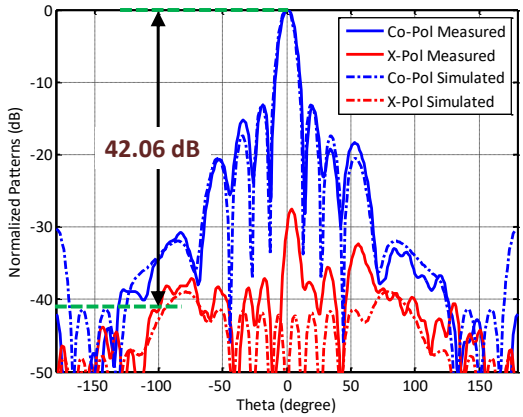

(a)

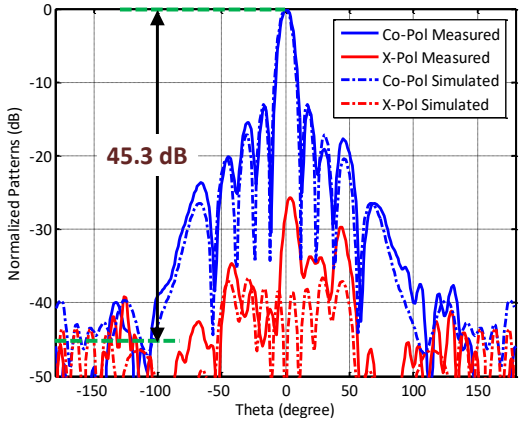

(b)

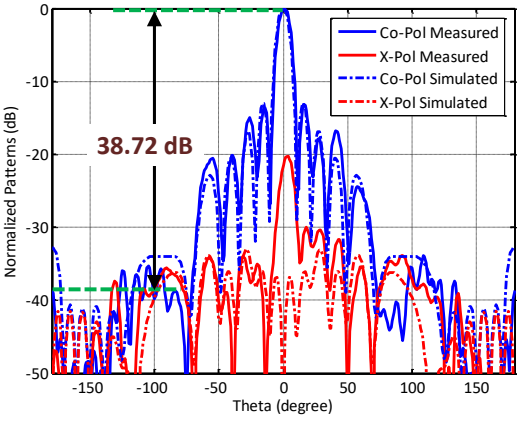

(c)

Fig. 12. Measured and simulated normalized co- and cross-pol radiation patterns for broadside radiation: (a) 8 GHz; (b) 9 GHz; (c) 10 GHz.

V. CONCLUSION

Stacked geometries are widely used to enhance the impedance matching characteristics of the microstrip antenna. In this work, stacked microstrip antenna consisting of foam and radome layers is used as the antenna elements of a broadband phased array. The array is designed to scan the beam in horizontal plane at $-40^o \leq \theta \leq 40^o$ angular range. By altering the physical size of the substrate materials, back lobe suppression is achieved. FBR values that are more than 38 dB is achieved for broadside radiation. It is above 20 dB when the beam is steered to $\theta = 40^o$. Besides, its scanning loss is lower for all steering angles at all frequencies compared to its symmetrical counterpart. Asymmetrical stacked patch phased array prototype is fabricated and measured. Very high FBR is observed in the measurements, as well. With its broadband, high FBR and low scanning loss, asymmetrical stacked patch phased array is suitable as radar and base station antenna.

APPENDIX

Table App.I: Phase excitation values for the stacked microstrip phased array

θ	β_1	β_2	β_3	β_4	β_5	β_6	β_7	β_8
0	**0**	**0**	**0**	**0**	**0**	**0**	**0**	**0**
10^o	**0**	**-37.5**	**-75**	**-112**	**-150**	**-187.5**	**-225**	**-262.5**
20^o	**0**	**-73.8**	**-147.6**	**-221.4**	**-295.2**	**-9**	**-82.8**	**-156.6**
30^o	**0**	**-108**	**-216**	**-324**	**-72**	**-180**	**-288**	**-36**
40^o	**0**	**-138.8**	**-277.6**	**-56.4**	**-195.2**	**-334**	**-112.8**	**-251.6**

θ is the beam scanning angle. All units are in degrees.

REFERENCES

[1] R. B. Waterhouse, "Design of probe-fed stacked patches," *IEEE Trans. Antennas Propagat.*, vol. 47, no. 12, pp. 1780-1784, Dec. 1999.

[2] R. B. Waterhouse, "Stacked patches using high and low dielectric constant material combinations," *IEEE Trans. Antennas Propagat.*, vol. 47, no. 12, pp. 1767-1771, Dec. 1999.

[3] K. Klionovski and A. Shamim, "Physically connected stacked patch antenna design with 100% bandwidth," *IEEE Antennas and Wireless Propagat. Lett.*, vol. 16, pp. 3208-3211, Nov. 2017.

[4] P. K. Singhal, B. Dhaniram, and S. Banerjee, "A stacked square patch slotted broadband microstrip antenna," *Journal of Microwaves and Opto-electronics*, vol. 3, no. 2, pp. 60-66, Aug. 2003.

[5] M. A. Matin, B. S. Sharif, and C. C. Tsimenidis, "Probe fed stacked patch antenna for wideband applications," *IEEE Trans. Antennas Propag.*, vol. 55, no. 8, pp. 2385-2388, Aug. 2007.

[6] M. C. Tang, T. Shi, H. Xiong, and S. Qing, "Low-profile asymmetrical CSRR loaded stacked microstrip patch antenna," *Applied Computational Electromagnetics Society Journal*, vol. 30, no. 8, pp. 850-854, Aug. 2015.

[7] A. A. Lotfi Neyestanak, "Ultra wideband rose leaf microstrip patch antenna," *Progress in Electromagnetics Research*, vol. 86, pp. 155-168, Oct. 2008.

[8] A. Bhutani, H. Bulan, B. Goettel, C. Heine, T. Thelemann, M. Pauli, and T. Zwick, "122 GHz aperture-coupled stacked patch microstrip antenna in LTCC technology," *European Conf. Antennas & Propag. (EuCAP)*, Davos, pp. 1-5, 2016.

[9] A. Panther, A. Petosa, M. G. Stubbs, and K. Kautio, "A wideband array of stacked patch antennas using embedded air cavities in LTCC," *IEEE Microw. Wireless Compon. Lett.*, vol. 15, no. 12, pp. 916-918, Dec. 2005.

[10] W. Hong, A. Goudelev, K. H. Baek, V. Arkhipenkov, and J. Lee, "24-element antenna-in-package for stationary 60-GHz communication scenarios," *IEEE Antennas Wireless Propag. Lett.*, vol. 10, pp. 738-741, July 2011.

[11] H. S. Noh and U. H. Park, "Three-stacked microstrip patch array antenna for both transmitting and receiving," *IEE Proc. Microw. Antennas Propag.*, vol. 153, no. 4, pp. 385-388, Aug. 2006.

[12] G. Guo, L. S. Wu, Y. P. Zhang, and J. F. Mao, "Stacked patch array in LTCC for 28 GHz antenna in-package applications," *2017 IEEE Elect. Design of Adv. Packaging and Systems Symposium (EDAPS)*, Haining, China, Dec. 14-16, 2017.

[13] E. García-Marín, J. L. Masa-Campos, and P. Sánchez-Olivares, "4 x 4 stacked patch array with SIW and microstrip corporate feeding network for Ku-band," *2016 10th European Conference on Antennas and Propagation (EuCAP)*, Davos, Switzerland, Apr. 10-15, 2016.

[14] M. S. Khan, A. Iftikhar, S. A. Naqvi, B. Ijaz, A. Fida, R. M. Shubair, and S. A. Khan, "Circularly polarized 4× 8 stacked patch antenna phased array with enhanced bandwidth for commercial drones," *Int. J. RF Microw. Comput. Aided Eng.*, vol. 30, no. 3, Mar. 2020.

[15] S. Xiao, M. C. Tang, Y. Y. Bai, S. Gao, and B. Z. Wang, "Mutual coupling suppression in microstrip array using defected ground structure," *IET Microw. Antennas Propag.*, vol. 5, no. 12, pp. 1488-1494, Sep. 2011.

[16] G. Ramon, P. Maagt, and M. Sorolla, "Enhanced patch-antenna performance by suppression surface waves using photonic-bandgap substrates," *IEEE Trans. Microw. Theory Tech.*, vol. 47, no. 11, pp. 2131-2138, Nov. 1999.

[17] H. Y. Yang, N. G. Alexopoulos, and E. Yablonovitch, "Photonic band-gap materials for high-gain printed circuit antennas," *IEEE Trans. Antennas Propag.*, vol. 45, no. 1, pp. 185-187, Jan. 1997.

[18] L. Yang, M. Y. Fan, F. L. Chen, J. Z. She, and Z. H. Feng, "A novel compact electromagnetic

bandgap structure and its applications for microwave circuits," *IEEE Trans. Microw. Theory Tech.*, vol. 53, no. 1, pp. 183-190, Jan. 2005.

[19] M. Salehi and A. Tavakoli, "A novel low mutual coupling microstrip antenna array design using defected ground structure," *Int. J. Electron. Commun*., vol. 60, pp. 718-723, Nov. 2006.

[20] E. S. Silveira, D. C. Nascimento, and A. F. Tinoco, "Design of microstrip antenna array with suppressed back lobe," *Journal of Microwaves, Optoelectronics and Electromag. App*., vol. 16, no. 2, pp.460-470, June 2017.

[21] W.G. Lim, H. S. Jang, and J. W. Yu, "New method for back lobe suppression of microstrip patch antenna for GPS," *Proc. of the 40th European Microwave Conf*., Paris, France, pp. 679-682, Nov. 2010.

[22] Y. Li, P. Yang, F. Yang, and S. He, "A method to reduce the back radiation of the folded PIFA antenna with finite ground," *Applied Computational Electromagnetics Society Journal*, vol. 28. no. 2, pp. 110-115, Feb. 2013.

[23] T. J. Cho and H. M. Lee, "Front-to-back ratio improvement of a microstrip patch antenna by ground plane edge shaping," *2010 IEEE Antennas and Propagation Society Int. Symp.*, Toronto, Canada, pp. 1-4, July 2010.

[24] K. Klionovski and A. Shamim, "Back radiation suppression through a semitransparent ground plane for a millimeter-wave patch antenna," *IEEE Trans. Antennas Propag.*, vol. 65, no. 8, pp. 3935-3941, Aug. 2017.

[25] H. M. Lee and J. K. Kim, "Front-to-back ratio improvement of a microstrip patch antenna using an isolated soft surface structure," *Proc. of the 39th European Microwave Conf.*, Rome, Italy, pp. 385-388, Sep. 2009.

[26] Y. Rikuta, H. Arai, and Y. Ebine, "Enhancement of FB ratio for cellular base station antenna by optimizing reflector shape," *IEEE Antennas and Propagat. Society International Symp*., Boston, USA, pp. 456-459, July 2001.

[27] L. Zhang, S. Gao, Q. Luo, P. R. Young, Q. Li, Y.-L Geng, and R. A. Abd-Alhameed, "Single-feed ultra-wideband circularly polarized antenna with enhanced front-to-back ratio," *IEEE Trans. Antennas Propag.*, vol. 64, no. 1, pp. 335-360, Jan. 2016.

[28] Y. L. Chiou, J. W. Wu, J. H. Huang, and C. F. Jou, "Design of short microstrip leaky-wave antenna with suppressed back lobe and increased frequency scanning region," *IEEE Trans. Antennas Propag.*, vol. 57, no. 10, pp. 3329-3333, Oct. 2009.

[29] J. Wei, Z. N. Chen, X. Qing, J. Shi, and J. Xu, "Compact substrate integrated waveguide slot antenna array with low back lobe," *IEEE Antennas Wireless Propag. Lett.*, vol. 12, Aug. 2013.

[30] M. Karami, R. A. Sadeghzadeh, M. Noferesti, and M. Chegeni, "Suppressed back-lobe substrate-integrated waveguide slot array antenna for X-band," *IET Electron. Lett*., vol. 51, no. 11, pp. 811-813, May 2015.

[31] V. N Kumar, M. Satyanarayana, and S. P. Singh, "A novel back lobe reduction technique for microstrip antenna array using partial ground and DGS," *International Journal of Intelligent Engineering and Systems*, vol. 12, no. 2, pp. 182-191, Feb. 2019.

[32] E. Guo, J. Liu, and Y. Long, "A mode superposed microstrip patch antenna and its Yagi array with high front-to-back ratio," *IEEE Transactions on Antennas and Propagation*, vol. 65, no. 12, pp. 7328-7333, Oct. 2017.

[33] CST Microwave Studio, http://www.cst.com, CST GmbH, Darmstadt, Germany.

Melih Türk was born in Ordu, Turkey. He received his B.Sc. degree in Electronics and Communication Engineering from the Kocaeli University in 2011. He received M.Sc. degree in Electronics and Communication Engineering from the Yıldız Technical University in 2019. He is currently working on his Ph.D. in Communication Engineering at the same university. He has been working in the Scientific and Technological Research Council of Turkey (Tubitak) since 2016. Her research interests include radar systems, phase array antennas and RF circuits.

Fikret Tokan received his Ph.D. degree from Yıldız Technical University, Istanbul, in Communication Engineering in 2010. From October 2011 to October 2012, he was Postdoctoral Researcher in the EEMCS Department of Delft University of Technology. From October 2012 to May 2013, he was a Postdoctoral Fellow at the Institute of Electronics and Telecomm. (IETR), University of Rennes 1, France.

Since September 2002, he has been working in the Electromagnetic Fields and Microwave Technique Section of the Electronics and Communications Engineering Department of Yıldız Technical University. He has been currently working as an Assoc. Prof. at that department. His current research interests are UWB antenna design, dielectric lens antennas, reflector systems, electromagnetic waves, propagation, antenna arrays, scattering and numerical methods.

Dual-band (28/38 GHz) MIMO Antenna System for 5G Mobile Communications with Efficient DoA Estimation Algorithm in Noisy Channels

Asmaa E. Farahat and Khlaid F. A. Hussein

Microwave Engineering Department
Electronics Research Institute, Cairo, 11843, Egypt
asmaa@eri.sci.eg, Khalid_elgabaly@yahoo.com

Abstract ─ In this paper, a dual-band (28/38 GHz) linear antenna arrays of four and eight elements are proposed to work as a MIMO arrays for the 5G communication systems. Each element in the array is a dual-band Yagi-Uda antenna designed to operate at 28 and 38 GHz. The eight-elements array size has a total dimension of 79.4 mm × 9.65 mm excluding the feeding microstrip line. The maximum gain of the array is about 18 dB. The peaks of correlation at matched angles (PCMA) technique is applied to determine the direction of arrival for multiple incoming signals. The effects of phase noise and additive Gaussian noise on the error in the DoA estimation are studied showing good accuracy of the PCMA algorithm. Numerical and experimental investigations are achieved to assess the performance of both the single-element antenna and the eight-element MIMO linear antenna array. It is shown that the simulation results agree with the experimental measurements and both show good performance of the single antenna as well as the MIMO linear array system. The envelope correlation coefficient (ECC) and the diversity gain (DG) are calculated and the results show that the proposed MIMO antenna system is suitable for the forthcoming 5G mobile communications. The radiation patterns for single antenna and four-element array are measured and compared to the electromagnetic simulation results showing good agreement.

Index Terms ─ DoA, MIMO array, Yagi-Uda.

I. INTRODUCTION

Recently, the mm-wave in the 28 GHz and 38 GHz frequency bands has been reported to be used in wireless cellular communication systems [1]. Higher bandwidths for higher data rates are required for the future 5th generation mobile communication. This is provided by the millimeter wave bands [2]. Unfortunately, the wavelength of the signal becomes shorter as the operating frequency increases, and consequently the free-space path loss becomes higher, according to Friis transmission equation [3]-[4]. High gain antennas are needed to compensate for the free-space path losses and various forms of fading that can be observed in the communication channel [5], [6]. When considering multipath effects, the MIMO antenna system can offer many advantages. Good circuit solutions for mobile communication applications at mm-wave frequencies are achieved by using both high gain and MIMO configurations. This reduces the operating costs of any required supporting power amplifiers and control circuitry [7]. The estimated bands under consideration for 5G technology are the frequency spectrum around 28 GHz, 38 GHz, 60 GHz and 73 GHz. These millimeter wave bands would bring new challenges in the MIMO antennas implementation for handheld devices [8].

Dual band MIMO antennas have been reported in literature. A 4 × 4 28/38 dual-band MIMO antenna system with a round patch EBG Cell is introduced in [8]. Also, a dual band MIMO antenna composed of two orthogonal elements operating in the frequency bands 1.62-3.2 GHZ and 4.4-5.9 GHz is introduced in [9]. A dual band 28/45 microstrip circular patch antenna with an elliptical slot is presented in [10], with bandwidths of 1.3 GHz at 28 GHz and 1GHz at 45 GHz.

The DoA estimation is one of the key issues in the discipline of array signal processing and finds applications in the fields of radar, sonar, and wireless positioning applications [11]. The most popular DoA estimation algorithms commonly used are the maximum likelihood (ML) [12], multiple signal classification (MUSIC) [13], and estimation of signal parameters via rotational invariance techniques [14]. The DoA estimation technique used in this work is adapted from the peaks of the correlation at matched angles (PCAMA) technique proposed in [15].

II. THE PROPOSED YAGI_UDA ANTENNA AND ARRAY STRUCTURE

The present section describes the design of the proposed Yagi-Uda antenna used to construct the MIMO linear array system. Antenna is constructed as a driven dipole antenna, one director and two reflectors. Each reflector has a triangular shape to enhance the antenna gain. The length of the dipole is set to resonate at 38 GHz. Three equally spaced corrugations are added to

Submitted On: November 15, 2020
Accepted On: January 18, 2021

https://doi.org/10.47037/2020.ACES.J.360308

each dipole arm with dimensions set for good impedance matching. An extension strip is capacitively end-coupled to each dipole arm through an infinitesimal gap for dual-band operation. The total length of the gap and the extension strip are set such that extended corrugated dipole has additional resonance at 28 GHz. The driven dipole is fed through a transmission line of two parallel strips; one f them is printed on the top layer of the substrate and the other is printed on the bottom layer. For practical measurements using coaxial feed line, three stage microstrip line transitions is used between the coaxial feeder and the two-strip line. The transition is composed of three cascaded strip line regions with different lengths and widths designed for 50 Ω impedance matching. One of the dipole arms and its extension are printed on the bottom layer of the substrate and connected to the ground plane. The arrangement of the proposed antenna structure with the dimensional parameters is shown in Fig. 1. The MIMO array of this Yagi-Uda antenna is shown in Fig. 2.

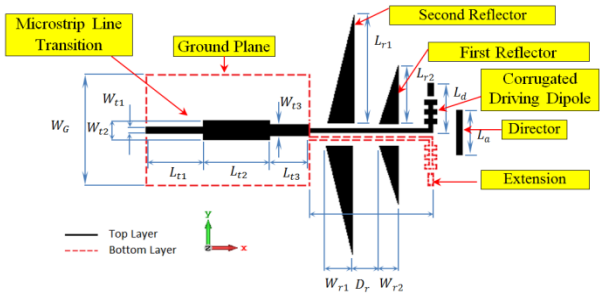

Fig. 1. Dual-band 28/38 GHz Yagi-Uda antenna.

III. DIRECTION OF ARRIVAL (DOA) ESTIMATION ALGORITHM

The DoA estimation algorithm applied to the proposed MIMO linear array is adapted from the PCMA algorithm presented in [15] for planar arrays. The PCMA is an efficient technique for detecting the DoA that depends on the correlation matrix between the steering matrix of the array and the matrix representing the received signals at the array elements. This correlation matrix will have its main diagonal elements nearly pure real when the steering matrix is set to get the same direction of maximum radiation of the array as the direction of arrival of one of the received signals.

The steering matrix for a linear array of N isotropic point sources can be written in the form:

$$\mathbf{S}(\theta) = [s_n(\theta)]_{n=1,2,..,N} = \left(e^{j\psi_1} \quad e^{j\psi_2} \quad \dots \quad e^{j\psi_N}\right), \tag{1}$$

where ψ_n is the phase of excitation of the n^{th}element of the linear array that can be expressed as:

$$\psi_n = (n-1)\beta, \quad n = 1,2,..,N, \tag{2}$$

where β is the progressive phase shift of the element excitations which can be expressed as:

$$\beta(\theta) = k_o \Delta sin\theta, \tag{3}$$

where k_o is the free space wave number and Δ is the spacing between the array elements.

Assuming p incoming waves, let the received voltage due to the p^{th} incoming wave under the effect of noise be,

$$\mathbf{X}_p = \alpha_p \mathbf{S}_p e^{j\varphi_e} + \mathbf{N}(\theta_p), \qquad p = 1,2,\dots,P, \tag{4}$$

where α_p is constant proportional to the strength of the p^{th} arriving signal, $\mathbf{S}_p$ is the steering matrix, φ_e is the phase error due to phase noise, and $\mathbf{N}(\theta_p)$ is the additive noise. It is assumed that each p incoming signal has different noise power level.

Consider the following correlation matrix:

$$\mathbf{R}_p(\theta) = E\{\mathbf{S}(\theta)\mathbf{X}_p^H\}, \qquad p = 1,2,\dots,P, \tag{5}$$

where the operator $E\{\cdot\}$ means the expected or mean value of the operand, $\mathbf{S}(\theta)$ is the steering matrix at θ direction. H is the hermitian operator.

At very high signal to noise ratio (SNR), i.e., $\varphi_e \approx 0$, and $A_p \approx 0$, the main diagonal elements of the matrix $\mathbf{R}_p(\theta)$ are approximately pure real at $\theta = \theta_p$. For an N-elements linear array, the $\mathbf{R}_p$ matrix can be written as,

$$\mathbf{R}_p(\theta) = \left[r_{p_{m,n}}(\theta,\phi)\right]_{\substack{m=1,2,\dots,N,\\ n=1,2,\dots,N}} \quad p = 1,2,\dots,P, \tag{6}$$

At low noise to carrier power ratio (NCR) or high SNR, each of the complex quantities $r_{p_{m,n}}(\theta,)$ has its imaginary part tending to zero as the angle θ approaches θ_p. Thus, the following quantity is important and can be used to detect the directions of arrival of multiple signals:

$$d_p(\theta) = \sum_{n=1}^{N} \frac{|imag(r_{p_{m,n}})|}{|r_{p_{m,n}}|^4}, \quad m = n. \tag{7}$$

Consequently, the peaks of the following function, when plotted against θ in the half-space domain, $0 < \theta < \frac{\pi}{2}$ give the angles determining the DoA for all the incoming signals,

$$P_{CAMA}(\theta) = \sum_{p=1}^{P} \frac{1}{d_p(\theta)}, \qquad p = 1,2,\dots,P. \tag{8}$$

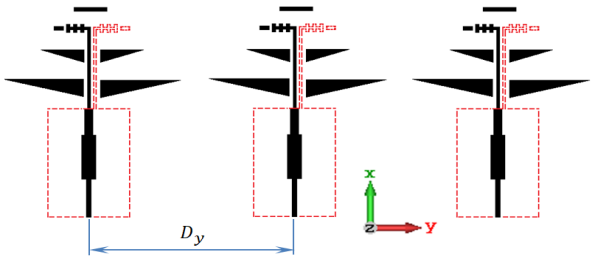

Fig. 2. MIMO array configuration of the proposed Yagi-Uda antenna.

IV. PHASE NOISE MODEL

Studying the effect of the phase error encountered due to the phase noise is of particular importance as the PCMA technique depends on the correctness and accuracy of the phases of the signals received at the array elements. The phase noise model presented in [16] is used to study the effect of phase noise on the PCMA technique. The phase noise is commonly characterized by its single-side band power spectral density (PSD), $L(f)$, in the frequency domain which is defined as the noise power within a bandwidth of 1 Hz at an offset frequency, f, from the carrier frequency relative to the carrier power P_r [16]. Hence, $L(f)$ is expressed as:

$$L(f) = \frac{\text{Noise power in 1Hz bandwidth}}{P_r}. \quad (9a)$$

To study the effect of phase noise on the error in the phase of the incoming signal, it is required to determine the instantaneous phase error samples.

As phase noise causes spectrum broadening, its effect is described by the noise-to-carrier power ratio (NCR) which is the ratio between the power contained within a bandwidth Δf around the carrier, and the power of the carrier,

$$\text{NCR} = 2\int_0^{\Delta f/2} L(f)\, df. \quad (9b)$$

Let the signal $s(t)$ received at the port of an antenna element of the array in the time domain be expressed as:

$$s(t) = V_o\, e^{j(2\pi f_r t + \psi_n + \varphi_e(t))}, \quad (10)$$

where V_o is the amplitude of the received signal, f_r is the frequency, ψ_n is the phase due to the path travelled by the signal received at the element number (n) of the linear array, and $\varphi_e(t)$ is the unknown instantaneous value of the phase error due to the phase noise. In the frequency domain, the discrete frequency domain samples S_k of the received signal are constructed as,

$$S_k = S(f_k) = A_k\, e^{j\psi_k}, \qquad k = 1,2,..,K, \quad (11)$$

where the discrete phase samples ψ_k are generated as a sequence of uniformly distributed random numbers in the closed interval $[-\pi, \pi]$ and the discrete magnitudes A_k are calculated from the PSD of the phase noise $L(f)$ as follows,

$$A_k = \sqrt{P_r\, L(f_k)}, \quad (12)$$

where P_r is the power of the received signal. The Discrete Inverse Fourier Transform (DIFT) is then applied to get the time samples of the noisy received signal,

$$s(t) = \text{DIFT}(S_k). \quad (13)$$

The corresponding instantaneous phase error, $\varphi_e(t)$ can be calculated as,

$$\varphi_e(t) = \tan^{-1}\left(\frac{\text{imag}(s(t))}{\text{real}(s(t))}\right) - (2\pi f_c t + \psi_{m,n}). \quad (14)$$

V. ADDITIVE GAUSSIAN NOISE MODEL

The additive noise samples in this study are modeled as a normal distributed random samples with zero-mean and standard deviation σ, its probability density function (pdf) has the form:

$$G(n) = \frac{1}{\sigma\sqrt{2\pi}} e^{-n^2/2\sigma^2}, \quad (15)$$

where n is the random variable that represents the instantaneous values corresponding to the white Gaussian noise. In the frequency domain $\mathbf{N}(\theta_p)$ can be obtained by applying the fast Fourier transform on the time samples $i = 1, 2, 3, \ldots \text{I}$:

$$N(\theta_p) = \text{FFT}(n(\theta_p)). \quad (16)$$

VI. RESULTS AND DISCUSSIONS

A. Performance assessment of the proposed Yagi-Uda antenna

The Rogers RO3003C™ with dielectric constant $\varepsilon_r = 3$, dielectric loss tangent $\tan\delta = 0.0021$, and height $h = 0.25$ mm is used for the design of the proposed Yagi-Uda antenna. The metal parts of the antenna are made of copper with conductivity $\sigma = 5.6 \times 10^7 \text{S/m}$ and thickness t = 0.032 mm. The design parameters are listed in Table 1. The antenna is placed in the xy-plane with the feed line aligned with the x-axis. The dependency of the reflection coefficient, $|S_{11}|$, on the frequency over a wide band is presented in Fig. 3. It is clear that the impedance is perfectly matched at the two frequencies 28 and 38 GHz with reflection coefficients -27 and -26 dB, respectively. At 28 GHz, the band width is about 3.32 GHz, whereas at 38 GHz, the band width is about 1.4 GHz. The radiation efficiencies are 96.3% at 28 GHz and 95.2% at 38 GHz.

The normalized radiation patterns for the proposed dual-band Yagi-Uda antenna at 28 GHz and 38 GHz in the planes $\phi = 0^\circ (xz-plane)$ and $\theta = 90^\circ (xy-plane)$ are presented in Figs. 4 (a) and 4 (b), respectively. The maximum gain is 9.3 dBi at 28 GHz with SLL -11 dB and 9.8 dBi at 38 GHz with SLL -10.1 dB.

Table 1: dimensional parameters for the proposed Yagi-Uda antenna

Name	Value (mm)	Name	Value (mm)
L_a	2.4	W_{t1}	0.5
L_{t1}	3.62	L_{t2}	4.02
W_{r2}	1.0	D_r	1.95
L_{r2}	3.4	L_d	2.79
W_{t2}	0.62	W_{t3}	0.35
L_{t3}	2.5	W_{r1}	1.0
W_G	6.72	L_{r1}	7.6
L_e	0.8	W_e	0.2

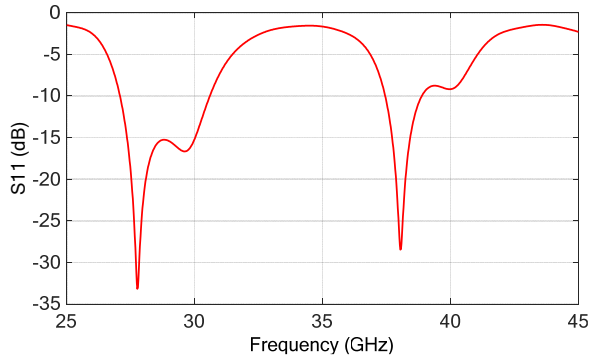

Fig. 3. The frequency response of the reflection coefficients $|S_{11}|$ of the proposed Yagi-Uda antenna with the dimensional parameters listed in Table 1.

B. Performance assessment of the Yagi-Uda array

An eight-element linear array of the proposed Yagi-Uda antenna is constructed and arranged on the $y-$ axis. For good beam-steering and in order to reduce the side lobes the distance between the array elements is set to $D_y = 8.85\,mm$ as shown in Fig. 5. This means that the elements are overlapped as shown in the figure with each two adjacent antennas sharing a common reflector. The total array dimensions are $79.4\text{ mm} \times 9.65\text{ mm}$ excluding the feeding microstrip line. The frequency response of the reflection coefficient and the coupling coefficients for the array elements are shown in Fig. 6 and Fig. 7, respectively. Also the radiation patterns for the proposed linear array at the operating frequencies 28 and 38 GHz are shown in Fig. 8.

C. Evaluation of the steering matrix of the proposed array

Instead of using the simple and approximate expressions (1-3) to evaluate the steering matrix for the proposed linear array of Yagi-Uda elements, it can be evaluated more accurately by rigorous numerical techniques. The commercial available CST® package is used for this purpose by calculating the received voltage signals at each of the array elements due to a plane wave incident on the array in the plane $\phi = 90^\circ$ and making an angle θ with the $z-$ axis. With varying the angle θ, the steering matrix of this linear array can be accurately evaluated. In this way the steeing matrix in (4) can be evaluated. The relation between the direction, θ, of the main beam and the progressive phase shift, β, is obtained by feeding the array elements with the progressive phase shifts ranging from $0°$ to $180°$ and then calculating the corresponding direction, θ, of the main beam through electromagnetic simulation. The relationship between β and θ is plotted in Fig. 9 (a). As shown in Fig. 9 (b), the gain of the Yagi-Uda array decrease as the steering angle of the radiation pattern is increased moving away from the direction normal to the array. The radiation patterns at different steering angles are shown in Fig. 10 (a) and Fig. 10 (b) at 28 and 38 GHz, respectively.

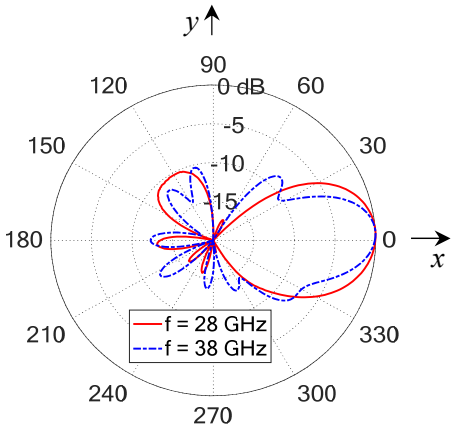

(a) $\theta = 90^\circ\ (xy-plane)$

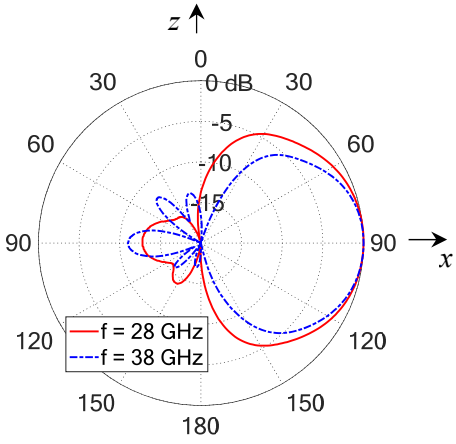

(b) $\phi = 0^\circ (xz-plane)$

Fig. 4. Normalized radiation patterns of the proposed dual-band antenna at 28 and 38 GHz in the $xy-plane$ ($\theta = 90^\circ$) and $xz-plane$ ($\phi = 0^\circ$).

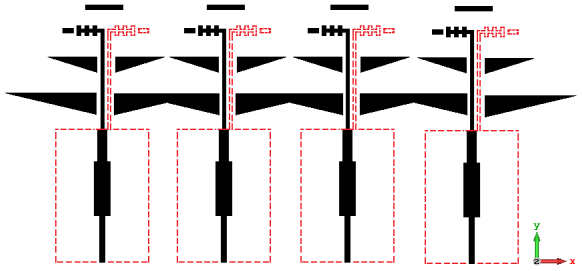

Fig. 5. Part of the eight overlapped elements linear array of the proposed Yagi-Uda antenna.

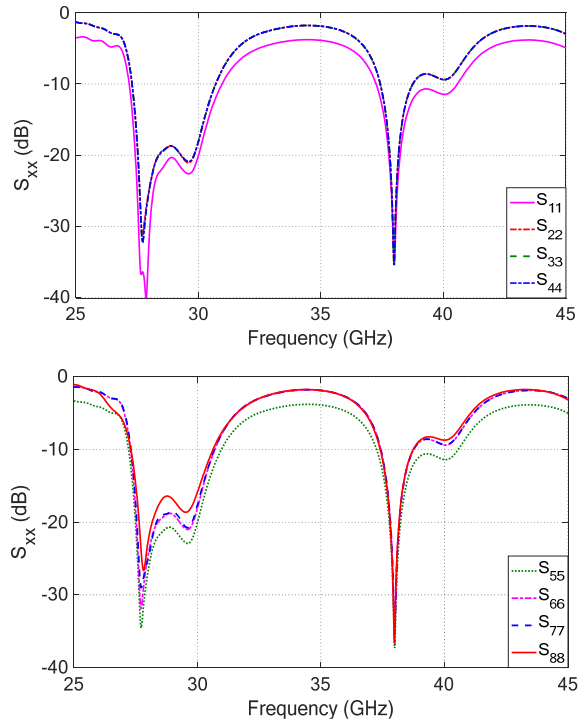

Fig. 6. The frequency response of the reflection coefficients $|S_{nn}|$ of each element of the proposed Yagi-Uda antenna array.

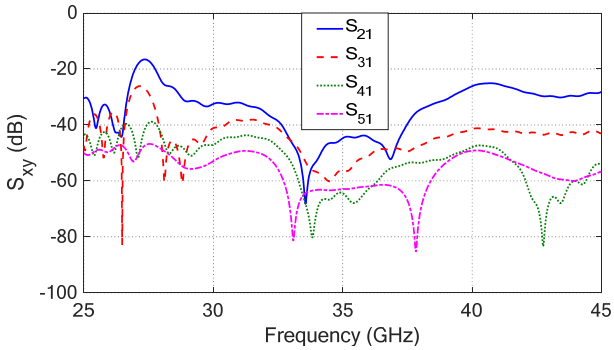

Fig. 7. Coupling coefficients of the proposed linear array of Yagi-Uda elements.

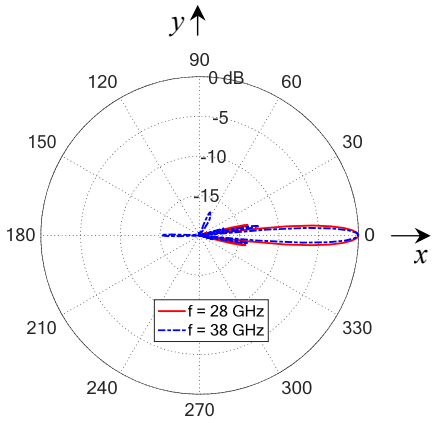

(a) $\theta = 90^{\circ}$ $(xy - plane)$

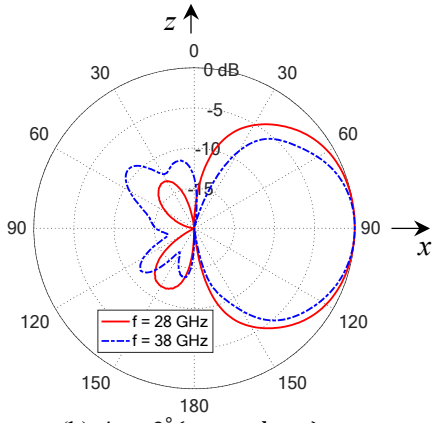

(b) $\phi = 0^{\circ}(xz - plane)$

Fig. 8. Normalized radiation patterns of the proposed linear array at 28 and 38 GHz in the $xy - plane$ ($\theta = 90^{\circ}$) and $xz - plane$ ($\phi = 0^{\circ}$).

D. DoA estimation of multiple signals using PCMA algorithm in the absence of noise

Three plane wave sources are assumed incident on the proposed Yagi-Uda linear array producing electromagnetic waves impinging on the antenna array from the directions $\theta = 10^{\circ}, 20^{\circ}$, and 40°. The electromagnetic simulation is performed to calculate the received voltage signals at each of the antenna array elements to get the matrix described by (4). No noise is added to the received signals. The received data due to the three signals coming simultaneously from the directions indicated are calculated through computer simulation using CST®. The normalized $P_{CMA}(\theta)$ function given by (8) is calculated using the steering matrix calculated as described in Section 4 and is plotted against θ as shown in Fig. 11 for $SNR \approx \infty$. The normalized $P_{CMA}(\theta)$ function shown in Fig. 11 has three peaks whose directions are assumed to give the three directions of arrival. Due to the high level of the SNR, it is found that the peaks of the normalized correlation function lie exactly at $\theta = 10^{\circ}, 20^{\circ}$, and 40°, that is, the

directions of arrival are retrieved exactly without any error.

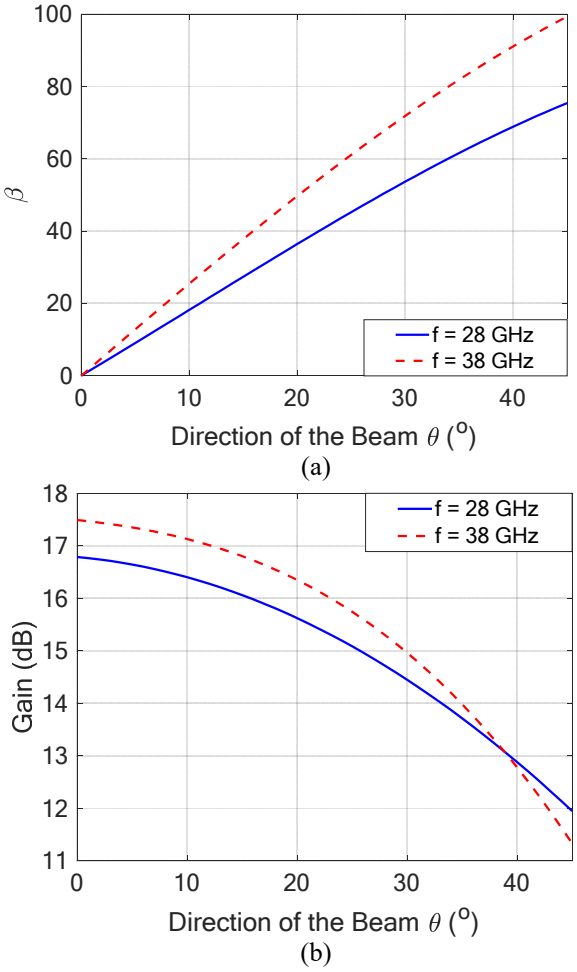

Fig. 9. The change in the (a) progressive phase shift β, and (b) maximum gain with the direction, θ, of the steered beam.

E. Effect of noise on the DoA estimation

For realistic simulation of the signals received at the array elements, phase noise and additive Gaussian noise are generated and added to the received signals (after being calculated by the CST®) as described in Sections 4 and 5 to get actual received signals.

E.1. Effect of phase noise

The effect of phase noise on the error in the estimation of DoA is investigated under the assumption that the received signals are affected by phase noise with PSD as that presented in Fig. 12 (a). The instantaneous phase noise samples $\varphi_e(t)$ are calculated as expressed in equation (14) and plotted in Fig. 12 (b) and also the NCR is obtained as given by (9b). The Error in DoA estimation by increasing the NCR is investigated for the directions $\theta = 10^\circ, 20^\circ, 30^\circ$, and 40°. The resulting error in the estimated DoA are plotted against NCR in Fig. 13. For realistic simulation the phase error samples are, first, calculated and, then, added to the samples of the received signals at the array elements which have been already calculated using the CST®. The PCMA algorithm is, then, applied to estimate the DoA.

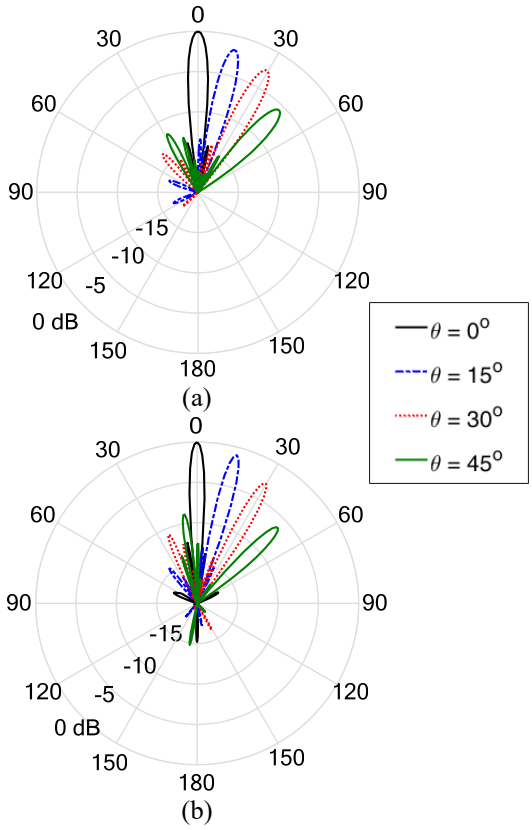

Fig. 10. The steered beam at different directions using the proposed linear array at: (a) 28 GHz and (b) 38 GHz.

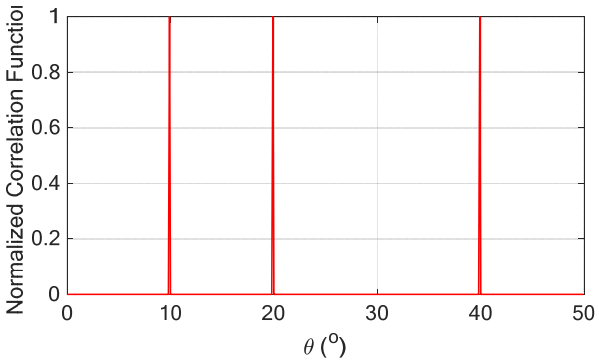

Fig. 11. Normalized correlation function in case of three received signals coming from the directions $\theta = 10^\circ$, 20°, and 30° under the assumption of very high SNR for each signal.

It is shown in Fig. 13 that the error in the estimated DoA increases with increasing the NCR. Also, it is shown that the error increases with increasing θ, i.e., the error in the estimated DoA increases as the received signal is incoming from a direction father away from the normal to the linear array.

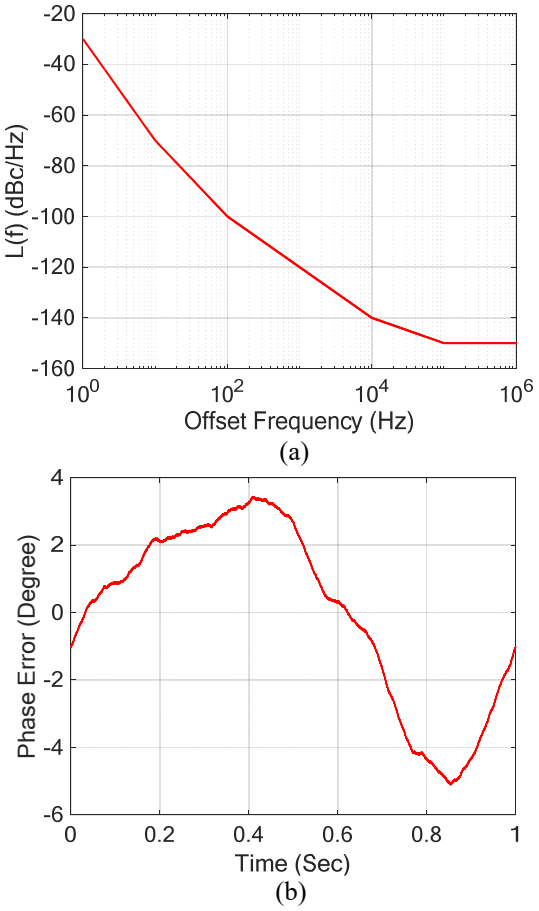

Fig. 12. Phase Noise characteristics: (a) $L(f)$ and (b) corresponding phase error time samples.

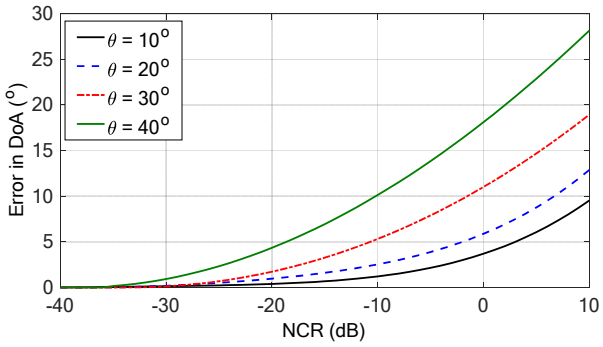

Fig. 13. Error in DoA estimation by increasing the noise to carrier power ratio (NCR) for different angles of reception.

E.2. Effect of additive noise

In this section, the method described for DoA estimation using the proposed Yagi-Uda array is examined in the presence of additive white Gaussian noise. The noise samples are generated and added to the received voltages at the different array elements as explained in Section 5.2, then the DoA is calculated. The angle of arrival of the received signal at different values of the SNR is estimated using the PCMA algorithm and plotted in Fig. 14. It is shown that the error in the estimated value of the DoA decreases with increasing the SNR. It is noticeable that as the signal is coming from a direction father from the normal to the array, the error in the estimated DoA increases.

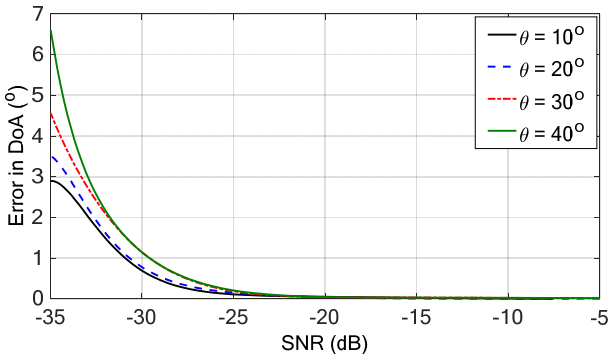

Fig. 14. Effect of additive white Gaussian noise on the error in DoA estimation for different direction of the incoming signal.

E.3. Receiving multiple signals in the presence of noise

In this section, the efficiency of the proposed linear array to estimate the DoA of multiple signals under the effect of phase noise and additive noise using the PCMA technique is numerically investigated. The CST® simulator is used to obtain the steering matrix for the array in the range $0^{\circ} < \theta < 45^{\circ}$ such that the side lobe level ≤ -13 dB, and the gain ≥ 15 dB. The steering matrix for the array is saved and stored for post processing. Four plane waves are simultaneously incident on the antenna array from different directions as listed in Table 2. For realistic simulation, the incoming signals are affected by different values of the phase and additive noise power. Thus, the estimated angles of arrival of the incoming waves are obtained for different values of the NCR and SNR as listed in Table 2. Figure 15 shows the normalized correlation function given by (8) for four incoming signals, each has a different noise to carrier power ratio.

F. Fabrication and measurements

This section is concerned with the experimental investigation of the characteristics of the proposed Yagi-

Uda antenna and the performance of the proposed MIMO array. For this purpose a prototype is fabricated for the Yagi-Uda antenna and another prototype is fabricated for four-element linear array.

Table 2: The estimated DoA for four plane waves coming from different directions affected by phase and additive noise of different power levels

Incoming DoA	Phase Noise NCR (dB)	Additive Noise SNR (dB)	Estimated DoA	Error (%)
$\theta = 10^{\circ}$	-25	-5	10	0
$\theta = 20^{\circ}$	-30	-10	20	0
$\theta = 30^{\circ}$	-8	-20	31.6	5.3
$\theta = 40^{\circ}$	-15	-10	39.8	0.5

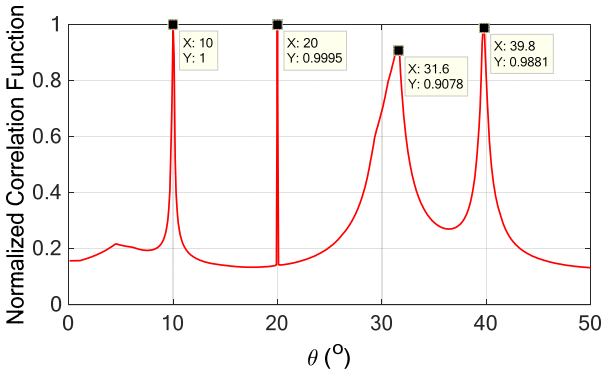

Fig. 15. Normalized PCAMA of four incoming signals on the proposed linear array of Yagi-Uda elements.

F.1. Single element Yagi-Uda antenna

For experimental verification, a prototype for the Yagi-Uda antenna is fabricated and it performance is evaluated through experimental measurements. The dependence of the reflection coefficient on the frequency is measured in the frequency band 25-45 GHz. Rogers RO3003™ with dielectric constant $\varepsilon_r = 3$, loss tangent $\delta = 0.0013$, and height $h = 0.25$ mm, is the substrate used for fabrication. The design dimensions for the single-element Yagi-Uda antenna are listed in Table 1. Figure 16 shows the photos of the fabricated prototype connected to a 2.4 mm coaxial end launch connector from the top and bottom views. The frequency dependence of the reflection coefficient $|S_{11}|$ of the antenna input port is measured using the vector network analyzer (VNA) Rohde and Schwartz model ZVA67 and plotted in Fig. 17 (a). Figure 17 (b) shows the fabricated antenna connected to the VNA ZVA67 for measuring the return loss. The measured frequency response of $|S_{11}|$ is compared with the simulation results obtained using the CST® simulator in the same figure. Good agreement is shown between the simulation and the measured return loss. The impedance matching bandwidth for a return loss ≤ -10 dB is about 2.6 GHz at 28 GHz and 1.35 GHz at 38 GHz.

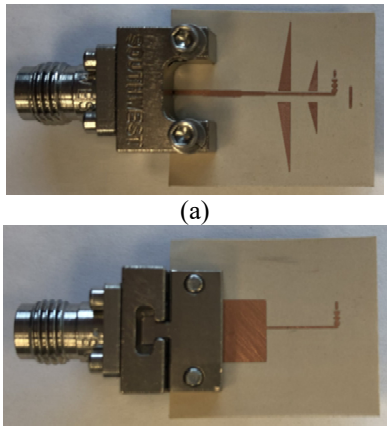

(a)

(b)

Fig. 16. (a) Top and (b) bottom views of the fabricated prototype Yagi-Uda dual-band (28/38 GHz) antenna connected to a 2.4 mm end-launch coaxial connector.

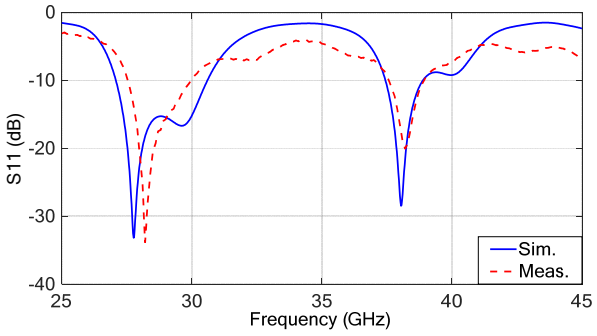

(a)

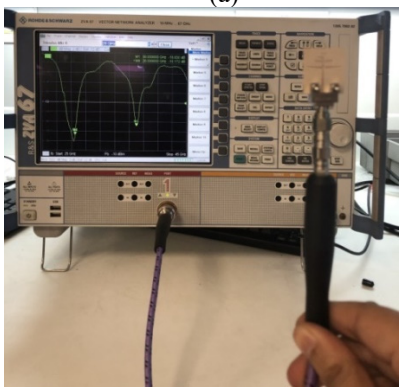

(b)

Fig. 17. (a) Measured return loss of the dual-band antenna with frequency compared with the simulation results. (b) The proposed dual-band Yagi-Uda antenna connected to the ZVA67 VNA.

The radiation patterns of the fabricated Yagi-Uda antenna are measured at 28 and 38 GHz using a standard gain horn antenna model LB-018400 in the principal planes $x-y$ ($\theta = 90°$) and $x-z$ ($\phi = 0°$). The antenna under-test (proposed Yagi-Uda) and the LB-018400 are placed in an anechoic chamber at a distance of 60 cm. The experimental setups for measuring the radiation patterns of the proposed antenna using the VNA of the Rohde and Schwartz ZVA67 are shown in Fig. 18. The reference standard gain horn antenna model LB-018400 is connected to port '2' of the VNA whereas the antenna under test is connected to port '1' to obtain its radiation pattern by measuring the transmission coefficient $|S_{21}|$ at the frequencies of concern. The two-dimensional radiation patterns at 28 and 38 GHz obtained by measurements are presented in Fig. 19 and Fig. 20, respectively, in the xy and xz planes, in comparison to that obtained by simulation showing good agreement.

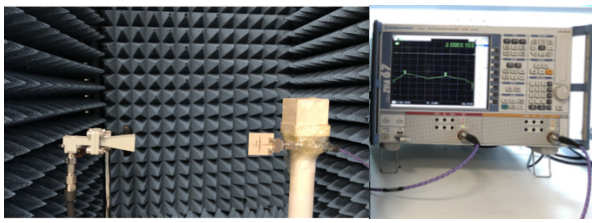

Fig. 18. Experimental setup for measuring the radiation pattern of the proposed dual-band Yagi-Uda antenna.

F.2. Four-element linear array of the proposed Yagi-Uda antenna

A four-element array of the printed Yagi-Uda antenna is fabricated to assess the array performance and compare the measurements with the electromagnetic simulations results. Due to the limiting dimensions of the end-launch connector size, the fabricated array has four elements separated by interelement spacing D_y 18 mm. The fabricated array is shown in Fig. 21. The simulated and measured dependency of the reflection coefficient $|S_{nn}|$ of each element on frequency is plotted in Fig. 22 (a) and 22 (b), respectively. In Fig. 23 (a) and 23 (b), the simulated and measured coupling coefficient $|S_{mn}|$ between the array elements is measured versus the frequency. It is clear from Fig. 22 that the fabricated array is matched at both of the operating frequencies 28 and 38 GHz. Also, it is shown in Fig. 23 that the MIMO array has very low coupling coefficients which make it suitable for MIMO systems that use multiple antennas to create different transmission paths for spatial diversity. The frequency responses of the envelope correlation coefficient (ECC) and the diversity gain (DG) of the proposed four-element array MIMO system are presented in Fig. 24. It is shown that the ECC is almost 0 and, consequently, the DG is almost 10 over the lower and upper frequency bands (centered at 28 and 38 GHz, which is the best achievable performance for a MIMO antenna system. The radiation patterns of the fabricated array are measured and compared to the radiation patterns obtained by electromagnetic simulation in the two planes $x-y$ ($\theta = 90°$) and $x-z$ ($\phi = 0°$) and presented in Figs. 25 and 26, respectively, showing excellent agreement.

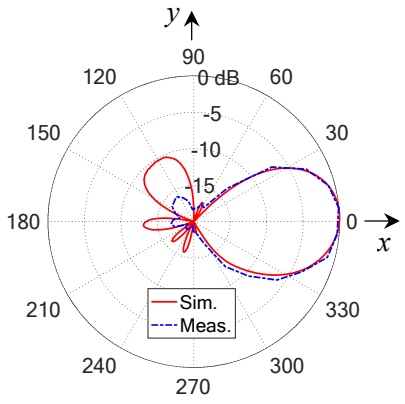

(a) $f = 28$ GHz, $\theta = 90°(xy-plane)$

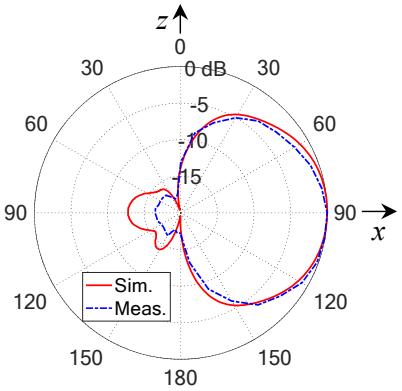

(b) $f = 28$ GHz, $\phi = 0°(xz-plane)$

Fig. 19. Measured radiation patterns of the dual-band Yagi-Uda antenna compared with the simulation results at 28 GHz.

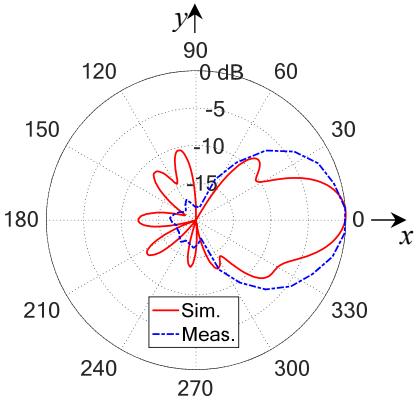

(a) $f = 38$ GHz, $\theta = 90°(xy-plane)$

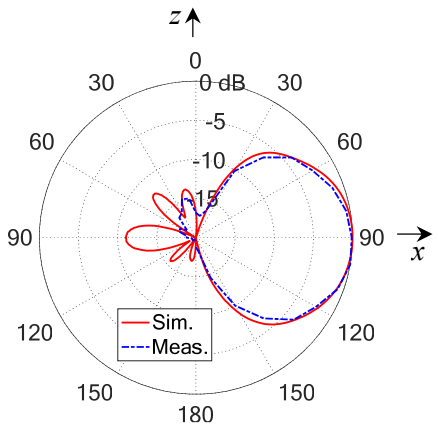

(b) $f = 38$ GHz, $\phi = 0°(xz-plane)$

Fig. 20. Measured radiation patterns of the dual-band Yagi-Uda antenna compared with the simulation results at 38 GHz.

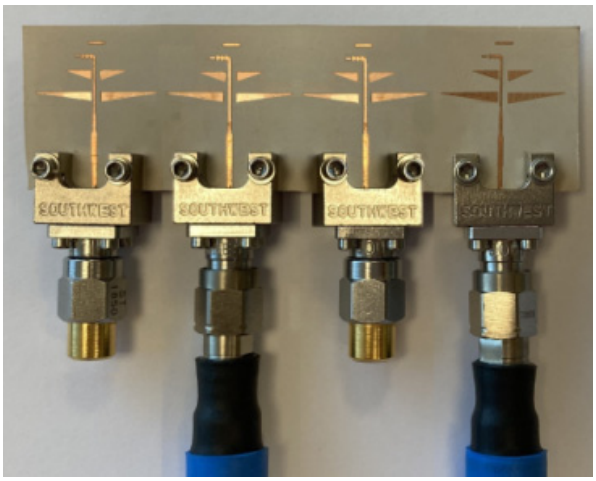

Fig. 21. Fabricated linear array composed of four elements of the proposed Yagi-Uda antenna.

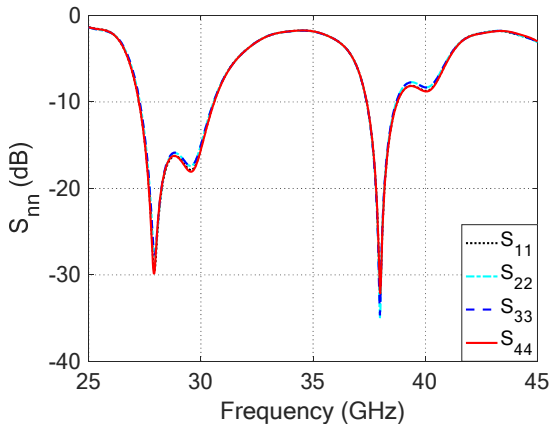

(a)

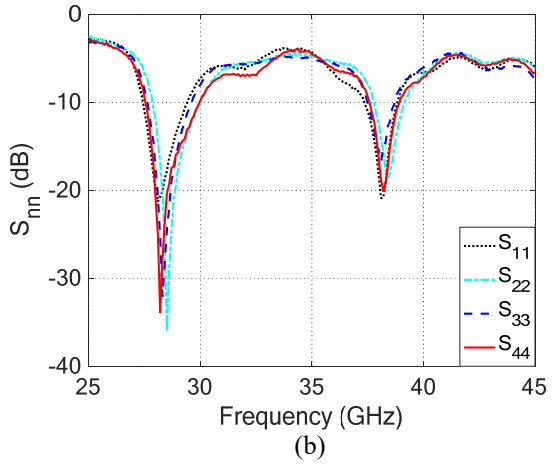

(b)

Fig. 22. (a) Simulated and (b) measured, reflection coefficients of the four elements of the fabricated array shown in Fig. 20.

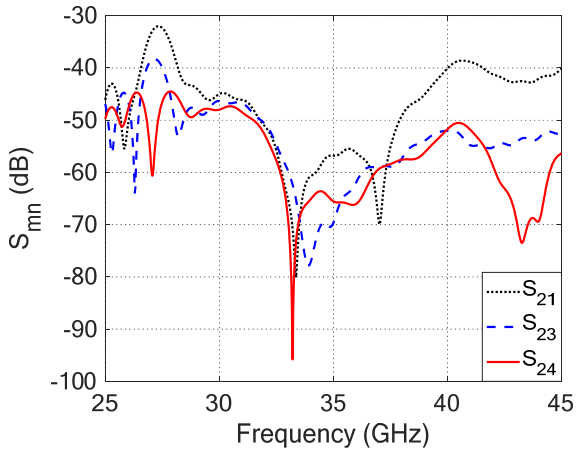

(a)

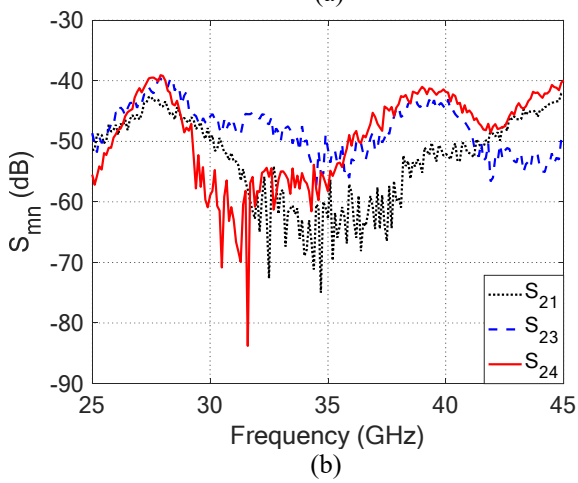

(b)

Fig. 23. (a) Simulated and (b) measured coupling coefficients between the elements of the fabricated array shown in Fig. 21.

A comparison between the proposed design and the antennas proposed in literature for mm-wave applications is performed. The proposed Yagi-Uda is compared to similar Yagi-Uda antennas in literature. The comparison criteria are the size, number of bands, the bandwidth for each band, and antenna gain, which are presented in Table 3. To the best of our knowledge, the present work proposes a dual-band Yagi-Uda antenna for MIMO applications which is not found in literature. In addition to its dual-band operation, the proposed design still has compact size, high gain, bandwidth, very low mutual coupling, and very high radiation efficiency, and it also has nearly perfect ECC and DG.

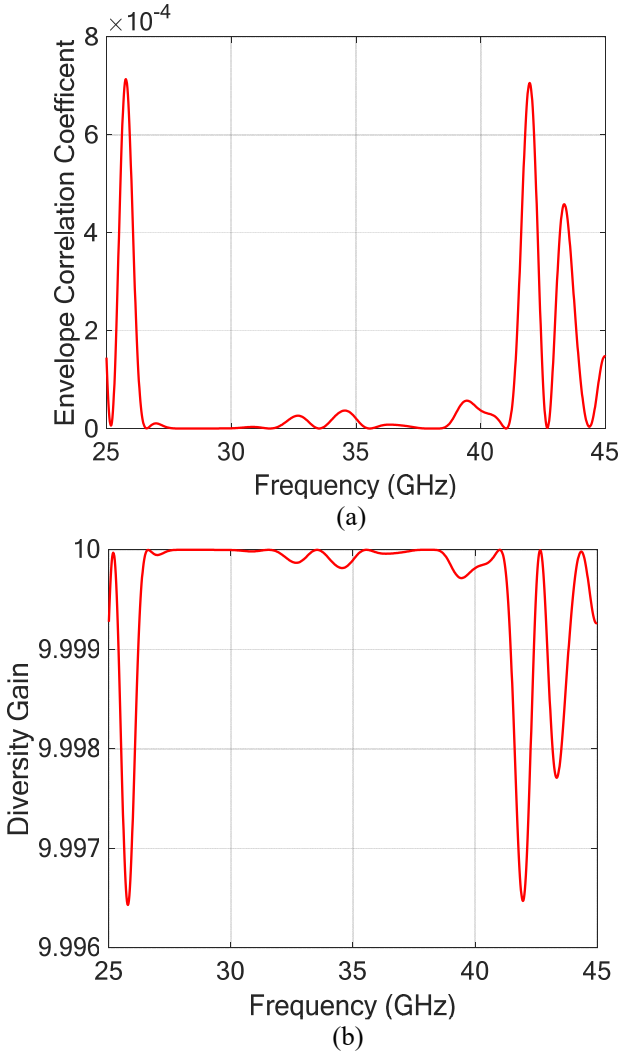

Fig. 24. Frequency dependence of the ECC and DG of the 4-port MIMO antenna proposed in the present work.

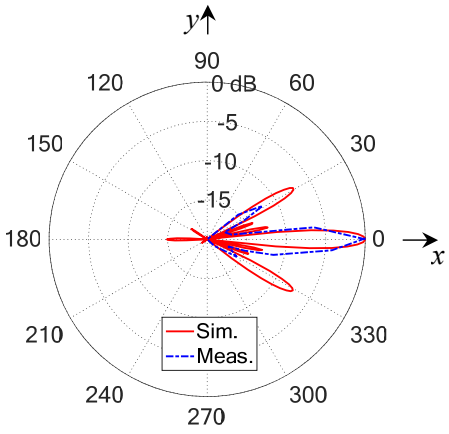

(a) $f = 28$ GHz, $\theta = 90°(xy-plane)$

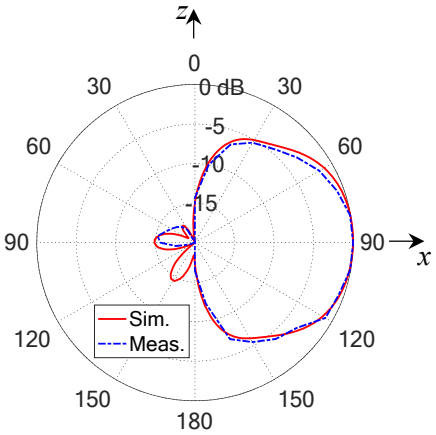

(b) $f = 28$ GHz, $\phi = 0°(xz-plane)$

Fig. 25. Measured radiation patterns of the fabricated four elements linear array compared with the simulation results at 28 GHz.

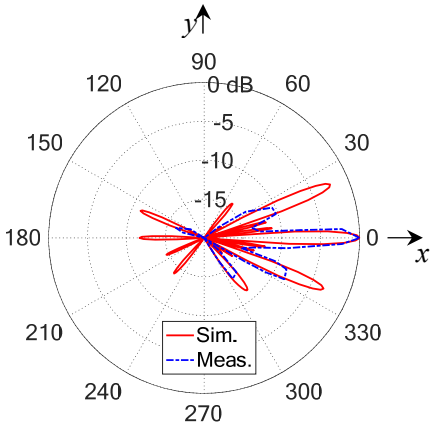

(a) $f = 38$ GHz, $\theta = 90°(xy-plane)$

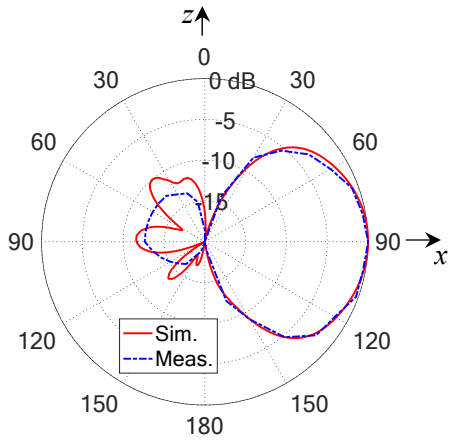

(b) $f = 38$ GHz, $\phi = 0°(xz-plane)$

Fig. 26. Measured radiation patterns of the fabricated four elements linear array compared with the simulation results at 38 GHz.

Table 3: Comparison with similar Yagi-Uda antennas for MIMO in literature

	[17]	[18]	[19]	Present Work
Size	14.8x5.1	11.2x8.1	40.7x22.9	9.7x18.2
Substrate Height (mm)	0.2	0.25	0.38	0.25
Number of bands	1	1	1	2
Freq. of first band (GHz)	28	24	24	28
Freq. of second band (GHz)	---	---	---	38
BW of first band	3.7	0.7	4.1	3.42
BW of second band	---	---	---	1.45
Gain (dBi)	8	9.3	8	9

VII. CONCLUSIONS

In this paper a dual-band (28/38 GHz) linear antenna array is proposed to work as a MIMO array for the 5G communication systems. Each element in the array is a dual-band Yagi-Uda antenna that is well designed at the 28 and 38 GHz. The array is composed of eight elements with total dimension of 79.4 mm × 9.65 mm excluding the feeding microstrip line. The array exhibits a high gain about 18 dB in the forward direction. The PCAMA direction of arrival estimation technique is applied to the received signals at the array elements to determine the direction of arrival for multiple incoming signals. The effect of phase noise and additive Gaussian noise on the error in the DoA estimation are studied showing good accuracy of the PCAMA algorithm. Numerical and experimental investigations are achieved to assess the performance of both the single-element antenna and the eight element MIMO linear antenna array. It is shown that the simulation results agree with the experimental measurements and both show good performance of the single antenna as well as the MIMO linear array system. The radiation pattern for single element and four element array are measured and compared to the electromagnetic simulation results showing good agreement.

REFERENCES

[1] T. S. Rappaport, S. Sun, R. Mayzus, H. Zhao, Y. Azar, K. Wang, G. N. Wong, J. K. Schulz, M. Samimi, and F. Gutierrez, "Millimeter wave mobile communications for 5G cellular: It will work!," *IEEE Access*, vol. 1, pp. 335-349, 2013.

[2] T. S. Rappaport, F. Gutierrez, E. Ben-Dor, J. N. Murdock, Y. Qiao, and J. I. Tamir, "Broadband millimeter-wave propagation measurements and models using adaptive-beam antennas for outdoor urban cellular communications," *IEEE Trans. Antennas Propag.*, vol. 61, no. 4, pp. 1850-1859, 2013.

[3] C. Narayan, *Antennas and Propagation*. Technical Publications, 2007.

[4] A. V. Alejos, M. G. Sanchez, and I. Cuinas, "Measurement and analysis of propagation mechanisms at 40 GHz: Viability of site shielding forced by obstacles," *IEEE Trans. Veh. Technology*, vol. 57, no. 6, pp. 3369-3380, 2008.

[5] S. Rajagopal, S. Abu-Surra, Z. Pi, and F. Khan, "Antenna array design for multi-gbps mm wave mobile broadband communication," in *Global Telecommunications Conference (GLOBECOM). IEEE*, pp. 1-6, 2011.

[6] A. I. Sulyman, A. T. Nassar, M. K. Samimi, G. R. MacCartney, T. S. Rappaport, and A. Alsanie, "Radio propagation path loss models for 5G cellular networks in the 28 GHz and 38 GHz millimeter wave bands," *IEEE Communications Magazine*, vol. 52, pp. 78-86, 2014.

[7] M. S. Sharawi, S. K. Podilchak, M. T. Hussain, and Y. M. M. Antar, "Dielectric resonator based MIMO antenna system enabling millimeter-wave mobile devices," *IET Microwaves, Antennas & Propagation*, pp. 287-293, 2017.

[8] D. T. T. Tu, N. G. Thang, and N. T. Ngoc, "28/38 GHz dual-band MIMO antenna with low mutual coupling using novel round patch EBG cell for 5G applications," *International Conference on Advanced Technologies for Communications*, 2017.

[9] J.-F. Li and Q.-X. Chu, "A compact dual-band MIMO antenna of mobile phone," *Journal of Electromagnetic Waves and Applications*, vol. 25, pp. 1577-1586, 2011.

[10] M. I. Khattak, A. Sohail, U. Khan, Z. Barki, and G. Witjaksono, "Elliptical slot circular patch antenna array with dual band behavior for future 5G mobile

communication networks," *Progress in Electromagnetics Research C*, vol. 89, pp. 133-147, 2019.

[11] M. V. Madhava, N. S. Jagadeesha, and T. Yerriswamy, "A comparative study of DoA estimation algorithms with application to traking using Kalman filter," *Signal & Image Processing: An International Journal (SIPIJ)*, vol. 6, no. 6, Dec. 2015.

[12] M. Li, Y. Lu, and B. He, "Array signal processing for maximum likelihood direction-of-arrival estimation," *Journal of Electrical & Electronic Systems*, 2013.

[13] M. Devendra and K. Manjunathachari, "DOA estimation of a system using MUSIC method," *International Conference on Signal Processing and Communication Engineering Systems*, 2015.

[14] R. Roy, A. Paulraj, and T. Kailath, "ESPIRT-estimation of signal parameters via rotational invariance techniques," *IEEE Trans. Acoust. Speech Signal Process*., vol. 34, no. 5, pp. 1340-1342, 1989.

[15] A. E. Farahat and K. F. A. Hussein, "Effect of phase noise on two-angle DoA estimation using planar arrays," *The 4th International Conference on Advanced Technology & Applied Sciences (ICaTAS2019)*, 2019.

[16] A. E. Farahat and K. F. A. Hussein, "Efficient computational model of phase noise and its applicability to assess the performance of digital modulation techniques," *Applied Computational Electromagnetics Society Journal*, vol. 34, no. 12, pp. 1931-1941, 2019.

[17] M. R. Naeini and M. Fakharzadeh, "A 28 GHz beam-switching Yagi-Uda array using Rotman lens for 5G wireless communications," *International Symposium on Antennas and Propagation & USNC/URSI National Radio Science*, 2017.

[18] P. R. Grajek, B. Schoenlinner, and G. M. Rebeiz, "A 24-GHz high-gain Yagi-Uda antenna array," *IEEE Trans. Antennas Propag*., vol. 52, pp. 1257-1261, May 2004.

[19] R. A. Alhalabi and G. M. Rebeiz, "High-gain Yagi-Uda antennas for millimeter-wave switched beam systems," *IEEE Trans. Antennas Propag*., vol. 57, no. 11, pp. 3672-3676, Nov. 2009.

A Broadband H-plane Printed Horn Antenna with Sandwich Substrate Structure for Millimeter-wave Applications

Hafiz Usman Tahseen [1], Lixia Yang [2], and Wang Hongjin [1]

[1] School of Computer Science and Communication Engineering
Jiangsu University, Zhenjiang, 212013, China
drengrtahseen@gmail.com, 2405302396@qq.com

[2] Department of Communication Engineering
Anhui University, Hefei, 230601, China
Lixiayang@yeah.net

Abstract ─ Antenna is a very important element and plays a key role in communication systems for radiating energy. Based on high data rate speed requirements and large volume multimedia applications, 3G, 4G and now 5G technologies have been introduced and implemented. This paper presents a low profile antenna with novel structure and large continuous bandwidth for 5G broadband and millimeter-wave wireless applications. It is an H-plane printed horn antenna with multi-layered sandwich substrate. There are two Rogers (RO3003(tm)) substrates that make a sandwich structure with eight stainless steel columns. The proposed antenna is expected to give an impedance bandwidth 20-45 GHz with S11 < -10dB and 8.64dBi gain at 28 GHz design frequency. ANSYS 18.2 HFSS simulator is used for designing and optimization of the profile antenna. A comparison between simulated and measured results confirms the validity of the proposed design.

Index Terms ─ Millimeter wave antenna, 5G (fifth generation), wireless applications.

I. INTRODUCTION

Fifth generation technology is a hot topic for researchers these days due to the current and upcoming multimedia high speed and large data volume challenges. Substrate integrated horn antenna is a low profile and compact millimeter wave antenna with ease of integration [1]. Horn antennas are directional with wider bandwidth feature that make them feasible for high gain broadband applications. This property makes the horn shape more attractive choice for researchers to design a substrate integrated horn shape patch antennas for high bandwidth packages which is a need of the hour for 5G applications. In substrate integrated horn patch antennas, bandwidth is improved by using different impedance transformers if mismatching occurs at the edges of dielectric slab [2],[3].

With the recent developments in communication systems, all wireless applications like multimedia or cellular applications, IOT (internet of things), ITS and other broadcast applications need high data rate large volume speed that is not fully supported by 4G technology [4].

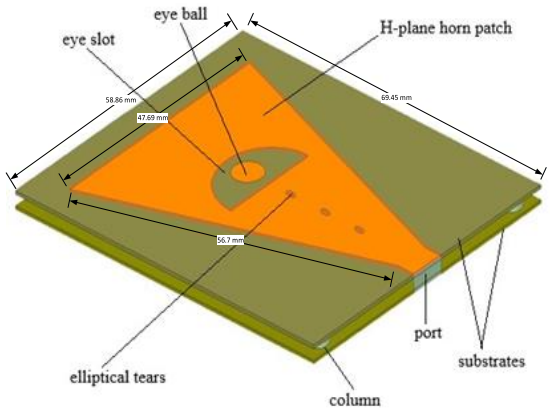

Fig. 1. Multilayer novel structure millimeter wave antenna.

So, ITU (International Telecommunication Union) issued new licensed high frequency bands in millimeter wave range for 5G and beyond applications [5]. Improvement of impedance bandwidth has been a hot topic for researchers in low profile micro strip antennas for high data rate 5G applications. There are various techniques that have been introduced to improve impedance bandwidths in past years including substrate integrated patches [1], slotted patches [6], [7] stacked patches [8], [9], [10] multilayers strip lines [11] and aperture coupled feed techniques [12], [13]. Multilayers technique has been used in most of these mentioned papers to improve bandwidths from 10.9% to 29% maximum.

Submitted On: December 1, 2020
Accepted On: January 18, 2021

https://doi.org/10.47037/2020.ACES.J.360309

To overcome the multilayers alignment and high cost issues, a single-layered wideband planar antenna substrate based topology has also been presented in [14], [15], [16] to get improved bandwidth 12.4% to 25.5% maximum. For long range communication systems, a narrow beam antenna radiation pattern is required to get high gain while for short range communication systems; a wide beam pattern is useful for wide coverage [17]. For substrate integrated horn antennas, gain was enhanced using different correction structures like metal via arrays [18], SIW gap technology [19] and horn walls [20]. But these designs could give impedance bandwidth less than 20%. By adding electric and magnetic currents radiations, a stable and uniform radiation pattern [21] and end fire radiations [22], [23] are achieved.

The detailed literature review of the above mentioned papers traces a hypothesis to get wideband and high gain features. So, a broadband, low cost, low profile and a compact antenna is designed for wireless 5G applications. It is observed from literature review that the multi-layered and substrate integrated waveguide (SIW) structures are used for broadband and gain enhancement features respectively. So, in the proposed antenna design, a multi-layered topology is used with a sandwich structure. Instead of using a SIW structure, a sandwich structure is proposed. Two RO3003(tm) dielectric substrates make a sandwich structure with stainless steel columns without any holes as shown in Fig. 1. Furthermore, a sectoral H-plane slotted horn patch is printed on the top surface of the upper substrate to get a stable high gain radiation pattern with wide band feature. In comparison with the previous H-plane sectoral SIW horn antennas [1], [2] and [3], the proposed antenna gives better impedance bandwidth and gain.

In the first step, a broadband, high gain WR28 horn antenna is simulated for inspiration. In the 2nd step, an H-plane sectoral horn antenna is simulated on a single RO3003(tm) substrate. In the 3rd step, the proposed multi-layered sectoral H-plane slotted horn antenna is designed to get wide band high gain features. All antennas are optimized and simulated in ANSYS18.2 HFSS simulator. The proposed antenna is fabricated for measuring results.

The paper is organized as follows. Design of the proposed antenna and EM analysis is presented is Section II. Simulated and experimental results lie in Section III. The final summary is in Section IV.

II. ANTENNA DESIGN AND EM ANALYSIS

A. Antenna design

To design a millimeter wave antenna that can support wideband 5G wireless applications, the hypothesis through a detailed literature review creates a topology for an H-plane sectoral printed horn antenna with multi-layered sandwich substrate structure. Furthermore, the sandwich substrate structure with the air gap between two dielectric substrates affects the permittivity and height of substrate and increases the resonance frequency and operational bandwidth [24]-[28]. In [29], a millimeter wave SIW antenna is designed at 28 GHz for indoor applications. It has 11.6 dB gain and impedance bandwidth 24.5 to 29.5 GHz. Out of all these mentioned papers, the proposed antenna gives the large and wide bandwidth with high gain in E- and H-planes both.

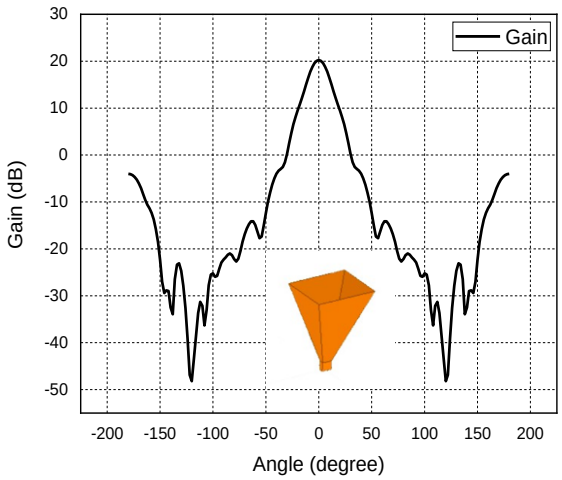

Fig. 2. Simulated full wave WR28 horn antenna gain.

In the first step, a WR28 horn antenna is simulated with the parameters and dimensions using design equations (1-6) [30]. Antenna parameters are calculated with reference to 20dBi high gain. The wide bandwidth and high gain characteristic of the full wave horn antenna gives a clear inspiration and hypothesis along with multi-layered topology from SIW H-plane sectoral horn antennas to design a multilayered sectoral H-plane printed horn antenna for wireless millimeter applications. It is observed from Fig. 2 that the full wave WR28 exhibits 20.23dBi gain at 28 GHz:

$$\left(\sqrt{2x}-\frac{b}{\lambda}\right)^2(2x-1)=\left(\frac{G_0}{2\pi}\sqrt{\frac{3}{2\pi}}\frac{1}{\sqrt{x}}-\frac{ba}{\lambda}\right)^2\left(\frac{G_0}{6\pi^3}\frac{1}{x}-1\right), \quad (1)$$

$$\frac{\rho_e}{\lambda}=x, \quad (2)$$

$$\frac{\rho_h}{\lambda}=\frac{G_0^2}{8\pi^3}\left(\frac{1}{x}\right), \quad (3)$$

$$x_{trial}=x_1=\frac{G_0}{2\pi\sqrt{2\pi}}, \quad (4)$$

$$a_1=\sqrt{3\lambda\rho_2}\cong\sqrt{3\lambda\rho_h}=\frac{G_0}{2\pi}\sqrt{\frac{2\lambda}{2\pi x}}, \quad (5)$$

$$b_1=\sqrt{3\lambda\rho_1}\cong\sqrt{2\lambda\rho_e}=\sqrt{2x\lambda}. \quad (6)$$

Where G_0 is the required gain, λ is a wavelength, a & b are dimensions of wave guide, a_1 & b_1 are dimensions of the horn aperture and ρ_e & ρ_h are the distances from wave guide to the horn. The WR28 horn antenna parameters are calculated from all these equations (1-6).

B. EM analysis

The WR28 horn antenna parameters are relevant to a high directional gain as mentioned in Table 1. So, in the 2nd step these parameters and dimensions are used to print a sectoral H-plane un-slotted horn patch on a dielectric substrate to design a single substrate H-plane sectoral horn antenna as shown in Fig. 3. It is clear from the Fig. 3 that the horn patch is actually the one face of the full wave horn antenna. Dimensions of the substrate and printed horn patch are same as in Fig. 1 and are mentioned in Table 1. So, the printed H-plane sectoral horn patch has dimensions of one face of the full horn antenna.

Table 1: Horn antenna dimensions

Description	Value	Unit
f	28	GHz
a	7.11	mm
b	3.55	mm
$\boldsymbol{\rho_e}$	56.7	mm
$\boldsymbol{\rho_h}$	56.7	mm
$\boldsymbol{a_1}$	47.69	mm
$\boldsymbol{b_1}$	37.43	mm
Substrate length	58.86	mm
Substrate width	69.45	mm
Substrate height (each)	0.5	mm
Length of eye-slot centered curve	20	mm
Radius of eye ball-patch	3	mm
Major radius of slotted elliptic tears	0.5	mm

It is observed from Figs. 4 and 5 that the antenna gain is 5.8dBi with impedance bandwidth 26.6-30.6 GHz. This antenna gain and impedance bandwidth is not good enough, so in the 3rd step, a multi-layered topology is further used along with this H-plane sectoral horn patch to enhance the gain and wide bandwidth.

To increase the operational bandwidth with resonance frequency and gain, the multi-layered and slotted substrate topology is used with printed H-plane sectoral horn. A multi-layered sandwich substrate with H-plane printed slotted horn patch antenna is proposed. Patch has a crying eye with slotted tears. The slotted tears and crying eye gives a further boost to the bandwidth while keeping radiation pattern stable that makes it unstoppable below 10dB. Horn patch is at the top substrate and ground patch is connected below the bottom substrate.

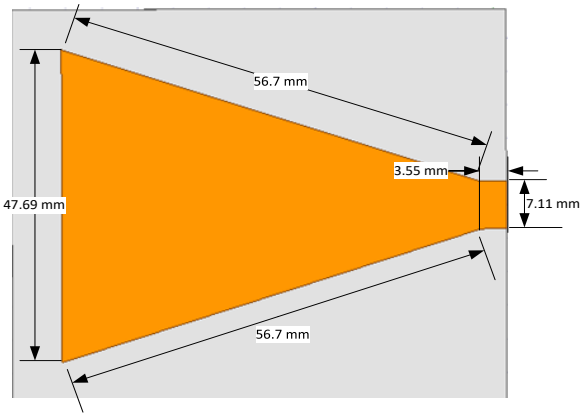

Fig. 3. Single substrate sectoral H-plane printed horn antenna.

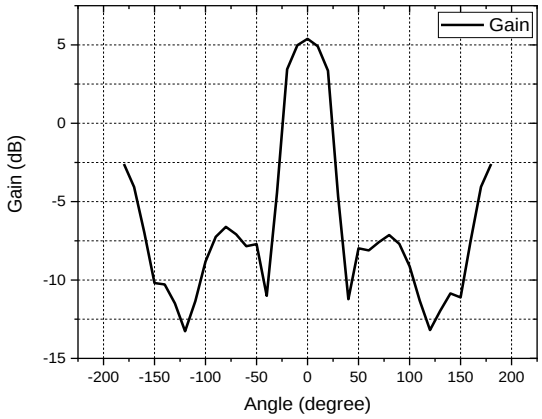

Fig. 4. Antenna gain of the single substrate H-plane sectoral horn antenna.

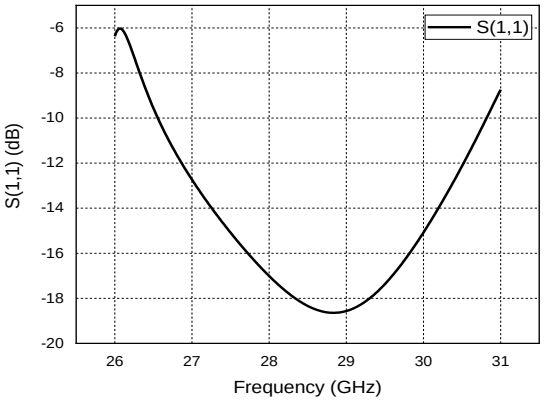

Fig. 5. Reflection coefficient of the single substrate H-plane sectoral horn antenna.

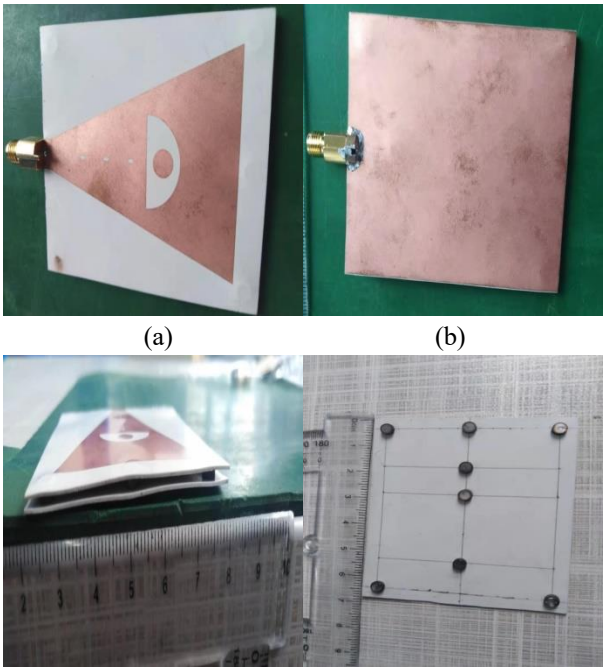

(a) (b)

(c) (d)

Fig. 6. Fabricated proposed antenna.

A 2.92 mm (K) female edge launch connector is used for excitation joining ground below the bottom substrate and patch on the top substrate Fig. 6. Both substrates make a sandwich with air gap of 1.5 mm and are supported by the stainless steel cylinders of the same dielectric constant as of air. Hence, the use of horn patch on a multi layered-substrate with cutting elliptic slots and an emotional eye collectively make a novel structure radiator. Both substrates have the same dimensions (58.86 mm × 69.45 mm). The stain less steel columns are fixed with a gum/bond at designated positions on the substrate as shown in Fig. 6 (d). It has 2 mm diameter and 1.5 mm height with dielectric constant 1. A high gain, narrow beam millimeter wave antenna with very large bandwidth is proposed for wireless 5G applications.

III. SIMULATION AND EXPERIMENTAL RESULTS

The proposed antenna is a prototype as shown in Fig. 6. A single substrate sectoral H-plane horn antenna produces a directional gain and a bandwidth up to 4 GHz in millimeter wave range as shown in Figs. 4 and 5. The proposed antenna is further optimized with sandwich substrate structure and sectoral H-plane slotted horn patch to get high gain and very large bandwidth for wireless 5G applications. The antenna measurement was completed in an anechoic chamber using vector network analyzer. It produces a high gain of 8.64dBi with continuous large bandwidth at 28 GHz center frequency.

The simulated and measured radiation patterns of the proposed antenna at 28 GHz design frequency in E- and H-planes are shown in Figs. 7 and 8 respectively. The E-plane and H-plane simulated and measured radiation patterns are very consistent and stable. It is observed that the simulated and measured patterns are in well agreement with little discrepancies. The simulated and measured reflection coefficient is shown in Fig. 9. It is observed that the proposed antenna gives a very large continuous bandwidth 20 GHz to onward with S11 < -10dB. It produces a narrow beam radiation pattern which validates the proposed antenna a good candidate for 5G wireless communication systems within the premises even for commercial usage.

The overall antenna size is 69.4554 mm × 58.8685 mm × 2.5 mm. It is clear from simulated and measured results that there is no big evident influence on antenna performance. Figure 9 shows the simulated and measured S-parameters of the proposed antenna with little differences. There is a large impedance bandwidth below 10dB. A little discrimination is observed due to the soldering effect and high frequency millimeter wave connector. Although this profile antenna gives a large continuous band, so a small 5G operational band out of entire available band is considered for displaying results. The surface current distributions of the proposed antenna are shown in Fig. 10. Figure 11 shows the measured radiation patterns of the proposed antenna at 30 GHz, 32 GHz, 34 GHz, 36 GHz and 38 GHz within the operational band. It is observed that the radiation pattern is stable throughout the operational band with a little difference. The gain reduces over the entire band very little that is due to the radiation pattern deformation and impedance mismatching. The measured gain of the proposed antenna over the entire proposed band is 8.64 ± 0.65dBi. The measured antenna gain is shown in Fig. 12. Both simulated and measured results agree well and give a radiation pattern in the broadside direction like a waveguide horn antenna with large impedance bandwidth. The validity of the proposed antenna design is confirmed through a comparison between simulated and measured results.

In comparison with the reference papers [1], [2] and [3] where an H-plane sectoral SIW horn antenna was designed, the proposed antenna gives a high gain antenna element with better impedance bandwidth 20 GHz to onward. The very large continuous bandwidth, i.e., 20 GHz to 45 GHz and onward with a high gain stable radiation pattern makes this profile antenna an attractive candidate for 5G broadband and millimeter-wave wireless applications. A comparison of the proposed antenna with full horn antenna and single substrate printed horn antenna is presented in Table 2.

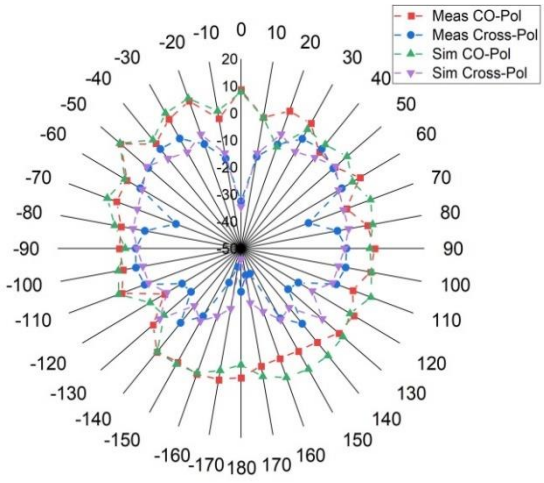

Fig. 7. Radiation patterns of the proposed antenna at 28 GHz in E-plane.

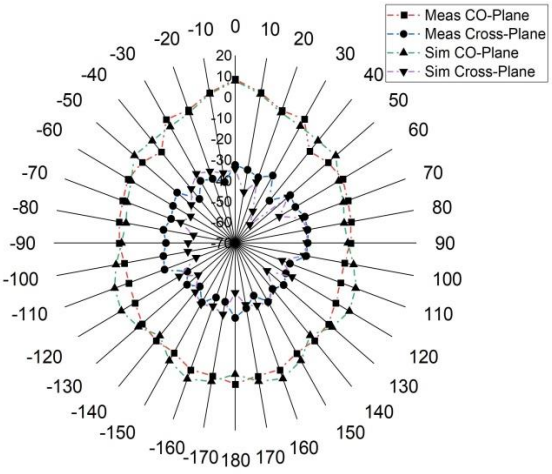

Fig. 8. Radiation patterns of the proposed antenna at 28 GHz in H-plane.

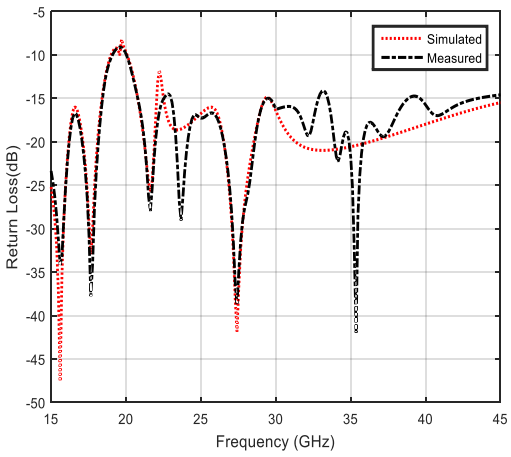

Fig. 9. Reflection coefficient of the proposed antenna.

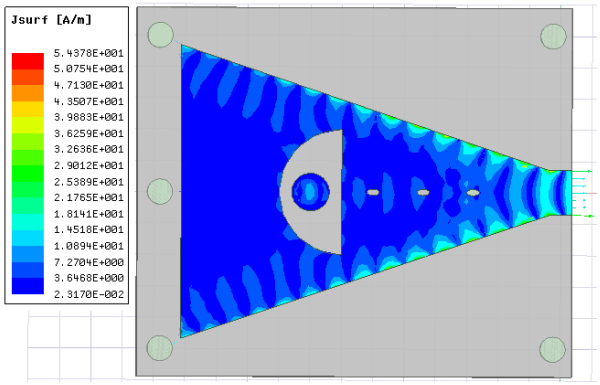

Fig. 10. Surface current of the proposed antenna.

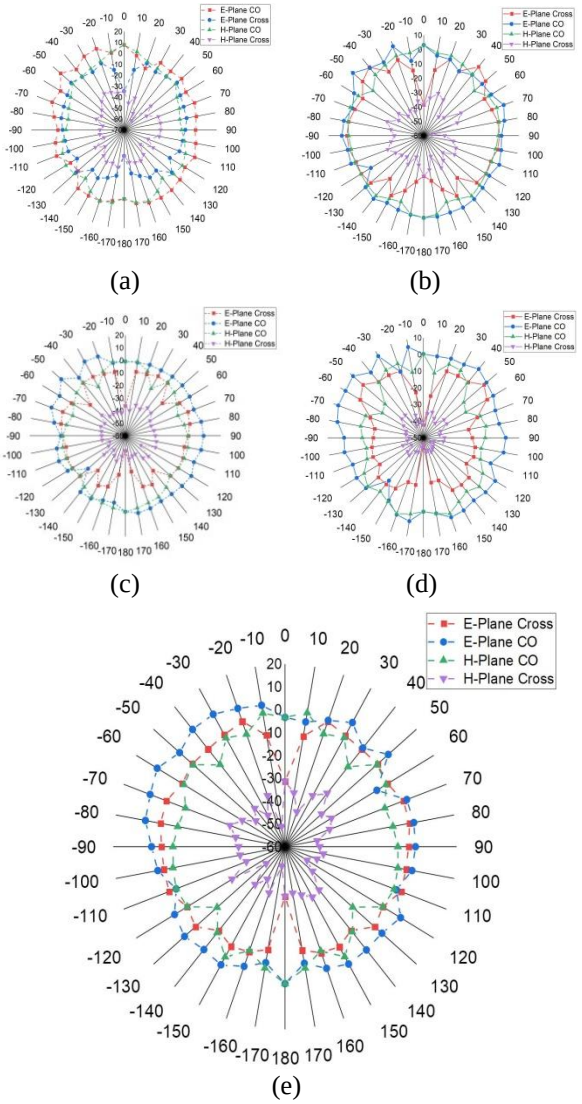

Fig. 11. Measured radiation patterns of the proposed antenna in E- and H-planes: (a) at 30 GHz, (b) at 32 GHz, (c) at 34 GHz, (d) at 36 GHz, and (e) at 38GHz.

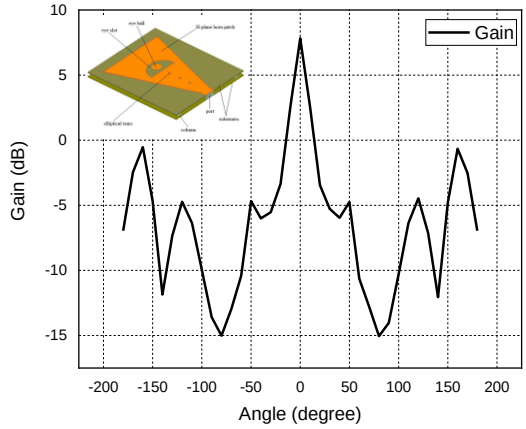

Fig. 12. Measured antenna gain of the proposed antenna.

Table 2: Comparison of antennas

No.	Antenna Description	Frequency	Gain (dB)	Bandwidth
1	WR28 full horn antenna	28 GHz	20.2	18-40 GHz
2	Single substrate printed horn antenna	28 GHz	5.8	26.5-30.8 GHz
3	Proposed multilayered antenna	28 GHz	8.64	20-45 GHz (onward)

VI. CONCLUSION

In this article, an H-plane sectoral printed horn antenna with a novel multi-layered sandwich substrate is proposed for wireless 5G millimeter wave applications. The sectoral H-plane printed horn topology is used to get high gain radiation pattern. The multi-layered sandwich substrate structure gives a large continuous bandwidth from 20 GHz to onward. The proposed antenna exhibits measured bandwidth (20 GHz to 45GHz or onward) below -10dB reflection coefficient. The antenna has a sufficient measured gain of 8.64dBi in E- and H-planes both. It is experimentally demonstrated that the proposed antenna can be used for different wireless 5G millimeter wave indoor and outdoor applications.

ACKNOWLEDGMENT

This paper is supported by National Science Foundation of China (Nos. 62071003, 41874174, 61901004, 61801194), the Opening Foundation of National Key Laboratory of Electromagnetic Environment (No. 201802003), The fund for Key Laboratory of Electromagnetic Scattering (No. 61424090107), Natural Science Foundation of Anhui Province (2008085MF186).

REFERENCES

[1] J. Wang, Y. Li, L. Ge, J. Wang, M. Chen, Z. Zhang, and Z. Li, "Wideband dipole array loaded substrate integrated H-plane horn antenna for millimeter waves," *IEEE Transactions on Antennas and Propagation*, vol. 65, no. 10, pp. 5211-5219, Oct. 2017. doi: 10.1109/TAP.2017.2741025.

[2] M. E. Morote, B. Fuchs, J. F. Zurcher, and J. R. Mosig, "A printed transition for matching improvement of SIW horn antennas," *IEEE Transactions on Antennas and Propagation*, vol. 61, no. 4, pp. 1923-1930, Apr. 2013.

[3] A. R. Mallahzadeh and S. Esfandiarpour, "Wideband H-plane horn antenna based on ridge substrate integrated waveguide (RSIW)," *IEEE Antennas Wireless Propagation Letters*, vol. 11, pp. 85-88, Mar. 2012.

[4] C.-X. Mao, M. Khalily, P. Xiao, T. W. C. Brown, and S. Gao, "Planar sub-millimeter-wave array antenna with enhanced gain and reduced sidelobes for 5G broadcast applications," *IEEE Transactions on Antennas and Propagation*, vol. 67, no. 1, pp. 160-168, Jan. 2019. doi: 10.1109/TAP.2018.2874796.

[5] M. J. Marcus, "5G and 'IMT for 2020 and beyond' [spectrum policy and regulatory issues]," *IEEE Wireless Communications*, vol. 22, no. 4, pp. 2-3, Aug. 2015.

[6] H. Sun, Y.-X. Guo, and Z. Wang, "60-GHz circularly polarized U-slot patch antenna array on LTCC," *IEEE Transactions on Antennas and Propagation*, vol. 61, no. 1, pp. 430-435, Jan. 2013.

[7] W. Yang and J. Zhou, "Wideband low-profile substrate integrated waveguide cavity-backed E-shaped patch antenna," *IEEE Antennas Wireless Propagation Letters*, vol. 12, pp. 143-146, Jan. 2013.

[8] K.-S. Chin, W. Jiang, W. Che, C.-C. Chang, and H. Jin, "Wideband LTCC 60-GHz antenna array with a dual-resonant slot and patch structure," *IEEE Transactions on Antennas and Propagation*, vol. 62, no. 1, pp. 174-182, Jan. 2014.

[9] S. L. Smith, T. Merkle, K. W. Smart, S. G. Hay, M. Shen, and F. Ceccato, "Design aspects of an antenna-MMIC interface using a stacked patch at 71–86 GHz," *IEEE Transactions on Antennas and Propagation*, vol. 61, no. 4, pp. 1591-1598, Apr. 2013.

[10] N. Ghassemi, K. Wu, S. Claude, X. Zhang, and J. Bornemann, "Low-cost and high-efficient W-band substrate integrated waveguide antenna array made of printed circuit board process," *IEEE Transactions on Antennas and Propagation*, vol. 60, no. 3, pp. 1648-1653, Mar. 2012. doi: 10.1109/TAP.2011.2180346.

[11] L. Wang, Y. X. Guo, and W. X. Sheng, "Wideband high-gain 60-GHz LTCC L-probe patch antenna array with a soft surface," *IEEE Transactions on Antennas and Propagation*, vol. 61, no. 4, pp. 1802-1809, Apr. 2013. doi: 10.1109/TAP.2012.2220331.

[12] J. F. Xu, Z. N. Chen, X. M. Qing, and W. Hong, "Bandwidth enhancement for a 60 GHz substrate integrated waveguide fed cavity array antenna on LTCC," *IEEE Transactions on Antennas and Propagation*, vol. 59, no. 3, pp. 826-832, Mar. 2011. doi: 10.1109/TAP.2010.2103018.

[13] Y. Liand and K. M. Luk, "60-GHz substrate integrated waveguide fed cavity backed aperture-coupled microstrip patch antenna arrays," *IEEE Transactions on Antennas and Propagation*, vol. 63, no. 3, pp. 1075-1085, Mar. 2015. doi: 10.1109/TAP.2015.2390228.

[14] M. Li and K.-M. Luk, "Low-cost wideband microstrip antenna array for 60-GHz applications," *IEEE Transactions on Antennas and Propagation*, vol. 62, no. 6, pp. 3012-3018, June 2014. doi: 10.1109/TAP.2014.2311994.

[15] T. Y. Yang, W. Hong, and Y. Zhang, "Wideband millimeter-wave substrate integrated waveguide cavity-backed rectangular patch antenna," *IEEE Antennas and Wireless Propagation Letters*, vol. 13, pp. 205-208, 2014. doi: 10.1109/LAWP.2014.2300194.

[16] T. Zhang, Y. Zhang, S. Yu, W. Hong, and K. Wu, "A Q-band dual-mode cavity-backed wideband patch antenna with independently controllable resonances," *2013 Proceedings of the International Symposium on Antennas & Propagation*, Nanjing, pp. 118-121, 2013.

[17] K. Fan, Z. Hao, and Q. Yuan, "A low-profile wideband substrate-integrated waveguide cavity-backed E-shaped patch antenna for the Q-LINKPAN applications," *IEEE Transactions on Antennas and Propagation*, vol. 65, no. 11, pp. 5667-5676, Nov. 2017. doi: 10.1109/TAP.2017.2748181.

[18] L. Wang, X. X. Yin, S. L. Li, H. X. Zhao, L. L. Liu, and M. Zhang, "Phase corrected substrate integrated waveguide H-plane horn antenna with embedded metal-via arrays," *IEEE Transactions on Antennas and Propagation*, vol. 62, no. 4, pp. 1854-1861, Apr. 2014.

[19] L. Wang, M. E. Morote, H. Y. Qi, X. X. Yin, and J. R. Mosig, "Phase corrected H-plane horn antenna in gap SIW technology," *IEEE Transactions on Antennas and Propagation*, vol. 65, no. 1, pp. 347-353, Jan. 2017. doi: 10.1109/TAP.2016.2623656.

[20] N. Bayat-Makou and A. A. Kishk, "Substrate integrated horn antenna with uniform aperture distribution," *IEEE Transactions on Antennas and Propagation*, vol. 65, no. 2, pp. 514-520, Feb. 2017. doi: 10.1109/TAP.2016.2640144.

[21] K. M. Luk and H. Wong, "A new wideband unidirectional antenna element," *Itn. J. Microw. Opt. Technol.*, vol. 1, no. 1, pp. 35-44, June 2006.

[22] A. Chlavin, "A new antenna feed having equal E - and H-plane patterns," *Transactions of the IRE Professional Group on Antennas and Propagation*, vol. 2, no. 3, pp. 113-119, July 1954. doi: 10.1109/T-AP.1954.27983.

[23] Y. Li and K. Luk, "A multibeam end-fire magneto-electric dipole antenna array for millimeter-wave applications," *IEEE Transactions on Antennas and Propagation*, vol. 64, no. 7, pp. 2894-2904, July 2016. doi: 10.1109/TAP.2016.2554601.

[24] J. S. Dahele and K. F. Lee, "Theory and experiment on microstrip antennas with airgaps," *IEEE Proceedings H-Microwaves, Antennas and Propagation*, vol. 132, no. 7, pp. 455-460, Dec. 1985. doi: 10.1049/ip-h-2.1985.0081.

[25] M. Jusoh, T. Sabapathy, M. F. Jamlos, and M. R. Kamarudin, "Reconfigurable four-parasitic-elements patch antenna for high-gain beam switching application," *IEEE Antennas and Wireless Propagation Letters*, vol. 13, pp. 79-82, 2014.

[26] M. S. Alam and A. M. Abbosh, "Beam-steerable planar antenna using circular disc and four PIN-controlled tapered stubs for WiMAX and WLAN applications," *IEEE Antennas and Wireless Propagation Letters*, vol. 15, pp. 980-983, 2016.

[27] S. Shi and W. Ding, "Radiation pattern reconfigurable microstrip antenna for WiMAX application," in *Electronics Letters*, vol. 51, no. 9, pp. 662-664, Apr. 30, 2015. doi: 10.1049/el.2015.0568.

[28] M. Burtowy, M. Rzymowski, and L. Kulas, "Low-profile ESPAR antenna for RSS-based DoA estimation in IoT applications," *IEEE Access*, vol. 7, pp. 17403-17411, 2019.

[29] J. Xu, W. Hong, H. Tang, Z. Kuai, and K. Wu, "Half-mode substrate integrated waveguide (HMSIW) leaky-wave antenna for millimeter-wave applications," *IEEE Antennas and Wireless Propagation Letters*, vol. 7, pp. 85-88, 2008. doi: 10.1109/LAWP.2008.919353.

[30] C. A. Balanis, *Antenna Theory - Analysis and Design*. New Jersey: John Wiley & Sons, pp. 780-783, 2005.

Multiband Triple L-Arms Patch Antenna with Diamond Slot Ground for 5G Applications

Dalia H. Sadek [1], Heba A. Shawkey [2], and Abdelhalim A. Zekry [1]

[1] Faculty of Engineering, Ain Shams University, Cairo, Egypt
Doly_sadek@hotmail.com, aaazekry@hotmail.com

[2] Electronics Research Institute (ERI) Giza – Egypt
heba_shawkey@eri.sci.eg

Abstract ─ This paper reported a pioneering 5G multiband microstrip line fed patch antenna for IoT, wireless power transfer (WPT) and data transmission. The proposed antenna is accomplished using a triple L-arms patch antenna responsible for the multiband response. A diamond-shaped ground slot is added to control and increase the bandwidth of the resonant frequency. The antenna is designed to resonate at 10, 13, 17 and 26 GHz with 10 dB impedance bandwidths of 0.67, 0.8, 2.45 and 4.3 GHz respectively. The proposed antenna is fabricated using microstrip technology with total area of 16.5x16.5 mm^2. The 5G multiband antenna has sufficient realized gain of 4.95, 5.72, 4.94 and 7.077 dB respectively. The antenna is designed and simulated using the CST Microwave Studio Suite (Computer Simulation Technology). Measurements show good agreement with simulations in all frequencies of operation.

Index Terms ─ 5G wireless communication, diamond-shaped slot, Internet of Things (IoT), Millimeter Wave (MMW), multiband antenna, Triple-L Arms (TLA), Global System for Mobile Communications (GSM).

I. INTRODUCTION

The demand for the high data rate transfer and large capacities of traffic is continuously growing so, the world will witness 5G technology very soon with the fastest broadband speed and low latency. It needs to operate in three frequency ranges to ensure widespread coverage and support for all networks covered by previous technology. These ranges are Sub-1GHz, 1–6 GHz and above 6 GHz [1]. With a strength of sub-1GHz, it cannot meet the requirements in terms of absolute high bandwidth. It is used to provide broad coverage in urban areas and suburbs. The 1–6 GHz band provide both capacity and coverage advantages. The band above 6 GHz fulfills the requirements of an ultra-high broadband speed of 5G. There would be a need to use MMW bands starting from 24 GHz to satisfy the need for high broadband speeds up to 20 Gb/s [2]. GSM has proposed mobile bands of 26 GHz (24.25 GHz-27.5 GHz), 40 GHz (37.5 GHz-43.5 GHz) and (67 GHz-71 GHz) [3],[4]. The infrastructure for 5G mobile channels will be able to support much better data speeds, higher aggregate capacity, minimal latency, lower infrastructure cost, and many new capabilities due to increased bandwidth [5]. Antenna for 5G communications should consider some key requirements of 5G technology. It should resonate over a wide bandwidth, continuous strong connections with minimum latency. Multiband antenna is a potential solution for battery-less wireless applications that need multiple channels for simultaneous data and power transfer as wearable/implantable medical devices, smart farming sensors and portable electronics devices [6]–[8].

There are many proposed antennas for 5G bands with different applications. For example, Yahia et al. have designed a compact directional microstrip grid array antenna at 10 GHz. The antenna was designed on a cheap FR4 substrate and has achieved a dual band with peak gain of 8.03 dBi [9]. For wireless power transfer and harvesting applications, there are appropriate choices of frequency to ensure high RF-DC power conversion. In [10], Abderrahim et al. designed multiband rectenna for microwave applications. The antenna can harvest ambient power at different radio frequencies of 12, 17, and 20 GHz. Some studies have been done at 26 and 28 GHz [11] by Mahmoud et al. The antenna has been fabricated using standard commercial materials, to produce MMW antenna on textile for radio frequency energy harvesting (RFEH), enabling high efficiency reception of MMW radiation for wearable rectennas. In [12], Farzad et al. designed broadband circularly polarized array antenna using FR4 substrate with a thickness of 0.8 mm. It designed with an L-shaped patch and a rhombic slot in the ground. This antenna can cover the frequency band 4.66–5.30 GHz. In [13], the Varum et al. introduced a microstrip antenna for IoT which resonates at band 17 GHz with More than 2 GHz bandwidth and gain 5.8 dBi. In [14], Ebenezer et al. designed a compact ultra-light weight and efficient

Submitted On: October 11, 2020
Accepted On: February 8, 2021

https://doi.org/10.47037/2020.ACES.J.360310

circularly polarized asymmetric slit patch antenna. It is fabricated using RT/DUROID 5880 material to operate at the center frequency of 11.3 GHz and constant gain through the operating bandwidth with an apprehended peak gain of 5.6 db for vehicular satellite communication applications. In this work, a multiband microstrip antenna was designed to achieve a high gain with small size at 5G bands of 10, 13, 17 and 26 GHz. The antenna is small enough to be included in sensors, domestic equipment's and wearables. Also, it is appropriate for WPT and energy harvesting systems, the multiband operation increases the harvesting power compared with single band operation, where the receiving antenna collects the power from multiband. The designed antenna has the advantages of structural simplicity, planar geometry, ease of fabrication and relatively lower complexity. This paper is comprised of four sections. Section 2 includes the design and layout of the presented antenna, Section 3 contains the implementation and measurement while the last section concludes the paper.

II. ANTENNA DESIGN AND LAYOUT

The structure geometry of the proposed Triple – L arms patch slotted antenna (TLA) is shown in Fig. 1. The antenna is designed using ROGERS(RO4003c) substrate with relative dielectric permittivity ε_r=3.38, thickness 0.81 mm and dissipation factor tanδ=0.0026. The feeding line with width of W_f =2.1mm and length of L_f =6.3 mm to feed the antenna.

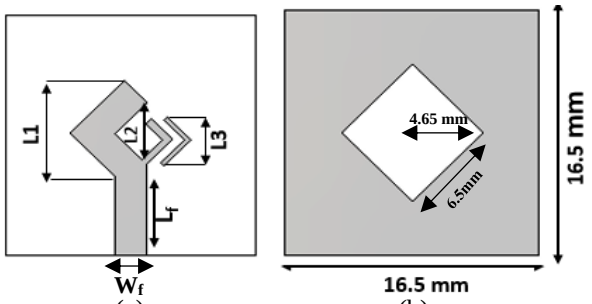

(a) (b)

Fig. 1. Configuration of the proposed antenna with dimensions: (a) top view and (b) bottom view.

The design consists of a slotted antenna having a microstrip feed line and three L-shaped arms, each responsible for a certain resonant frequency. To improve resonant frequencies' bandwidth, a diamond slot shown in Fig. 1 (b), has been carved on the opposite side of the radiation patch on the ground plane of the antenna at a distance of 4.65 mm from the center of the ground with length 6. 5mm.The key design is to set the length of each arm close to the half wavelength of the resonant frequency (L~λ/2). L_1~ 15mm, L_2~5.7mm, L_3~8.8mm. Because of the existence of an electromagnetic coupling between the 3 arms, a parametric study has been carried out to define the optimum length for the required frequency bands.

Design flow was done in 3 steps. In the first step, only one arm patch L_1 is set with its dimensions are adjusted to (5.9mm,4.83mm) to generate the 10 GHz resonant frequency. To get the second band another arm L_2 with length of (2.5mm,2.9mm) has been added to get resonant at 26 GHz. Finally, the arm L_3 with length of (3mm,3.4mm) generates a resonant at 17 GHz. Figure 2 illustrates simulation results for the 3 design steps of the TLA antenna with diamond slot ground. The length of the feed line is made 4.6 mm, and its width is made 2.1 mm in order to match the impedance of the patch. To optimize operation bandwidth of the proposed antenna, the dimensions of the diamond slot ground are changed. Figure 3 indicates a comparison of S11 parameter for the proposed antenna with different slot size .The figure clarifies that the bandwidth of resonant frequencies can be adjusted by changing the values of ground slot to reach a wider bandwidth specially at the higher bands of resonant frequencies which is suitable to WPT and harvesting systems application. The wide bandwidth aims to solve traffic-related issues. And the wide bandwidth antennas are necessary to harvest power efficiently from the full spectrum.

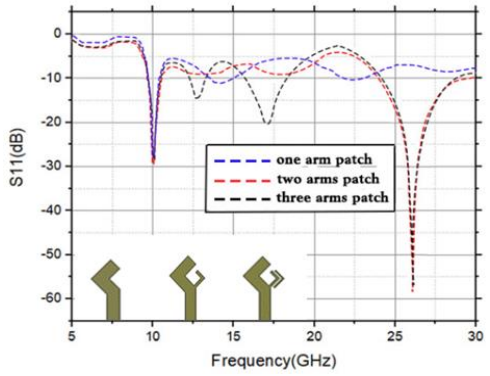

Fig. 2. The reflection coefficient of the design steps for the proposed antenna.

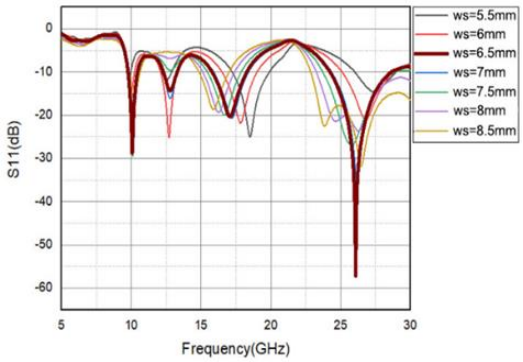

Fig. 3. Adjustment in the bandwidth of the antenna for different values of ground slots.

III. ANTENNA IMPLEMENTATION AND MEASUREMENT

The TLA antenna fabricated using Photolithography technology with wet etching and the track's pattern plotted on a dark-film mask in Microstrip Fabrication Laboratory, Electronics Research Institute (ERI). Figure 4 shows a photograph for the fabricated TLA. Figure 5 clarifies the test feature to connect the proposed antenna with vector network analyzer (VNA). Figure 6 shows the VNA (ROHDE&SCHWARZ ZVA6) that it is used to perform the return loss measurements.

A. Designed antenna S-parameters

Figure 7 depicts the simulated in addition to measured results of the proposed antenna for sake of validation and comparison. The antenna was initially simulated and optimized for 10, 17 and 26 GHz, but the simulation shows an extra resonant frequency at 13 GHz this can be explained due to the effect of the ground slot. It is clear that the antenna has sufficient bandwidth at the resonant frequencies. 10 GHz band has bandwidth of 0.67 GHz with minimum return loss of 28.17 dB,13 GHz band with 0.8GHz bandwidth and 15dB minimum return loss, 17GHz band has a bandwidth of 2.45 GHz with minimum return loss of 20.327 dB and 26 GHz band has bandwidth of 4.3 GHz with minimum return loss of 57.15dB, where the bandwidth is determined at -10dB reflection coefficient level as a reference. It is clear from Fig. 7 that there is good agreement at the lower frequencies while there is an appreciable loss at the higher frequency side of the S11 curve This is due to the additional parasitic capacitance in experimental device in addition to the effects of the connectors at such higher frequencies. Moreover, there are also fabrication tolerances [17].

B. Equivalent circuit of the TLA antenna (modeling of patch antenna)

This section describes the electrical equivalent circuit of the TLA antenna Fig. 8 (a) shows the equivalent circuit used to model the electrical behavior of the antenna in response to an incoming RF input signal. It is particularly useful to implement this model using basic components R1, L1, and C1, which influence the first resonant frequency ($f1$), R2, L2, and C2 influence the second resonant frequency ($f2$), R3, L3, and C3 influence the third resonant frequency ($f3$) and finally, R4, L4, and C4 influence the fourth resonant frequency ($f4$). Elements L5 and C5 are included in the equivalent circuit model to represent the electrical length of the feed line and the slot coupling, respectively. The corresponding values of the equivalent circuit elements are depicted in Table 1. Figure 8 (b) shows the reflection coefficient response of the antenna obtained from CST simulation compared to the calculated response of the equivalent circuit model by using Agilent ADS software in addition to the measured reflection coefficient. The results of simulated, measured, and ADS model are in good agreement.

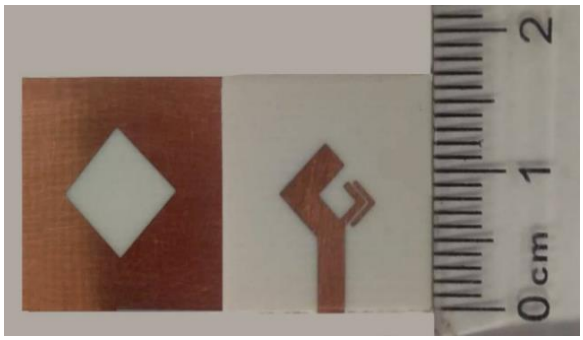

(a) (b)

Fig. 4. Photograph of the fabricated patch antenna: (a) bottom layer and (b) top layer.

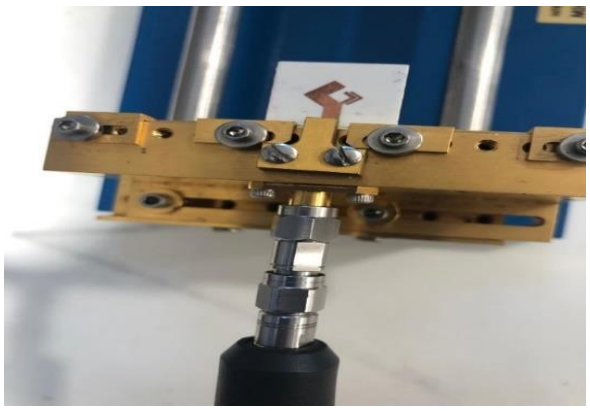

Fig. 5. Microwave test feature to connect the antenna with Vector Network Analyzer.

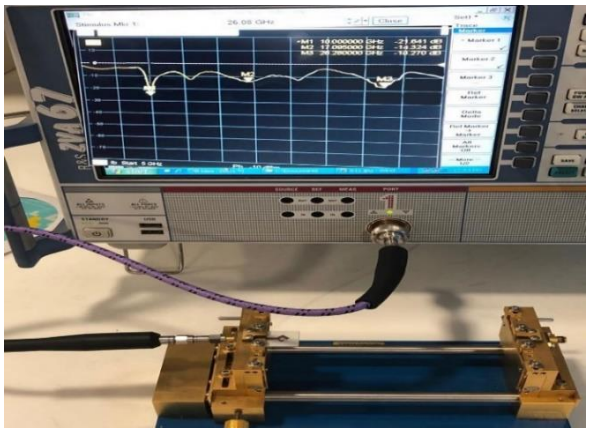

Fig. 6. The measurement of S11 parameter using the VNA ROHDE&SCHWARZ ZVA6.

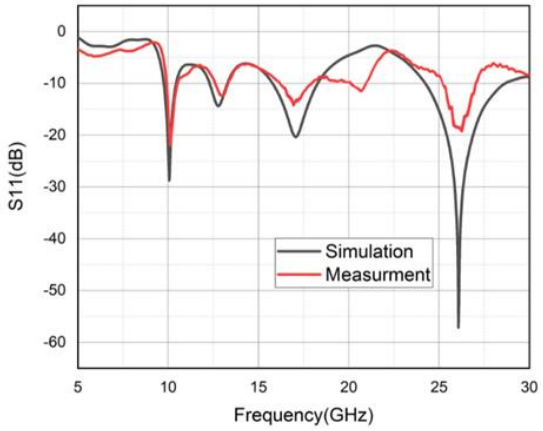

Fig. 7. Comparison between simulation and measured reflection coefficient versus frequency.

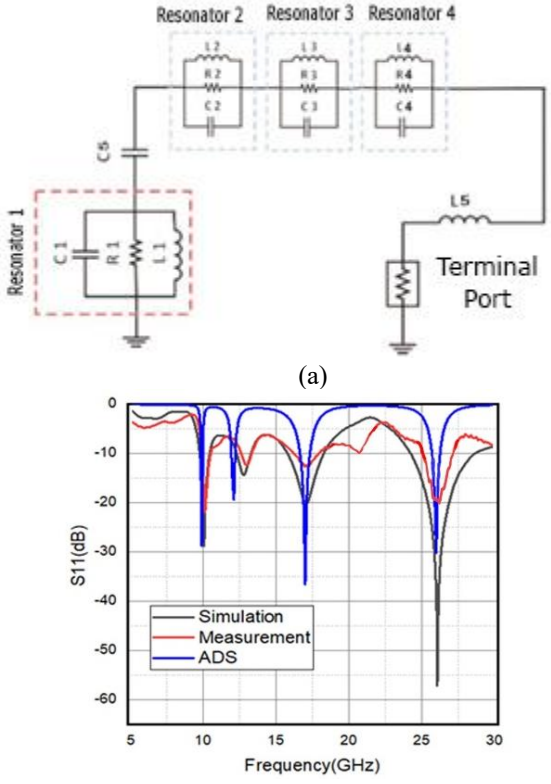

Fig. 8. (a) Equivalent lumped-elements circuit for antenna in ADS. (b) Comparison of the reflection coefficient responses of CST, ADS and measurement.

C. Surface current distribution

Figures 9 (a), (b), (c) and (d) describes the current distribution of the TLA antenna at frequency bands 10, 13, 17 and 26 GHz, respectively. It is observed from these figures that the currents are concentrated at the outer edges of radiating patches. Also indicates that each arm is responsible for a specific resonant frequency [18]. This means that the largest arm gives 10 GHz resonant and the smallest arm gives 26 GHz resonant, as mentioned before in the design antenna procedure. The current distribution on the antenna at 13 GHz indicates that the ground slot is responsible for this resonant frequency.

D. 2D-Polar radiation patterns

The radiation pattern comparison measured and simulated of the antenna at 10 and 13 GHz are depicted in Figs. 10 (a) and (b). The solid red and black line represents the simulated E-plane and H-plane respectively. Also, the dashed red and black line represents the measured E-plane and H-plane. The pattern depicts a dipole-like pattern in both measured and simulated results. The simulated radiation patterns at operating bands 17 and 26 GHz frequencies shown in Figs. 10 (c) and (d). The solid red and black line represents the simulated E-plane and H-plane. Measurements were only made for frequencies 10 and 13GHz due to the instrumentation capabilities available at the ERI lab. It can be observed that the slot in the ground plane influences the patterns in the backward direction at the resonant frequencies. This is because the slot in the ground plane is itself resonators. Also, it can be notice that at the higher frequency (26 GHz) the radiation pattern deteriorates because of unequal phase distribution and significant magnitude of higher order modes. For a further completing the antenna performance, plot of antenna's gain is presented in Fig. 11. The plot illustrates that antenna has a relatively high gain at frequencies 10,13,17 and 26 GHz of 4.95, 5.72, 4.94 and 7.077 dB respectively. which is a good gain compared to the antenna introduced by the author in [11] that provides a gain of 5.4 dB in space at 26 GHz. Also, with total efficiency of 90%, 94.6%, 92% and 93.3% respectively.

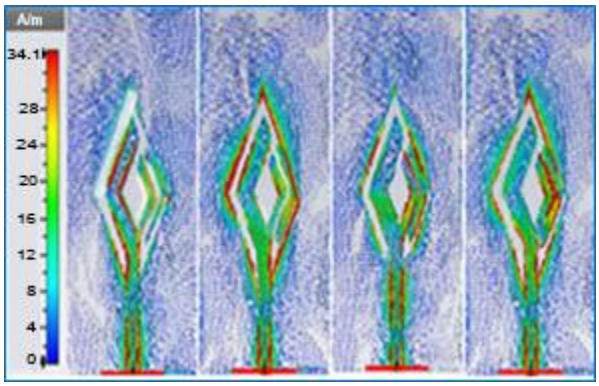

Fig. 9. Current distribution of 5G antenna at the resonant frequencies (a) 10 GHz (b) 13 GHz (c) 17 GHz (d) 26 GHz.

Table 1: Elements values of the equivalent circuit model

Parameter	R1 (Ω)	L1 (nH)	C1 (pF)	R2 (Ω)	L2 (nH)	C2 (pF)	R3 (Ω)	L3 (nH)	C3 (pF)	R4 (Ω)	L4 (nH)	C4 (pF)	L5 (nH)	C5 (pF)
Value	383	0.1	3.5	340	.14	1.3	332	0.2	.47	516	0.1	0.4	1.1	10

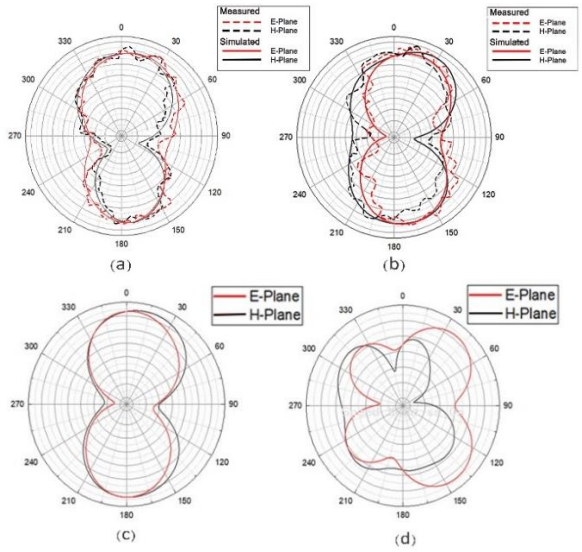

Fig. 10. The radiation pattern of the proposed antenna in E-plane and H-plane.

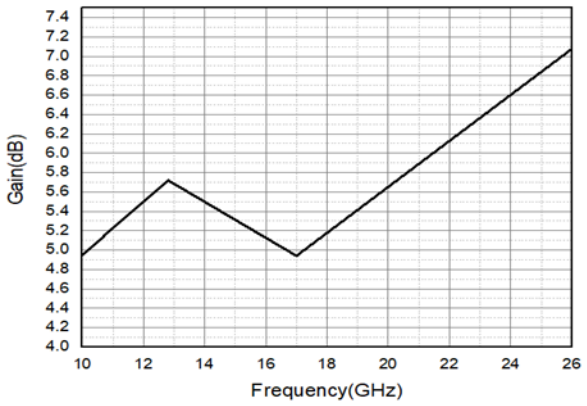

Fig. 11. Gain versus frequency.

Table 2 shows the performance comparison between the TLA antenna and other previously reported in literature within the same frequency range. Compared with other types, the TLA antenna has large number of resonant frequencies, except for [10] the TLA antenna has one more band with smaller area. Besides it operates in the low frequencies 10 and 13 GHz with no area overhead compared with other types operate in comparable frequency band. The proposed antenna has larger gain at 26 GHz compared with that antenna presented in [11] but the antenna uses a commercial textile material for wearable ambient RFEH. While in [12] and [13] a single band of operation, for [12] with one arm patch, larger area and lower gain and for [13] with smaller area and higher gain compared to the proposed antenna. In [15], multiband antenna with lower frequencies and larger area but with larger bandwidth compared with the lower frequency of the TLA antenna. The area of antenna designed in [16] is smaller than the proposed antenna but with less bandwidth such area is compatible to be a unit of an array.

Table 2: Comparison of the proposed antenna with other antennas

Reference	Operating frequency (GHz)	BW (GHz)	S11 dB	Gain (dBi)	Antenna size (mm^2)
[9]	10-10.68/ 10.7-12.23	0.65-1.5	16.33/ 31.9	8.03	48x55
[10]	12/17/20	--------	35/14/ 16	11.7/ 11.7/ 17.6	19.5x19.5
[11]	26/28	--------	18/21	5.4/5.5	30x55
[12]	4.95	0.64	30	3.39	32 x 46
[13]	17	2.2	---------	5.8	4x4
[15]	5.2/5.4/5.8	1.3	~14	6.5	50x50
[16]	26/28	2.28	>12	---------	6x6
This work	10/13/17/ 26	0.67/ 0.8/ 2.45/ 4.3	28/15/ 20/57	4.95/ 5.72/ 4.94 / 7.077	16.5x16.5

IV. CONCLUSION

A slotted microstrip patch antenna having four resonant modes for use in IoT, WPT and data transmission. has been proposed and studied.

The antenna is a very low-profile structure with dimensions 16.5×16.5×0.81mm^3. It can hence, be easily integrated into devices with space constraints. The TLA antenna is designed to operate at 10, 13, 17 and 26 GHz with a bandwidth of 0.67, 0.8, 2.45 and 4.3 GHz, respectively. The wide bandwidth antennas are necessary to harvest power efficiently from the full spectrum. The maximum efficiency is achieved at 13 and 26 GHz. The antenna was fabricated and measured with a good agreement between the simulation results and measurement results for reflection coefficient in addition to radiation characteristics.

REFERENCES

[1] A. Morgado, K. M. Huq, S. Mumtaz, and J. Rodriguez, "A survey of 5g technologies: Regulatory, standardization and industrial perspectives," *Digital Communications and Networks*, vol. 4, no. 2, pp. 87-97, 2018.

[2] T. S. Rappaport, R. W. Heath, Jr., R. C. Daniels, and J. N. Murdock, *Millimeter Wave Wireless*

Communications. Pearson Education, 2014.

[3] T. S. Rappaport, Y. Xing, G. R. Mac Cartney, Jr., A. F. Molisch, E. Mellios, and J. Zhang, "Overview of millimeter wave communications for fifth-generation (5g) wireless networks-with a focus on propagation models," arXiv preprint arXiv:1708. 02557, 2017.

[4] Y. Niu, Y. Li, D. Jin, L. Su, and A. V. Vasilakos, "A survey of millimeter wave communications (mmwave) for 5g: Opportunities and challenges," *Wireless Networks*, vol. 21, no. 8, pp. 2657-2676, 2015.

[5] C. X. Wang, F. Haideret, X. Gao, Y. Xiaohu, Y. Yang, D. Yuan, H. M. Aggoune, H. Haas, S. Fletcher, and E. Hepsaydir, "Cellular architecture and key technologies for 5G wireless communication networks," *IEEE Communication Mag*., vol. 52, no. 2, pp. 122-130, Feb. 2014.

[6] H. Shawkey and D. Elsheakh, "Multiband dual-meander lie antenna for body-centric networks' biomedical applications by using UMC 180 nm," *Electronics MDPI Journal*, 2020.

[7] Q. Bai, R. Singh, K. L. Ford, T. O. Farrell, and R. J. Langley, "An independently tunable tri-band antenna design for concurrent multiband single chain radio receivers," *IEEE Transactions on Antennas and Propagation*, vol. 65, no. 12, Dec. 2017.

[8] D. Zhai, R. Zhang, J. Du, Z. Ding, and F. R. Yu, "Simultaneous wireless information and power transfer at 5G new frequencies: Channel measurement and network design," *IEEE Journal on Selected Areas in Communications*, 2018.

[9] M. S. Yahya, I. A Dalyop, Y. Saleh, and M. Aminu-Baba, "Antenna for 5G mobile communications systems at 10 GHz," in *International Journal of Engineering & Technology*, 7 (3.36), pp. 13-15, 2018.

[10] A. Okba, A. Takacs, H. Aubert, S. Charlot, and P. F. Calmon, "Multiband rectenna for microwave applications," *Elsevier Comptes Rendus Physique*, vol. 18, no. 2, pp. 107-117, Feb. 2017.

[11] M. Wagih, A. S. Weddell, and S. Beeby, "Millimeter-wave textile antenna for on-body RF energy harvesting in future 5G networks," in *Wireless Power Transfer Conference (WPTC), IEEE*, 2019.

[12] F. Zandikiya and L. Asadpor," Broadband circularly polarized slot antenna array fed by asymmetric CPW for C-band applications," *IETE Journal of Research*, 2017.

[13] T. Varum, M. Duarte, J. N. Matos, and P. Pinho, "Microstrip antenna for IoT/WLAN applications in smart homes at 17GHz," *12th European Conference on Antennas and Propagation (EuCAP)*, 2018.

[14] A. B. Ebenezer, A. Raaza, S. Ramesh, S. Jerritta, and V. Rajendran, "Circularly polarized circular slit planar antenna for vehicular satellite applications," *Applied Computational Electromagnetics Society Journal*, vol. 34, no. 9, pp. 1340-1345, Sep. 2019.

[15] M. Simone, A. Fanti, L. Boccia, G. Amendola, and G. Mazzarella, "A dual polarized stacked antenna for 5G mobile devices," *Photonics & Electromagnetics Research Symposium | Spring (PIERS | SPRING)*, 2019.

[16] M. Simone and N. Curreli, "Design of a multiband WLAN antenna," *Loughborough Antennas and Propagation Conference (LAPC). IEEE*, 2014.

[17] G. S. Karthikeya, M. P. Abegaonkar, and S. K. Koul, "Low cost high gain triple band mmwave Sierpinski antenna loaded with uniplanar EBG for 5G applications," *IEEE International Conference on Antenna Innovations & Modern Technologies for Ground, Aircraft and Satellite Applications*, 2017.

[18] P. Bhartia, I. Bahl, R. Garg, and A. Ittipiboon, *Handbook of Microstrip Antennas Design*. Norwood: Artech House, 2001.

Design and Comparative Analysis of Ultra-wideband and High Directive Antennas for THz Applications

Ali Yahyaoui [1], Jawad Yousaf [2], Amira Dhiflaoui [3], Majid Nour [1], Mohamed Zarouan [1], Mohammed Aseeri [4], and Hatem Rmili [1]

[1] Electrical and Computer Engineering Department, Faculty of Engineering, King Abdulaziz University
P.O. Box 80204, Jeddah 21589, Saudi Arabia
hmrmili@kau.edu.sa

[2] Department of Electrical, Computer and Biomedical Engineering, Abu Dhabi University, United Arab Emirates

[3] University of Tunis El Manar (UTM), National Engineering School of Tunis (ENIT)
Communications Systems Laboratory (SysCom), BP 37, Belvédère 1002 Tunis, Tunisia

[4] National Center for Telecommunications and Defense System Technologies (TDST)
King Abdulaziz City of Science and Technology (KACST), Riyadh, Saudi Arabia

Abstract ─ This work presents a comprehensive detailed comparative study of the three ultra-wideband and high directive antennas for the THz imaging, spectroscopy, and communication applications. Three different types of photoconductive antennas (log-spiral, Vivaldi, and bowtie antennas) are designed and simulated in the frequency range of 1 to 6 THz in the CST microwave studio (MWS). The enhanced directivity of the designed PCAs is achieved with the integration of the hemispherical silicon-based lens with the PCA gold electrode and quartz substrate of the proposed antennas. The performance of the designed PCAs is compared in terms of impedance and axial ratio bandwidths, directivity, and radiation efficiency of the proposed antennas. The reported log spiral, Vivaldi PCAs with added silicon lens exhibit the -10 dB impedance bandwidth of 6 THz, 3dB AR bandwidth of 5 THz, 6 THz, and 6 THz and peak total radiation efficiencies of 45%, 65%, and 95% respectively.

Index Terms ─ Bowtie antenna, high directivity, log spiral antenna, photoconductive THz antenna, Vivaldi antenna, wideband.

I. INTRODUCTION

The development of the terahertz (THz) technology is helping to alleviate the crowded microwave band spectrum for the wide range of future applications in the field of high-speed (terabit-per-second) wireless communication system, spectroscopy, imaging, sensing, material characterization, and medical fields [1-7]. The 3 mm to 30 μm free-space wavelength (or 0.1 to 10 THz) band is referred to as the THz frequency band. This band is gaining a lot of attention because of the distinctive characteristics of the non-ionizing nature of THz radiations, easy penetration through various materials, and their minimal effect on the human body [4, 7-9].

The photoconductive antennas (PCAs) are among the favorite choices of the THz antenna designers for the generation of THz radiations due to their associated advantages of broadband radiations, compact size as well as normal operation at the room temperature [8, 10, 11]. In PCA, THz waves are generated with the interaction of the ultrafast femtosecond photon with the biased photoconductive substrates having ultra-short (sub-picosecond) carrier lifetime as well as ultrafast carrier mobility. The common examples of used substrates for this purpose are LTGaAs [10, 12, 13], SiGaAs [10, 14], and InGaAs [10, 15]. Besides the aforementioned advantages, the limitation of the PCA includes the low optical-to-THz conversion efficiency [4, 8] which limits its applications especially for the imaging systems which demands high directive and polarization-insensitive THz radiations.

The commonly employed approaches for the enhancement of the laser coupling to increase the conversion efficiency of the PCAs are 3D nonplasmonic structures [16], anti-reflection coatings of PCA substrates [17, 18], plasmonic nanoantennas [19] and electrodes [20]. The requirements of the electron beam lithography for the fabrication of the PCAs using proposed approaches [16-20] significantly increase the time and cost of the fabrication process [4]. The reported other examples of the photoconductive antennas are bow tie [8, 11, 17, 21], dipole planner array [22], Yagi-Uda [23], spiral-shaped [24], and the conical horn [25]. The researchers used the microlens array [12, 13, 17, 21, 26, 27], adding of the

Submitted On: July 8, 2020
Accepted On: December 31, 2020
https://doi.org/10.47037/2020.ACES.J.360311

silicon-based lenses on the PCA structures [8, 17, 21, 25, 28], and sandwiching of an antenna structure with metasurfaces [8, 22] for the enhancement of the poor directivity performance of the designed THz antennas. Although the utilization of the aforementioned approaches results in the enhancement of the directivity of the realized antennas, the reported designs [8, 11, 17, 21-25, 28, 29] have limitations of lower impedance bandwidth (0.2 THz to 1 THz), axial ratio (AR) bandwidth, and overall large size of reported antenna designs.

In this work, we report a detailed comparative study about the design and analysis of the three different types of the ultra-wideband, high directive, and high-efficiency PCAs for the frequency range of the 1 to 6 THz. The realized antenna designs are of log spiral [6] (Fig. 1), Vivaldi [7] (Fig. 2), and bowtie [9] (Fig. 3) types. The full-wave EM simulation of the proposed THz antennas is performed in CST MWS for the frequency range of 1 to 6 THz without the lens. Subsequently, the directivity performance of the proposed antennas is enhanced by adding a silicon-based hemispherical lens on the backside of the used quartz ($\varepsilon_r = 3.78$, $\tan\delta = 0.0001$) substrate of the antennas. The study compares the performance of the reported antennas in terms of impedance bandwidth, axial ratio bandwidth, and radiation characteristics (gain, directivity, efficiency) of the antennas. The reported log spiral, Vivaldi, and bowtie PCAs exhibit the -10 dB impedance bandwidth of 6 THz respectively. The observed 3dB AR bandwidth is 5 THz, 6 THz, and 6 THz for the designed spiral, Vivaldi, and bowtie antenna structure with the lens. The peak values of the total radiation efficiencies for the realized spiral, Vivaldi, and bowtie antenna structure with the lens are 45%, 65%, and 95% respectively. The observed -10 dB impedance and 3-dB AR bandwidth of the designed optimized antenna with the lens are the largest among all the reported legacy designs [8, 11, 17, 21-25, 28, 29] as per our best knowledge.

The structure of the rest of the paper is as follows. Section II presents a comprehensive review of the performance of the legacy THz antennas. The details about the design of the reported three antennas are described in Section III. Section IV details the comparison of the performance of the reported antennas without the lens. The comparison of the designed antennas performance with the added lens in the antenna structure is presented in Section V. Last section VI concludes the study.

II. RELATED WORK

This section presents a comprehensive review of the relevant reported designs of the non-nano based PCA antenna designs. The authors in [23] reported a Yagi-Uda antenna without a lens with high input impedance in the frequency range of 580 GHz to 600 GHz. The design of a spiral-shaped THz antenna working in the frequency range of 1.8 – 2.05 THz is reported in [24]. In [11], Park *et al.* covered the antenna structure with metal nanoislands to form nanoplasmonic PCA for the increase in the emission properties of the antenna.

Jyothi *et al.* [21] reported a bow-tie PCA with a Si-hemispherical lens for the enhanced directivity in the frequency range of 1 to 1.2 THz. The authors in [17] investigated the effect of the dielectric coating and added hemispherical Si-lens on bow-tie PCA structure for the enhancement of optical-to-THz conversion efficiency of the designed antenna. The authors in [28] proposed that the utilization of the aspheric lenses can improve the radiation coupling of the PCAs. Deva *et al.* [25] reported a fixed-frequency (0.8 THz) conical horn and Si-lens based PCA for the gain enhancement with the better physical fitting of the horn-shape with commercially available Si-lenses.

In [8, 29], authors combined the PCA with the artificial magnetic conductor (AMC) [8] and metasurface-based flat lens [29] for the enhancement of directivity of the antenna without the need of large-sized silicon-based lenses as needed for [17, 21, 25]. In [22], authors combined the planner dipole array with frequency selective surface to enhance the radiation properties of the array type PCA. However, the integration of the metasurface in the antenna structure increases the side-lobe levels and front-to-back ratio of the antenna. Array design of antennas are used to enhance the radiation efficiency and front to back ratio of the antennas at the cost of the large antenna size [8, 23, 24, 30]. Generally, the periodic structures are used for the enhancement of the antenna bandwidth. However, as reported in [31], the use of a log-periodic circular-toothed structure with an outer diameter of 1.28 mm results in relatively lower bandwidth (< 1 THz). It depicts that the proper designing of the periodic antenna structure is essential to achieve the wideband operation.

Table 1 summarizes the performance of the reviewed designs in terms of the antenna type, used substrate, the material of antenna electrodes, lens, impedance bandwidth, AR bandwidth, and directivity. The maximum impedance bandwidth of 1 THz for the non-lens based THz antenna is reported for the nano THz antenna of [11]. The integration of the lens enhances the directivity to 18.5 dBi for [25] with maximum noted bandwidth of 0.80 THz for the dipole array PCA of [28]. As shown in Table 1, the reported -10 dB impedance bandwidths for the PCA structures with frequency selective surfaces (FSS) are 0.18 THz [8] and 0.37 THz [22], respectively.

The proposed log-spiral, Vivaldi, and bowtie PCAs did not only produce the high directivity but also exhibit wideband impedance and AR bandwidths characteristics as compared to all reviewed legacy designs of [8, 11, 17, 21-25, 28, 29].

Table 1: Comparison of proposed UWB PCA design with the legacy design

References	Antenna Type	Substrate	Antenna Electrode Material	Lens/FSS	-10 dB Impedance Bandwidth (THz)	Maximum Directivity (dBi)
Han [23]	Yagi-Uda	GaAs	Ti-Au	No lens	0.02	10.9
Singh et al. [24]	Spiral-shaped	Si	Al	No lens	0.25	-
Park [11]	Nanoplasmonic bow-tie PCA	GaAs	Cr/Au	No lens	1.00	-
Jyothi [21]	Bow-tie PCA	GaAs	TiAu /AuGe / AuCr	Si hemispherical lens	0.20	10.85
Gupta et al. [17]	Bow-tie PCA with a dielectric coating	SI-GaAs	AuGe	HRFZ-Si lens	-	-
Formanek [28]	Dipole-type PCA	GaAs	Gold	Aspheric lens	0.80	-
Deva [25]	Conical horn	GaAs	-	Si-lens	-	18.5
Zhu [8]	Bow-tie PCA	LT-GaAs	Ti-Au	No lens	0.18	8.0
	Bow-tie PCA			Si hemispherical lens		11.8
	Bow-tie PCA with lens and combined with metasurface superstrate			FSS		11.9
Malhotra [22]	Dipole planner array	LT-GaAs	Ti-Au	FSS	0.37	13.2

III. ANTENNAS DESIGN PROCEDURE

This section details the design procedure of the realized THz antenna types. The first type of the realized antenna is of a log-spiral type which belongs to the class of frequency-independent antennas [32]. The realized antenna as shown in Fig. 1 schematic is designed to obtain wideband impedance characteristics and good pattern efficiency. In Fig. 1, *r2* describes the outer radius of the antenna which limits the lowest operating frequency of the antenna. The flare rate or the growth rate of the spiral for the increment angle (α) is represented by '*a*', and it controls the wrapping nature of the antenna. Table 2 lists the optimized values of the designed parameter of the proposed antenna of Fig. 1.

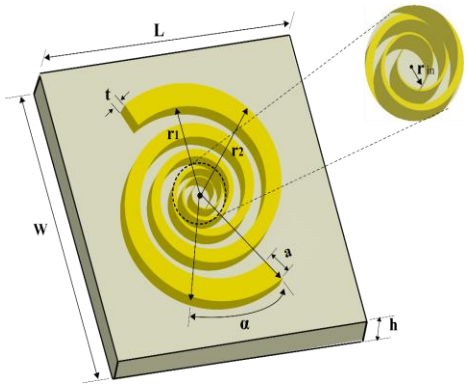

Fig. 1. Schema of the proposed log-spiral THz antenna without lens; *r2*: outer radius of the spiral, *r*: inner radius of the spiral, α: increment angle, *a*: growth rate, *t*: thickness of the conductor (gold) material, *L*: length of the substrate, *W*: width of the substrate, and *h*: thickness of the substrate [6].

Table 2: Log-spiral Antenna design parameters [6]

Parameter	Values(μm)
L (substrate length)	50
W (substrate width)	36
h (substrate thickness)	1
r2 (outer radius of the spiral)	15
r (inner radius of the spiral)	1.03
N (number of turns)	2.5
δ (spiral-patch width)	151
α (increment angle)	12°
a (growth rate)	0.31
t (spiral-patch thickness)	0.05

The Vivaldi antenna structure as shown in Fig. 2 constitutes an exponential curved tapped slot. Besides compact planner structure, the Vivaldi antenna offers additional advantages of the high directive, wider impedance bandwidth, and linear polarization. The exponential tapered profile of the Fig. 2 antenna slot is obtained using the exponential function of (1):

$$f(x) = A\,(e^{ax} - e^{-ax}) + \frac{g}{2}, \tag{1}$$

where

$$A = \frac{\frac{g_2}{2} - \frac{g}{2}}{e^{aL_G} - e^{a}}. \tag{2}$$

In (1), *a* defines curvature coefficient, *g* and g_2 refer to the minimum and maximum width of the tapered slot respectively, and L_G is the length of the antenna patch. Table 2 summarizes the optimized design parameters of the proposed ultra-wideband and high directive Vivaldi antenna for the THz range.

The proposed antenna design of the bowtie THz antenna is shown in Fig. 3. The values of the design parameters of the Fig. 3 antenna are shown in Table 4.

The optimized values of the designed antennas parameters of Tables 2, 3, and 4 are obtained after the detailed conducted parametric study for each antenna type.

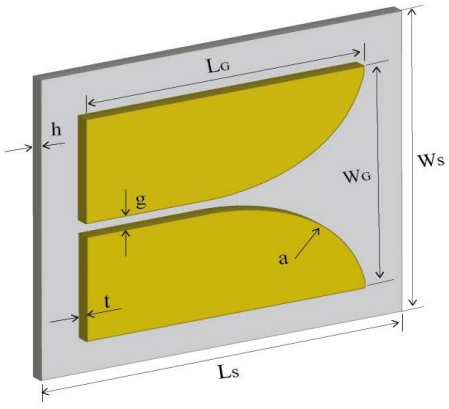

Fig. 2. Schematic of the designed Vivaldi THz antenna without lens: L_S: substrate length, W_S: substrate width, h: substrate thickness, L_G: length of Vivaldi patch, W_G: width of Vivaldi patch, g: minimum width of the tapered slot, a: curvature coefficient, and t: thickness of the Vivaldi patch [7].

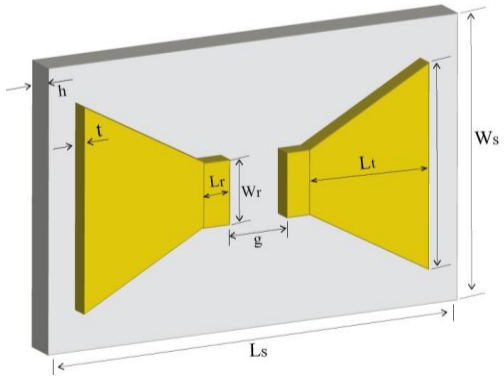

Fig. 3. Schematic of the designed bowtie THz antenna without lens: L_S: substrate length, W_S: substrate width, h: substrate thickness, L_t: length of bowtie patch, g: gap between the bowtie patches, and t: thickness of the bowtie patch [8].

Table 3: Vivaldi Antenna design parameters

Parameter	Values(μm)
L_S (substrate length)	134
W_S (substrate width)	60
h (substrate thickness)	3
L_G (Vivaldi-patch length)	120
W_G (Vivaldi-patch width)	20
g (Minimum width of the tapered slot)	0.1
g_2 (Maximum width of the tapered slot)	22
a (curvature coefficient)	0.7
t (Vivaldi-patch thickness)	0.05

Table 4: Bowtie Antenna design parameters [8]

Parameter	Values(μm)
L_s (substrate length)	347
h (substrate thickness)	2.3
t (bowtie-patch thickness)	0.03
W_s (substrate width)	350
L_t (bowtie-patch length)	117
W_t (bowtie-patch width)	260
W_r (bowtie-port patch length)	13
L_r (bowtie-port patch width)	8
g (gap between the bowtie patches)	3.6

The metal conductor of the designed spiral, Vivaldi, and bowtie antennas has a thickness of 't' and is made of gold conductor (Au) whereas the substrate is made of quartz. The relative permittivity and loss tangent of the used substrate material is 3.78 and 0.0001, respectively. We have used the quartz because of its low-loss characteristics and better capturing of the incident electric fields which is necessary for the high frequencies range operation [33].

The full-wave numerical analysis of the proposed THz antennas is performed in CST MWS for the frequency range of 1 to 6 THz. All antennas are excited using a discrete port in CST MWS. We have used the three-dimensional full-wave electromagnetic field finite integral technique (FIT) available in CST microwave studio-software to precisely calculate. The FIT is a consistent discretization for Maxwell's-equations and it provides a spatial discretization scheme applicable to several electromagnetic problems. The matrix of the discretized fields can be used for efficient simulations. The full-wave numerical simulation of the antennas is performed for the analysis of the antenna's impedance, axial ratio, current distribution, and radiation characteristics.

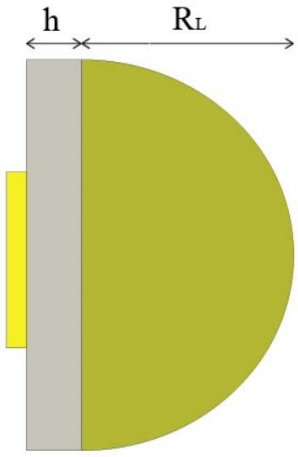

Fig. 4. Schema of the designed spiral THz antenna with hemispherical lens having diameter of R_L [6].

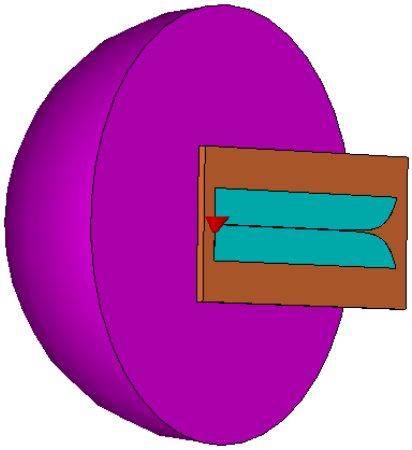

Fig. 5. Schema of the designed Vivaldi THz antenna with hemispherical lens having diameter of R_L [7].

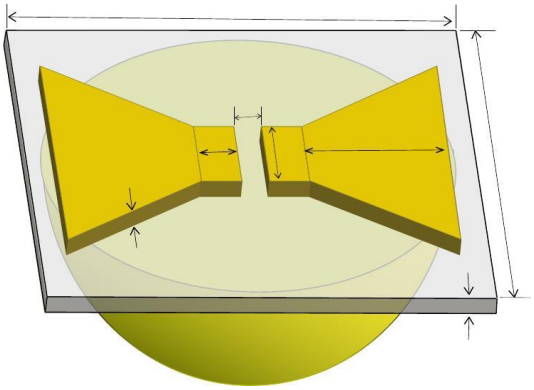

Fig. 6. Schema of the designed bowtie THz antenna with hemispherical lens having diameter of R_L [8].

The analysis of the change in the designed antennas performances is performed by adding hemispherical lenses of silicon on each antenna structure. Figures 4, 5, and 6 depicts the schematics of the antenna structures with the added silicon lens. The diameter (R_L) of the lens is optimized to obtain the wideband impedance, axial ratio bandwidth, and to produce high directivity, gain, and total efficiency of the designed THz antennas. The obtained optimized values of the R_L for spiral, Vivaldi, and bowtie antenna are 140 µm, 85 µm, and 120 µm respectively.

IV. COMPARISON OF DESIGN ANTENNAS WITHOUT LENS

The performance of the designed THz antennas of Figs. 1, 2, and 3 is compared for their -10 dB impedance bandwidth (for $|S_{11}| <$ -10 dB), directivity, maximum directivity, total efficiency, realized gain, total efficiency, and axial ratio characteristics.

Figure 7 shows the comparison of the reflection characteristics of the designed THz antennas. The results show that all three antenna exhibit ultra-wideband impedance matching properties as the $|S_{11}|$ is less than -10 dB for the entire analyzed frequency range of 1 to 6 THz for the spiral and Vivaldi antennas. The -10 dB impedance bandwidth of the realized bowtie antenna is around 2 THz as shown in Fig. 7.

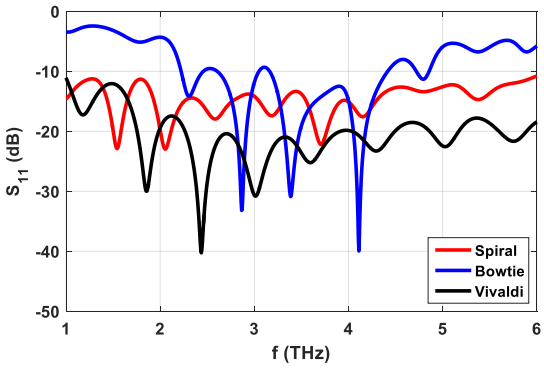

Fig. 7. Comparison of reflection characteristics of the designed THz antennas.

The directivity and maximum directivity results of all three antennas are shown in Figs. 8 and 9 respectively. The comparison reflects that a log-spiral antenna has the best performance as its directivity is higher than the other antenna types as shown in Fig. 8. The results of Fig. 8 reflect that the directivity of all three realized antennas has some variations with the increase in the frequency. The maximum directivity of 10.2 dBi is noted for the Vivaldi antenna as depicted in Fig. 9.

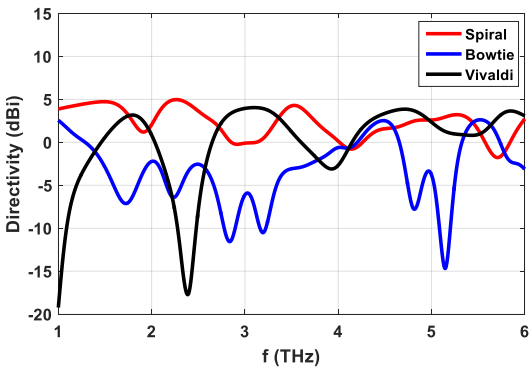

Fig. 8. Comparison of directivity of the designed THz antennas.

Figure 10 shows that the total efficiency of the bowtie antenna is higher than the other two antenna types. The observed total efficiency of the bowtie antenna is higher than 60% in the frequency range of 2.2 THz to 4.9 THz and > 70% efficiency from 2.3 THz to 4.4 THz. The spiral antenna shows good performance with almost flat > 50% total efficiency in the entire analyzed frequency band. The Vivaldi antenna total efficiency is

greater than 10% from 2.2 THz to 6 THz range.

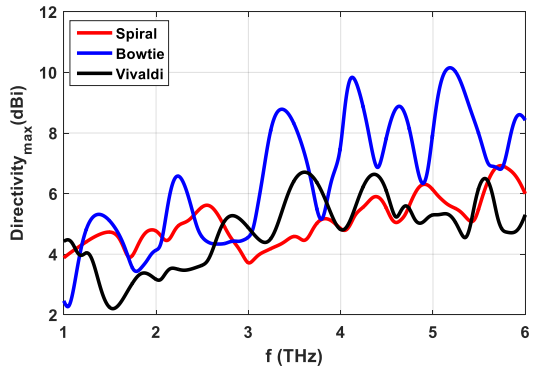

Fig. 9. Comparison of maximum directivity of the designed THz antennas.

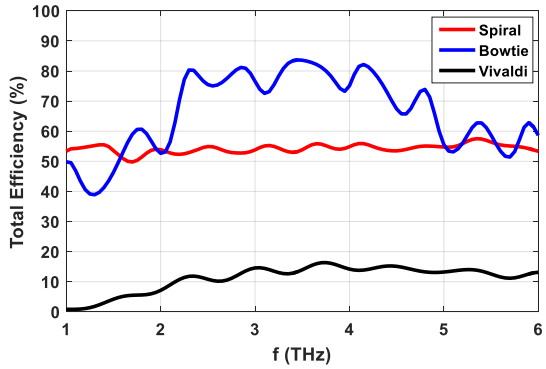

Fig. 10. Comparison of total efficiency of the designed THz antennas.

The difference in the realized gain of the three designed antennas is illustrated in Fig. 11. The realized gain of the spiral antenna is around 0 dBi in the entire frequency range of 1 to 6 THz. The bowtie antenna has realized gain of > -10 dBi in almost whole frequency band of 1 to 6 THz while the Vivaldi antenna shows a similar performance of > -10 dBi realized gain as like bowtie antenna in the frequency range of 2.6 THz to 6 THz. The comparison of results shows that the realized gain of spiral THz antenna is relatively flatter as compared to the other antennas gain characteristics.

Figure 12 reflects the comparison of the axial ratio variations of the spiral, bowtie, and Vivaldi antennas. The AR of the spiral antenna shows that antennas show good circular polarization characteristics from 2 THz to 6 THz frequency range as its AR is less than 3 dB in this frequency band. On the other hand, the other two designed antennas (bowtie and Vivaldi) show very good linear polarization performance with 6 THz AR bandwidth as depicted in Fig. 12. The difference between the AR and impedance bandwidth properties of the spiral antenna could be attributed to the reflections from the end arm of the antenna. The polarizing sense of the reflected waveform is opposite of the outward traveling wave polarization sense and it impacts the lower frequency AR characteristics for the case of the log-spiral antenna as can be noted from the Fig. 12 results.

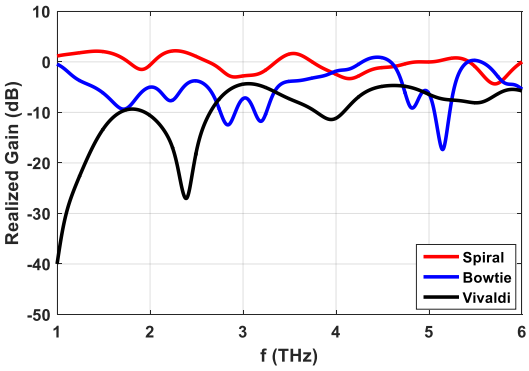

Fig. 11. Comparison of realized gain of the designed THz antennas.

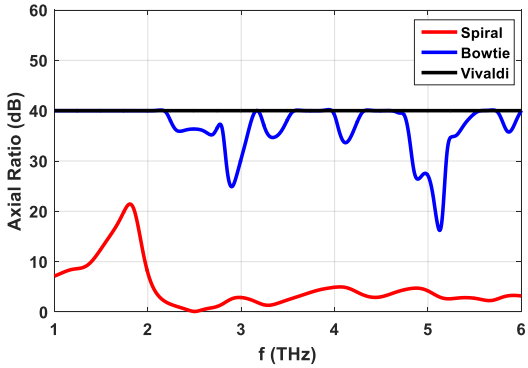

Fig. 12. Comparison of axial ratio of the designed THz antennas.

Figure 13 (a) shows the far-field radiation patterns of the designed spiral antenna at the resonance frequencies of 1.55 THz, 2.05 THz, 3.7 THz, and 5.4 THz respectively. The far-field radiation patterns for the Vivaldi antenna at the resonance frequencies of 1.85 THz, 2.45 THz, 3.6 THz, and 5 THz are shown in Fig. 13 (b). Figure 13 (c) depicts the far-field radiation pattern of the realized bowtie PCA at the resonance frequencies of 2.3 THz, 2.85 THz, 3.35 THz, and 4.1 THz respectively. The spiral and Vivaldi antennas radiation pattern shows an omnidirectional pattern at lower frequencies which changes directional pattern with higher directivity as the frequency increase. The observed gain of the spiral antenna at 1.55 THz and 5.4 THz is 4.68 dBi and 5.11 dBi respectively. The increase in the gain of the Vivaldi antenna from 1.85 THz to 3.6 THz is 3.33 dBi as the observed gain at 1.85 THz and 3.6 THz is 3.38 dBi and 6.71 dBi respectively. As expected, the directional

antenna characteristics for the bowtie antenna can be noted from the directional far-field radiation patterns of the bowtie antenna in Fig. 13 (c). It can be noted that the gain of the bowtie antenna at 2.3 THz and 4.1 THz is 6.33 dBi and 9.8 dBi respectively.

The comparison of Figs. 7-12 results illustrates that all designed antenna shows excellent performance in terms of the impedance and AR bandwidth as compared to all reported antenna structures in [8, 11, 17, 21-25, 28, 29].

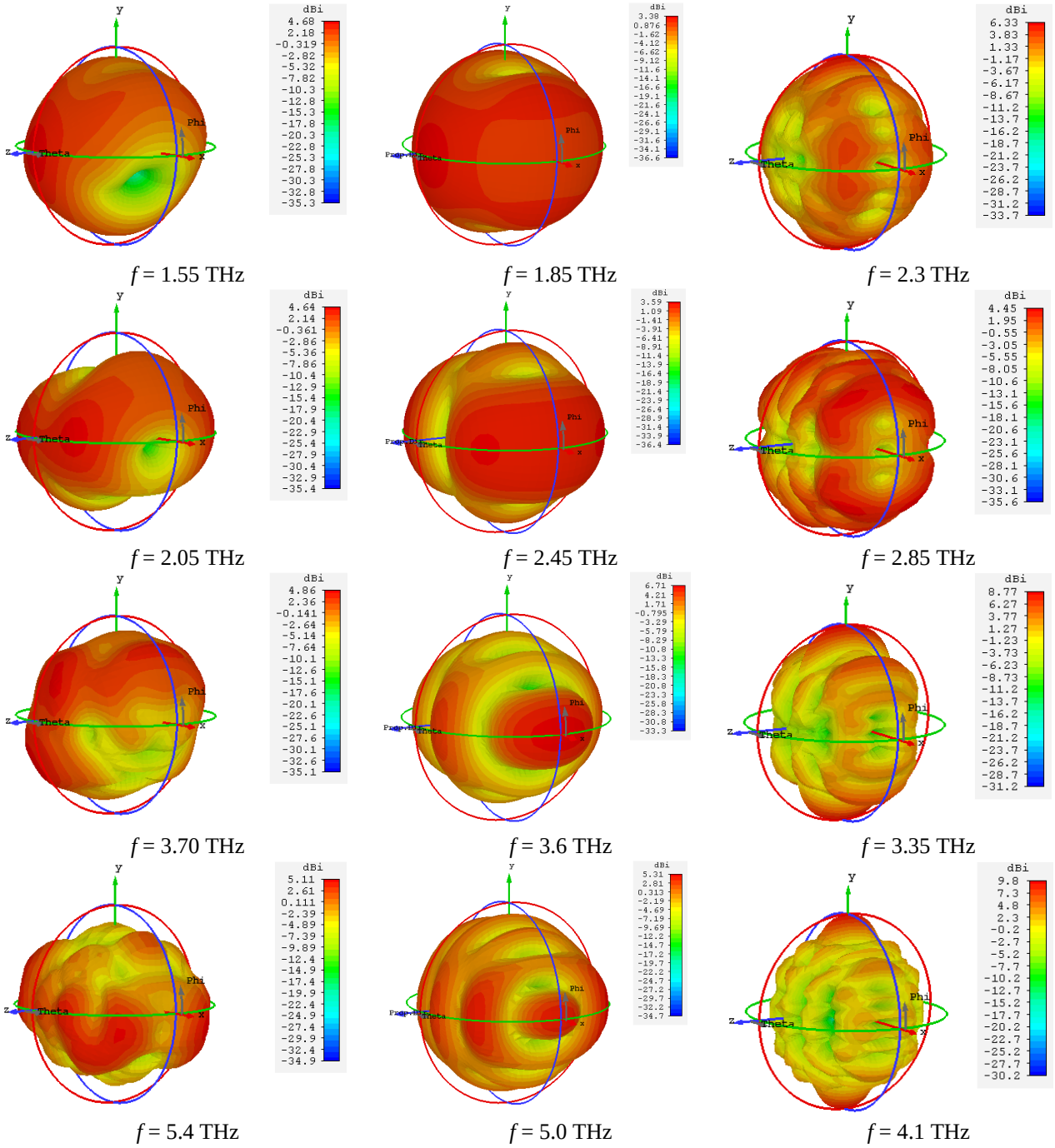

Fig. 13. Comparison of far field radiation patterns of analyzed PCAs without lens.

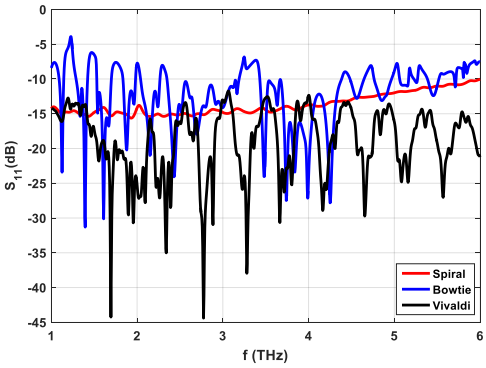

Fig. 14. Comparison of reflection parameter of the designed THz antennas with lens.

V. COMPARISON OF DESIGN ANTENNAS WITH LENS

The performance of the designed spiral, Vivaldi, and bowtie THz antennas is also compared with the integration of the hemispherical lens in the antenna structures. Figures 3-6 depict the structure of antennas with the added lenses.

The comparison of the reflection parameters of the antennas for Figs. 3-6 designs is shown in Fig. 14. It can be noted from Fig. 14 that the addition of the lens in the antenna structure brings a significant change in the resonance characteristics of the antennas. The S_{11} of the spirals antenna becomes flattered with the addition of the lens as compared to the reflection parameter waveform of the same antenna (see Fig. 7). The modification of the bowtie PCA structure for the added lens brings a lot of improvement in its reflection parameters as compared to its characteristics without a lens. The comparison of Figs. 14 and 7 results illustrates that the impedance matching of the designed antenna improves with the addition of the lens in the antenna structure as we are getting lower values of the antenna input reflections. The increase of the intensity of the current distribution around the source point and fewer reflections from the antenna arms results in the better impedance characteristics of the antennas as illustrated in Fig. 14. The results of Fig. 14 deduce that now spiral and Vivaldi antennas exhibit ultra-wideband impedance bandwidth of 6 THz as their reflection properties are less than -10 dB in the analyzed frequency band of 1 to 6 THz.

Figure 15 depicts the comparison of the directive characteristics of the designed antenna with the modified structures of Figs. 3-6. The comparison of Fig. 15 results with Fig. 13 results reflects that the directivity of the antenna has been improved comprehensively in the entire frequency range of 1 to 6 THz. The addition of the lens significantly improves the antenna directivity in the frequency band of 1 to 4 THz as compared to the without lens results of the same antenna in Fig. 8. Around 40-50% increase in the directive of the spiral antenna is observed in the frequency range of the 1 to 5 THz as compared to the without lens directivity results of the same antenna (see Fig. 8). The best improvement is noted for the bowtie antenna with more than 100% improvement in its directivity with the addition of the lens in its structure. The maximum observed directivity of the spiral, Vivaldi, and bowtie antennas is 12 dBi, 10 dBi, and 14 dBi respectively. The radiation performance of the antennas in terms of its total efficiency was also analyzed with the added lenses. The comparison of the total efficiency results of the three analyzed PCAs is depicted in Fig. 16. We note that the total efficiency of the bowtie is highest too for the integrated lens structures of the antennas. The observed total efficiency of the bowtie antenna is more than 60% in the entire band and > 80% in the frequency range of 2 to 5 THz respectively. The average observed total efficiency of the spiral antenna is around 60% from 3 to 6 THz while 50% for the frequency band of 1 to 3 THz. A little decrease in the spiral antenna efficiency is observed in the low-frequency band of 1 to 3 THz as compared to Fig. 10 results of the same antenna without lens structure. The Vivaldi antenna total efficiency performance is much improved as we can observe the average value of around 40% efficiency for this antenna for the frequency range of 2 to 6 THz from Fig. 16 while the around 15% value was noted for the same antenna from Fig. 10 results. The average improvement in the total efficiency of the antennas with the integration of the lens is around 20%, 10%, and 25% for the bowtie, spiral, and Vivaldi antennas as compared to the without lens results of Fig. 10. The improvement of directivity and total efficiency of the antennas with added lens structures is per the improves radiation properties of the antenna as shown in Fig. 14 results.

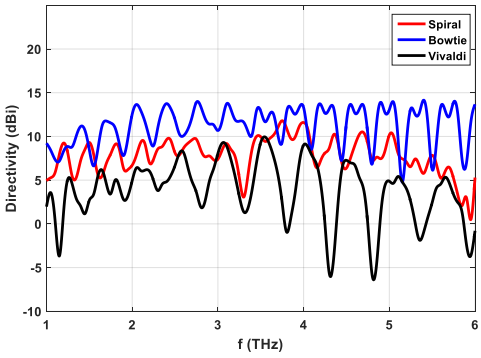

Fig. 15. Comparison of directivity of the designed THz antennas with lens.

The variations in the AR properties of the antennas with added lenses are shown in Fig. 17. The addition of the lens improves the CP characteristics of the spiral antenna in the lower frequency band of 1 to 2 THz while

decorates its performance in a higher frequency region of 5 to 6 THz when compared to the AR characteristics of the same antenna without lens structure in Fig. 12. The AR properties of the Vivaldi antenna remain unchanged while a minor change in the AR variations of the bowtie antenna can be noted as compared to the without lens results of Fig. 12. As like the without lens structure, the performance of the proposed antennas is superior as compared to the legacy designs of [8, 11, 17, 21-25, 28, 29] in terms of -10 dB impedance as well as AR bandwidths.

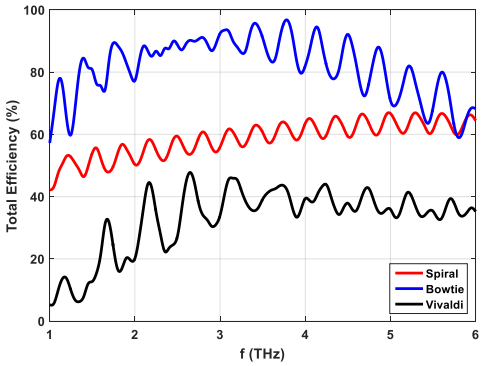

Fig. 16. Comparison of total efficiency of the designed THz antennas with lens.

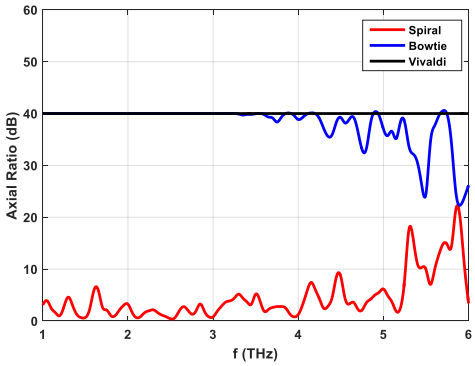

Fig. 17. Comparison of axial ratio of the designed THz antennas with lens.

Figure 18 presents the simulated far-field radiation patterns of the realized PCAs with added lenses in the antenna structures. Figure 18 (a) shows the radiation patterns of the spiral antenna at the resonance frequencies of 1.85 THz, 2.15 THz, 3.45 THz, and 4 THz respectively. It can be noted from Fig. 18 (a) results that the antenna radiation pattern has become directive with the addition of the silicon lens at the backside of the substrate of the designed THz spiral antenna. The observed values of the peak gain at 1.85 THz, 2.15 THz, 3.45 THz, and 4 THz are 9.47 dBi, 10.2 dBi, 10.1 dBi, and 11.3 dBi, respectively. These observed values are greater than the observed gain values from Fig. 13 (a) results.

The simulated far-field radiation pattern at the various resonance frequencies is shown in Fig. 18 (b) for the Vivaldi antenna. The observed values of maximum gain 11.2 dBi @ 1.4 THz, 11.8 dBi @ 2.15 THz, 14.6 dBi @ 4 THz, and 15.3 dBi @ 5.05 THz reflects that the gain of the realized antenna increases with the increase in the operating frequency. These observed gain values are much higher than the recorded gain values for the Vivaldi antenna structure without the lens as depicted in Fig. 13.

The far-field radiations patterns in Fig. 18 (c) for the bowtie antenna reflects that as like the other two antenna types, the gain of the antenna increases due to the directional radiation pattern of the realized antenna structure with the lens. We can note the maximum gain values of 6.75 dBi, 8.39 dBi, 18.6 dBi, and 12.3 dBi for the analyzed resonance frequencies of 1.5 THz, 2.45 THz, 3.05 THz and 4.15 THz respectively for the proposed bowtie antenna.

The comparison of the proposed spiral, Vivaldi, and bowtie antenna structure results with and without lens confirm that the addition of the lens did not only improves the impedance matching and AR properties of the realized antennas but also enhances the directivity of the antennas.

Table 5 summarizes the performance of the proposed antennas in terms of their impedance matching, directivity, and AR bandwidths. The comparison of Tables 1 and 5 results confirms that the proposed antennas impedance, as well as AR bandwidth, is higher than all reported legacy antenna models [8, 11, 17, 21-25, 28, 29] in with/without lens or with frequency selective surfaces.

VI. CONCLUSION

In this study, we reported a detailed comparative study of the performance of the three proposed photoconductive THz antennas. Three different kinds of log spiral, Vivaldi and bowtie PCAs are designed with and without added silicon-based hemispherical lens and their performance in terms of their impedance, as well as AR bandwidth and radiation characteristics (gain, directivity, and efficiency), is compared. The comparison reflects that the designed spiral and Vivaldi PCAs exhibit ultra-wideband impedance bandwidths of 6 THz and bowtie PCA have impedance bandwidth of around 2-3 THz with the added lens in each antenna structure. The bowtie antenna shows superior performance in terms of the high directivity (peak value of 18.2 dBi) and total radiation efficiency (peak value of 95%) as compared to spiral and Vivaldi antennas.

The peak recorded directivity/total radiation efficiencies of the realized spiral and Vivaldi PCAs are 12 dBi/45% and 15 dBi/65%, respectively. The wideband impedance, as well as AR bandwidth and higher radiation characteristics of the proposed THz antennas, makes

them a favorable choice for the wide range of the THz applications (imaging and sensing application, etc.).

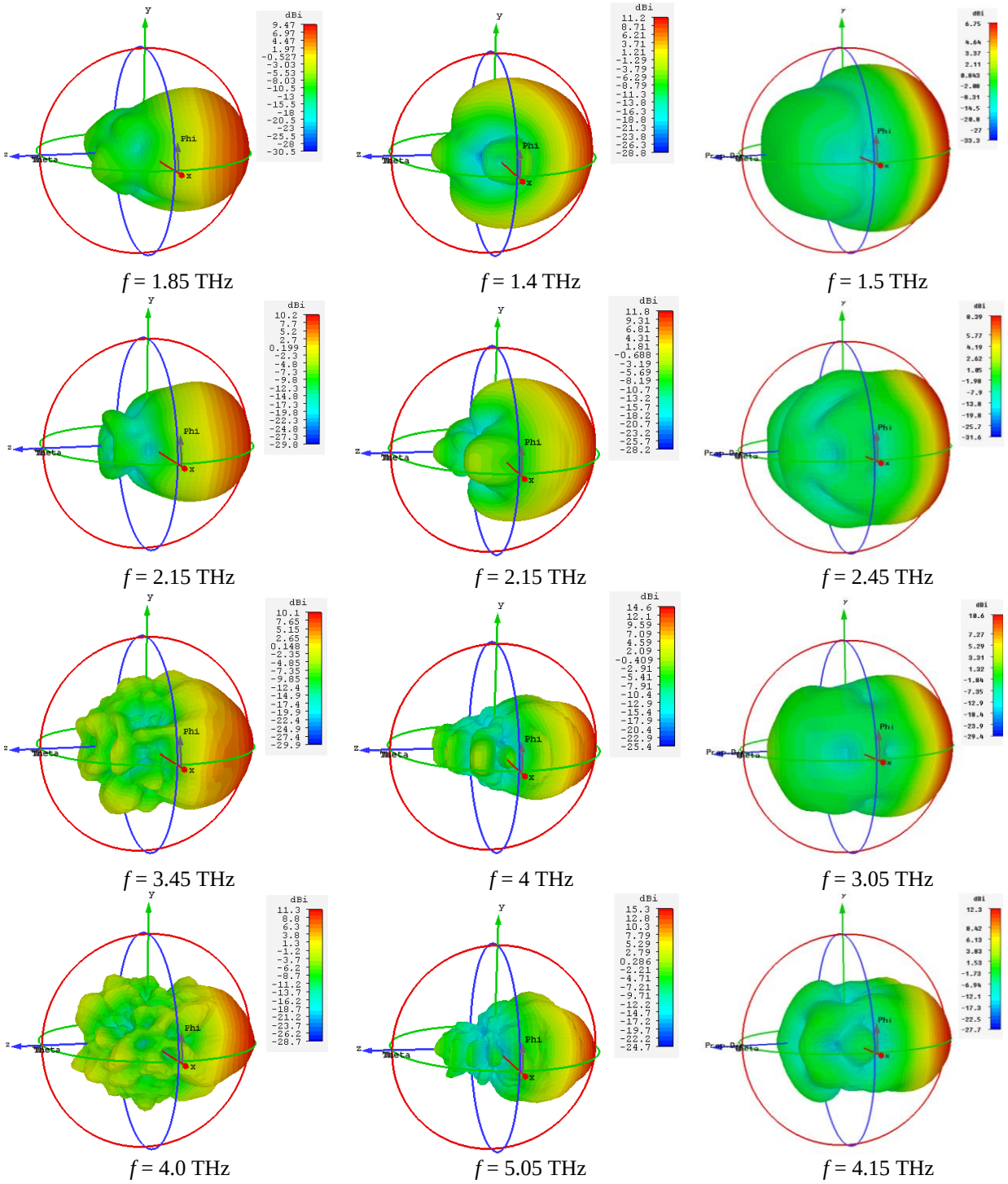

Fig. 18. Comparison of far-field radiation patterns of designed PCAs with lens for different frequencies.

ACKNOWLEDGMENT

The project was funded by the Deanship of Scientific Research (DSR), King Abdulaziz University, Jeddah, Saudi Arabia under grant no. KEP-Msc-6-135-39. The authors, therefore, acknowledge with thanks DSR technical and financial support.

REFERENCES

[1] P. U. Jepsen, D. G. Cooke, and M. Koch, "Terahertz spectroscopy and imaging – Modern techniques and applications," *Laser & Photonics Reviews*, vol. 5, no. 1, pp. 124-166, Jan. 3, 2011.

[2] I. Kasalynas, R. Venckevicius, and G. Valusis, "Continuous wave spectroscopic terahertz imaging with InGaAs bow-tie diodes at room temperature," *IEEE Sensors Journal*, vol. 13, no. 1, pp. 50-54, 2013.

[3] Y. C. Shen, T. Lo, P. F. Taday, B. E. Cole, W. R. Tribe, and M. C. Kemp, "Detection and identification of explosives using terahertz pulsed spectroscopic imaging," *Applied Physics Letters*, vol. 86, no. 24, p. 241116, June 13, 2005.

[4] M. Bashirpour, M. Forouzmehr, S. E. Hosseininejad, M. Kolahdouz, and M. Neshat, "Improvement of terahertz photoconductive antenna using optical antenna array of ZnO nanorods," *Scientific Reports*, vol. 9, no. 1, p. 1414, Feb. 5, 2019.

[5] I. Malhotra, K. R. Jha, and G. Singh, "Terahertz antenna technology for imaging applications: A technical review," *International Journal of Microwave and Wireless Technologies*, vol. 10, no. 3, pp. 271-290, 2018.

[6] A. Dhiflaoui, A. Yahyaoui, J. Yousaf, T. Aguili, B. Hakim, H. Rmili, and R. Mittra, "Full wave numerical analysis of wideband and high directive log spiral THz photoconductive antenna," *International Journal of Numerical Modelling: Electronic Networks, Devices and Fields*, p. e2761.

[7] J. Yousaf, A. Yahyaoui, B. Hakim, M. Zarouan, W. Zouch, T. Aguili, and H. Rmili, "Design and analysis of ultra-wideband and high directive THz photoconductive Vivaldi antenna," *Applied Computational Electromagnetic Society (ACES) Journal*, vol. 35, no. 10, pp. 1242-1254, Oct. 2020.

[8] N. Zhu and R. W. Ziolkowski, "Photoconductive THz antenna designs with high radiation efficiency, high directivity, and high aperture efficiency," *IEEE Transactions on Terahertz Science and Technology*, vol. 3, no. 6, pp. 721-730, 2013.

[9] A. Dhiflaoui, A. Yahyaoui, J. Yousaf, S. Bashir, B. Hakim, T. Aguili, H. Rmili, and R. Mittra, "Numerical analysis of wideband and high directive bowtie THz photoconductive antenna," *Applied Computational Electromagnetic Society (ACES) Journal*, vol. 35, no. 6, pp. 662-672, June 2020.

[10] N. M. Burford and M. O. El-Shenawee, *Review of Terahertz Photoconductive Antenna Technology* (no. 1 %J Optical Engineering). *SPIE*, 2017, pp. 1-20, 2017.

[11] S.-G. Park, Y. Choi, Y.-J. Oh, and K.-H. Jeong, "Terahertz photoconductive antenna with metal nanoislands," *Optics Express*, vol. 20, no. 23, pp. 25530-25535, Nov. 5, 2012.

[12] L. Hou and W. Shi, "An LT-GaAs terahertz photoconductive antenna with high emission power, low noise, and good stability," *IEEE Transactions on Electron Devices*, vol. 60, no. 5, pp. 1619-1624, 2013.

[13] A. Jooshesh, F. Fesharaki, V. Bahrami-Yekta, M. Mahtab, T. Tiedje, T. E. Darcie, and R. Gordon, "Plasmon-enhanced LT-GaAs/AlAs heterostructure photoconductive antennas for sub-bandgap terahertz generation," *Optics Express*, vol. 25, no. 18, pp. 22140-22148, Sep. 4, 2017.

[14] M. Tani, S. Matsuura, K. Sakai, and S.-I. Nakashima, "Emission characteristics of photoconductive antennas based on low-temperature-grown GaAs and semi-insulating GaAs," *Applied Optics*, vol. 36, no. 30, pp. 7853-7859, Oct. 20, 1997.

[15] M. S. Kong, J. S. Kim, S. P. Han, N. Kim, K. Moon, K. H. Park, and M. Y. Jeon, "Terahertz radiation using log-spiral-based low-temperature-grown InGaAs photoconductive antenna pumped by mode-locked Yb-doped fiber laser," *Optics Express*, vol. 24, no. 7, pp. 7037-7045, Apr. 4, 2016.

[16] S. Yang, M. R. Hashemi, C. W. Berry, and M. Jarrahi, "7.5% optical-to-terahertz conversion efficiency offered by photoconductive emitters with three-dimensional plasmonic contact electrodes," *IEEE Transactions on Terahertz Science and Technology*, vol. 4, no. 5, pp. 575-581, 2014.

[17] A. Gupta, G. Rana, A. Bhattacharya, A. Singh, R. Jain, R. D. Bapat, S. P. Duttagupta, and S. S. Prabhu, "Enhanced optical-to-THz conversion efficiency of photoconductive antenna using dielectric nano-layer encapsulation," *APL Photonics*, vol. 3, no. 5, p. 051706, May 1, 2018.

[18] C. Headley, L. Fu, P. Parkinson, X. Xu, J. Lloyd-Hughes, C. Jagadish, and M. B. Johnston, "Improved performance of GaAs-based terahertz emitters via surface passivation and silicon nitride encapsulation," *IEEE Journal of Selected Topics in Quantum Electronics*, vol. 17, no. 1, pp. 17-21, 2011.

[19] S.-G. Park, K. H. Jin, M. Yi, J. C. Ye, J. Ahn, and K.-H. Jeong, "Enhancement of terahertz pulse emission by optical nanoantenna," *ACS Nano*, vol. 6, no. 3, pp. 2026-2031, Mar. 27, 2012.

[20] M. Bashirpour, S. Ghorbani, M. Forouzmehr, M. R. Kolahdouz, and M. Neshat, "Optical absorption enhancement in LTG-GaAs for efficiency improvement of THz photoconductive antennas," in *2016 Fourth International Conference on Millimeter-Wave and Terahertz Technologies (MMWaTT)*, pp. 14-16, 2016.

[21] A. Jyothi, C. Saha, B. Ghosh, R. Kini, and C. Vaisakh, "Design of a gain enhanced THz bow-tie photoconductive antenna," in *2016 International Symposium on Antennas and Propagation (APSYM)*, pp. 1-3, 2016.

[22] I. Malhotra, K. R. Jha, and G. Singh, "Design of highly directive lens-less photoconductive dipole antenna array with frequency selective surface for terahertz imaging applications," *Optik*, vol. 173, pp. 206-219, Nov. 1, 2018.

[23] K. Han, Y. Park, S. Kim, H. Han, I. Park, and H. Lim, "A terahertz Yagi-Uda antenna for high input impedance," in *2008 33rd International Conference on Infrared, Millimeter and Terahertz Waves*, pp. 1-2, 2008.

[24] R. Singh, C. Rockstuhl, C. Menzel, T. P. Meyrath, M. He, H. Giessen, F. Lederer, and W. Zhang, "Spiral-type terahertz antennas and the manifestation of the Mushiake principle," *Optics Express*, vol. 17, no. 12, pp. 9971-9980, June 8, 2009.

[25] U. Deva and C. Saha, "Gain enhancement of photo-conductive THz antenna using conical GaAs horn and Si lens," in *2016 International Symposium on Antennas and Propagation (APSYM)*, pp. 1-3, 2016.

[26] G. Matthäus, S. Nolte, R. Hohmuth, M. Voitsch, W. Richter, B. Pradarutti, S. Riehemann, G. Notni, and A. Tünnermann, "Large-area microlens emitters for powerful THz emission," *Applied Physics B*, vol. 96, no. 2, pp. 233-235, Aug. 1, 2009.

[27] A. Singh and S. S. Prabhu, "Microlensless interdigitated photoconductive terahertz emitters," *Optics Express*, vol. 23, no. 2, pp. 1529-1535, Jan. 26, 2015.

[28] F. Formanek, M.-A. Brun, T. Umetsu, S. Omori, and A. Yasuda, "Aspheric silicon lenses for terahertz photoconductive antennas," *Applied Physics Letters*, vol. 94, no. 2, p. 021113, Jan. 12, 2009.

[29] Q. Yu, J. Gu, Q. Yang, Y. Zhang, Y. Li, Z. Tian, C. Ouyang, J. Han, J. F. O. Hara, and W. Zhang, "All-dielectric meta-lens designed for photo-conductive terahertz antennas," *IEEE Photonics Journal*, vol. 9, no. 4, pp. 1-9, 2017.

[30] B. Pradarutti, R. Müller, W. Freese, G. Matthäus, S. Riehemann, G. Notni, S. Nolte, and A. Tünnermann, "Terahertz line detection by a microlens array coupled photoconductive antenna array," *Optics Express*, vol. 16, no. 22, pp. 18443-18450, Oct. 27, 2008.

[31] R. Mendis, C. Sydlo, J. Sigmund, M. Feiginov, P. Meissner, and H. L. Hartnagel, "Spectral characterization of broadband THz antennas by photoconductive mixing: toward optimal antenna design," *IEEE Antennas and Wireless Propagation Letters*, vol. 4, pp. 85-88, 2005.

[32] V. Rumsey, "Frequency independent antennas," in *1958 IRE International Convention Record, IEEE*, vol. 5, pp. 114-118, 1966.

[33] W. Amara, A. Alghamdi, D. Oueslati, N. Eltresy, M. Sheikh, H. Rmili, "Analysis of infrared nano-antennas material properties for solar energy collection," *Applied Computational Electromagnetic Society (ACES) Journal*, vol. 35, no. 3, pp. 258-266, Mar. 2020.

Radar Cross Section Reduction and Shape Optimization using Adjoint Method and Automatic Differentiation

Ming Li, Junqiang Bai, and Feng Qu

School of Aeronautics
Northwestern Polytechnical University, Xi'an, 710072, China
2014200130@mail.nwpu.edu.cn, junqiang@nwpu.edu.cn, qufeng@nwpu.edu.cn

Abstract ─ An efficient Radar Cross Section (RCS) gradient evaluation method based on the adjoint method is presented. The Method of Moments is employed to solve the Combined Field Integral Equation (CFIE) and the corresponding derivatives computing routines are generated by the program transformation Automatic Differentiation (AD) technique. The differential code is developed using three kinds of AD mode: tangent mode, multidirectional tangent mode, and adjoint mode. The differential code in adjoint mode is modified and optimized by changing the "two-sweeps" architecture into the "inner-loop two-sweeps" architecture. Their efficiency and memory consumption are tested and the differential code using modified adjoint mode demonstrates the great advantages in both efficiency and memory consumption. A gradient-based shape optimization design method is established using the adjoint method and the mechanism of RCS reduction is studied. The results show that the sharp leading can avoid the specular back-scattering and the undulations of the surface could change the phases which result in a further RCS reduction.

Index Terms ─ Adjoint method, automatic differentiation, method of moments, sensitivity, shape optimization.

I. INTRODUCTION

During the last decades, the shape optimization design method has been widely applied to the aircraft design. The scattering response of an object depends on its geometry and materials, as well as the incoming wave characteristics (frequency and polarization). In general, a large number of design variables are required for the shape optimization design due to the fact that the shape of the aircraft is complicated [1]. Using the gradient-based optimization algorithms to deal with this optimization problem is a better choice since they usually converge quickly to a local optimum, regardless of the number of design variables. These algorithms require the gradient of the objective function, therefore the design sensitivity analysis is a vital step in the gradient-based shape optimization.

The adjoint method can obtain the sensitivities with respect to all design variables by solving the adjoint equation once. Due to this advantage, the adjoint method has been developed for Computational Electromagnetics (CEM) techniques, such as the Method of Moments (MoM) [2]-[5], the multilevel fast multipole algorithm (MLFMA) [6], the finite element method [7]-[8], the finite-difference time-domain (FDTD) method[9]-[10], and the transmission line method (TLM) [11]-[12]. Also, it's has been applied to the multidisciplinary optimization design, e.g., the aero-stealth coupled optimization design [1],[13].

The drawback of the adjoint method for the MoM is that the derivatives of the impedance matrix need to be differentiated which might be a complicated task. The derivatives of the impedance matrix can be computed analytically [14]-[16] or obtained by the finite difference method [2]. In [4], the Broyden update of the impedance matrix is used to estimate these derivatives. But in [17], the authors point out that in MoM discretization, the matrix elements can depend on the nodal coordinates of the mesh in a very complicated manner. With very few exceptions, straightforward analytical differentiation of the matrix elements may not be feasible. Moreover, it would require complete reprogramming of the existing codes, which is an insurmountable complication for most researchers and code developers.

An alternative way is computing the derivatives with the help of the automatic differentiation (AD) technique [18]-[19]. Using the AD tools to develop code is much more efficient and time-saving, and is suitable for dealing with these error-prone tasks. Toivanen et al. [18] demonstrate how sensitivity analysis can be incorporated into an existing in-house MoM solver with a relatively small amount of labor by using the automatic differentiation technique.

In this paper, an RCS gradient calculation approach based on the adjoint approach of Maxwell's integral equation is presented. The MoM solver is employed in the solution of the scattering problem. We adopt a parallel LU factorization driver routine of ScaLAPACK [20] to solve the Combined Field Integral Equation (CFIE). Both the current coefficient and the adjoint

Submitted On: October 28, 2020
Accepted On: February 1, 2021

https://doi.org/10.47037/2020.ACES.J.360312

coefficient would be obtained by factorizing the matrix once. The program transformation AD tool Tapenade [21] is applied to analyze the functions and subroutines of the MoM and generate the corresponding differential code. As for the derivatives of the impedance matrix computing routine, we develop the code in three different AD modes: tangent mode, multidirectional tangent mode, and adjoint mode. And then their accuracy, efficiency, and memory consumption are tested. After that, a gradient-based shape optimization design method is established by coupling the MoM, the adjoint method, the Free-Form Deformation approach (FFD)[22], and the Sequential Quadratic Programming algorithm (SQP) [23]. Finally, we apply this method to optimize an almond geometry and study the mechanism of RCS reduction.

The main objective, and the novel nontrivial contribution, of this paper, is that we modify and optimize the adjoint AD code and make it more efficient and less consumed by changing the "two-sweeps" architecture into an "inner-loop two-sweeps" architecture.

This paper is organized as follows. In Section II, the discrete adjoint equation of the integral form of the Maxwell equation based on the MoM is derived. In Section III, the derivative computing routines developed in three AD modes are presented, and the "inner-loop two-sweeps" architecture of the adjoint AD mode is discussed. Next, the flow chart of the gradient-based shape optimization design method and the numerical methods employed in the optimization framework are described in Section IV. After that, in Section V, the accuracy of the gradient is validated using the finite difference method. Besides, the CPU time and the memory consumption of three AD modes are tested. The benchmark geometry almond is optimized using the method described in this paper and the mechanism of RCS reduction is studied. Finally, the conclusions are summarized in Section VI.

II. ADJOINT METHOD

Consider a three-dimensional scattering problem where the Radar Cross Section (RCS) is defined by:

$$\sigma = 4\pi \lim_{R\to\infty} R^2 \frac{\left|\boldsymbol{E}_{\mathrm{s}}\right|^2}{\left|\boldsymbol{E}_{\mathrm{i}}\right|^2}, \tag{1}$$

where $\boldsymbol{E}_{\mathrm{s}}$ and $\boldsymbol{E}_{\mathrm{i}}$ are the scattered and incident electric field at the distance R. The scattered electric field is given by:

$$\boldsymbol{E}_{\mathrm{s}} = -\mathrm{j}k\eta \int_S \left[\boldsymbol{J}G + \frac{1}{k^2}\nabla\cdot\boldsymbol{J}\nabla G \right] dS, \tag{2}$$

where η refers to the wave impedance and k means the wavenumber. And G means the Green's function. Only the surface current $\boldsymbol{J}$ is unknown. The Rao–Wilton–Glisson (RWG) [24] basis function is adopted to discretize the surface current and then it could be expanded into a sum of N weighted basis function as shown in Eq. (3):

$$\boldsymbol{J} \cong \sum_{n=1}^{N} I_n \boldsymbol{f}_n(\boldsymbol{r}), \tag{3}$$

where $\boldsymbol{I}$ is the current coefficient and $\boldsymbol{f}_n(\boldsymbol{r})$ denotes the basis function. According to the Method of Moments, the solution of the CFIE with the Galerkin method leads to the solution of the linear system:

$$\boldsymbol{Z}\boldsymbol{I} = \boldsymbol{V}, \tag{4}$$

where $\boldsymbol{Z}$ is the impedance matrix, and $\boldsymbol{V}$ is the excitation vector. In this paper, the parallel LU factorization driver routine of ScaLAPACK[20] is applied to solve the linear system. When the parameters of the incident wave including frequency, direction, and polarization mode are given, the scattered electric field and RCS only depend on the target surface and the induced current. The derivative of the scattered electric field is given by:

$$\frac{d\boldsymbol{E}_{\mathrm{s}}}{d\boldsymbol{X}} = \frac{\partial \boldsymbol{E}_{\mathrm{s}}}{\partial \boldsymbol{X}} + \frac{\partial \boldsymbol{E}_{\mathrm{s}}}{\partial \boldsymbol{I}}\frac{d\boldsymbol{I}}{d\boldsymbol{X}}, \tag{5}$$

where $\boldsymbol{X}$ means the nodal coordinates of the target mesh. This derivative is also called the surface sensitivity, which represents the sensitivity of the scattered electric field to changes in the surface geometry. It would be of particular use for retrofitting the device on an existing object geometry where a whole new design is not feasible. Assume that the residual of the matrix equation is equal to zero:

$$\boldsymbol{R} = \boldsymbol{Z}\boldsymbol{I} - \boldsymbol{V} = 0. \tag{6}$$

The shape derivatives of the residual depend on the geometry surface and the surface current solution, that is:

$$\frac{\partial \boldsymbol{R}}{\partial \boldsymbol{X}} + \frac{\partial \boldsymbol{R}}{\partial \boldsymbol{I}}\frac{d\boldsymbol{I}}{d\boldsymbol{X}} = 0. \tag{7}$$

It is intensely inefficient to calculate the term d$\boldsymbol{I}$/d$\boldsymbol{X}$ directly since that would require a mass of the MoM evaluations. Therefore we rewrite Eq. (7) as:

$$\frac{d\boldsymbol{I}}{d\boldsymbol{X}} = -\left[\frac{\partial \boldsymbol{R}}{\partial \boldsymbol{I}}\right]^{-1}\frac{\partial \boldsymbol{R}}{\partial \boldsymbol{X}}. \tag{8}$$

Replacing the term d$\boldsymbol{I}$/d$\boldsymbol{X}$ in Eq. (5) and we obtain:

$$\frac{d\boldsymbol{E}_{\mathrm{s}}}{d\boldsymbol{X}} = \frac{\partial \boldsymbol{E}_{\mathrm{s}}}{\partial \boldsymbol{X}} - \frac{\partial \boldsymbol{E}_{\mathrm{s}}}{\partial \boldsymbol{I}}\left[\frac{\partial \boldsymbol{R}}{\partial \boldsymbol{I}}\right]^{-1}\frac{\partial \boldsymbol{R}}{\partial \boldsymbol{X}}. \tag{9}$$

And the adjoint variable vector $\boldsymbol{\psi}$ is defined as:

$$\boldsymbol{\psi}^{\mathrm{T}} = \frac{\partial \boldsymbol{E}_{\mathrm{s}}}{\partial \boldsymbol{I}}\left[\frac{\partial \boldsymbol{R}}{\partial \boldsymbol{I}}\right]^{-1}. \tag{10}$$

According to Eq. (6), the derivative of residual with respect to the surface current coefficient is just the impedance matrix:

$$\frac{\partial \boldsymbol{R}}{\partial \boldsymbol{I}} = \frac{\partial(\boldsymbol{Z}\boldsymbol{I} - \boldsymbol{V})}{\partial \boldsymbol{I}} = \boldsymbol{Z}. \tag{11}$$

Thus, the adjoint equation is written as:

$$\boldsymbol{Z}^{\mathrm{T}}\boldsymbol{\psi} = \left[\frac{\partial \boldsymbol{E}_{\mathrm{s}}}{\partial \boldsymbol{I}}\right]^{\mathrm{T}}. \tag{12}$$

We do not need to solve the adjoint equation

anymore since the matrix $\boldsymbol{Z}$ has been already factorized into upper and lower triangular matrices for the scattering problem. Finally, the surface sensitivity of RCS could be computed by:

$$\frac{d\sigma}{d\boldsymbol{X}} = \frac{d\sigma}{d\boldsymbol{E}_s}\frac{d\boldsymbol{E}_s}{d\boldsymbol{X}} = \frac{d\sigma}{d\boldsymbol{E}_s}\left(\frac{\partial \boldsymbol{E}_s}{\partial \boldsymbol{X}} - \boldsymbol{\psi}^T \frac{\partial \boldsymbol{R}}{\partial \boldsymbol{X}}\right). \tag{13}$$

The Free-Form Deformation (FFD) approach [22] is adopted to parameterize the geometry and manipulate the mesh. It's more efficient to change the shape through the FFD volume than to modify the surface mesh directly. The surface mesh of the object is embedded inside the FFD volume, and all changes of the surface mesh are performed on the outer boundary of the FFD volume. Any modification of the boundary of FFD volume can be applied to indirectly modify the embedded surface mesh. The displacements of the FFD control points are selected as the design variables $\boldsymbol{x}$. And then the gradient required from the gradient-based optimization algorithm is easily obtained:

$$\frac{d\sigma}{d\boldsymbol{x}} = \frac{d\sigma}{d\boldsymbol{X}}\frac{d\boldsymbol{X}}{d\boldsymbol{x}}. \tag{14}$$

The code can be developed with $d\sigma / d\boldsymbol{X}$ (geometry nodal derivatives) or $d\sigma / d\boldsymbol{x}$ (control point derivatives). If the surface sensitivity analysis is required, the code must be developed with $d\sigma / d\boldsymbol{x}$. And then the gradient of the cost function is obtained by multiplying the surface sensitivity with $d\boldsymbol{X} / d\boldsymbol{x}$. When using the AD tools to differentiate the code in tangent mode, it's suitable to develop the code with $d\sigma / d\boldsymbol{x}$ directly:

$$\frac{d\sigma}{d\boldsymbol{x}} = \frac{d\sigma}{d\boldsymbol{E}_s}\left(\frac{\partial \boldsymbol{E}_s}{\partial \boldsymbol{x}} - \boldsymbol{\psi}^T \frac{\partial \boldsymbol{R}}{\partial \boldsymbol{x}}\right). \tag{15}$$

When the code is differentiated in adjoint mode, we can develop the code with either $d\sigma / d\boldsymbol{X}$ or $d\sigma / d\boldsymbol{x}$. The differences between the tangent mode and the adjoint mode of the AD technique would be discussed in the next section.

III. AUTOMATIC DIFFERENTIATION TECHNIQUE

Automatic Differentiation technique is developed to differentiate computer programs exactly without large user intervention. It's more efficient and time-saving to apply AD tools to obtain analytical derivatives of differentiable functions, in the case where these functions are provided in the form of a computer program. There are two principal ways to code the algorithm program, namely, *operator overloading* and *program transformation*. We choose the program transformation approach since it allows the tool to apply some global analysis on the program, such as the data-flow, to produce more efficient differentiated code. Tapenade [21] is an AD tool using the program transformation which, given a Fortran or C code that computes a function, creates a new code that computes its tangent or adjoint derivatives.

There are two basic modes of operation for program differentiation: tangent mode and adjoint mode. The tangent mode propagates the sensitivity at the same time as the solution is being computed. The derivative Jacobian is computed column by column, as shown in Fig. 1. Tapenade also provides an advanced tangent mode, called the multidirectional tangent mode. This mode calculates the derivative Jacobian multicolumn by multicolumn. On the contrary, the adjoint mode calculates the Jacobian row by row so that it is extremely efficient to compute the gradient of a function with respect to a large number of design variables.

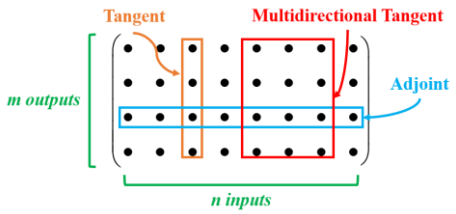

Fig. 1. Elements of the Jacobian computable by tangent mode and adjoint mode.

The crucial task of our work is the computation of residual derivative shown in Eq. (16):

$$\frac{\partial \boldsymbol{R}}{\partial \boldsymbol{X}} = \frac{\partial \boldsymbol{Z}\bar{\boldsymbol{I}}}{\partial \boldsymbol{X}} - \frac{\partial \boldsymbol{V}}{\partial \boldsymbol{X}}, \tag{16}$$

where $\bar{\boldsymbol{I}}$ refers to the current coefficient obtained from the scattering problem. Both of the vectors $\boldsymbol{X}$ and $\boldsymbol{R}$ have a large dimension so that it's extremely time-consuming to calculate the term $\partial \boldsymbol{R} / \partial \boldsymbol{X}$ no matter whether using the tangent mode or the adjoint mode. A feasible way to improve efficiency is computing the term $\partial \boldsymbol{R} / \partial \boldsymbol{x}$ directly instead of $\partial \boldsymbol{R} / \partial \boldsymbol{X}$ due to the fact that the number of design variables is much smaller than the number of coordinate points:

$$\frac{\partial \boldsymbol{R}}{\partial \boldsymbol{x}} = \frac{\partial \boldsymbol{R}}{\partial \boldsymbol{X}}\frac{d\boldsymbol{X}}{d\boldsymbol{x}} = \frac{\partial \boldsymbol{Z}\bar{\boldsymbol{I}}}{\partial \boldsymbol{x}} - \frac{\partial \boldsymbol{V}}{\partial \boldsymbol{x}}. \tag{17}$$

The finite difference method is a popular way to compute derivatives Jacobian since it requires a small amount of code modification. However, the step size has a great influence on the accuracy of the finite difference method. Large step size causes truncation error whereas too small a step size may lead to cancellation error. Also, we find that the appropriate step size changes with the geometric parameterization method, object shape, electromagnetic frequency, and incidence angle. In this section, we discuss the application of AD to a specific in-house MoM solver.

A. Parallel matrix filling algorithm

Before applying the AD tool to differentiate the

code, we should introduce the parallel matrix filling algorithm used in this paper. The pseudo-code of the serial matrix filling algorithm [25] is given in Fig. 5, where N_T denotes the number of triangles. First of all, the coordinates of the target surface are updated through the FFD approach according to the design variables. Next, the serial matrix filling algorithm loops over the field triangles and source triangles, and then performs the integral on each triangle pair, followed by the inner loops over the edges of the triangles. Some computational routines marked in gray show the route of information transfer from the design variables to the impedance matrix. The AD tool would analyze these routines and generate the corresponding derivative computational routines according to the chain rule.

Figure 6 depicts the pseudo-code scheme of the parallel matrix filling algorithm [25]. The modifications and improvements of the parallel matrix filling algorithm are marked in gray. In the parallel matrix filling algorithm, only a portion of the matrix is placed on each process after the computation thus the memory required for each process is reduced. The integral routine "interactions(*p*, *q*, ***X***)" (line 4 in Fig. 5), which compute the interactions between the triangle pair (*p*, *q*), is moved inside the innermost loop over the edge of a source patch (line 15 in Fig. 6). This modification avoids the redundant computations that all the processes calculate all the integrals between a pair of the source and the field triangles. To further reduce the redundancy, some computations of the intermediate data needed in the integration, such as the triangle area and the normal vector, are picked out and moved out of the innermost loop (line 9 in Fig. 6). In Fig. 6, ***v*** denotes the intermediate data. The entire procedure of the parallel matrix filling algorithm is now described.

The coordinates of the surface mesh are computed by the FFD approach, and then the code loops over all the field triangles, the source triangles, the edges on a certain field triangle, and the edges on a certain source triangle. In order to reduce the redundancy in the calculation of the integral, only the process that corresponds to the *m*th row and the *n*th column will calculate the integral over the surfaces of the triangle pair (line 7 to line 21 in Fig. 6). The corresponding processes that are about to calculate the *m*th row and the *n*th column of the matrix are picked up according to the two-dimensional block-cyclic decomposition [26] data distribution required by ScaLAPACK (line 7 and line 12 in Fig. 6). The 4 steps involved in using ScaLapack are now described.

Step 1. Create a Logical Process Grid.

Assume that the MoM solver is running on 6 processes with a 2 × 3 array of process grid layout shown in Fig. 2. The subscript of the symbol ***P*** represents the process number.

	0	1	2
0	$\boldsymbol{P_0}$	$\boldsymbol{P_1}$	$\boldsymbol{P_2}$
1	$\boldsymbol{P_3}$	$\boldsymbol{P_4}$	$\boldsymbol{P_5}$

Fig. 2. The 2 × 3 array of process grid layout.

We could use the routine "Cblacs_gridinit" to set up and initialize a process grid and run the routine "Cblacs_gridinfo" to obtain the process grid information of the current process.

Step 2. Distribute Matrices and Vectors on the Process Grid.

In this significant step, the matrics and vectors are distributed to each process according to the two-dimensional block-cyclic decomposition. The impedance matrix ***Z*** is partitioned into *MB* by *NB* blocks, and the recommended block sizes are 32 × 32 or 64 × 64. An illustration is shown in Fig. 3. The first 3 blocks in the top block row are mapped to the top row of the process grid in order, the next 3 blocks in the top row are also mapped to these same processes, and so on. Similarly, the second block row is mapped to the second grid row. When the 3rd row is reached, the mapping returns back to the first grid row. This mapping method leads to a two-dimensional block-cyclic decomposition shown in Fig. 4.

Z_{11}	Z_{12}	Z_{13}	Z_{14}	Z_{15}	Z_{16}	Z_{17}
Z_{21}	Z_{22}	Z_{23}	Z_{24}	Z_{25}	Z_{26}	Z_{27}
Z_{31}	Z_{32}	Z_{33}	Z_{34}	Z_{35}	Z_{36}	Z_{37}
Z_{41}	Z_{42}	Z_{43}	Z_{44}	Z_{45}	Z_{46}	Z_{47}
Z_{51}	Z_{52}	Z_{53}	Z_{54}	Z_{55}	Z_{56}	Z_{57}
Z_{61}	Z_{62}	Z_{63}	Z_{64}	Z_{65}	Z_{66}	Z_{67}
Z_{71}	Z_{72}	Z_{73}	Z_{74}	Z_{75}	Z_{76}	Z_{77}

Fig. 3. An example of the block matrix construction.

Each process holds a local matrix with several non-contiguous portions of the global matrix. For instance, the process $\boldsymbol{P_1}$ marked in yellow holds blocks from block rows 1,3,5,7 and block columns 2 and 5, while the process $\boldsymbol{P_3}$ marked in green holds blocks from block rows 2, 4, 6 and block columns 1, 4, and 7. We could call the ScaLAPACK routine "descinit" to create a descriptor for this block matrix. After completing the matrix distribution, we can proceed to the next step.

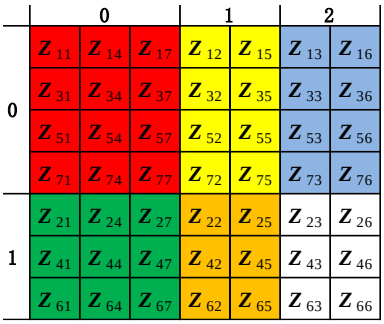

Fig. 4. An example of the two-dimensional block-cyclic decomposition.

Step 3. Call the LU Factorization Routine.

In this step, we call the ScaLAPACK routine "pzgesv" to solve the matrix equation. And then, the impedance matrix $\boldsymbol{Z}$ is replaced by the $\boldsymbol{LU}$ triangular matrix after the factorization, and the excitation vector $\boldsymbol{V}$ is replaced by the current coefficient vector.

Step 4. Release the Process Grid.

Two routines are used after finishing the calculation. A particular process grid is released with the routine "Cblacs_gridexit", and after all the computations are finished, the routine "Cblacs_exit" should be called.

B. Tangent AD

In general, the dimension of residual is far larger than the number of design variables so that it's advisable to code the program using tangent mode. Most of the CPU time is spent on computing the term $\partial \boldsymbol{Z}\bar{\boldsymbol{I}} / \partial \boldsymbol{x}$ since the impedance matrix is a large dimension dense matrix. The corresponding pseudo-code scheme of the derivatives matrix filling algorithm generated by Tapenade using tangent mode is shown in Fig. 7. Some additional routines added by Tapenade are marked in gray. It has an extra loop that loops over the design variables. In the ith cycle, the derivatives of all dependent variables with respect to the ith design variable are calculated. The variable with suffix "_d" represents the derivative of the corresponding variable with respect to the ith design variable and is calculated by the corresponding tangent routines which are suffixed with "_d". These routines are usually executed before the corresponding regular routines. Of particular note that it is unnecessary to compute the coordinates of triangles (line 4 in Fig. 7) in order to reduce the redundancy. We list it here just for the sake of program integrity. The vector $\boldsymbol{x\_d}$ has the same dimension as the design variables and the ith element is set to 1 while the others are set to 0. The vector $\boldsymbol{X\_d}$ means $d\boldsymbol{X}/dx_i$ and the matrix $\boldsymbol{Z\_d}$ refers to $\partial \boldsymbol{Z} / \partial x_i$.

C. Multidirectional tangent AD

Although the derivatives calculation accuracy of tangent AD is higher than that of the finite difference method, there is a shortcoming that reduces its efficiency. As can be seen from Fig. 7, there are masses of redundant calculations at each outermost loop, such as the computations of intermediate data $\boldsymbol{v}$. It should be noted that the subroutines, "temporary(p, q, $\boldsymbol{X}$)" and "interactions(p, q, $\boldsymbol{X}$, $\boldsymbol{v}$)", actually contain plenty of calculations and intermediate variables. Hence, it is unrealistic to store all of the intermediate variables in memory. One way to improve efficiency is by using the multidirectional tangent mode provided by Tapenade. The pseudo-code of the parallel derivative matrix filling algorithm using multidirectional tangent mode is shown in Fig. 8. Some improvements are explained as follows. The integer variable N_{out} means the number of outer loops and is given by:

$$N_{out} = \text{ceiling}(N_{DV} / n_{col}),\ n_{col} \in [1, N_{DV}], \tag{18}$$

where n_{col} indicates how many columns (see Fig. 1) are calculated in one AD multidirectional tangent calculation. The function "ceiling(x)" returns the least integer greater than or equal to x. In the AD multidirectional tangent mode, it loops over the N_{out} instead of the number of design variables N_{DV}. The larger n_{col} we set, the less redundant calculations it requires. If n_{col} equates to the N_{DV}, the Jacobian $\partial \boldsymbol{Z}\bar{\boldsymbol{I}} / \partial \boldsymbol{x}$ would be obtained by looping once. If n_{col} is set to 1, it would be the same as the ordinary tangent mode. Upon most occasions, the n_{col} might not be a factor of N_{DV} so that we define a new parameter n_{dv} which depicts the actual number of columns calculated for one particular run. This parameter is calculated by:

$$n_{dv} = \begin{cases} n_{col} & , \text{if } i \times n_{col} \le N_{DV} \\ N_{DV} - (i-1) \times n_{col} & , \text{if } i \times n_{col} > N_{DV} \end{cases}. \tag{19}$$

The code has to compute the starting index i_s and ending index i_e at the beginning of each outermost cycle (line 2 in Fig. 8). These two indexes indicate that from the i_sth to the i_eth columns of the Jacobian $\partial \boldsymbol{Z}\bar{\boldsymbol{I}} / \partial \boldsymbol{x}$ would be computed in this loop. These indexes are calculated through Eq. (20):

$$\begin{cases} i_s = (i-1) \times n_{col} + 1 \\ i_e = i \times n_{col} \end{cases}. \tag{20}$$

And then we could set some elements of $\boldsymbol{x\_dv}$ to 1 (line 3 in Fig. 8) according to the starting and ending indexes. Matrix $\boldsymbol{x\_dv}$ is an $N_{DV} \times n_{dv}$ matrix described in (21):

$$\boldsymbol{x\_dv} = \begin{bmatrix} 0 & 0 & 0 \\ \vdots & \vdots & \vdots \\ 1 & 0 & 0 \\ 0 & 1 & 0 \\ 0 & 0 & 1 \\ \vdots & \vdots & \vdots \\ \underbrace{0 \quad 0 \quad 0}_{n_{dv}} \end{bmatrix} \begin{matrix} \\ \\ \rightarrow i_s \\ \\ \rightarrow i_e \\ \\ \rightarrow N_{DV} \end{matrix}. \tag{21}$$

The multidirectional variables with the suffix "***_dv***" (in Fig. 8) can be seen as a collection of the multiple corresponding variables with the suffix "***_d***" (in Fig. 7). For instance,

$$\boldsymbol{v\_dv} = \left[\boldsymbol{v\_d}^{(i_s)}, \boldsymbol{v\_d}^{(i_s+1)}, \ldots, \boldsymbol{v\_d}^{(i_e)} \right]. \tag{22}$$

The element $\boldsymbol{v\_d}^{(i_s)}$ is equal to the $\boldsymbol{v\_d}$ computed in the i_sth loop in Fig. 7. The data storage form of these variables depends on the user. Similarly,

$$\boldsymbol{X\_dv} = \left[\boldsymbol{X\_d}^{(i_s)}, \boldsymbol{X\_d}^{(i_s+1)}, \ldots, \boldsymbol{X\_d}^{(i_e)} \right], \tag{23}$$

$$\boldsymbol{Z\_dv} = \left[\boldsymbol{Z\_d}^{(i_s)}, \boldsymbol{Z\_d}^{(i_s+1)}, \ldots, \boldsymbol{Z\_d}^{(i_e)} \right]. \tag{24}$$

In every outermost cycle of the AD multidirectional tangent mode, the matrix ***Z_dv*** needs to be filled and stored, whose memory requirement is n_{dv} times larger than the impedance matrix. Unfortunately, we can't avoid storing the whole matrix ***Z_dv*** before the matrix-vector product due to the fact that the matrix is filled by looping triangle-to-triangle, rather than edge-to-edge. In brief, the multidirectional tangent mode is faster than the tangent mode by setting a large value of n_{col}, but it requires more memory space.

D. Adjoint AD

Both the tangent mode and multidirectional tangent mode are dependent on the number of design variables. They are inefficient if there are hundreds or thousands of design variables. On the contrary, the adjoint mode is independent of the number of design variables. However, it's impractical to compute $\partial \boldsymbol{Z}\bar{\boldsymbol{I}} / \partial \boldsymbol{x}$ directly using the adjoint mode. The Jacobian matrix $\partial \boldsymbol{Z}\bar{\boldsymbol{I}} / \partial \boldsymbol{x}$ has a large number of rows but the adjoint mode could only obtain a single row for one particular run. In order to deal with this problem, we rewrite the sensitivity of RCS Eq. (13) as:

$$\frac{d\sigma}{d\boldsymbol{X}} = \frac{d\sigma}{d\boldsymbol{E}_s}\frac{\partial \boldsymbol{E}_s}{\partial \boldsymbol{X}} - \left(\frac{d\sigma}{d\boldsymbol{E}_s}\boldsymbol{\psi}^{\mathrm{T}}\frac{\partial \boldsymbol{Z}\bar{\boldsymbol{I}}}{\partial \boldsymbol{X}} - \frac{d\sigma}{d\boldsymbol{E}_s}\boldsymbol{\psi}^{\mathrm{T}}\frac{\partial \boldsymbol{V}}{\partial \boldsymbol{X}} \right). \tag{25}$$

Instead of computing $\partial \boldsymbol{Z}\bar{\boldsymbol{I}} / \partial \boldsymbol{X}$ alone, we compute the term $\left[d\sigma / d\boldsymbol{E}_s \right] \boldsymbol{\psi}^{\mathrm{T}} \left[\partial \left(\boldsymbol{Z}\bar{\boldsymbol{I}} \right) / \partial \boldsymbol{X} \right]$ together. Thus, we define a new function:

$$F(\boldsymbol{Z}, \boldsymbol{X}) = \frac{d\sigma}{d\boldsymbol{E}_s}\boldsymbol{\psi}^{\mathrm{T}}\boldsymbol{Z}\bar{\boldsymbol{I}} . \tag{26}$$

The surface current coefficient is a constant vector, and the adjoint field does not depend directly on the design variables. Although the term $d\sigma / d\boldsymbol{E}_s$ depends on $\boldsymbol{X}$ actually, we assume that it has been computed and is regarded as a constant as well. Thus, the major calculation of this function is the matrix filling. Take the partial derivatives of F and we obtain:

$$\frac{\partial F}{\partial \boldsymbol{X}} = \frac{d\sigma}{d\boldsymbol{E}_s}\boldsymbol{\psi}^{\mathrm{T}}\frac{\partial \boldsymbol{Z}\bar{\boldsymbol{I}}}{\partial \boldsymbol{X}} , \tag{27}$$

$$\frac{\partial F}{\partial \boldsymbol{Z}} = \frac{d\sigma}{d\boldsymbol{E}_s}\boldsymbol{\psi}^{\mathrm{T}}\bar{\boldsymbol{I}} . \tag{28}$$

And then the routine that computing this function $F(\boldsymbol{Z},\boldsymbol{X})$ is analyzed by Tapenade using the adjoint mode. The mesh coordinates $\boldsymbol{X}$ are set as the inputs while F is set as the outputs when differentiating the code using Tapenade. As shown in Fig. 9, the pseudo-code depicts the procedure of derivatives evaluation and the vector $\partial F / \partial \boldsymbol{X}$ would be obtained for a single adjoint AD run. The last term of Eq. (25) is also computed in the same way.

The Tapenade adopts the *store-all* strategy [21] to differentiate the code when using the adjoint mode. In this strategy, the intermediate values are saved just before a statement, which leads to a "two-sweeps" architecture for the control-flow reversal. As shown in Fig. 9, these two sweeps are separated by a dotted line. The first sweep is called the forward sweep and is basically a copy of matrix filling (shown in Fig. 7), augmented with a recording of the control. This recorded control would be used by the second sweep, called the backward sweep, to orchestrate control-flow reversal. The intermediate data ($\boldsymbol{v_1}$ and $\boldsymbol{v_2}$) that would be used by the backward sweep to evaluate the elements of the derivatives Jacobian is also recorded. The natural way to record is to use a stack that grows during the forward sweep and shrinks during the backward sweep. Of particular note that the subroutine "interactions'(p, q, $\boldsymbol{X}$, $\boldsymbol{v_1}$)" (line 19 in Fig. 9) is the simplification of the original integral subroutine "interactions(p, q, $\boldsymbol{X}$, $\boldsymbol{v_1}$)" (line 15 in Fig. 6). The simplified subroutine only calculates the intermediate data used for the integral on the triangle, not the matrix elements.

The Tapenade uses the PUSH and POP primitives for stack manipulations and applies the global data-flow analysis To-Be-Recorded (TBR) [21] to reduce significantly the number of intermediate values that need to be stored on that tape. In Fig. 9, the variables with suffix "_b" represent the derivatives of the F with respect to the corresponding variables. For instance, ***X_b*** means $\partial F / \partial \boldsymbol{X}$. The corresponding backward sweep subroutines are suffixed by "_b". The PUSH/POP subroutines provided by Tapenade are used to record the intermediate values whereas the PUSHCONTROL and POPCONTROL subroutines are called for the control-flow recording. These PUSH and POP primitives are marked in gray in Fig. 9. The vector $\partial F / \partial \boldsymbol{X}$ could be obtained by running these two sweeps once which shows the great merit of the adjoint mode. However, there is still a serious problem that affects its application. As we mentioned above, the forward sweep is basically a copy of the matrix filling augmented with the data recording. Assume that the number of unknowns is N, the regular matrix filling routine only needs to store an $N \times N$ complex matrix in total. But for the forward sweep, if computing each element of Jacobian requires to store n intermediate values, it will push at least $n \times N \times N$ data into the stack. The memory cost is unacceptable even though it would not compute and store the elements of the

impedance matrix.

In order to address this problem, we propose an "inner-loop two-sweeps" architecture for the adjoint mode. Note that the computation of each element of the impedance matrix or Jacobian is independent. Therefore the backward sweep routine could be executed straight after the corresponding forward sweep is done in an inner cycle. In other words, we could change the "two-sweeps" architecture into the "inner-loop two-sweeps" architecture. The modified adjoint AD pseudo-code using the "inner-loop two-sweeps" architecture is depicted in Fig. 10. These modifications can only be done by hand. The manual programming work depends on the architecture of the existing codes. If the framework of the existing codes is clear and modularized, the complete reprogramming work could be done within a couple of days.

```
1.  X = FFD(x)                                  ! compute the coordinates of triangles
2.  Do p = 1, N_T                               ! loop over the field (testing) triangles
3.    Do q = 1, N_T                             ! loop over the source triangles
4.      dZ = interactions(p, q, X)              ! calculate integral on the triangle pair (p, q)
5.      Do ii = 1, 3                            ! loop over edges of the field triangle
6.        mm = edge_num(p, ii)                  ! compute the global index of the iith edge of the pth field triangle
7.        If (mm .NE. 0) then                   ! the mmth edge is a valid common edge
8.          Do jj = 1, 3                        ! loop over edges of the source triangle
9.            nn = edge_num(q, jj)              ! compute the global index of the jjth edge of the qth source triangle
10.           If (nn .NE. 0) then               ! the nnth edge is a valid common edge
11.             Z(mm, nn) += dZ(mm, nn)         ! add into the impedance matrix
12.           Endif
13.         Enddo                               ! end loop over edges of the source triangle
14.       Endif
15.     Enddo                                   ! end loop over edges of the field triangle
16.   Enddo                                     ! end loop over the source triangles
17. Enddo                                       ! end loop over the field (testing) triangles
```

Fig. 5. The serial matrix filling algorithm.

```
1.  X = FFD(x)                                  ! compute the coordinates of triangles
2.  Do p = 1, N_T                               ! loop over the field (testing) triangles
3.    Do q = 1, N_T                             ! loop over the source triangles
4.      flag = 0                                ! initialize the flag of whether do integration
5.      Do ii = 1, 3                            ! loop over edges of the field triangle
6.        m = edge_num(p, ii)                   ! compute the global index of the iith edge of the pth field triangle
7.        If (m .NE. 0 .and. m is on this process) then   ! the mth edge is valid and on this process
8.          mm = local_index(m)                 ! get the local index of the global index m
9.          v = temporary(p, q, X)              ! compute the intermediate data needed in the integration
10.         Do jj = 1, 3                        ! loop over edges of the source triangle
11.           n = edge_num(q, jj)               ! compute the global index of the jjth edge of the qth source triangle
12.           If (n .NE. 0 .and. n is on this process) then   ! the nth edge is valid and on this process
13.             nn = local_index(n)             ! get the local index of the global index n
14.             If (flag == 0) then
15.               dZ = interactions(p, q, X, v) ! calculate integral on the triangle pair (p, q)
16.               flag = 1                      ! set flag that the integration has been done
17.             Endif
18.             Z(mm, nn) += dZ(mm, nn)         ! add into the impedance matrix
19.           Endif
20.         Enddo                               ! end loop over edges of the source triangle
21.       Endif
22.     Enddo                                   ! end loop over edges of the field triangle
23.   Enddo                                     ! end loop over the source triangles
24. Enddo                                       ! end loop over the field (testing) triangles
```

Fig. 6. The parallel matrix filling algorithm.

```
1.  Do i = 1, N_DV                                   ! loop over the design variables
2.    x_d = [0,..,0,1,0,..,0]^T                      ! set the ith element to 1 and the others to 0
3.    X_d = FFD_d(x, x_d)                            ! compute dX/dx_i
4.    X = FFD(x)                                     ! compute the coordinates of triangles
5.    Do p = 1, N_T                                  ! loop over the field (testing) triangles
6.      Do q = 1, N_T                                ! loop over the source triangles
7.        flag = 0                                   ! initialize the flag of whether do integration
8.        Do ii = 1,3                                ! loop over edges of the field triangle
9.          m = edge_num(p, ii)                      ! compute the global index of the iith edge of the pth field triangle
10.         If (m .NE.0 .and. m is on this process) then   ! the mth edge is valid and on this process
11.           mm = local_index(m)                    ! get the local index of the global index m
12.           v_d = temporary_d(p, q, X, X_d)        ! compute the derivatives of the intermediate data
13.           v = temporary(p, q, X)                 ! compute the intermediate data needed in the integration
14.           Do jj = 1, 3                           ! loop over edges of the source triangle
15.             n = edge_num(q, jj)                  ! compute the global index of the jjth edge of the qth source triangle
16.             If (n .NE. 0 .and. n is on this process) then   ! the nth edge is valid and on this process
17.               nn = local_index(n)                ! get the local index of the global index n
18.               If (flag == 0) then
19.                 dZ_d = interactions_d(p,q,X, X_d, v, v_d)   ! calculate the derivatives matrix elements
20.                 flag = 1                         ! set flag that the integration has been done
21.               Endif
22.               Z_d(mm, nn) += dZ_d(mm, nn)      ! add into the derivatives matrix
23.             Endif
24.           Enddo                                  ! end loop over edges of the source triangle
25.         Endif
26.       Enddo                                      ! end loop over edges of the field triangle
27.     Enddo                                        ! end loop over the source triangles
28.   Enddo                                          ! end loop over the field (testing) triangles
29.   ZI_d(:, i) = multiplications(Z_d, I)           !compute ∂Z̄I / ∂x_i and release the memory of Z_d
30. Enddo                                            !end loop over design variables
```

Fig. 7. The parallel derivative matrix filling algorithm using the tangent mode.

```
1.  Do i = 1, N_out                                  ! loop over the outermost loops
2.    compute_index(i, i_s, i_e, n_dv)               ! compute the starting and ending indexes
3.    x_dv = set_ones(i_s, i_e)                      ! set some elements to 1 and others to 0
4.    X_dv = FFD_dv(x, x_dv, n_dv)                   ! compute the derivatives of the coordinates
5.    X = FFD(x)                                     ! compute the coordinates of triangles
6.    Do p = 1, N_T                                  ! loop over the field (testing) triangles
7.      Do q = 1, N_T                                ! loop over the source triangles
8.        flag = 0                                   ! initialize the flag of whether do integration
9.        Do ii = 1, 3                               ! loop over edges of the field triangle
10.         m = edge_num(p, ii)                      ! compute the global index of the iith edge of the pth field triangle
11.         If (m .NE. 0 .and. m is on this process) then   ! the mth edge is valid and on this process
12.           mm = local_index(m)                    ! get the local index of the global index m
13.           v_dv = temporary_dv(p, q, X, X_dv, n_dv)   ! compute the derivatives of the intermediate data
14.           v = temporary(p, q, X)                 ! compute the intermediate data needed in the integration
15.           Do jj = 1, 3                           ! loop over edges of the source triangle
16.             n = edge_num(q, jj)                  ! compute the global index of the jjth edge of the qth source triangle
17.             If (n .NE. 0 .and. n is on this process) then   ! the nth edge is valid and on this process
18.               nn = local_index(n)                ! get the local index of the global index n
19.               If (flag == 0) then
20.                 dZ_dv = interactions_dv(p, q, X, X_dv, v, v_dv, n_dv)   ! calculate the derivatives matrix elements
21.                 flag = 1                         ! set flag that the integration has been done
22.               Endif
23.               Z_dv(mm, nn, :) += dZ_dv(mm, nn, :)   ! add into the derivatives matrix
24.             Endif
25.           Enddo                                  ! end loop over edges of the source triangle
26.         Endif
27.       Enddo                                      ! end loop over edges of the field triangle
28.     Enddo                                        ! end loop over the source triangles
29.   Enddo                                          ! end loop over the field (testing) triangles
30.   ZI_d(:, (i-1) × n_dv + 1: i × n_dv) = Multiplications(Z_dv, I)   ! matrix multiplications and release memory
31. Enddo                                            ! end loop over design variables
```

Fig. 8. The parallel derivative matrix filling algorithm using the multidirectional tangent mode.

```
1.  X = FFD(x)                                          ! compute the coordinates of triangles
2.  Do p = 1, N_T                                       ! loop over the field (testing) triangles
3.    Do q = 1, N_T                                     ! loop over the source triangles
4.      flag = 0                                        ! initialize the flag of whether do integration
5.      Do ii = 1, 3                                    ! loop over edges of the field triangle
6.        m = edge_num(p, ii)                           ! compute the global index of the iith edge of the pth field triangle
7.        If (m .NE.0 .and. m is on this process) then  ! the mth edge is valid and on this process
8.          PUSH(mm)                                    ! push data into the stack
9.          mm = local_index(m)                         ! get the local index of the global index m
10.         PUSH(v_1)                                   ! push data into the stack
11.         v_1 = temporary(p, q, X)                    ! compute the  intermediate data
12.         Do jj = 1, 3                                ! loop over edges of the source triangle
13.           n = edge_num(q, jj)                       ! compute the global index of the jjth edge of the qth source triangle
14.           If (n .NE. 0 .and. n is on this process) then ! the nth edge is valid and on this process
15.             PUSH(nn)                                ! push data into the stack
16.             nn = local_index(n)                     ! get the local index of the global index n
17.             If (flag == 0) then
18.               PUSH(v_1, v_2)                        ! push data into the stack
19.               v_2 = interactions'(p, q, X, v_1)     ! calculate the  intermediate data
20.               flag = 1                              ! set flag that the integration has been done
21.               PUSHCONTROL(1)                        ! push control parameter into the stack
22.             Else
23.               PUSHCONTROL(0)                        ! push control parameter into the stack
24.             Endif
25.             PUSHCONTROL(1)                          ! push control parameter into the stack
26.           Else
27.             PUSHCONTROL(0)                          ! push control parameter into the stack
28.           Endif
29.         Enddo                                       ! end loop over edges of the source triangle
30.         PUSHCONTROL(1)                              ! push control parameter into the stack
31.       Else
32.         PUSHCONTROL(0)                              ! push control parameter into the stack
33.       Endif
34.     Enddo                                           ! end loop over edges of the field triangle
35.   Enddo                                             ! end loop over the source triangles
36. Enddo                                               ! end loop over the field (testing) triangles
-------------------------------------------------------------------------------------------------------
37. Z_b = ∂F / ∂Z                                       ! set the input derivatives
38. Do p = N_T,1,-1                                     ! loop over the field (testing) triangles
39.   Do q = N_T,1,-1                                   ! loop over the source triangles
40.     Do ii=3,1,-1                                    ! loop over edges of the field triangle
41.       POPCONTROL(branch)                            ! pop the control parameter from stack
42.       If (branch) then
43.         Do jj=3,1,-1                                ! loop over edges of the source triangle
44.           POPCONTROL(branch)                        ! pop the control parameter from stack
45.           If (branch) then
46.             dZ_b(mm, nn) += Z_b(mm, nn)             ! set the derivatives matrix elements
47.             POPCONTROL(branch)                      ! pop the control parameter from stack
48.             If (branch) then
49.               POP(v_1, v_2)                         ! pop the data from stack
50.               interactions_b(p, q, X, X_b, v_1, v_1_b, v_2, v_2_b, dZ_b) ! calculate the derivatives of the  intermediate data
51.             Endif
52.             POP(nn)                                 ! pop the data from the stack
53.           Endif
54.         Enddo                                       ! end loop over edges of the source triangle
55.         POP(v_1)                                    ! pop the data from stack
56.         temporary_b(p, q, X, X_b, v_1, v_1_b)       ! calculate the derivatives ∂F / ∂X
57.         POP(mm)                                     ! pop the data from the stack
58.       Endif
59.     Enddo                                           ! end loop over edges of the field triangle
60.   Enddo                                             ! end loop over the source triangles
61. Enddo                                               ! end loop over the field (testing) triangles
62. x_b = FFD_b(x, X, X_b)                              ! compute ∂F / ∂x
```

Fig. 9. The parallel derivative matrix filling algorithm generated by the Tapenade using adjoint mode.

```
1.  Z_b = ∂F / ∂Z                                          ! set the input derivatives
2.  X = FFD(x)                                             ! compute the coordinates of triangles
3.  Do p = 1, N_T                                          ! loop over the field (testing) triangles
4.    Do q = 1, N_T                                        ! loop over the source triangles
5.      flag = 0                                           ! initialize the flag of whether do integration
6.      Do ii = 1, 3                                       ! loop over edges of the field triangle
7.        m = edge_num(p, ii)                              ! compute the global index of the iith edge of the pth field triangle
8.        If (m .NE.0 .and. m is on this process) then     ! the mth edge is valid and on this process
9.          mm = local_index(m)                            ! get the local index of the global index m
10.         PUSH(v1')                                      ! push data into the stack
11.         v1' = temporary(p, q, X)                       ! compute the  intermediate data
12.         Do jj = 1, 3                                   ! loop over edges of the source triangle
13.           n = edge_num(q, jj)                          ! compute the global index of the jjth edge of the qth source triangle
14.           If (n .NE. 0 .and. n is on this process) then ! the nth edge is valid and on this process
15.             nn = local_index(n)                        ! get the local index of the global index n
16.             If (flag == 0) then
17.               PUSH(v1', v2')                           ! push data into the stack
18.               v2' = interactions'(p, q, X, v1')        ! calculate the  intermediate data
19.               flag = 1                                 ! set flag that the integration has been done
20.               PUSHCONTROL(1)                           ! push control parameter into the stack
21.             Else
22.               PUSHCONTROL(0)                           ! push control parameter into the stack
23.             Endif
-------------------------------------------------------------------------------------------------------------------------------
24.           dZ_b(mm, nn) += Z_b(mm, nn)                  ! set the derivatives matrix elements
25.           POPCONTROL(branch)                           ! pop the control parameter from stack
26.           If (branch) then
27.             POP(v1', v2')                              ! pop the data from the stack
28.             interactions_b(p, q, X, X_b, v1', v1_b', v2', v2_b', dZ_b) ! calculate the derivatives of the  intermediate data
29.           Endif
30.         Endif
31.       Enddo                                            ! end loop over edges of the source triangle
32.       POP(v1')                                         ! pop the data from the stack
33.       temporary_b(p, q, X, X_b, v1', v1_b')            ! calculate the derivatives ∂F / ∂X
34.     Endif
35.   Enddo                                                ! end loop over edges of the field triangle
36.  Enddo                                                 ! end loop over the source triangles
37. Enddo                                                  ! end loop over the field (testing) triangles
38. x_b = FFD_b(x, X, X_b)                                 ! compute ∂F / ∂x
```

Fig. 10. The parallel derivative matrix filling algorithm using the "inner-loop two-sweeps" architecture.

As for the "two-sweeps" architecture, the forward sweep loop over the field triangles, the source triangles, the edges on a certain field triangle, and the edges on a certain source triangle in order to compute and store the intermediate data ($\boldsymbol{v_1}$ and $\boldsymbol{v_2}$). This intermediate data is used for the backward subroutine (such as "interactions_b" and "temporary_b") to calculate the derivatives. The intermediate data will change in each loop, therefore all of the intermediate data needs to be pushed into the stack (lines 10 and 18 in Fig. 9) before starting the backward sweep. The intermediate data will be popped out of the stack when it is needed for the backward subroutines (lines 49 and 55 in Fig. 9).

As for the "inner-loop two-sweeps" architecture, all of the backward sweep routines are moved into the loops of the forward sweep. The backward subroutine "interactions_b" is in the same loop as the subroutine "interactions' ", the intermediate data calculated by the subroutine "interactions' " can be sent into the backward subroutine "interactions_b" directly. Similarly, the backward subroutine "temporary_b" is in the same loop as the subroutine "temporary". The memory consumption is much lower than before since it is hardly inevitable to record plenty of intermediate data values and control parameters. Even though there are still some small amounts of data values ($\boldsymbol{v_1'}$ and $\boldsymbol{v_2'}$) that need to be stored, they would be pulled out of the stack before the end of the current loop.

IV. OPTIMIZATION FRAMEWORK

The flow chart of the gradient-based shape optimization design method is presented in Fig. 11. The numerical methods applied in the optimization process consist of the geometric parameterization, the MoM solver, the adjoint-based gradient evaluations, and the SQP algorithm. The operational process and relationships among the methods mentioned above are described below.

First of all, the mesh of the baseline geometry is parameterized through the FFD approach. And then the parameterize method updates the mesh and transfers it to the MoM solver. After solving the scattering problem, the gradient could be obtained through the adjoint method. Next, the RCS, gradient, and some geometrical

parameters (e.g., thickness) are sent to the optimizer to search the optimized direction and step. The SQP algorithm will generate new design variables and start the next iteration process until the convergence tolerance reaches the required accuracy. Of particular note is that the gradient calculation is not required at every iteration, it is determined by the SQP algorithm. In this paper, the implementation of the SQP algorithm is SNOPT [27], which is useful for solving large-scale constrained problems with smooth objective functions and constraints. SNOPT is a sparse nonlinear optimizer that uses a smooth augmented Lagrangian merit function while making explicit provision for infeasibility in the original problem and in the quadratic programming subproblems. The Hessian of the Lagrangian is approximated through a limited-memory quasi-Newton method, and a reduced-Hessian algorithm is used for solving the quadratic programming subproblems [27].

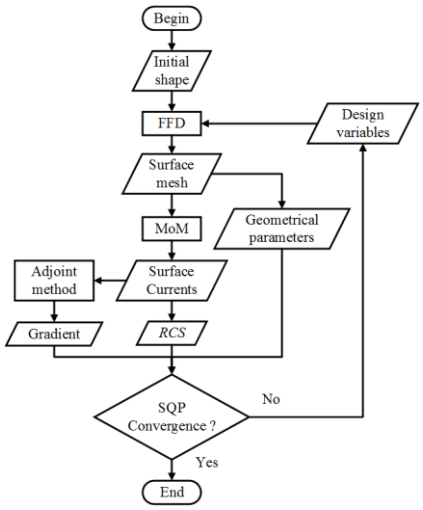

Fig. 11. The flow chart of the gradient-based shape optimization design method.

V. NUMERICAL EXAMPLES

In this section, we present some numerical examples. Firstly, we verify the accuracy of the gradient computed by the adjoint method. Then we study the CPU time and memory consumption of adjoint AD compared to the tangent AD and multidirectional tangent AD. Finally, we apply the presented method to a shape optimization problem.

A. Verification

To gain confidence in the effectiveness of the gradient for use in the optimization design, the adjoint method is compared with the traditional forward finite difference method. The metallic almond [28] model is applied for the electromagnetic analysis. The frequency of the incident wave is 7 GHz and the polarization mode is horizontal polarization. Figure 12 shows the mesh, the FFD control frame, and the incident direction. Each edge length of the triangle facet is less than the 1/10 wavelength and the amount of unknowns is 12618. The almond model is parameterized by the FFD approach with 56 control points in total. The displacements at the z-direction of the FFD control points are selected as the design variables.

The gradients computed by the adjoint method and the finite difference method are shown in Fig. 13. Notice that several step sizes are tested to find the appropriate step size before using the finite difference method to compute the gradient. The gradients obtained by the adjoint method are in good agreement with those computed by the finite difference method. The absolute error and relative error between these two results are shown in Fig. 14. The relative error is given by $\varepsilon_r = \left|F' - F'_{\text{ref}}\right| / \left|F'_{\text{ref}}\right|$, where $F'_n = \mathrm{d}\sigma / \mathrm{d}x_n$, $n = 1,2,\ldots,56$. The values calculated by the finite difference method are selected as the reference values. From this figure, it can be seen that both the absolute error and relative error are less than 10^{-2}. The gradient computed by the adjoint method has acceptable accuracy for the gradient-based shape optimization design.

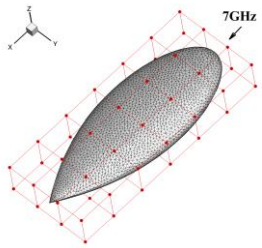

Fig. 12. The mesh of almond and the FFD control frame.

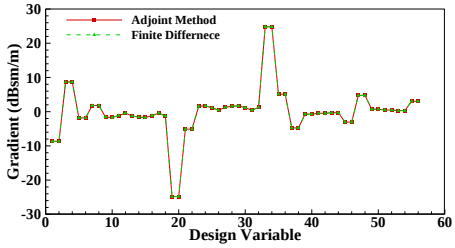

Fig. 13. Comparison of the gradients.

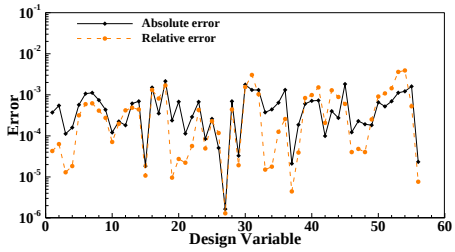

Fig. 14. Absolute error and relative error.

B. Computation time and memory consumption

In this section, the comparisons of efficiency and consumption between (multidirectional) tangent AD and adjoint AD are studied. These simulations are run on a cluster with 28 CPU cores. The total CPU time and the memory consumption are tested through a different number of design variables and the results are shown in Fig. 15 and Fig. 16. The total CPU time is the sum of the CPU time of all cores. Notice that solving a regular scattering problem is about 1.28 hours total CPU time and requires 3.08 GB memory space.

As for the adjoint AD using "inner-loop two-sweeps" architecture, it requires minimal time and memory space, which are a little bit large than the requirements of solving a regular scattering problem. The total CPU time and the memory consumption are consistent when increasing the number of design variables.

The tangent AD (red broken line) requires maximum running time but less memory consumption. The total CPU time grows linearly with the number of design variables while the memory consumption keeps stable.

The multidirectional tangent AD is tested using different n_{col} values (16 in blue dotted line and 32 in green dash-dot line). The larger n_{col} we set, the less CPU time it spends. But the multidirectional tangent with larger n_{col} requires more memory space, especially when dealing with the problem with a large number of design variables.

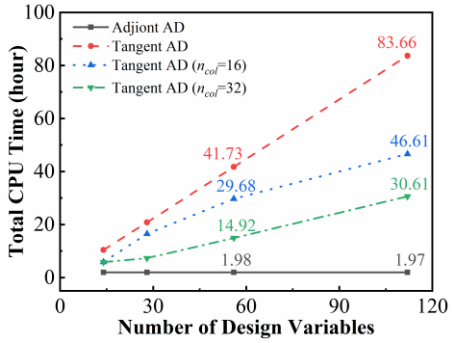

Fig. 15. Total CPU time consumption.

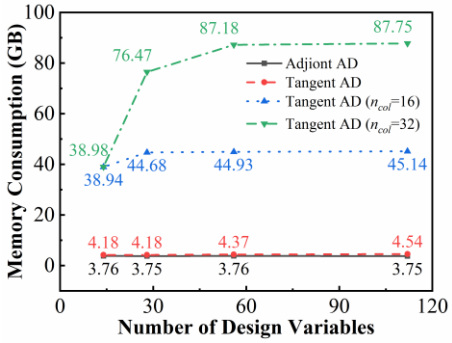

Fig. 16. Memory consumption.

In order to show the evidence for the advantages of our proposed method, we perform a comparison between our code and the commercial software HFSS-IE (HFSS Integral Equation) [29]. The cube model shown in Fig. 17 is used for the electromagnetic analysis.

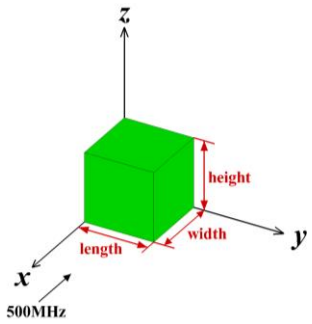

Fig. 17. Cube model and incident wave.

The side length of the cube is 1 meter, and the frequency of the incident wave is 500MHz. The length, width, and height of this cube are selected as the design variables. Thus, there are 3 design variables in total. Firstly, we compute the gradients of RCS using our code in adjoint AD mode. The unknowns of the matrix equation is 8118 and the total CPU time and the memory consumption are listed in Table 1. And then, we do the same simulation using the HFSS-IE. The Adaptive Cross Approximation (ACA) [29] technique provided by the HFSS-IE is applied to solve the integral equation, and the maximum residual error is set to 0.004. The HFSS-IE employs the central finite difference approximation to calculate the RCS derivatives with respect to the design variables. The maximum number of iterations is set to 6 and the approximate error in master is set to 0.001 when running the sensitivity analysis. Both the electromagnetic simulations are running on a workstation with 16 CPU cores.

These comparison results are listed in Table 1. It has been found that the total CPU time required by the proposed method is less than that required by the HFSS-IE, while the memory consumption of the proposed method is only a little higher than that of the HFSS-IE.

Table 1: Comparison of the total CPU time and the memory consumption

	Total CPU Time	Memory Consumption
Proposed method	48.5 min	2010 MB
HFSS-IE	451.7 min	1720 MB

In short, the adjoint AD shows great advantages in both efficiency and memory consumption, and the tangent AD is inefficient whereas the multidirectional tangent AD requires large memory consumption.

C. Application to the shape optimization

We study the shape optimization of the almond and the requirements for a low observable shape. The optimization problem is described in Eq. (29):

$$\begin{aligned} &\min: \ \sigma(\boldsymbol{x}) \\ &\text{s.t.}: \ t^{(n)}(\boldsymbol{x}) \geq 0.1 t_0^{(n)}, \ n = 1,2,...,130, \\ &\quad \forall \boldsymbol{x} \in [x_1, x_2, ..., x_{56}]^{\mathrm{T}} \end{aligned} \tag{29}$$

where t denotes the thickness at a certain point of optimized shape whereas t_0 is the initial thickness. The thickness constraints are imposed at points on the surface of the object to avoid unrealistic designs. As shown in Fig. 18, there are 130 segments inside the almond and their length represents the local thickness. They should not less than 10% of the initial shape to prevent the thickness from being so thin. The objective function is the RCS and the design variables are the displacements at the z-direction of the FFD control points. The frequency of the incident wave is 7GHz and the polarization mode is vertical polarization.

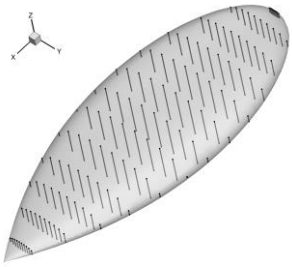

Fig. 18. Thickness constraints.

The optimizer arrives after 4 iterations, and 11 evaluations of RCS, to a local optimum σ_* = -61.629 dBsm (decibel square meter, $\sigma_{\mathrm{dBsm}} = 10\log(\sigma_{m^2})$). Figure 19 shows the convergence history of the objective function. We refine the mesh of the optimized shape since large deformation would lead to distorted mesh elements. The final RCS of the optimized shape after mesh refinement is -53.194 dBsm. Figure 20 presents the profiles (Coordinate Y=0m) of the almond and optimized shape. The optimized shape has undulations and a sharp leading edge. The sharp leading edge could change the specular scattering into the edge diffraction and lead to a large RCS reduction. Figure 21 shows the distribution of the surface current density and the optimized shape has a lower current magnitude around the leading edge when compared to the almond. As for the instantaneous magnitude of the surface current, it's a periodic distribution from the leading edge to the end. The interval is approximately equal to a wavelength.

In order to study the RCS reduction mechanism of the undulations, we divide the model shape into several parts according to the length of a quarter wavelength. As shown in Fig. 22, two parts (part5 and part9) are picked out to study their scattering field contribution. These two parts are located on either side of the maximum thickness and are one wavelength apart. The scattering electric field contribution of each part is computed by integrating the surface current on this part individually. Figure 23 shows the instantaneous scattering electric field along the reflection direction (negative direction of x-axis) from the origin of the coordinate system and Fig. 24 depicts the phase of the scattering electric field.

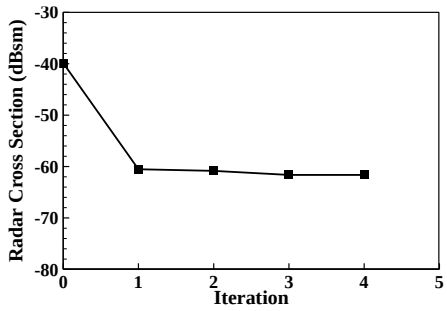

Fig. 19. The convergence history of the objective function.

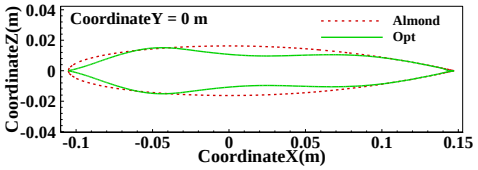

Fig. 20. Comparison of the profiles.

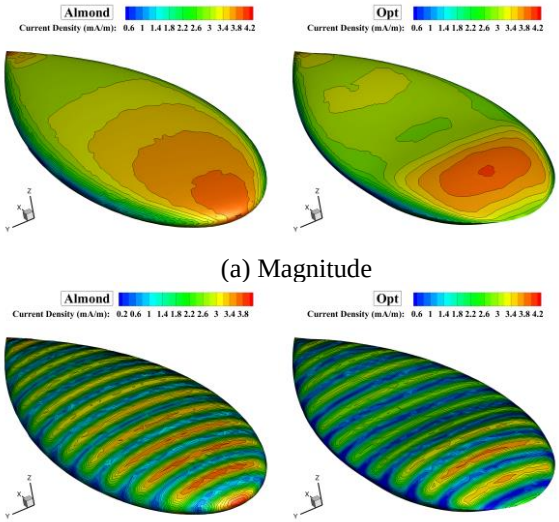

(a) Magnitude

(b) Instantaneous magnitude

Fig. 21. Comparison of the surface current density.

As for the almond, the scattering electric fields generated by these two parts are in the same phase. The

total amplitude increases after the superimposition of these two scattering electric fields.

On the contrary, the undulations of the optimized shape change the phase of the scattering electric fields. The phase difference between them is approximately 180 degrees which leads to a cancellation of the total amplitude. As for the other parts, the undulations would enlarge the phase difference of each pair and weaken the superimposed effect.

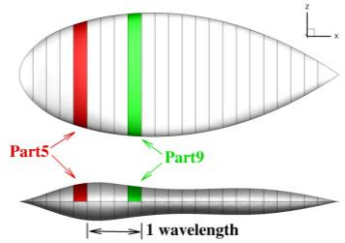

Fig. 22. Schematic of the part division.

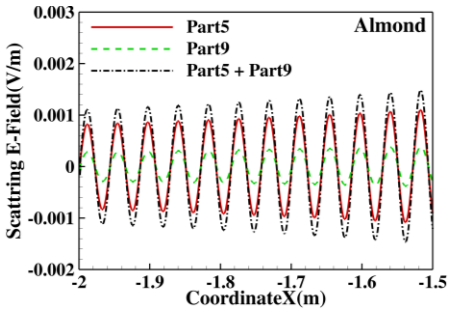

(a) Almond

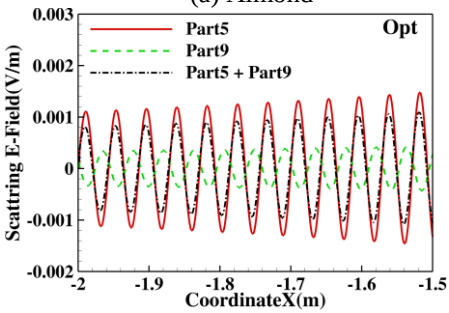

(b) Opt

Fig. 23. Scattering electric field from each part.

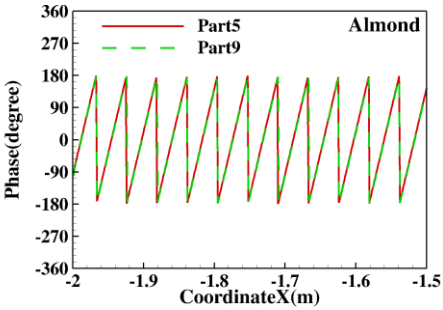

(a) Almond

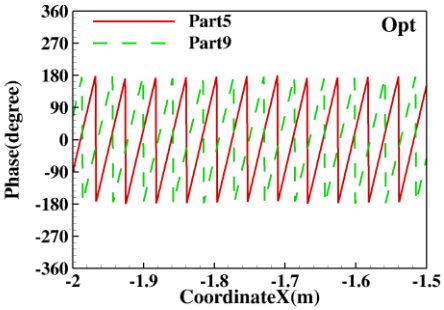

(b) Opt

Fig. 24. The phase of the instantaneous scattering electric field.

VI. CONCLUSION

In this work, the MoM is applied to solve the CFIE and evaluate the RCS of the object. The adjoint equation based on MoM is derived to compute the gradient of RCS efficiently. The LU factorization routine of ScaLAPACK is called to solve the large scale complex dense matrix equation so that the adjoint equation no longer needs to be solved.

The most difficult task for the gradient evaluation is the computation of the derivatives of the impedance matrix. The program transformation AD tool Tapenade is applied to generate the derivatives computation routines. We develop the code in three AD modes and test their efficiency and memory consumption. One of the bright spots of our work is that the subroutine which computes the derivatives of impedance matrix using adjoint AD mode is optimized by changing the "two-sweeps" architecture into the "inner-loop two- sweeps" architecture. This modification makes it far faster than the codes generated by tangent and multidirectional tangent modes. In addition, the memory consumption of this architecture is friendly.

The gradient calculated through the adjoint method is compared with those computed by the finite difference method. The results show that the accuracy is satisfactory. Both of the absolute errors and relative errors are in an acceptable region. The accuracy of the gradient meets the requirement of gradient-based shape optimization.

A gradient-based shape optimization design method is developed by coupling the MoM, the adjoint method, the FFD approach, and the SQP algorithm. The almond geometry is optimized through this design method and the SQP reaches a local minimum within 10 iterations. The optimized shape has undulations and sharp leading edges. Further studies show that the sharp leading edge could reduce the surface current magnitude and avoid the specular back-scattering, resulting in a large RCS reduction. The undulations on the upper surface and lower surface could change the phases which leads to a further RCS reduction.

REFERENCES

[1] M. Li, J. Bai, L. Li, X. Meng, Q. Liu, and B. Chen, "A gradient-based aero-stealth optimization design method for flying wing aircraft," *Aerosp. Sci. Technol.*, vol. 92, pp. 156-169, June 2019.

[2] N. Georgieva, S. Glavic, M. Bakr, and J. Bandler, "Feasible adjoint sensitivity technique for EM design optimization," *IEEE Trans. Microw. Theory Techn*., vol. 50, no. 12, pp. 2751-2758, Dec. 2002.

[3] A. Bondeson, Y. Yang, and P. Weinerfelt, "Optimization of radar cross section by a gradient method," *IEEE Trans. Magn.*, vol. 40, pp. 1260-1263, Mar. 2004.

[4] N. K. Nikolova, R. Safian, E. A. Soliman, M. H. Bakr, and J. W. Bandler, "Accelerated gradient based optimization using adjoint sensitivities," *IEEE Trans. Antennas Propag*., vol. 52, pp. 2147-2157, Aug. 2004.

[5] Y. Zhang, R. K. Nikolova, and R. H. Bakr, "Input impedance sensitivity analysis of patch antenna with discrete perturbations on method-of-moment grids," *Applied Computational Electromagnetics Society Journal*, vol. 10, no. 25, pp. 867-876. Oct. 2010.

[6] J. Kataja, S. J. Rvenp, J. I. Toivanen, R. M. Kinen, and P. Y. Oijala, "Shape sensitivity analysis and gradient-based optimization of large structures using MLFMA," *IEEE Trans. Antennas Propag.*, vol. 62, Nov. 2014.

[7] X. Zhang, J. C. I. Newman, W. Lin, and W. K. Anderson, "Time-dependent adjoint formulation for metamaterial optimization using Petrov-Galerkin methods," *Applied Computational Electromagnetics Society Journal*, vol. 32, no. 2, pp. 236-239. Feb. 2018.

[8] H. Igarashi and K. Watanabe, "Complex adjoint variable method for finite-element analysis of eddy current problems," *IEEE Trans. Magn*., vol. 46, no. 8, pp. 2739-2742, Aug. 2010.

[9] M. M. T. Maghrabi, M. H. Bakr, S. Kumar, A. Z. Elsherbeni, and V. Demir, "FDTD-based adjoint sensitivity analysis of high-frequency nonlinear structures," *IEEE Trans. Antennas Propag.*, vol. 68, pp. 4727-4737, June 2020.

[10] Y. Song, N. K. Nikolova, and M. H. Bakr, "Efficient time-domain sensitivity analysis using coarse grids," *Applied Computational Electromagnetics Society Journal*, vol. 23, no. 1, pp. 5-15, Mar. 2008.

[11] S. M. Ali, N. K. Nikolova, and M. H. Bakr, "Semi-analytical approach to sensitivity analysis of lossy inhomogeneous structures," *Applied Computational Electromagnetics Society Journal*, vol. 22, no. 2, pp. 219-227, July 2007.

[12] L. S. Kalantari and M. H. Bakr, "Optical cloak design exploiting efficient anisotropic adjoint sensitivity analysis," *Applied Computational Electromagnetics Society Journal*, vol. 32, no. 5, pp. 449-454, May 2017.

[13] L. Zhou, J. Huang, Z. Gao, and W. Zhang, "Three-dimensional aerodynamic/stealth optimization based on adjoint sensitivity analysis for scattering problem," *AIAA Journal*, pp. 1-14, Mar. 2020.

[14] J. Kataja and J. I. Toivanen, "On shape differentiation of discretized electric field integral equation," *Eng. Anal. Bound. Elem.*, vol. 37, pp. 1197-1203, May 2013.

[15] M. S. Dadash, N. K. Nikolova, and J. W. Bandler, "Analytical adjoint sensitivity formula for the scattering parameters of metallic structures," *IEEE Trans. Microw. Theory Tech.*, vol. 60, pp. 2713-2722, Sep. 2012.

[16] J. Kataja, A. G. Polimeridis, J. R. Mosig, and P. Yla-Oijala, "Analytical shape derivatives of the MFIE system matrix discretized with RWG functions," *IEEE Trans. Antennas Propag.*, vol. 61, pp. 985-988, Feb. 2013.

[17] N. K. Nikolova, J. W. Bandler, and M. H. Bakr, "Adjoint techniques for sensitivity analysis in high-frequency structure CAD," *IEEE Trans. Microw. Theory Tech*, vol. 52, pp. 403-419, Jan. 2004.

[18] J. I. Toivanen, R. A. E. Mäkinen, S. Järvenpää, P. Ylä-Oijala, and J. Rahola, "Electromagnetic sensitivity analysis and shape optimization using method of moments and automatic differentiation," *IEEE Trans. Antennas Propag.*, vol. 57, pp. 168-175, Jan. 2009.

[19] V. Fischer, L. Gerbaud, and F. Wurtz, "Using automatic code differentiation for optimization," *IEEE Trans. Magn*., vol. 41, pp. 1812-1815, May 2005.

[20] J. Dongarra and L. S. Blackford, "ScaLAPACK tutorial," in *Proceedings of the Third International Workshop on Applied Parallel Computing*, Industrial Computation and Optimization, 1997.

[21] L. Hascoet and V. Pascual, "The tapenade automatic differentiation tool: principles, model, and specification," *ACM Transactions on Mathematical Software*, vol. 39, pp. 1-43, Apr. 2013.

[22] T. W. Sederberg and S. R. Parry, "Free-form deformation of solid geometric models," in *ACM SIGGRAPH Computer Graphics*, pp. 151-160, Aug. 1986.

[23] A. Barclay, "SQP methods for large-scale optimization," *Dissertation Abstracts International*, vol. 60-06, Section B, p. 2730, Chair: Philip Gill, 1999.

[24] S. Rao, D. Wilton, and A. Glisson, "Electromagnetic scattering by surfaces of arbitrary shape," *IEEE Trans. Antennas Propag*., vol. 30, pp. 409-418, May 1982.

[25] Y. Zhang, T. K. Sarkar, D. D. Oro, H. Moon, and R. Geijn, "A parallel mom code using RWG basis functions and ScaLAPACK-based in-core and out-of-core solvers," in *Parallel Solution of Integral*

Equation-Based EM Problems in the Frequency Domain: John Wiley & Sons, pp. 81-84, 2009.
[26] V. Eijkhout, J. Langou, and J. Dongarra, "Parallel Linear Algebra Software," *Netlib Repository at UTK and ORNL*, 2006.
[27] P. E. Fill, W. Murray, and M. A. Saunders, "SNOPT: An SQP algorithm for large-scale constrained optimization," *SIAM Journal on Optimization*, vol. 12, no. 4, pp. 979-1006, Apr. 2002.
[28] A. C. Woo, H. Wang, M. J. Schuh, and M. L. Sanders, "Benchmark radar targets for the validation of computational electromagnetics programs," *IEEE Antennas Propag. Mag.*, vol. 35, pp. 84-89, Feb. 1993.
[29] HFSS help manual (ANSYS ED).

Ming Li was born in Liuzhou, Guangxi, China, in 1992. He received the B.S. degree in Aircraft Design and Engineering from Beijing Institute of Technology, Beijing, in 2014, and the M.S. degree in Aircraft Design from Northwestern Polytechnical University, Xi'an, in 2017, where he is currently pursuing the Ph.D. degree in Aircraft Design with the School of Aeronautics.

His current research interests include computational electromagnetics, aerodynamics, and multidisciplinary optimization design of flight vehicles.

Junqiang Bai was born in Xinxiang, Hernan, China, in 1971. He received the B.S. in Aerodynamics from the National University of Defense Technology, Changsha, in 1991, the M.S. degree in Aerodynamics from Northwestern Polytechnical University, Xi'an, in 1994, and the Ph.D. degree in Aircraft Design from Northwestern Polytechnical University, Xi'an, in 1999.

From 1999 to 2004, he was an Associate Professor with the Department of Aircraft Design Engineering, Northwestern Polytechnical University, Xi'an. He was a Visiting Scholar with the Institute of Aerodynamic and Flow Technology, German Aerospace Center (DLR), Braunschweig, Germany, in 2006. Since 2004, he has been a Professor with the Department of Aircraft Design Engineering, Northwestern Polytechnical University, Xi'an. Since 2017, he has been a Deputy Dean with the Unmanned System Research Institute, Northwestern Polytechnical University, Xi'an, China. He has authored or co-authored over 100 papers and he holds or has applied for 5 Chinese patents. His current research interests include the conceptual design of aircraft, the aircraft aerodynamic shape design, and the aircraft multidisciplinary optimization.

Feng Qu was born in Pizhou, Jiangsu, China, in 1988. He received the B.Eng. degree in Mathematics and Applied Mathematics from China University of Petroleum, Beijing, in 2010, and the Ph.D. degree in Fluid Mechanics from Beihang University, Beijing, in 2015.

From 2015 to 2017, he was an Engineer with the Institute of Manned Space System Engineering, China. Since 2018, he has been an Associate Professor with the Northwestern Polytechnical University, Xi'an, and he is currently a Director of fluid mechanics in National Natural Science Foundation of China. His current research interests involve the flux schemes for all speeds, the high-order schemes, and the turbulence modeling. He is authoring a structured CFD software which is capable of simulating configures of all speeds in both laminar flow and turbulent flow.

A Fully Connected Cluster with Minimal Transmission Power for IoT Using Electrostatic Discharge Algorithm

Mohammed A. Alanezi [1], Houssem R. E. H. Bouchekara [2,*], Muhammad. S. Javaid [2], and Mohammad S. Shahriar [2]

[1] Computer Science and Engineering Technology
University of Hafr Al Batin, Hafr Al Batin 31991, Saudi Arabia

[2] Department of Electrical Engineering
University of Hafr Al Batin, Hafr Al Batin 31991, Saudi Arabia
*bouchekara.houssem@gmail.com

Abstract **—** In the emerging age of the Internet of Things (IoT), energy-efficient and reliable connection among sensor nodes gain prime importance. Wireless engineers encounter a trade-off between sensors energy requirement and their reliable full connectivity. Consequently, the need to find the optimal solution draws the attention of many researchers. In this paper, the Electrostatic Discharge Algorithm (ESDA) is proposed, implemented, and applied to minimize energy needs of a sensor node while ensuring the fully-connectedness of each node. The obtained results show that the proposed method achieves better results than those found in the literature using the particle swarm optimization method in terms of energy savings and reliable connectivity.

Index Terms **─** IoT, WSN, Network Power, Energy Saving.

I. INTRODUCTION

Internet of Things (IoT) has emerged as an intrinsic part of modern lifestyle [1]. Things, objects, and devices that serve us on a day-to-day basis must effectively communicate to provide comfort without much human intervention. When it comes to nodal communication, energy efficiency is of prime importance. Therefore, strategies are to be devised to ensure that no energy is wasted during signal transmission and reception among various nodes. However, reduced transmission energy leads to connectivity issues. Thus, researchers have been trying to devise an optimal strategy since the last two decades, where nodes transmit signals with minimal power form a fully connected network [2]. Similar efforts are reported in [3] to reduce power usage in Wireless Local Area Network (WLAN) using energy-efficient antennas. Alternatively, harvested power can be wirelessly provided to the nodes fulfilling their power needs [4], [5]. Since new challenges appear in this field every day due to new networking protocols and interconnection of heterogeneous devices, the research is ongoing as discussed in [6].

Centralized connection algorithms experience limited efficiency due to increased communication overhead and added latency required to gather up and synchronise the flow of information from and to all coordinator nodes. However, a theoretical way to determine the optimal power requirements of these nodes is pivotal in exploiting the advantages of centralized systems. Providing full-area coverage with minimum energy requirements makes a centralized Wireless Sensor Network (WSN) control system a viable option with an added advantage of utilizing the central unit's high processing capabilities to make a well-informed decision. Additionally, the centralized hub for WSNs offers various networking benefits, including, optimal node localization and deployment, data aggregation, and energy-aware clustering [7]. Optimal localization of sensor nodes, otherwise, could have been a computationally-intensive process, as covered in [8].

Clustered WSNs promises extended network life. While designing simplistic networks of clustered topology, researchers generally consider the region without any obstacle [9]. Due to a rise in the need for wireless data collection, massive deployment of sensors at various locations is inevitable. This dense deployment of sensors, along with their independent nature, mount up a set of logistic challenges that inhibit their frequent recharging. Hence, energy efficiency becomes a crucial parameter to ensure reliability and longevity of a clustered WSN.

Communication overhead deteriorates network's reliability and energy efficiency. Data aggregation is a way to overcome the adverse effects of communication overhead, ultimately saving energy that would have been wasted otherwise in communicating with the far located

Submitted On: December 19, 2020
Accepted On: January 24, 2021

https://doi.org/10.47037/2020.ACES.J.360313

base station [10]. For data aggregation, sensors operating in the near vicinity form a cluster, based on an efficient network organization algorithm. Each cluster is composed of member sensors and a coordinator, known as the headset, to coordinate with other clusters and base station, as shown in Fig. 1.

Reference [6] provides a survey focusing on control techniques and cluster selection to extend the battery lifetime of WSN. The topology control in WSNs, highlighting improved coverage, lifetime, and the reduced energy consumption is implemented in [11]. The selection of a neighboring cluster depends on energy reserve, node identifier and network density. A couple of surveys [12], [13] cover and classify clustering algorithms highlighting taxonomy of various clustering schemes. They provide a summary of classification algorithms based on constant convergence time algorithms and variable convergence time protocols. Their objectives, features and complexity are contrasted with each other while their performance is measured and compared on convergence rate, location awareness, cluster overlapping and stability, and node mobility within a cluster.

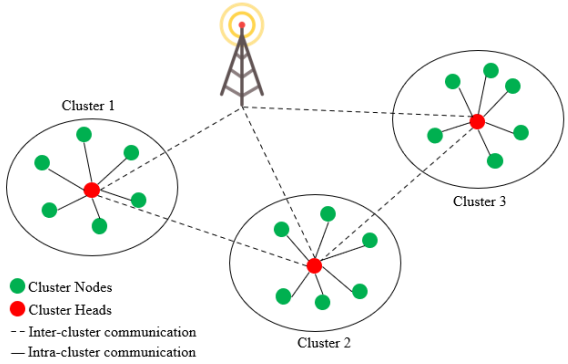

Fig. 1. Topology of clustered WSN.

This work focuses on the communications occurring within a single cluster. Electrostatic Discharge Algorithm (ESDA) is proposed to minimize energy consumptions by determining optimal transmission power while ensuring the fully-connectedness of the whole network. A comparison will be drawn with other commonly used metaheuristic optimization algorithms assessing the gain in energy-saving.

This remaining paper is organized as follows. Section 2 deals with problem formulation where the problem will be defined using a specific mathematical model and under due considerations. Once the foundation of the problem is established, Section 3 provides the details of the proposed optimization algorithm; ESDA. The section covers the step-by-step procedure of the entire algorithm. Next, in Section 4, the algorithm detailed in Section 3 will be applied to the problem of Section 2. Later, the obtained results will be explained. Section 5 concludes the paper and give some future recommendation.

II. PROBLEM FORMULATION

The main objective of this work is to optimize the location of each sensor node in a WSN to ensure the minimum power handling at each node. The sensors at the edge of the network tend to connect with inward neighboring sensors while utilizing minimal transmission power. However, the sensors in-between the edges and the core tend to provide full connection outwards in all directions of the network. As the network grows, it becomes computationally impossible to check every possible location each sensor can take to ensure optimality. Hence, metaheuristic search techniques are employed to find the optimal solution. Sometimes, optimality is traded-off with the computational cost.

A. System model

A single cluster comprising of *N* wireless sensors is considered in this work, creating a mesh network. The objective is to transmit all measurement packets to a sink node. A square bounds the positions of both sink and sensor nodes. The global neighbor matrix Γ is given by:

$$\Gamma_{ij}(\gamma) = \begin{cases} 0, \text{if } \rho_j < \rho_{th} \\ 1, \text{if } \rho_j \geq \rho_{th}, \end{cases} \quad (1)$$

where γ_i denotes the transmitting power of node i, and ρ_j represents power received at node j. ρ_{th} is the measure of receiver sensitivity. Equation (1) indicates that the two nodes are connected if the signal is transmitted with enough paper such that the received power is higher than the receiver's sensitivity. Figure 2 represents the circular region of each node, where signal strength is strong enough to ensure connectivity. Therefore, at the boundary of each circle, the measured signal strength is ρ_{th} and so any receiver inside this circular region will be able to receive the signal.

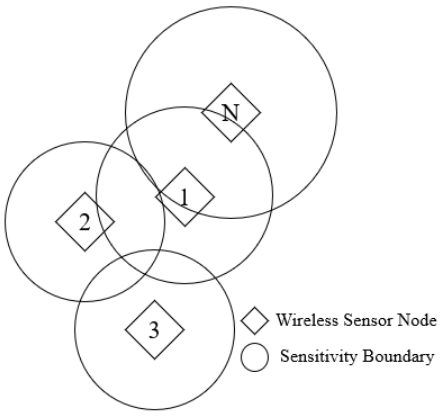

Fig. 2. System model.

The received signal power, P_R, depends on the transmitted power, P_t, and the distance of the receiver from the transmitter, d, as given below:

$$\frac{P_R}{P_t} = \frac{A_r A_t}{d^2 \lambda^2}, \tag{2}$$

where A_r, and A_t represent the effective areas of receiving and transmitting antennas, respectively, and λ denote the wavelength of the signal being transmitted. Equation (2) is also referred to as Friis Formula [14]. Since this work is not focused on sensors' antenna design, a single isotropic transmission and reception antenna at each sensor node is used to model the antenna's effective area, $A_{isotropic}$:

$$A_{isotropic} = \frac{\lambda^2}{4\pi}. \tag{3}$$

Therefore, if $A_{isotropic} = A_r = A_t$, (2) will be simplified to become:

$$\frac{P_R}{P_t} = \left(\frac{\lambda}{4\pi d}\right)^2. \tag{4}$$

Once the global neighbour matrix is calculated using (1), an algorithm determines if a pair of nodes is connected, as explained next.

B. Ascertaining full connectivity

Full connectivity is defined as the scenario if each node has at least one active connection link, and all those links can form an unbroken path, as shown in Fig. 3 (a). When each node has one connection link but cannot be connected in a single path, a fake fully connected network is formed, shown in Fig. 3 (b). For networks with a few nodes, fully connectedness is quickly realizable and easy to check. However, in a real IoT application, due to many nodes, determining the associated connectedness becomes both computationally and visually challenging.

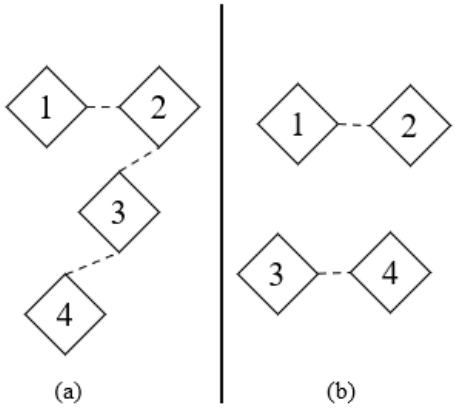

Fig. 3. (a) Fully connected network, and (b) disconnected network.

Calculating the Laplacian Matrix of the global neighbour matrix, Γ, is the first step in determining connectivity. If n_i is the i^{th} node, n represents the total number of nodes, and $\deg(n_i)$ denotes the number of other nodes connected to i^{th} node, n_i:

$$L = \left(l_{ij}\right)_{n \times n}, \tag{5}$$

$$l_{ij} = \begin{cases} \deg(n_i) & \text{if } i = j \\ -1 & \text{if } i \neq j \text{ and } \Gamma_{ij} = 1 \\ 0 & \text{otherwise} \end{cases}, \tag{6}$$

$$\deg(n_i) = (\Gamma^2)_{ij} \leftrightarrow i = j. \tag{7}$$

Equation (7) signifies that if $i = j$ then number of nodes connected to i^{th} node is the same as the square of the neighbour matrix. After calculating the Laplacian Matrix, L, its eigen values, ψ, are computed using the equation below:

$$L.E = \psi.E, \tag{8}$$

where E is $n \times 1$ eigenvector satisfying (8). Each eigenvalue φ can be grouped to form a vector Ψ, as shown below:

$$\Psi = [\psi_1, \psi_2, \psi_3, \dots, \psi_n]^t. \tag{9}$$

Here essentially, $\psi_1 < \psi_2 < \psi_3 < \cdots < \psi_n$ indicating that ψ_2, the second smallest eigenvalue must be positive in order to achieve a fully-connected condition. ψ_2 is also known as algebraic connectivity of Γ. Hence, observing the second smallest Laplacian eigenvalue of the neighbour matrix and verifying that there exists at least one connection for every node, determine if the network is fully connected. These conditions would ensure that transmission power is sufficient to establish a fully connected network.

III. PROPOSED ALGORITHM FOR PROBLEM SOLUTION

As aforesaid, the ESDA is used in this paper to solve the problem of optimal energy saving in a clustered WSN by calculating power transmission of sensors and keeping all of them connected. The ESDA, proposed in [15], is a competitive optimization algorithm, and it is inspired by the electrostatic discharge (ESD) event. More details about this algorithm are given in the following subsections.

A. ESD definitions

The advancement of solid-state electronics has revealed several concerning ESD issues in the design of the modern electronic system. Being a natural phenomenon, ESD has been discussed widely in numerous research articles, addressing the pros and cons [16]. A number of important definitions are presented in [17] where the ESD is presented as the abrupt transfer

of charged particles between different electrostatic potential bodies.

The paper addresses the ESD event as an interval of electromagnetic fields, ESD current and corona effects at the time of ESD and before that. It defines the electronic equipment which got affected by an ESD event as equipment victim. The victim experiences the stress generated by ESD, and it may belong to the receptors or the intruders.

B. ESD basic working principle

The conductivity of the materials varies from one to another. It affects the ability to contain charged particles. Some materials can accumulate positive charge quickly (like animal fur or human skin) whereas materials like plastic cups hold the negative charges effortlessly [18]. There are two approaches that an ESD may occur:

- Direct approach: when a moving object, also known as intruder, approaches to a stationary object (receptor) and transfer the charges. In such a case, intruder or receptor, anyone can be the equipment victim (Fig. 4).
- Indirect approach: where a third party sensitive object around the intruder and receptor gets affected by the electromagnetic field and thus becomes the victim (Fig. 5) [17].

While flowing through an integrated circuit, ESD current often passes through some PN junction paths, apart from the main least resistive channel. This may cause some degrees of unexpected dissipation. Moreover, it may result in some thermal damages to the neighbouring zones. Thus, repeated occurrence of ESD event inadequately affects the device and thus leads the system to malfunction [18].

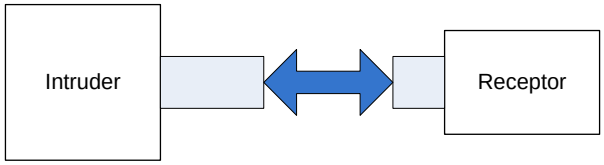

Fig. 4. Direct ESD event.

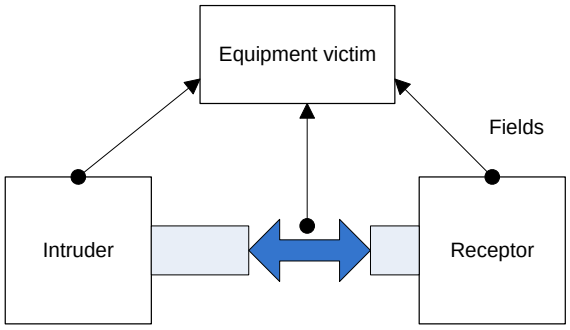

Fig. 5. Indirect ESD event.

C. ESDA steps

The steps of the proposed algorithm are explained below in details and then summarized in Fig. 6.

STEP 1: Like genetic algorithm or similar heuristic optimization approaches, ESDA also generates a number of a random population of 'ObjectsSize' objects in its initialization stage. These generated objects are the electrical equipment, made of design variables like various components. In the given search space, the position of special equipment is analyzed to calculate its fitness value, which reflects the immunity of the equipment. Besides, a counter counts the number of times each equipment becomes a victim.

STEP 2: The proposed ESD algorithm iterates for 'MaxIter' times in this stage to solve the assigned optimization problem. Each iteration randomly selects three objects in descending order, keeping the best one in the first position. Instead of three objects, the same operation occurs between two if the randomly generated number 'r_1' appears to be higher than the predetermined value (0.5 in this case). In such a case of two-object involvement, the object with lower fitness value proceed to another one (with higher fitness) by following the rule:

$$\boldsymbol{x_{2_{new}} = x_2 + 2 \cdot \beta_1 \cdot (x_1 - x_2)}, \quad (1)$$

where object 1 has better fitness than object 2, and their previous positions are denoted by x_1 and x_2, respectively. The object with the lower value will get the newer position ($x_{2_{new}}$) where β_1 is a randomly generated number with a normal distribution. It has the mean parameter (μ) of 0.7 and a standard deviation (σ) of 0.2. The mentioned case between two objects is an example of direct ESD event.

If the value of r_1 is found lower than the predetermined value 0.5, three objects will join in ESD operation. If the third object moves toward the other two, it will follow the rule mentioned below:

$$\boldsymbol{x_{3_{new}} = x_3 + 2 \cdot \beta_2 \cdot (x_1 - x_3) + 2 \cdot \beta_3 \cdot (x_2 - x_3)}, \quad (2)$$

where the random numbers β_2 and β_3 are generated with the same standard deviation and mean parameter like β_1. Thus, the indirect ESD incident occurs where the object 3 got exposed to the electromagnetic fields of discharge and becomes the victim of the event.

In every step of ESD event occurrence, the counter gets incremented by one for the participant object.

STEP 3: This step checks the bound imposed over the objects, whether any of them appears outside of the search space or not. If found such, it brings it back to the required region.

STEP 4: This step checks all the objects one by one, to find whether any of them has gone through the ESD process for at least 3 times or not. Any such object is considered destroyed and a randomly generated new

object will replace that within the search space. With less than three times of ESD occurrence, remaining objects will be assigned with the random number r_2 each. The objects with $r_2 > 0.2$ are also considered destroyed and subjected to the replacement procedure. Other components are marked as safe and kept for further operations.

1 **Inputs** ObjFunction (objective function), ProblemSize (dimension of the problem), LB (lower bounds), UB upper bounds, ObjectsSize (number of objects), and MaxIter (maximum number of iterations)
2 **Output** X_{best}, F_{best} and $FunctionEvolution_{best}$
3 Initialization
4 **for** Iter=1: MaxIter
5 **for** i=1: round(ObjectsSize/3)
6 Select three objects randomly from the population of objects
7 r_1=rand(0,1)
8 **if** r_1>0.5
9 $x_{2_{new}} = x_2 + 2 \cdot \beta_1 \cdot (x_1 - x_2)$
10 $x_{2\,\mathrm{ESDcounter}} = x_{2\,\mathrm{ESDcounter}} + 1$
11 **else**
12 $x_{3_{new}} = x_3 + 2 \cdot \beta_2 \cdot (x_1 - x_3) + 2 \cdot \beta_3 \cdot (x_2 - x_3)$
13 $x_{3\,\mathrm{ESDcounter}} = x_{3\,\mathrm{ESDcounter}} + 1$
14 **end if**
15 **end for**
16 Check if there are objects outside the search space
17 **for** i_1=1: ObjectsSize
18 **if** $x_{i_1\,\mathrm{ESDcounter}} \leq 3$
19 **for** i_2=1: ProblemSize
20 r_2=rand(0,1)
21 **if** r_2>0.2
22 A component must be changed
23 **end if**
24 **end for**
25 **Else**
26 The equipment must be changed $x_{i1} = LB + rand \cdot (UB - LB)$
27 **end for**
28 Select the new population from the old and the archived ones
29 **end for**

Fig. 6. Pseudocode of the ESDA.

STEP 5: This step updates the archive by saving the fit population into the old. The elements of the archive are sorted carefully in best-to-worse order. Finally, the number of objects equal to ObjectsSize is selected from the top of the list, for the next iteration.

IV. APPLICATION AND RESULTS

For the experiments, minimum transmission power as -30 [dBm] has been selected. The maximum power is determined to provide a connection for the largest possible distance of 28.284 [m] inside the area for random distribution, whereas the transmission frequency has been chosen to give the worst possible attenuation considering the frequency range of 915 [MHz], as typically used in WSN applications. Finally, the sensitivity defined as the lowest received power that allows information recovery is chosen to be -60 [dBm]. All the parameters used in this study are given in Table 1.

In order to compare our proposed approach using the ESDA, it has been applied to the same scenarios investigated in [19]. In that paper, there were six scenarios, in each scenario, there are 20 sensors spread in a square region defined by (20 [m] x 20 [m]) as shown in Fig. 7. The used algorithms were the Particle Swarm Optimization (PSO) and a simplistic method. For further comparison, other well-known algorithms like Genetic Algorithm (GA), Differential Evolution (DE), Black Hole (BH) algorithm, Electromagnetism-like algorithm (EM), Salp Swarm Algorithm (SSA) and Sine Cosine Algorithm (SCA) have been tested. It is worth mentioning that the real number of scenarios investigated in [19] is 10. However, after an in-depth analysis, it has been found that scenarios 1 and 3 are the same, scenarios 2 and 5 are identical, scenarios 4 and 6 are same, and scenarios 7 and 9 are same. Therefore, the number of scenarios has been reduced from 10 to 6 in this paper.

Table 1: Simulation parameters used in this work [19]

Parameter (Notation)	**Value [Unit]**
Number of sensor nodes	20
Sensors transmission power range	-30 [dBm]
Sensor Transmission frequency (f)	915 [MHz]
Area for sensors random locations (L x L)	20 [m] x 20 [m]
Sensor sensitivity (ρ_{th})	-60 [dBm]

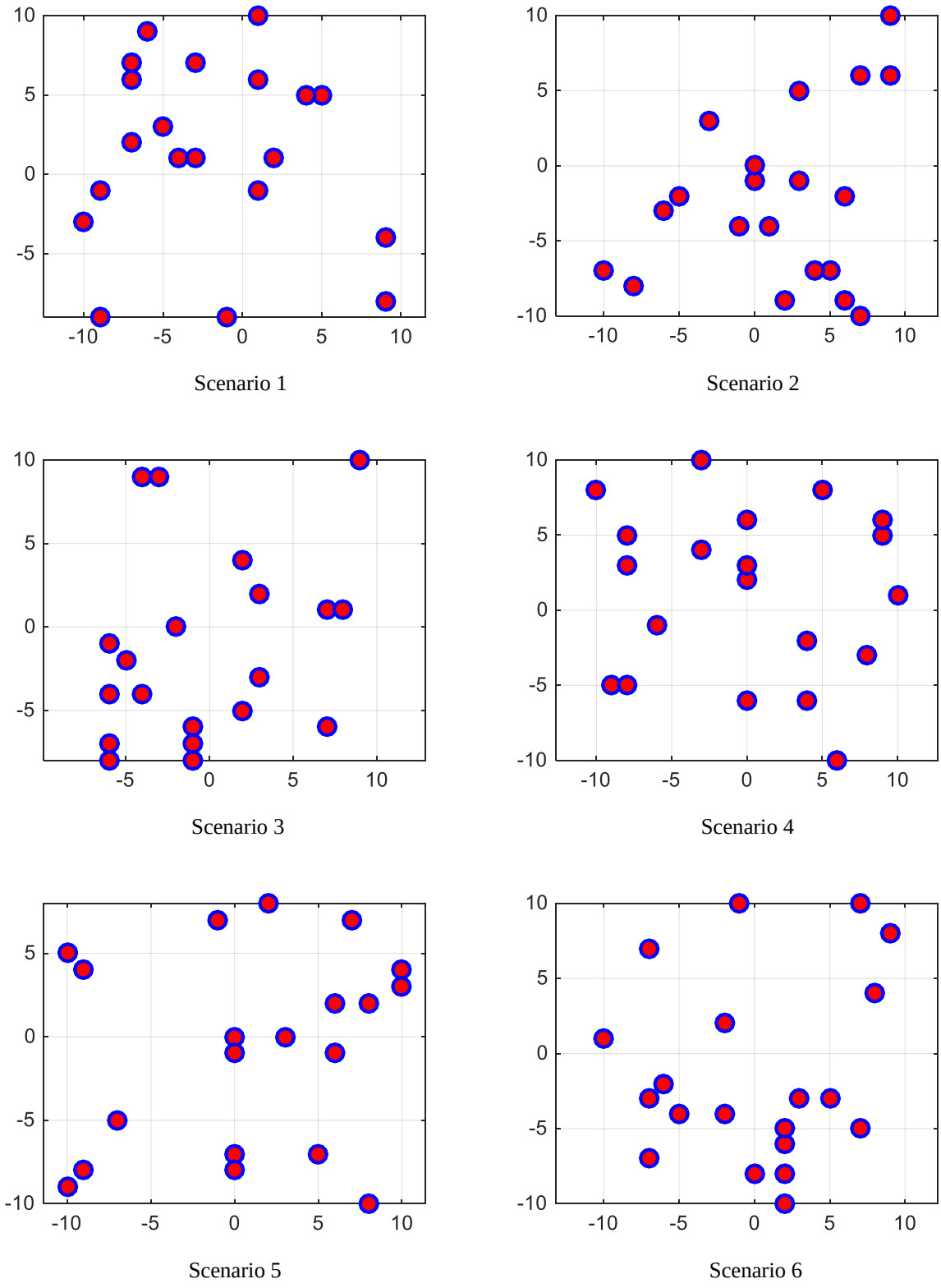

Fig. 7. The 6 investigated scenarios in [19] with 20 sensors spread in a square region with (20 [m] x 20 [m]) dimensions.

For a fair comparison, five runs have been performed for each scenario, and the best results are tabulated in Table 2 and graphically represented in Fig. 8. The following comments can be made from Table 2:

- The ESDA achieved the following results: -5.044 [dBm], -7.683 [dBm], -6.26 [dBm], -5.044 [dBm], -7.288 [dBm] and -4.507 [dBm], for scenarios 1 through 6, respectively.
- The ESDA achieved better results in 4 out of 6 scenarios, i.e., scenario 1, scenario 2, scenario 3 and scenario 5.
- The ESDA achieved the second-best result in 2 scenarios, i.e., scenario 4 and scenario 6, where the PSO achieved the best results.
- The ESDA was able to solve all scenarios while BH could not solve 2 scenarios and EM was not able to solve 3 scenarios.

The curves of convergence obtained using the proposed ESDA for the investigated scenarios are sketched in Fig. 9. The x-axis and y-axis represent the iterations and objective function, respectively. The following comments can be made from that figure:

- The ESDA has converged, i.e., most of the objective function minimization is achieved while solving all the scenarios before 300 iterations. This shows the excellent convergence ability of the ESDA, as reported in the literature.
- The objective function in almost all the scenarios is infinity at the first iterations of the optimization process. This is because the connection between sensors was not achieved initially.

The sensor transmission powers for each sensor for the investigated scenarios obtained using the ESDA are tabulated in Table 3. The following can be noticed from the table:

- The transmission power of each sensor is different from the remaining sensors.
- Depending on the scenario, the transmission is different from one scenario to another.
- The minimum sensor transmission powers for scenarios 1 through 6 are -28.329 [dBm], -28.328 [dBm], -28.329 [dBm], -28.330 [dBm], -28.328 [dBm] and -28.318 [dBm], respectively.
- The maximum sensor transmission powers for scenarios 1 through 6 are -10.262 [dBm], -15.775 [dBm], -9.192 [dBm], -14.350 [dBm], -15.776 [dBm] and -11.797 [dBm], respectively.
- The average sensor transmission powers for scenarios 1 through 6 are -21.327 [dBm], -22.547 [dBm], -23.809 [dBm], -20.502 [dBm], -22.725 [dBm] and -20.059 [dBm], respectively.

Table 2: Results comparison using different algorithms

Algorithm	ESDA [dBm]	PSO [19] [dBm]	Simplistic Method [19] [dBm]	DE [dBm]	GA [dBm]	BH [dBm]	EM [dBm]	SSA [dBm]	SCA [dBm]
Scenario 1	**-5.044**	-3.624	2.827	-4.026	-0.343	Inf	Inf	-4.074	4.353
Scenario 2	**-7.683**	-6.669	-2.699	-6.758	-1.090	-6.798	7.214	-5.841	7.636
Scenario 3	**-6.260**	-3.353	2.827	-5.725	-2.499	-5.112	5.878	-5.161	7.610
Scenario 4	**-5.044**	-5.113	3.842	-4.014	-0.529	-4.281	Inf	-3.389	8.473
Scenario 5	**-7.288**	-6.669	-2.744	-6.475	-1.639	-6.031	3.445	-3.400	5.682
Scenario 6	**-4.507**	-5.226	3.865	-3.363	1.766	Inf	Inf	-0.541	6.532

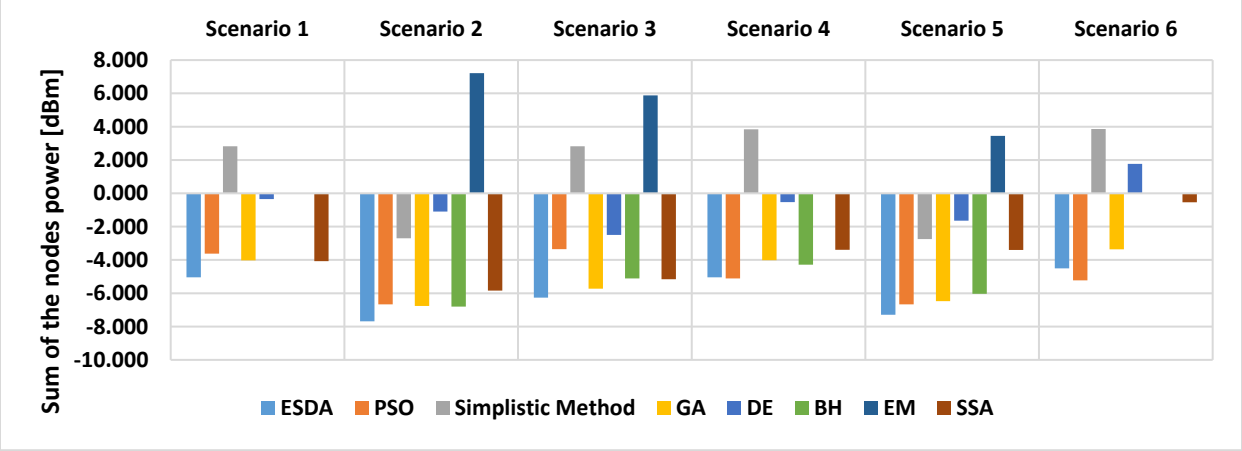

Fig. 8. Sum of all sensor nodes transmission power (fitness) for different methods.

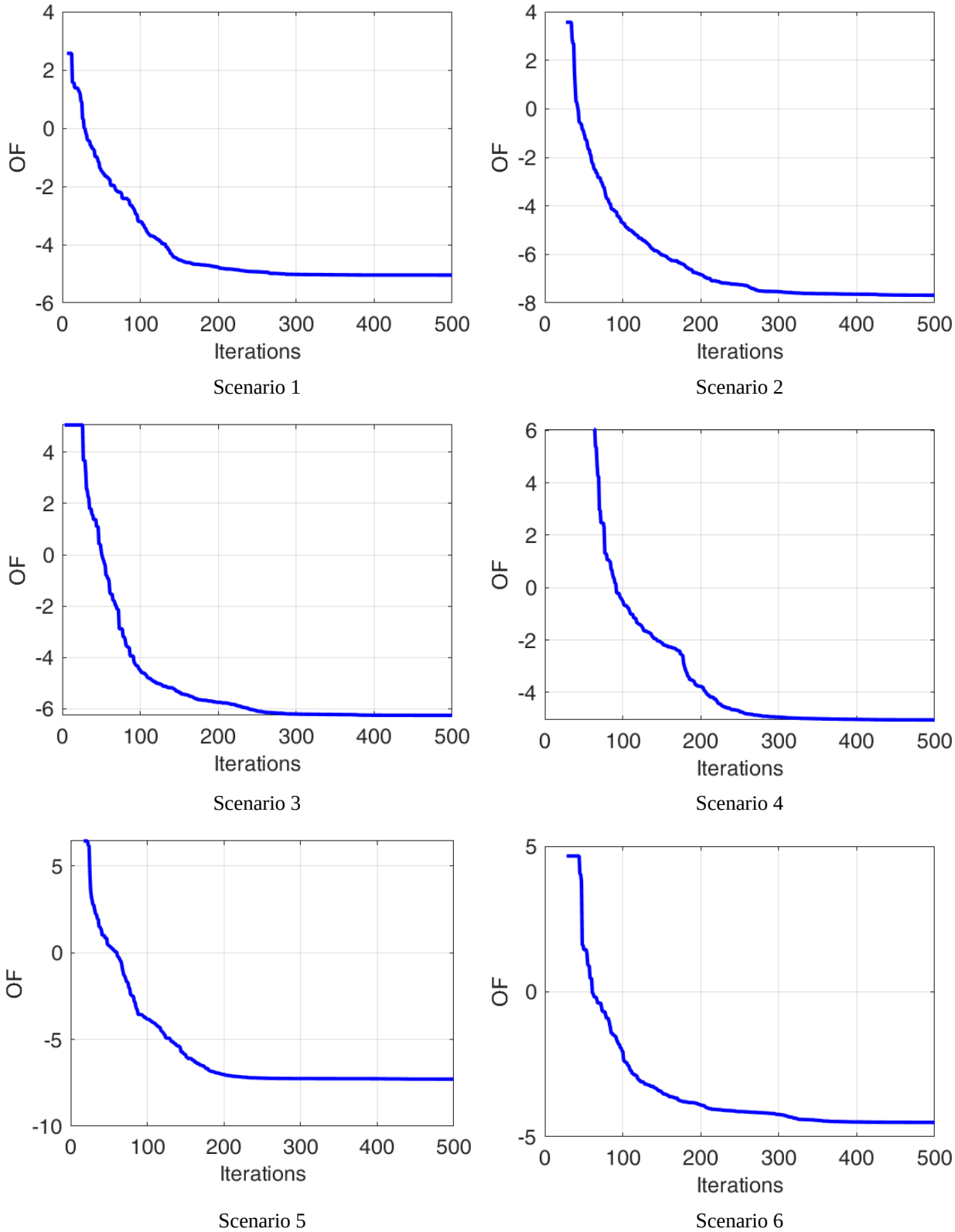

Fig. 9. Convergence curves of the ten investigated scenarios obtained using ESDA.

Table 3: The sensor transmission powers for each sensor for the six investigated scenarios obtained using the ESDA

	Scenario 1	Scenario 2	Scenario 3	Scenario 3	Scenario 5	Scenario 6
Sensor 1	-17.190	-18.329	-21.340	-28.329	-25.314	-14.349
Sensor2	-21.340	-25.318	-28.322	-15.318	-28.328	-16.025
Sensor 3	-16.288	-21.334	-28.326	-28.307	-22.232	-25.298
Sensor 4	-28.253	-16.288	-28.328	-28.317	-18.329	-11.797
Sensor 5	-28.327	-19.296	-21.326	-15.319	-22.308	-11.797
Sensor 6	-12.648	-25.302	-22.308	-16.025	-17.190	-22.296
Sensor 7	-18.330	-25.319	-28.329	-16.288	-15.776	-25.314
Sensor 8	-16.289	-21.339	-14.350	-28.326	-28.327	-22.307
Sensor 9	-21.333	-16.025	-28.329	-16.284	-28.324	-28.318
Sensor 10	-21.340	-18.784	-25.319	-14.350	-28.321	-13.278
Sensor 11	-28.315	-22.308	-28.320	-17.190	-25.313	-21.337
Sensor 12	-28.329	-28.325	-28.329	-28.328	-25.319	-28.297
Sensor 13	-21.340	-28.318	-9.192	-28.330	-28.326	-19.295
Sensor 14	-21.340	-15.775	-28.251	-18.328	-15.777	-22.307
Sensor 15	-28.328	-25.318	-25.315	-22.309	-15.777	-22.307
Sensor 16	-10.262	-22.306	-21.340	-22.307	-18.787	-19.295
Sensor 17	-21.340	-28.328	-21.340	-18.758	-28.325	-19.298
Sensor 18	-28.328	-22.308	-28.324	-15.319	-18.787	-22.303
Sensor 19	-16.289	-28.317	-22.309	-16.024	-18.328	-18.770
Sensor 20	-21.339	-22.308	-17.190	-16.288	-25.313	-17.190

V. CONCLUSION

In this work, the ESDA has been proposed and applied to save energy in a WSN by determining different sensor powers under the constraint of all nodes must be connected. This algorithm has been compared to PSO, GA, DE, BH, EM, SSA, and SCA, found in the literature, and the results are found to be satisfactory. In 4 cases out of 6, the ESDA has obtained results than the PSO. In all cases, the ESDA has been able to converge to a solution (i.e., to find a fully connected network).

In future, different frequencies to account for other technologies like WiFi, WiMax, Zigbee, and Bluetooth can be included. Furthermore, transmission rates and power consumption can also be included in the order in order to evaluate their effects on energy-saving and network connectivity.

ACKNOWLEDGEMENT

The authors extend their appreciation to the Deanship of Scientific Research, University of Hafr Al Batin for funding this work through the research group project No G-101-2020.

REFERENCES

[1] X. Li and H. Jiang, "Artificial intelligence technology & engineering applications," *Appl. Comput. Electromagn. Soc. J.*, vol. 32, no. 5, pp. 381-388, 2017.

[2] V. Rodoplu and T. H. Meng, "Minimum energy mobile wireless networks," in *International Conference on Communications - Proceedings*, vol. 3, pp. 1633-1639, 1998.

[3] S. Jahanbakhsh, M. Ojaroudi, and S. Kazemi, "Small low power rectenna for wireless local area network (WLAN) applications," *Appl. Comput. Electromagn. Soc. J.*, vol. 30, no. 3, pp. 332-337, 2015.

[4] X. Jin, J. M. Caicedo, and M. Ali, "Near-field Wireless power transfer to embedded smart sensor antennas in concrete," *Appl. Comput. Electromagn. Soc. J.*, vol. 30, no. 3, pp. 261-269, 2015.

[5] D. Murali and N. Ida, "An ultra-low power sensing node for use with harvested power," in *29th Annual Review of Progress in Applied Computational Electromagnetics*, 2013.

[6] A. A. Aziz, Y. A. Şekercioğlu, P. Fitzpatrick, and M. Ivanovich, "A survey on distributed topology control techniques for extending the lifetime of battery powered wireless sensor networks," *IEEE Communications Surveys and Tutorials*, vol. 15, no. 1. pp. 121-144, 2013.

[7] R. V. Kulkarni and G. K. Venayagamoorthy, "Particle swarm optimization in wireless-sensor networks: A brief survey," *IEEE Trans. Syst. Man. Cybern. Part C Appl. Rev.*, vol. 41, no. 2, pp. 262-267, Mar. 2011.

[8] R. M. Shubair, S. A. Jimaa, and A. A. Omar, "Robust adaptive beamforming using least mean mixed norm algorithm," *Appl. Comput. Electromagn. Soc. J.*, vol. 23, no. 3, pp. 262-269, 2008.

[9] H. P. Gupta, S. V. Rao, A. K. Yadav, and T. Dutta, "Geographic routing in clustered wireless sensor networks among obstacles," *IEEE Sens. J.*, vol. 15,

no. 5, pp. 2984-2992, May 2015.
[10] O. Younis, M. Krunz, and S. Ramasubramanian, "Node clustering in wireless sensor networks: Recent developments and deployment challenges," *IEEE Netw.*, vol. 20, no. 3, pp. 20-25, May 2006.
[11] G. Zheng and Q. Liu, "A survey on topology control in wireless sensor networks," *2nd Int. Conf. Futur. Networks, ICFN 2010*, pp. 376-380, 2010.
[12] A. A. Abbasi and M. Younis, "A survey on clustering algorithms for wireless sensor networks," *Comput. Commun.*, vol. 30, no. 14-15, pp. 2826-2841, Oct. 2007.
[13] M. Haneef and D. Zhongliang, "Design challenges and comparative analysis of cluster based routing protocols used in wireless sensor networks for improving network life time," *Advances in Information Sciences and Service Sciences*, vol. 4, no. 1, pp. 450-459, Jan. 2012.
[14] H. T. Friis, "A note on a simple transmission formula," *Proc. IRE*, vol. 34, no. 5, pp. 254-256, 1946.
[15] H. R. E. H. Bouchekara, "Electrostatic discharge algorithm (ESDA): A novel nature-inspired optimization algorithm and its application to worst-case tolerance analysis of an EMC filter," *IET Sci. Meas. & Technol.*, pp. 1-11, 2019.
[16] M. Masugi, "Multiresolution analysis of electrostatic discharge current from electromagnetic interference aspects," *IEEE Trans. Electromagn. Compat.*, vol. 45, no. 2, pp. 393-403, 2003.
[17] F. Drake, *et al.*, *IEEE Guide On Electrostatic Dischage (ESD) Characterization of the ESD Enviroment*, 1993.
[18] "Electrostatic Discharge: Causes, Effects, and Solutions | Electrical Construction & Maintenance (EC&M) Magazine." [Online]. Available: http://www.ecmweb.com/content/electrostatic-discharge-causes-effects-and-solutions. [Accessed: Jan. 2, 2018].
[19] G. L. Da Silva Fre, J. De Carvalho Silva, F. A. Reis, and L. Dias Palhao Mendes, "Particle swarm optimization implementation for minimal transmission power providing a fully-connected cluster for the Internet of Things," in *IWT 2015 - 2015 International Workshop on Telecommunications*, 2015.

Mohammed A. Alanezi is an Associate Professor in the Department of Computer Science in the Department of Computer Science and Engineering Technology of the University of Hafr Al-Batin University where he has been serving as Vice-rector for Academic Affairs. His research interests include eGovernment, E-Services, E-Health, IoT and Knowledge Management. He contributes also to the development of various projects and systems; much of his work has been in embracing digital transformation and improving the current technology to solve challenges facing the University of Hafr Al-Batin.

Houssem R. E. H. Bouchekara is a Full Professor at the Electrical Engineering Department of the University of Hafr Al Batin. He has received his B.S. in Electrical Engineering from University Mentouri Constantine, Algeria, in 2004. He has received his Master in Electronic Systems and Electrical Engineering from Polytechnic School of the University of Nantes, France, 2005. He received his Ph.D. in Electrical Engineering from Grenoble Institute of Technology, France, in 2008. His research interest includes: Optimization techniques, Magnetic refrigeration, Electromagnetics, Electric machines, and Power systems

Muhammad Sharjeel Javaid received his B.S. in Electronic Engineering from GIK Institute, Pakistan in 2013. Later he completed his M.S. in Electrical Engineering from King Fahd University of Petroleum and Minerals, Saudi Arabia, in 2017. He has worked as an active member of the IET GIKI Chapter, and as general secretary in the IEEE KFUPM Chapter. Currently, he is serving as Lecturer at the University of Hafr al Batin. He has a keen interest to work on Energy Markets, Distributed Generation Optimization.

Compact Tri-Band Microstrip Patch Antenna Using Complementary Split Ring Resonator Structure

N. Rajesh Kumar [1], P. D. Sathya [2], S. K. A. Rahim [3], M. Z. M. Nor [4], Akram Alomainy [5], and Akaa Agbaeze Eteng [6]

[1,2] Department of Electronics and Communication Engineering, Annamalai University, India
rajeshavc2004@gmail.com, pd.sathya@yahoo.in

[3] Wireless Communication Center (WCC), Universiti Teknologi Malaysia, UTM Skudai Johor Malaysia
sharulkamal@fke.utm.my

[4] Faculty of Electrical Engineering, Universiti Teknologi Mara (UiTM) Johor, Kampus Pasir Gudang Masai, Johor Malaysia
zairil398@uitm.edu.my

[5] School of Electronic Engineering and Computer Science, Faculty of Science and Engineering
Queen Mary University of London, Mile End Road, London E1 4NS, UK
alomainy@qmul.ac.uk

[6] Department of Electrical/Electronic Engineering, Faculty of Engineering, University of Port Harcourt, Nigeria
akaa.eteng@uniport.edu.ng

Abstract – In this letter, a compact complementary split ring based tri-band antenna is proposed. The proposed antenna resonates at 1.9 GHz (1.70-1.91 GHz), 2.45 GHz (2.23-2.52 GHz) and 3.2 GHz (2.9-3.25 GHz); the input match values are 24.56 dB, 27.21 dB and 22.46 dB, respectively. The antenna's realised peak gain is 4.15 dBm at 1.9 GHz, 4.25 dBm at 2.4 GHz and 4.74 dBm at 3.2 GHz, with approximately 42% of reduction in antenna size. The results demonstrate that the proposed metamaterial antenna is tunable, electrically small and highly efficient, which makes it a suitable candidate for RF energy harvesting. The antenna is numerically and experimentally analysed and validated with very good comparison between the simulated and measured results.

Index Terms – CSRR, patch antenna, radiation pattern, tri-band.

I. INTRODUCTION

In the advancement of wireless communication systems, low-profile interconnecting devices and non-complex proprietary structures are required, often operating in multiband frequencies [1]. L and S Band operating systems, with applications such as 3G (1.9 GHz), WLAN (2.45 GHz) and WiMAX (2.5-2.69 GHz) are size-constrained [2]. Although microstrip patch antennas are required to satisfy these requirements of modern communication systems, general microstrip patch antennas fail due to small bandwidths, radiation inefficiency, and heavy general weights [3]. In order to overcome the limitations of standard microstrip patch antennas, extensive research has been conducted by many investigators in an attempt to realize compact multiband designs [4].

Various methods have been reported to achieve a reduced size of the printed multiband antenna. Metamaterials have been used in designing low-profile multiband antennas [5]. Recent work in literature has shown that rectangular microstrip patch antennas loaded with mender lines facilitate multiband performance, with continuous size reduction [6]. In addition, a small-scale multiband antenna design by U and L strips, with a grounded defected structure to increase the antenna radiation strength and improve impedance simulation ability is shown in [7]. In [8, 9], fractal antennas with a magnitude associated with multiband performance are studied. In recent years, the coplanar waveguide (CPW) feeding approach has attracted a lot of research and development activities, as it improves the performance of multiband characteristics. Employing a single-metallic layer CPW has several advantages such as simple integration of passive and active elements, less dispersion, low cost, less surface waves and good omnidirectional pattern, compared to other feeding techniques [10-13]. Recent surveys introduce many CPW-fed microstrip patch antennas for WLAN and WiMAX applications

Submitted On: July 25, 2020
Accepted On: January 24, 2021
https://doi.org/10.47037/2020.ACES.J.360314

[14-19]. A straight strip of CPW-fed antenna with asymmetrical ring and inverted L strip [14] achieved tri-band frequencies covering WLAN (2.4 GHz, 5.2 GHz, and 5.8 GHz) bands and WiMAX (3.5 GHz, 5.5 GHz) bands. A CPW-fed monopole antenna with a band-notch at 1.4 GHz was described in [15]. Inclusion of open split-ring resonator (SRR) antenna with tri-band metamaterial covering 2.4 GHz, 5.2 GHz and 5.8 GHz (WLAN), 5.5 GHz (WiMAX) and 7.4 GHz (C-band) applications are employed, as in [16]. The role of metamaterials in the development of electrically small antennas, and how the efficiency of antennas is improved, are demonstrated in [17]. In [18], the work demonstrates the electrically small printed monopole antenna with two SRRs to achieve multiple resonance and printed slot antenna using DGS also used to achieve multiband is studied in [20]. In [21], using non-foster active elements increased the bandwidth significantly for SRR-based monopole antenna. However, in [20-29] the individual SRR performances to achieve required resonant frequencies are not explained, in addition to increases in the turns to achieve the multiband performance. Even though various compact, multiband operation antennas have been proposed, most of the designed antennas incorporate additional elements to realize the design objectives. In this work, in order to overcome the above drawbacks, a new antenna is introduced, namely a tri-band Complementary Split Ring Resonator (CSRR) antenna for L band and S ban2l8/wk7fg. The antenna is designed based on the equivalent circuit of spiral inductor modelling, and it is converted into a complimentary split ring resonator. An efficient CSRR unit cell antenna can be radiated at three required frequencies. According to Babinet's principle, the CSRR structure can be obtained from a SRR by inverting the copper parts on the antenna patch. Due to the concept of duality, these two structures resonate at almost the same frequency. The resonance in quasistatic resonators such as CSRRs and SRRs is the result of the interplay between the distributed capacitance and inductance of the structure. However, the main difference between both is that the SRR has negative permeability features, while the CSRR has negative permittivity features. These resonators are considerably reduced in size compared to conventional resonators, which have dimensions comparable to the wavelength, and resonance occurring based on the phase distribution. The proposed antenna is printed on FR4 substrate with 1.6 mm thickness and modelled and analysed by using the ANSYS HFSS 16 simulator tool. Simulations and measurements show that the proposed antenna gives good results in terms of operating frequency bands and omnidirectional patterns, as well as stable gain and radiation efficiencies.

II. ANTENNA DEVELOPMENT

In [23], the authors present the individual performance of split ring resonators. The corrected mathematical model predicts the left-hand behavior of split ring resonator-based metamaterial that shows it could resonate at several frequency bands [24-29]. Figure 1 shows the equivalent circuit of individual split ring resonator turns. This in turn shows that this method could be a systemized approach to design multiband antennas. As per the Babinet principle, split ring resonators are changed into CSRR to obtain the required frequencies.

The calculation of resonance frequency uses the formula [20]:

$$f_n = \frac{1}{2\pi\sqrt{L_D C_n}}. \quad (1)$$

Based on [17], the equivalent inductors and capacitors are approximately calculated for the four side of the split ring resonators, as show in Fig. 1. The self-inductors L_1, L_2, L_3, L_4 can be directly calculated by using the formulas,

$$L_D = K\frac{\mu_0 n^2 L}{2\Pi}\ [ln(\frac{2}{\rho}) + 0.5 + 0.178\rho + 0.0146\rho^2 + \frac{0.5(n-1)S^2}{(\rho n)^2}\ 0.178\frac{(n-1)S}{n} - \frac{1}{n}ln(\frac{W+t}{W})], \quad (2)$$

$$\rho = \frac{nW+(n-1)S}{L}, \quad (3)$$

$$K = \frac{(2L-2S)-D}{(2L-2S)}, \quad (4)$$

where t, n, W, S indicate the thickness, number of turns, width, and space between inner and outer rings of SRR, respectively. The calculation of distributed capacitance of SRR depends on two parameters, namely, the coupling capacitance between the outer and inner rings (C_0), and electric charge capacitance at the split's gaps (CCi).

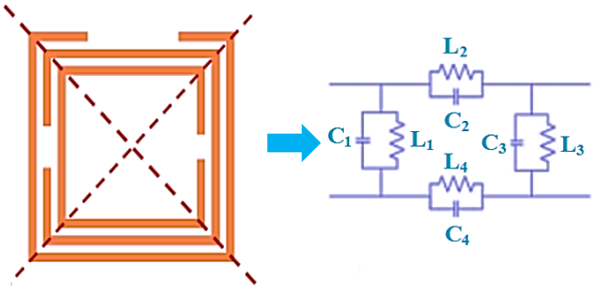

Fig. 1. Equivalent circuit model.

These capacitances can be estimated using the equations (5) and (6),

$$C_0 = \frac{1}{4}[0.06 + 3.5 \times 10^{-5}(R_{out} + R_{in})], \quad (5)$$

$$c_{ci} = \epsilon_0 \epsilon_r \frac{Wt}{ci}. \quad (6)$$

Here R_{out} and R_{in} indicate the radii of the outer and inner circumscribed circles of the SRR, respectively. The distributed capacitances of each side can then be

calculated as the sum of these capacitances, using these equations,

$$C_1 = C_0 + C_{C1}, \quad (7)$$

$$C_2 = C_0 + C_{C2}, \quad (8)$$

$$C_3 = C_0 + C_{C3}, \quad (9)$$

$$C_4 = C_0 + C_{C4}. \quad (10)$$

By using these mathematical expressions, the dimensions of the SRR are calculated and then tuned to achieve the desired frequencies of interest. The SRR is changed into a CSRR by the Babinet principle. The Table 1 shows the L_D and C_n values for each frequency of antenna results and compares analytical and simulated results.

Table 1: Comparison of analytical and simulated frequencies

Inductor (L_D)	Capacitor (C_n)	Analytical Resonating Frequency (GHz)	Simulated Resonating Frequency (GHz)
5.01 nH	1.2 pF	2.05	1.9
4.16 nH	1.02 pF	2.44	2.45
3.57 nH	0.72 pF	3.14	3.2

The analysis shows the difference between the analytical and simulated resonate frequencies with respect to inductor and capacitor values. In order to gets desired frequency using antenna design software the dimensions are varied, and all the calculated parameter are simulated and optimized in order to obtain a tri-band antenna at desired operating frequencies.

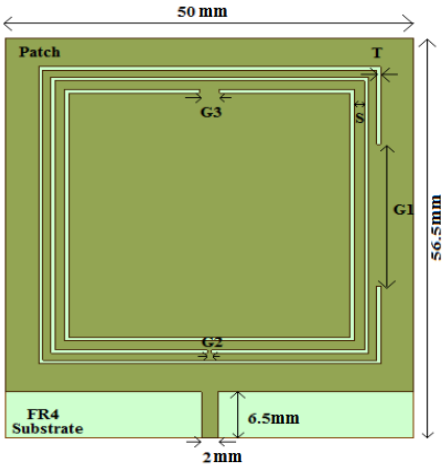

Fig. 2. Antenna geometry.

Then, the antenna is fabricated on FR4 substrate with 1.6 mm substrate height and a loss factor tan δ = 0.02. The final geometrical shape of the antenna is shown in Fig. 2 and its geometrical parameters are shown in Table 2.

Table 2: Design specification for the proposed antenna model

Parameter	Specifications (mm)
Substrate (FR4)	1.6
Length, width and thickness of substrate	50 × 56.5 × 1.6
Length and width of patch	50 × 50
Length and width of feed strip	6.5 × 2
Length of outer ring	42
Length of middle ring	39
Length of inner ring	35.5
Spacing between ring (S)	2
Thickness of the ring (T)	0.5
G1	20
G2	0.5
G3	1.5

III. PARAMETRIC ANALYSIS OF PROPOSED CSRR

The parametric analysis of Gap G1 in spiral rings plays an important role to determine the performance of the antenna. So, the analysis on the dimension of the Gaps G1 and their effect on Reflection Coefficient (dB) are shown in Fig. 3. From the graph, it is inferred that the antenna attains better impedance characteristics at G1=20 mm where it gives the triple operating band behaviour. It also shows that with G1 equal to 15mm and 25 mm, inferior triple band characteristics, as compared to G1=20 mm, are obtained. Hence G1=20 mm it considered an optimum dimension for G1. Next, The Gap G2 in spiral rings also plays a crucial role in determining the performance of the antenna and hence a parametric analysis on the effect of G2 on reflection coefficient (dB) is performed and shown in Figure 4. It is inferred that the antenna attains better impedance characteristics at G2=0.5 mm. Since this value provides better performance at desired operating bands, it is considered as an optimum dimension for G2.

Lastly, the impact of gap G3 on the performance of the antenna is shown in Fig. 5. It is shows that the antenna attains better impedance characteristics at G3= 2.5 mm at the desired operating bands, and hence it is considered as an optimum dimension for G3.

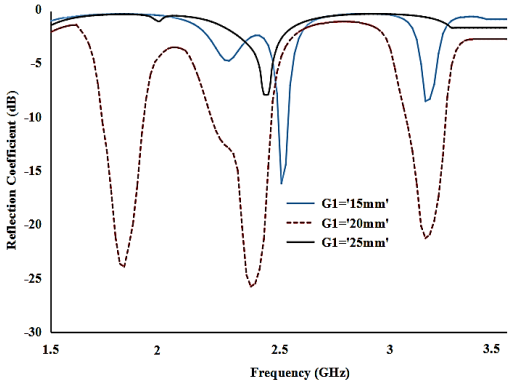

Fig. 3. Effect of Gap G1 on reflection coefficient (dB).

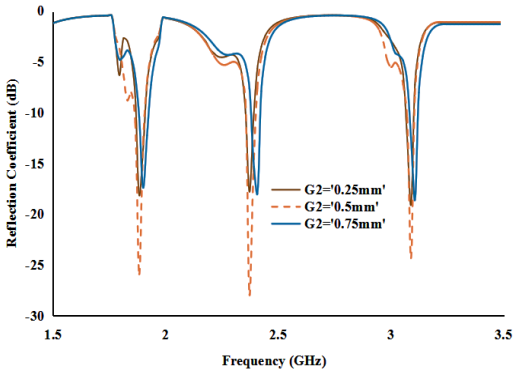

Fig. 4. Effect of Gap G2 on reflection coefficient (dB).

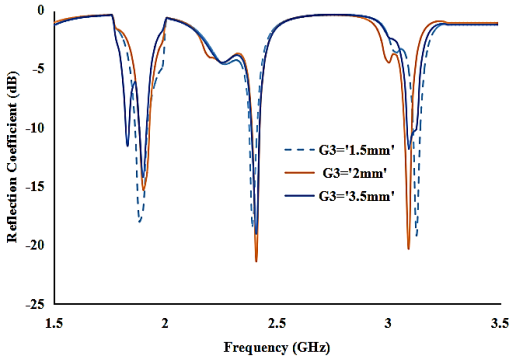

Fig. 5. Effect of Gap G_3 on reflection coefficient (dB).

IV. RESULTS AND DISCUSSIONS

The performance of the antenna is validated by fabricating the prototype on FR4 substrate and its characteristics are measured. The fabricated proposed CSSR antenna and the measurement setup are shown in Fig. 6 and Fig. 7, respectively. Figure 8 shows the impedance characteristics of the antenna. The antenna operates at three different bands in the L and S band regions. The -10 dB impedance bandwidth covers 1.78-1.91 GHz, 2.23-2.52 GHz and 2.9-3.25 GHz. In Fig. 8, it can be seen that the measured and simulated results are comparable. However, the shift in measurement results are due to imperfect fabrication processes. Also, while simulations are based on a perfect substrate material, there are slight variations in the thickness and dielectric constant of commercially available materials, which influence the measurement results.

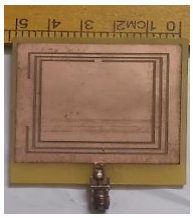

Fig. 6. Fabricated antenna.

Fig. 7. Network analyzer.

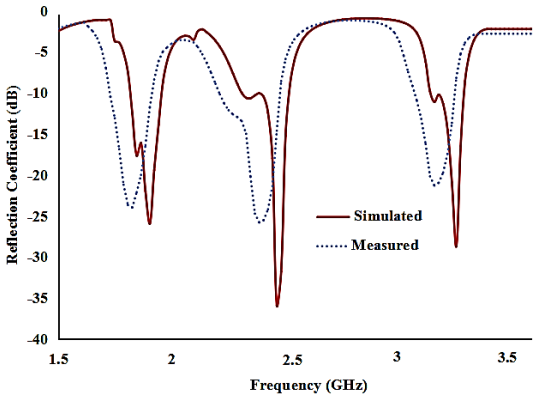

Fig. 8. Measurement and simulation impedance characteristics for proposed antenna.

In addition, the insertion loss of SMA connectors used, and connector losses have an effect on the response of the antenna. The radiation characteristic of the antenna is depicted in Fig. 9. It comprises of the radiation beam measured in both the E-plane and H-plane, and are compared with simulated results. The simulation and measured radiation characteristics of the proposed antenna operating at three different frequencies are plotted and compared. The results show clearly that the antenna gives symmetrical radiation and achieves a peak gain of 4.15 dBm at 1.9GHz, 4.25dm at 2.4GHz and

4.74dBm at 3.2GHz. A comparison of the proposed antenna with existing designs is presented in the Table 3.

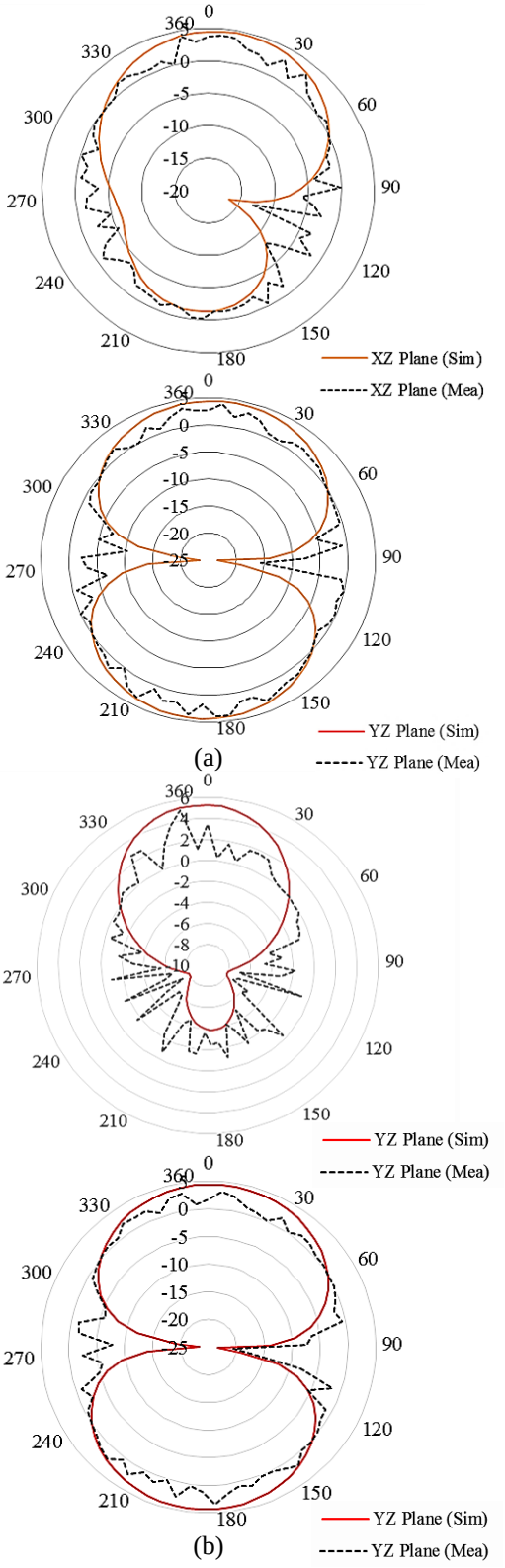

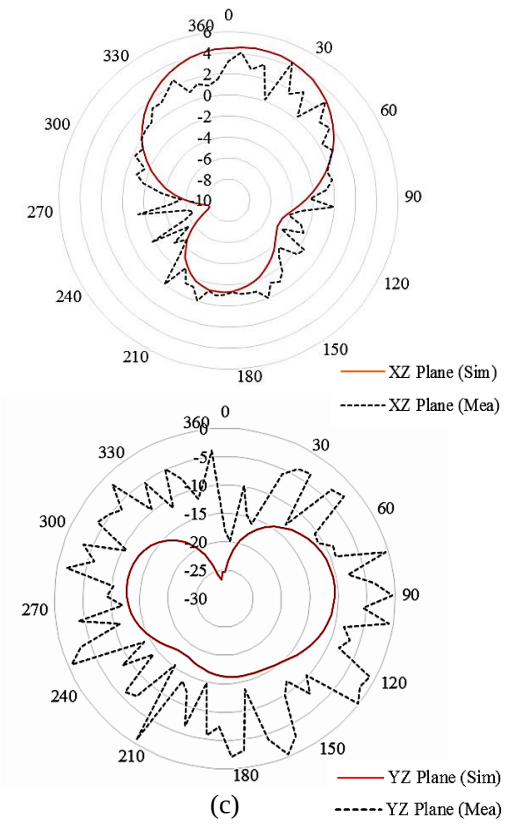

Fig. 9. Radiation characteristics of the antenna E-plane and H-plane: (a) (1.9GHz), (b) F_2 (2.45GHz), and (c) F_3 (3.2GHz).

It shows that the physical size of the proposed antenna is reduced by ~42 %. Due to its compact size, the proposed antenna is suitable for in-door wireless applications.

V. CONCLUSION

A novel metamaterial based antenna etched with a spiral shaped structure to behave as a complimentary split ring resonator (CSSR) antenna is presented. The antenna is fabricated on low cost FR4 substrate, and the geometrical parameters are optimized to yield better performance. The antenna operates at three distinct bands in the range 1.9 GHz (1.78-1.91 GHz), 2.45 GHz (2.23-2.52 GHz) and 3.2GHz (2.9-3.25 GHz). The peak gains of the proposed antenna are 4.15 dBm at 1.9 GHz, 4.25 dBm at 2.45 GHz and 4.74 dBm at 3.2 GHz, respectively. The design also accomplishes a miniaturization in size of around 42 % compared to existing solutions in the literature. The metamaterial antenna is tunable, electrically small and highly efficient, which makes it a suitable candidate for RF energy harvesting.

Table 3: Comparison of proposed antenna with existing antenna

Ref.	Year	Frequency Bands (GHz)	Return Loss (S11) (dB)	VSWR	Size of Antenna (mm^2)	Area (mm^2)
[30]	2013	1.81-1.87, 2.11-2.17	≈ 14,16	No data	145 × 55	7975
[31]	2018	1.8-2.45	≈ 18,26	No data	77 × 98	7546
[32]	2018	1.74-1.97, 2-2.22, 2.41-2.59	Not Mentioned	No data	70 × 65	4550
[33]	2019	1.7-1.925	≈ 30	No data	70 × 70	4900
This work		**1.9,2.45,3.19**	**24.56,27.21,22.46**	**1.09,1.05,1.12**	**50 x 56.5**	**2825**

REFERENCES

[1] W. W. Li, J. S. Su, J. H. Zhou, and Z. Y. Shi, "Compact wide triband multicavity coupled slot antenna," *Microwave and Optical Technology Letters*, pp. 157-163, 2017.

[2] H. Wong, K. M. Luk, C. H. Chan, Q. Xue, K. K. So, and H. W. Lai, "Small antennas in wireless communications," *Proceedings IEEE*, pp. 2109-2121, 2012.

[3] M. Fallahpour and R. Zoughi, "Antenna miniaturization rechniques," *IEEE Antenna and Propagation Magazine*, pp. 38-50, 2018.

[4] Geetanjali1 and R. Khanna, "A review of various multi-frequency antenna design techniques," *Indian Journal of Science and Technology*, pp. 1-6, 2017.

[5] T. Ali, M. M. Khaleeq, S. Pathan, and R. C. Biradar, "A multiband antenna loaded with metamaterial and slots for GPS/WLAN/WiMAX applications," *Microwave Optical and Technology Letters*, pp. 79-85, 2017.

[6] K. Srivastava, A. Kumar, and B. K. Kanaujia, "Design of compact penta-band and hexa-band microstrip antennas," *Frequenz*, pp. 101-111, 2016.

[7] Y. Mao, S. Guo, and M. Chen, "Compact dual-band monopole antenna with defected ground plane for internet of things," *IET Microwave and Antennas Propagation*, pp. 1332-1338, 2018.

[8] D. K. Naji, "Compact design of dual-band fractal ring antenna for WiMAX and WLAN applications," *International Journal of Electromagnetics and Applications*, pp. 42-50, 2016.

[9] V. Sharma, N. Lakwar, N. Kumar, and T. Garg, "Multiband low-cost fractal antenna based on parasitic split ring resonators," *IET Microwave and Antennas Propagation*, pp. 913-919, 2018.

[10] R. Pandeeswari and S. Raghavan, "A CPW-fed triple band OCSRR embedded monopole antenna with modified ground for WLAN and WIMAX applications," *Microwave and Optical Technology Letters*, pp. 2413-2418, 2015.

[11] C. Elavarasi and T. Shanmuganantham, "Multiband SRR loaded Koch star fractal antenna," *Alexandria Engineering Journal*, pp. 1-7, 2017.

[12] M. S. Sedghi, M. N.Moghadasi, and F. B. Zarrabi, "A dual band fractal slot antennaloaded with Jerusalem crosses for wireless and WiMAX communications," *Progress in Electromagnetics Research Letters*, pp. 19-24, 2016.

[13] A. KarimbuVallappil, B. A. Khawaja, I. Khan, and M. Mustaqim, "Dual-band Minkowski–Sierpinski fractal antenna for next generation satellite communications and wireless body area networks," *Microwave and Optical Technology Letters*, pp. 171-178, 2017.

[14] S. Huang, J. Li, and J. Zhao, "Miniaturized CPW-fed triband antenna with asymmetric ring for WLAN/WiMAX applications," *Hindawi Publishing Corporation Journal of Computer Networks and Communications*, 2014.

[15] T. Mandal and S. Das, "Coplanar waveguide fed 9-point star shape monopole antennas for worldwide interoperability for microwave access and wireless local area network applications," *The Journal of Engineering*, no. 4, pp. 155-160, 2014.

[16] R. Rajkumar and K. Usha Kiran, "A metamaterial inspired compact open split ring resonator antenna for multiband operation," *Wireless Personal Communication*, 2017.

[17] K. B. Alici and E. Ozbay, "Electrically small split ring resonator antennas," *J. Appl. Phys.*, vol. 101, p. 08314, 2007.

[18] M. Barbuto, F. Bilotti, and A. Toscano, "Design of a multifunctional SRR-loaded printed monopole antenna," *Int. J. RF Microw., CAE*, vol. 22, pp. 552-557, 2012.

[19] M. Barbuto, A. Monti, F. Bilotti, and A. Toscano, "Design of a non-foster actively loaded SRR and application in metamaterial-inspired components," *IEEE Transactions on Antennas and Propagation*, vol. 61, no. 3, pp. 1219-1227, Mar. 2013.

[20] M. F. Wu, F. Y. Meng, Q. Wu, J. Wu, and L. W. Li, "A compact equivalent circuit model for the SRR structure in metamaterials," *Asia-Pacific Microwave Conference Proceeding*, pp. 5-8, 2005.

[21] Q. Wu, M.-F. Wu, F.-Y. Meng, J. Wu, and J. Li, "Research on SRR structure metamaterial based on

transmission line theory," *Dianbo Kexue Xebio/ Chinese Journal of Radio Science*, pp. 310-314, 2006.

[22] Q. Wu, M. F. Wu, F. Y. Meng, J. Wu, and L. W. Li, "Modeling the effects of an individual SRR by equivalent circuit method," *IEEE Antennas and Propagation Society, AP-S International Symposium (Digest)*, 2005.

[23] A. Salim and S. Lim, "Complementary split-ring resonator-loaded microfluidic ethanol chemical sensor," *Sensors (Switzerland)*, pp. 1-13, 2016.

[24] A. Albishi and O. M. Ramahi, "Detection of surface and subsurface cracks in metallic and non-metallic materials using a complementary split-ring resonator," *Sensors (Switzerland)*, pp.19354-19370, 2014.

[25] J. D. Baena, J. Bonache, F. Martín, R. M. Silero, F. Falcone, T. Lopetegi, J. Garcia-Garcia, I. Gil, M. F. Partilo, and M. Sorolla, "Equivalent-circuit models for split-ring resonators and complementary split-ring resonators coupled to planar transmission lines," *IEEE Transactions on Microwave Theory and Technology*, pp. 1451-1460, 2005.

[26] F. Falcone, T. Lopetegi, M. A. G. Laso, J. D. Baena, J. Bonache, F. Martín, and R. M. Silero, "Babinet principle applied to the design of metasurfaces and metamaterials," *Physical Review Letters*, pp. 1-4, 2004.

[27] R. Marqués, J. D. Baena, F. Martín, and J. FJ. Bonache, "Left handed metamaterial based on dual split ring resonators in microstrip," *Proceeding International URSI*, pp. 23-27, 2004.

[28] M. F. Wu, K. Y. Meng, Q. Wu, J. Wu, and L. W. Li, "A compact equivalent circuit model for the SRR Structure in metamaterials," *Asia Pacific Microwave Conference Proceedings*, pp.5-8, 2005.

[29] H. Sun, Y. X. Guo, M. He, and Z. Zhong, "A dual-band rectenna using broadband Yagi antenna array for ambient rf power harvesting," *IEEE Antennas Wireless and Propagation Letters*, pp. 918-921, 2013.

[30] H. Takhedmiti, L. Cirio, and Z. Saddii J.D., and L. S. Luk, "A novel dual-frequency rectifier based on an 1800 hybrid junction for RF energy harvesting," *7th European Conference Antennas Propagation (EUCAP)*, pp. 2472-2475, 2013.

[31] Z. Li, M. Zeng, and H. Z. Tan. "A multi-band rectifier with modified hybrid junction for RF energy harvesting," *Microwave and Optical Technology Letters*, pp. 817-821, 2018.

[32] Z. Li, M. Zeng, and H. Z. Tan, "A multi-band rectifier with modified hybrid junction for RF energy harvesting," *Microwave and Optical Technology Letters*, pp. 817-821, 2018.

[33] M. A. Gozel, M. Kahriman, and O. Kasar, "Design of an efficiency enhanced Greinacher rectifier operating in the GSM 1800 band by using rat-race coupler for RF energy harvesting applications," *International journal of RF Microwave and Computer Engineering*, pp. 1-18, 2019.

N. RajeshKumar is a Research Scholar pursuing his Ph.D. degree at Department of Electronics and Communication Engineering, Annamalai University, Annamalai Nagar, Chidambaram, India. His current research interest includes antenna design and RF circuits.

P.D. Sathya is an Assistant Professor in the Department of Electronics and Communication Engineering at Annamalai University, India. She obtained B.E. (Electronics and Communication), M.E. (Applied Electronics) and Ph.D. degrees from Periyar University, Anna University and Annamalai University in the years 2003, 2005 and 2012, respectively. She has 15 years of experience in teaching and research & development with specialization in Signal Processing, Image and Video Processing and Communication fields. She has published more than 40 research papers in reputed International Journals including Elsevier and Inderscience, has presented 30 and above papers in various International Conferences. She has guided one Ph.D. scholar and 06 research scholars are doing research under her guidance. She has been a part of various seminars, paper presentations, research paper reviews, and conferences as a convener and a session chair, a guest editor in journals. Her Research interests include Signal Processing, Image and video processing and Optimization Techniques Applied to various Image Processing Applications.

Sharul Kamal Abdul Rahim received the degree in Electrical Engineering from The University of Tennessee, USA, the M.Sc. degree in Engineering (Communication Engineering) from Universiti Teknologi Malaysia (UTM), and the Ph.D. degree in Wireless Communication System from the University of Birmingham, U.K., in 2007. After his graduation from The University of Tennessee, he spent three years in industry. After graduating the M.Sc. degree, he joined UTM in 2001, where he is currently a Professor with the Wireless Communication Centre. He has published over

200 learned papers, including the IEEE Antenna and Propagation Magazine, the IEEE Transactions on Antenna and Propagation, IEEE Antenna and Propagation Letters, and taken various patents. His research interests include antenna design, smart antenna system, beamforming network, and microwave devices for fifth generation mobile communication. He is a Senior Member of IEEE Malaysia Section, a member of the Institute of Engineer Malaysia, a Professional Engineer with BEM, a member of the Eta Kappa Nu Chapter, University of Tennessee, and the International Electrical Engineering Honor Society. He is currently an Executive Committee of the IEM Southern Branch.

Akram Alomainy received the M.Eng. degree in Communication Engineering and the Ph.D. degree in Electrical and Electronic Engineering (specialized in Antennas and Radio Propagation) from Queen Mary University of London (QMUL), U.K., in July 2003 and July 2007, respectively. He joined the School of Electronic Engineering and Computer Science, QMUL, in 2007, where he is a Reader in Antennas & Applied EM. His current research interests include small and compact antennas for wireless body area networks, radio propagation characterisation and modelling, antenna interactions with human body, computational electro-magnetic, advanced antenna enhancement techniques for mobile and personal wireless communications, nano-scale networks and communications, THz material characterisation and communication links and advanced algorithm for smart and intelligent antenna and cognitive radio system. He has authored and co-authored four books, 6 book chapters and more than 350 technical papers (7200+ citations and H-index 37) in leading journals and peer-reviewed conferences. Alomainy won the Isambard Brunel Kingdom Award, in 2011, for being an outstanding young science and engineering communicator. He was selected to deliver a TEDx talk about the science of electromagnetic and also participated in many public engagement initiatives and festivals. He is an elected member of UK URSI (International Union of Radio Science) panel to represent the UK interests of URSI Commission B (1 Sept. 2014 until 31 Aug. 2020).

M.Zairil M. Nor received the bachelor's degree in Electrical Engineering (Telecommunication) from Universiti Teknologi Malaysia (UTM), Skudai, in 2009, and the M.Sc. degree in Electrical Engineering also from Universiti Teknologi Malaysia (UTM), Skudai, in 2013. He is currently a Lecturer in Faculty of Electrical Engineering, UiTM Cawangan Johor, Kampus P. Gudang. He has published more than 15 journal papers and technical proceedings on smart antenna systems, microwave devices, and reconfigurable antenna in national and international journals and conferences. His research interest includes smart antenna on communication systems.

Akaa Agbaeze Eteng obtained a B.Eng. degree in Electrical/Electronic Engineering from the Federal University of Technology Owerri, Nigeria in 2002, and a M.Eng. degree in Telecommunications and Electronics from the University of Port Harcourt, Nigeria in 2008. In 2016, he obtained a Ph.D. in Electrical Engineering from Universiti Teknologi Malaysia. Currently, he is a Lecturer at the Department of Electronic and Computer Engineering, University of Port Harcourt, Nigeria. His research interests include wireless energy transfer, radio frequency energy harvesting, and wireless powered communications.

2.4 GHz and 5.2 GHz Frequency Bands Reconfigurable Fractal Antenna for Wearable Devices using ANN

Sivabalan Ambigapathy [1] and Jothilakshmi Paramasivam [2*]

[1] Department of Electronics and Communication Engineering
Chennai Institute of Technology, Chennai, Tamil Nadu – 600 069, India
sivabalana@citchennai.net

[2] Department of Electronics and Communication Engineering
Sri Venkateswara College of Engineering, Chennai, Tamil Nadu – 602 117, India
jothi@svce.ac.in*

Abstract ─ Patch antenna is being used widely in wearable and implantable devices due to its lightweight characteristics. Multi-band patch antenna designs are possible by incorporating professional naturally inspired fractal pattern generating methodologies. Automated Frequency Characteristics Analyzer (AFCA), Artificial Neural Network based Fractal Pattern Generator (AFPG) and Nitinol based Pattern Selector (NPS) functional modules are proposed in this work to design a Dual band Reconfigurable Fractal Antenna for Wearable Devices (DRFA). Producing a miniature fractal patch antenna to support famed 2.4 GHz and 5.2 GHz frequency bands with lesser than 20db return loss is the objective of this work. Numerous fractal patterns are generated with the help of AFPG and their frequency responses are analyzed by Ansys HFSS (High Frequency Structure Simulator) through AFCA module. The results are provided to the AFPG part to train the neural network with proper biasing updates. The fitness function is set to the dimension restriction of 3000 square μm with less than 20 return loss at commonly used 2.4 GHz and 5.2 GHz. The feed type and length of the patches are also fine-tuned by the proposed AFPG module.

Index Terms ─ Artificial neural network, dual band antenna, fractal patterns, patch antenna, reconfigurable antenna, wearable device.

I. INTRODUCTION

Communication gadgets are getting tinier every so often. A range of these gadgets comes under the wearable communication sensor devices, which are involved hugely in health monitoring systems and remote patient monitoring systems. More than 761million people will be at their age 65 by 2025 [1] supposed to be overseen by the E-Health monitoring system. It requires an extensive number of wearable devices to be connected eventually under one or more networks. These devices frequently required to communicate with a centralized organizer to produce cumulative impact assessments. Sometimes they need to communicate directly with a network facility. These hypothetical situations require the support for multiband or reconfigurable communication facility. Leading communication technologies require 2.4 GHz for local Wi-Fi communications and 5.2 GHz for direct internet connectivity.

Lightweight, small size, sufficient gain and harmless flexible construction material are the presumed characteristics of a reconfigurable antenna for wearable devices [2]. Designing Antenna in the patch format is a known solution to achieve these characteristics. Selection of the shape and the dimension of the patch is a challenging work. The complexity of utilizing high cost multilayer Printed Circuit Board (PCB) can be avoided by selecting a suitable resonating antenna pattern in patch antenna design [3]. Microstrip patch antenna manufacturing is very economic while comparing conventional PCB based antenna designs.

Bandwidth enhancements are additional benefit of using microstrip patch antennas [4]. The frequency reconfigurable capability is achieved comfortably by selecting a suitable antenna pattern in microstrip patch antenna design [5]. Different approaches come into existence for optimizing antenna patterns such as Genetic Algorithm (GA) [6], Particle Swarm Optimization (PSO) [7], Bacterial Forage Optimization (BFO) [8] and Ant Colony Optimization (ACO) [9]. Blending one or more optimization algorithms or combining optimizations with ANN models are auxiliary approaches of finalizing an antenna pattern.

Recent studies show that the fractal patterns are used to devise astonishing antennas with multiband support [10, 11]. This work is indented to apply ANN to generate multiple fractal patterns based on a triangular structure mounted on different wearable substrates with different thickness to achieve an antenna pattern that supports 2.4

Submitted On: June 22, 2020
Accepted On: October 20, 2020
https://doi.org/10.47037/2020.ACES.J.360315

and 5.2 GHz. The bandwidth, return loss and gain of the generated fractal pattern antenna are evaluated along with similar existing antennas.

II. EXISTING WORKS

A compact dual band metamaterial antenna with $42 \times 32mm^2$ dimension is established in Dual Band Metamaterial Antenna for LTE / Bluetooth / WiMAX system (DMAL) work [12]. A Square metallic stripe is placedin such a way to cover the patch for lower band support. Similar magnetic current loop is provided near the feed to support upper band. The supporting frequency bands of this antenna are 0.6 ~ 0.64 GHz, 2.67 ~ 3.4 GHz and 3.61 ~ 3.67 GHz. Basic antenna designing principles are used to bring out the antenna patch pattern manually. There is no automatic optimizations are used to trim the pattern in this work. The authors used CST (Computer Simulation Technology) Microwave Studio Simulator to simulate the patch antenna pattern. The design is also fabricated for analyzing the frequency characteristics in real-time. The fabricated antenna is observed for 0.5 GHz to 4 GHz in Satimo StarLab – which can handle the frequency of up to 18 GHz. The gain and return loss graphs are provided to indicate that there is no significant difference between the simulated and observed results.

There are two different antenna designs are introduced in Integrated Dual-band Filtering/duplexing Antennas (IDFA) work [13]. The first design uses Coupled Resonator Technique to design a Dual-band Dual-polarization (DBDP) antenna. Each polarization has two bands obtained by placing a vertical hairpin resonator coupling with the patch. Both the bands show second order filtering performance and improved bandwidths. Dual-port dual-band antenna with integrated filtering and duplexing functionalities is introduced as the second antenna design. Two sets of resonator-based filtering channels are used to carry out the frequency duplexing functionality. The performance of the proposed antennas is measured in terms of gain and S-Parameters. The DBDP antenna resonates with 4.75 ~ 4.98 GHz band and 5.75 ~ 6.05 GHZ frequency bands. A good isolation index of less than 30 dB is achieved by the first design pattern. Two transmission voids are introduced between 4.8 and 5.85 GHz by cross coupling the resonators on purpose. These transmission voids are used to improve the isolation between the two polarizations.

A high gain Dual-polarized Dual-band Antenna (DDA) is designed in this work to support 2G, 3G and LTE indoor communication [14]. Two horizontal polarization and one vertical polarization elements are used to achieve the requirement. The upper horizontal polarization element is designed with four pairs of altered printed magneto-electric dipoles with four-way power divider feeding network. Eight pieces of arc shaped parasitic patches are printed on circular shaped printed circuit board. The lower horizontal polarization element is designed very similar to the upper horizontal polarization element except the parasitic patches. The four-way power divider feeding network enables a persistent radiation in $360°$ with high gain. The vertical polarization element is designed with 4-pairs of cone-shaped patches. Ansys HFSS is used to simulate the entire antenna pattern and a prototype is fabricated for real-time analysis. Based on the results, it is realized that the simulated and observed results are comparable to each other except some observation glitches.

This work Low-profile Dial-band Stacked Microstrip Monopolar Patch Antenna (LDSMMPA) is about to bring up a by coupling annular ring with conductive passages in the antenna structure [15]. The height of this antenna is set to be 4.175 mm. The utilization scope of this antenna is wireless local area network which operates in 2.4 to 2.48GHz and 5.75 to 5.825 GHz. Car-to-Car Communication networks with 5.85 to 5.925 GHz is another prime beneficial utilization of this antenna. The stacked-patch assembly of LDSMMPA is given in Fig. 1. A coaxial feed that connects directly to the center of the upper circular patch. The lower circular patch is fed by a coupling between interior probe and the lower circular with the clearance hole. This feeding arrangement enables better isolation between the two patches, so that the antenna can resonate at two frequency bands exquisitely. Ansys HFSS is used to simulate the antenna pattern and Agilent E5080A near filed measurement system is used to measure the frequency characteristics of the pattern. Both simulation and implementation results are in coherence, displays that the gain of 6 dBi is achieved for 2.24 ~ 2.53 GHz lower frequency band and the gain of 7.5 dBi is achieved for 5.42 ~ 5.98 GHz higher frequency band.

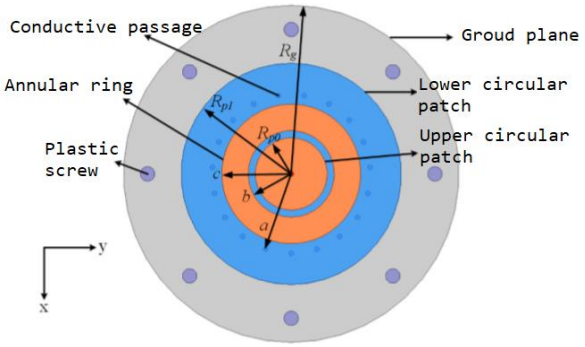

Fig. 1. Stacked-patch assembly.

A novel dual band hexagonal antenna for bluetooth and UWB applications with single band notched is indented to create a broadband antenna that supports 2.2 GHz ~ 2.52 GHz and 3.5 GHz to 10 GHz without interfering the WLAN frequency band 5.72 GHz ~ 5.825 GHz [16]. The core idea behind this work is to design an antenna that supports Bluetooth frequency and UWB

frequency bands without meddling WLAN frequency band. A circularly polarized dual-port dual-band RFID antenna that operates in UHF and UWB frequency bands is aimed in this work [17]. An adequate quadruple feed network in hybrid mode is used to achieve the wide frequency band resonance from 0.918 GHz ~ 0.926 GHz UHF band to 3.1 GHz ~ 4.8 GHz UWB band.

Miniature dual-band antennas are the major requirement in the multipurpose digital gadget world. Many communication devices are equipped with more than one communication facility such as GSM, LTE, Bluetooth and IEEE 802.11 b/g/n standards. Providing separate Antenna for every communication system will increase the size of the device significantly. Two widely used frequencies in these portable electronic communication devices are 2.4 GHz and 5 GHz. Manually designing a suitable dual-band antenna by checking various shapes and materials one-by-one will consume more time.

III. RELATED WORKS

There are two related works tracked down to the proposed DRFA work. They are Miniaturized Hexagonal-triangular Fractal Antenna for wide-band applications (MHFA) [18]and Novel Dualband Coaxial-fed SIW Cavity Resonator Antenna using ANN Modeling (NDCAANN) [19]. Certain salient points from these related works are discussed concisely in this section for better comprehension of the proposed DRFA method.

Fractal patterns are getting importance in antenna designing in recent times due to their multiband supporting characteristics. Generating fractal patterns is an amusing mathematical process which can develop multitudinous splendid effective patterns. There are several procedures introduced recently to create fractal patterns. In MHFA work, a hexagonal triangle fractal antenna design is proposed to get multiband resonating antenna between 3GHz ~ 25GHz. The size of the fractal antenna is restricted to $25mm \times 30mm$ with $0.8mm$ substrate thickness.

The following equation is used to find the resonant frequency of circular patch antenna:

$$f_\gamma = \frac{Ymn C}{5.714\, R_e \sqrt{\epsilon_{reff}}}, \quad (1)$$

where $Ymn = y_{11}$ for mode $TM_{11} = 1.8412$, $Ymn = y_{21}$ for mode $TM_{21} = 3.0542$, C refers the speed of light, ϵ_{reff} refers the effective dielectric constant, R_e refers the effective radius of the circular patch antenna.

R_e can be calculated using the following equation:

$$R_e = R_c \times \sqrt{\left(1 + \frac{2 \cdot t}{R_c \cdot \pi \cdot \epsilon_r} \times \left[\ln\left(\frac{\pi \cdot R_c}{2 \cdot t}\right) + 1.7726\right]\right)}, \quad (2)$$

where R_c refers the radius of circular patch antenna.

The value of f_γ hexagonal patch antenna can be calculated using the following equation:

$$f_\gamma = \pi \times (R_e)^2 = \frac{3}{2} \times \sqrt{3} \cdot S_h^2, \quad (3)$$

where S_h is the side length of the hexagonal patch antenna.

The effective dielectric constant ϵ_{reff} is calculated as:

$$\epsilon_{reff} = \frac{1+\epsilon_r}{2}. \quad (4)$$

The formation of hexagonal patch antenna over the circular shape is arranged with four 1mm hexagonal rings placed with a 2.5mm separation distance. Symmetrical triangular slots are used in the rear side of the hexagonal patch antenna to provide the channel insulation properly. This antenna achieved less than 20dB return loss in center frequencies 8GHz, 11GHz, 16GHz and 24GHz makes it eligible to use in 3GHz~25GHz bands.

Substrate Integrated Waveguide (SIW) is one of the most resent methodologies in generating compact low-loss comprehensive systems. SIW cavity resonators are widely used most modern antennas that supports millimeter and microwave devices. The dimensions involved in designing SIW cavity antenna is a strategically challenging task. This challenging task can be handoff to the computers with the help of machine learning computer aided tuning methods. There are several cover the counter machine learning algorithms exist such as Linear Regression, Logistic Regression, Decision Tree, Support Vector Machines and Random Forest.

ANN is a simple straight forward method used in many machine learning applications. NDCAANN takes advantage of this method to fine-tune the antenna pattern with computer aided tuning. The resonant frequency of the SIW cavity antenna can be calculated based on dimension of the SIW cavity using the following equation:

$$f_{mnp} = \frac{c}{2\pi\sqrt{\varepsilon_r \mu_r}} \sqrt{\left(\frac{p_{nm}}{R}\right)^2 + \left(\frac{p\pi}{h}\right)^2}, \quad (5)$$

where c is the speed of light in free space, ε_r is the filling material's permittivity, μ_r is the relative permeability, R is the radius of SIW cavity, p_{nm} is the corresponding Bessel function root, m, n, p are the number of variations in standing wave pattern and h refers the thickness of the substrate.

The ANN architecture uses the basic information to fine tune the antenna pattern and dimensions iteratively. By this way, in NDCAANN work, a SIW cavity resonator coaxial antenna is introduced to support 10.84 GHz and 14.82 GHz center resonant frequencies with 15 dB and 30 dB return losses.

In general, antenna prototyping and characteristics analysis is performed manually with the help of some microwave structure analysis software. The input antenna pattern is modified manually based on the simulated or observed results. Changing the antenna pattern in micro-meter precision repeatedly is a tedious process if performed manually. In this proposed method, we introduced an interface to automate the antenna design calibration process which can load a principle antenna

pattern, simulate the characteristics by calling corresponding analytical software and to make changes to the principle base pattern with the help of Artificial Neural Network (ANN). Contribution of Automatic Frequency Characteristics Analyzer, ANN based Fractal Pattern Generator and Nitinol based Pattern selector is the innovation of this proposed method.

IV. PROPOSED METHOD

A Dual band Reconfigurable Fractal Antenna for Wearable Devices (DRFA) work consists of three major modules, they are Automated Frequency Characteristics Analyzer, Artificial Neural Network based Fractal Pattern Generator and Nitinol based Pattern Selector. Same fractal base pattern is used to create different iterative fractal patterns with different dimensions to achieve higher gain for multiband support with higher gain values. The shape memory and super elasticity properties of the Nitinol is used as the key for the reconfigurability of this proposed antenna.

A. Automatic Frequency Characteristics Analyzer (AFCA)

In general, the frequency characteristics of an antenna is observed in a well-equipped laboratory before voluminous manufacturing. Measuring the antenna pattern in a laboratory is a costlier process. Therefore, the researchers and industrial people are using software widely before proceeding with the prototyping of the antenna patterns. These software enables the cost-effective primary characteristics analysis of the antenna patterns.

This kind of software operate on the basis of manual processes such as selecting substrates, feed types, channel guides, sub-band filters, waveguides and dielectric resonators. The patterns are to be drawn manually by the user in the software to get a clear analysis report. Some software possesses the provision of importing images from other compatible applications. If the loaded pattern needs any modifications, then it has to be edited in the software itself to get updated results. Drawing an antenna pattern is a time-consuming process if done manually. AFCA provides a way to automate this process. Ansys HFSS software is used here to analyze the frequency characteristics of the antenna pattern. A dedicated user interface and a service is coded in VC++ to associate with HFSS to feed the vector pattern automatically and retrieve the results from it. AFCA is used as an agent between the user and the HFSS software to reduce repetitive manual processes and to reduce tremendous amount of time.

B. Artificial Neural Network based Fractal Pattern Generator (AFPG)

ANN based fractal pattern generator is designed with the microstrip patch antenna basics and fractal pattern generation. Let L be the length of the microstrip patch antenna, then the fundamental dimension restriction is $L < \frac{\lambda_g}{2}$ where λ_g is the substrate guide wavelength. A basic microstrip patch antenna is illustrated in Fig. 2.

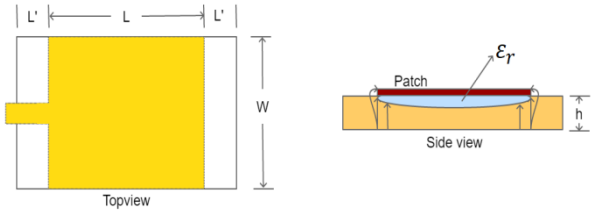

Fig. 2. Microstrip patch antenna.

There are two key points are to be considered while designing a microstrip patch antenna. They are:

- Better efficiency antennas can be designed using thicker substrates and lesser dielectric constants. But the larger element size is high-priced.
- Thin substrate with high dielectric constants will entail tiny element sizes and minimized coupling, but the toll is taken from the efficiency and bandwidths.

Holding these points in consideration, the width w, fringing length correction $\frac{L'}{h}$, patch length L, effective dielectric constant ϵ_{reff}, and feed position z_i are calculated by the following equations for the condition $w \neq \lambda_0$:

$$w = \frac{1}{2f_r\sqrt{\mu_0\epsilon_0}}\sqrt{\frac{2}{\epsilon_r+1}} = \frac{v_0}{2f_r}\sqrt{\frac{2}{\epsilon_r+1}}, \tag{6}$$

$$\frac{L'}{h} = 0.412 \times \frac{(\epsilon_{reff}+0.3)\left(\frac{w}{h}+0.264\right)}{(\epsilon_{reff}+0.258)\left(\frac{w}{h}+0.8\right)}, \tag{7}$$

$$L = \frac{1}{2f_r\sqrt{\epsilon_{reff}}\sqrt{\mu_0\epsilon_0}} - 2L', \tag{8}$$

$$\epsilon_{reff} = \frac{\epsilon_r+1}{2} + \frac{\epsilon_r-1}{2} \times \sqrt{1+\frac{12h}{w}}, \tag{9}$$

$$z_i = \frac{1}{2k}, \tag{10}$$

where,

$$k = \begin{cases} \frac{1}{90}\left(\frac{w}{\lambda_0}\right)^2 if w < \lambda_o \\ \frac{1}{120}\left(\frac{w}{\lambda_0}\right)^2 if w > \lambda_o \end{cases}. \tag{11}$$

The Fractal pattern generation relies on the fractal geometry – which is also known as nature's geometry. The fractal geometry contains chaotic rules with specific interspace rules. Self-similarity at same and different scales, random repetitions, time series scaling or repetitions, detailed small-scale structure and local or global irregularities are the customary characteristics of fractal patterns. The fractal patterns can be generated by some techniques such as Stochastic or deterministic fixed geometry replacement rules, iteration of a map, replicating branching patterns with or without transformations, recurrent relation special time fractals,

random fractals and finite subdivision rules. Iterated Function System (IFS) is used in AFGP module.

Let F_i be the n number of two-dimensional IFS functions and S be the solution set. The Hutchinson's recursive equation states that:

$$S = \bigcup_{i=0}^{n-1} F_i(s). \quad (12)$$

Based on the Barnsley implementation of Equation 12, the two-dimensional function F_i can be represented as a 2×3 matrix that contains Rotation, Scaling, Translation, horizontal flip, vertical flip, incremental 45° flip and shear transformations as follows:

$$F_i(x, y) = (a_i x + b_i y + e_i, c_i x + d_i y + f_i). \quad (13)$$

The first phase of AFPG module is to extract the essential elements from the base antenna pattern. A triangular shape and a rectangular shape as in Fig. 3 are given as the base patterns to the AFPG. The rectangular shape is limited to use with the patch and waveguide where are the triangular shape is set free to construct the fractal pattern.

Fig. 3. Triangle and rectangle base patterns.

Let η be the expected number of central resonant frequencies,Γ be the expected central resonant frequency and ω be the expected bandwidth. Then $\forall i = 1 \rightarrow \eta: (\Gamma_i, \omega_i)$ are the inputs given to the AFPG pattern generation algorithm. Since the pattern generation algorithm has the freedom to generate multiple number of iterations based on Equation (13), getting the fine-tuned dimension vectors the antenna pattern is possible altogether.

The AFPG pattern generation algorithm is given below.

Algorithm 1: AFPG pattern Generation <Input: $(\Gamma_i, \omega_i)[\eta]$, Output: Vector Image>

Step 1: Interpret and load base patterns

Step 2: Estimate and assign dimensions based on equations 6 to 11

Step 3: Call AFCA module

Step 4: Observe generated pattern's frequency characteristics

Step 5: Check observed results with $\forall i = 1 \rightarrow \eta: (\Gamma_i, \omega_i)$ *and go to step 9 if match found*

Step 6: Scale pattern to next size

Step 7: If size exceeds maximum permitted dimension
Resize pattern
Apply pattern generation function by Equation 13

Step 8: Go to step 3

Step 9: Halt process and load converged result to memory

The output of this AFPG algorithm is a vector image that epitomizes the fractal antenna pattern. The amalgamated flow of AFCA and AFPG is given in Fig. 4.

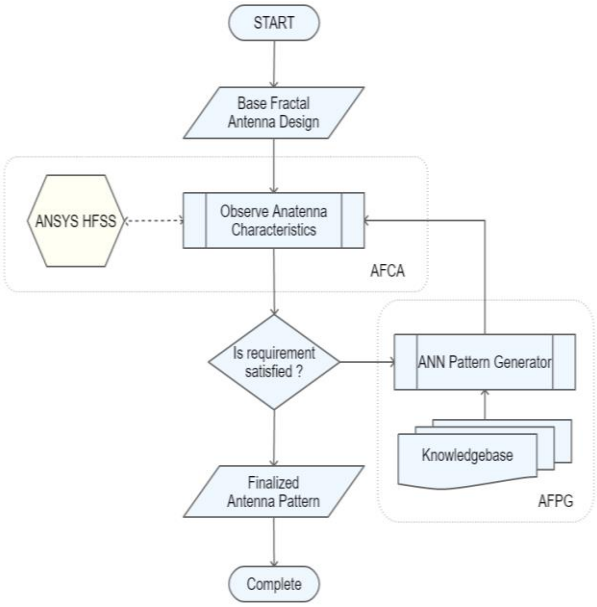

Fig. 4. AFCA and AFPG combined flow diagram.

C. Nitinol based pattern selector

Microstrip patch antennas cannot afford heavy electromagnetic switching arrangements. Therefore, a lightweight switching arrangement is required to alter the connectivity pathways for reconfigurability. Nickel Titanium – which is often represented as Nitinol has the property of shape memory, which is a boon for designing different pathways in microstrip patch antenna. Different pathways of an antenna make it reconfigurable and enables the multiband support attribute. A Nitinol strip is made up of three main substances. The first one is the nitinol substrate which is placed over an elastic steel surface with Kapton insulation [20] material between them. The side view of a typical nitinol switching arrangement is given in Fig. 5.

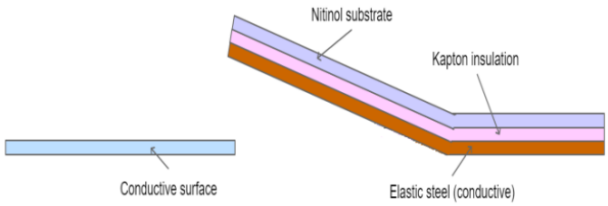

Fig. 5. Nitinol switching arrangement.

The shape of the Nitinol can be controlled using resistive heating methodology. The interesting fact about nitinol is many of the materials get enlarge during the heating process whereas the Nitinol gets shrunk by heating. Since it works as a resistor, it gets some heat naturally while conducting the current and it can be restored to normal position when the heat is reduced by removing current through it. The elastic steel, Kapton insulation and the Nitinol substrate altogether forms the Nitinol strip. The elastic steel is used as the contact, the nitinol substrate us used as the actuator and the Kapton insulation functions as the shape memory by reducing the recovery speed of Nitinol.

This nitinol switching arrangement is used as the antenna pattern selector based on the required bandwidth of proposed dual-band reconfigurable fractal antenna.

V. EXPERIMENTAL SETUP

A high-power computer is required to get the converged result of ANN since the AFPG module overstepped thousands of iterations. HFSS software is also a fairly high computational resource demanding one. Therefore, the experimental setup is split into two different computational environments. A dedicated cloud server with Xeon E5-2620v4 12 core processor equipped with 16GB DDR4 2400MHz RAM is leased to execute the AFPG and AFCA modules. A laptop with Intel Core i5 processor and 4GB RAM is used as the remote loader and monitor for the AFPG and AFCA modules. A dedicated UI is used to initialize, execute and monitor the proposed method in the server. The server will continue to run and log the converged antenna patterns even after shutting down the remote-control laptop. The UI will fetch the most recent converged pattern whenever it is getting executed in the remote laptop. Experimental setup architecture is given in Fig. 6.

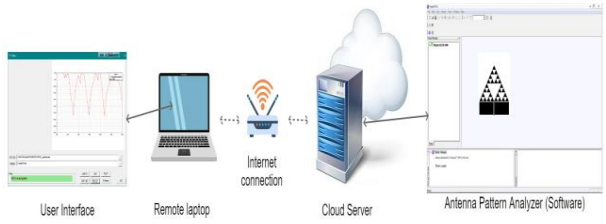

Fig. 6. Experimental setup.

VI. RESULTS AND ANALYSIS

The converged ANN antenna pattern based on the elementary based patterns as in Fig. 3 at 211602nd iteration is given below in Fig. 7 (a) and Nitinol Strip switching placements are given in Fig. 7 (b).

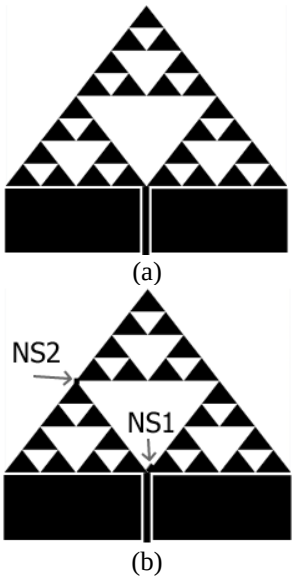

Fig. 7. (a) Converged antenna pattern, and (b) Nitinol switch placement.

NS1 and NS2 in Fig. 7 (b) are the first and second nitinol switch placements. The switching configurations can be set to four possible cases as in Table 1.

Table 1: Switching status and selected modes

NS1	NS2	Configuration
Off	Off	Mode 0
Off	On	Mode 1
On	Off	Mode 2
On	On	Mode 3

Obtained antenna patterns by using NS1 and NS2 in all 4 configuration modes are given in Fig. 8.

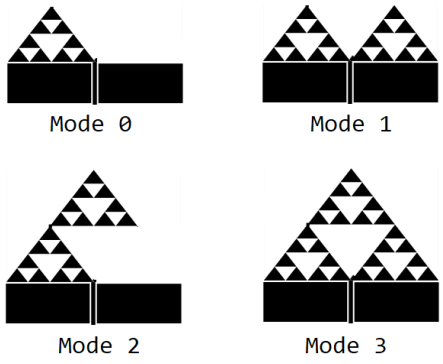

Fig. 8. Mode pattern configuration.

A. Configuration mode 0

Configuration mode 0 is selected when both NS1 and NS2 Nitinol strips are on off state. The resonant frequency characteristics of this configuration are given in Fig. 9.

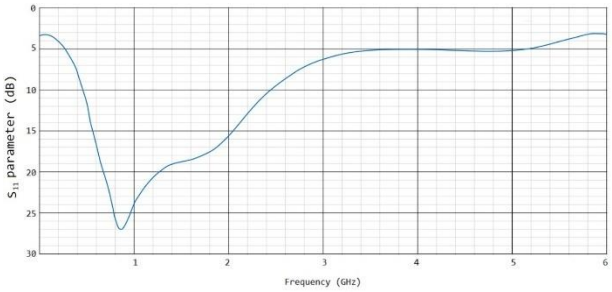

Fig. 9. Return loss graph of configuration mode 0.

Based on the observations, mode 0 reached less than 25 dB between 800MHz and 950 MHz which comes under GSM bandwidth. The gain is about 6 ~ 7.2 dB in the resonant frequency band. This mode does not get enough gain for 2.4 GHz which reveals that mode 0 is not suitable for Bluetooth or Wi-Fi communication.

B. Configuration mode 1

Configuration mode 1 is achieved while NS1 is on position and NS2 is in off position. This mode supports two different frequency bands of 850 MHz ~ 1.05 GHz and 2 GHz ~ 2.6 GHz which is suitable for GSM, Bluetooth and Wi-Fi applications. The peak gain 7.7 dB is achieved in 2.38 GHz resonance frequency as shown in Fig. 10.

C. Configuration mode 2

This configuration mode is achieved by turning off NS1 and turning on NS2. This mode also supports two different resonant frequency bands with 2.4 GHz and 5.18 GHz center frequency. The 2.4 GHz band ranges from 2.2 GHz to 2.76 GHz and the 5.18 GHz band ranges from 4.96 GHz to 5.38 GHz with lesser then 25 dB of return loss. The simulation graph is given in Fig. 11.

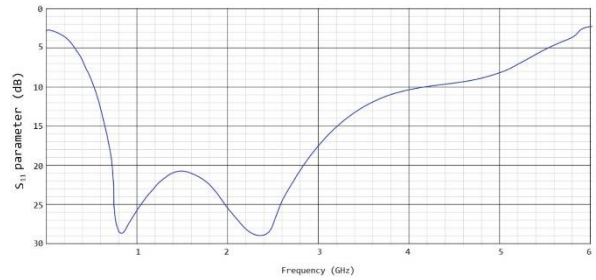

Fig. 10. Return loss graph of configuration mode 1.

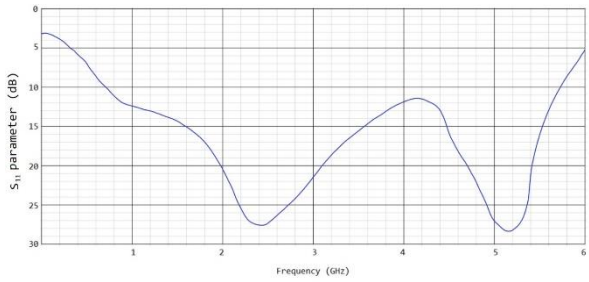

Fig. 11. Configuration mode 2 return loss graph.

Configuration mode 2 can be used for Bluetooth and Wi-Fi applications with its 7.7 dB gain at 2.4 GHz. The gain of 8.2 dB at 5.18 GHz makes it possible to use for 5G applications.

D. Configuration mode 3

This pattern configuration is accomplished by turning on both NS1 and NS2 Nitinol switching arrangements. Three frequency band widths with 700 MHz, 2.38 GHz and 5.1 GHz center frequencies are achieved in this configuration. The obtained bandwidths are 580 MHz ~ 1.1 GHz, 2.18 GHz ~ 2.6 GHz and 4.82 GHz ~ 5.23 GHz with less than 25 dB return loss. This mode is suitable for GSM, Bluetooth, Wi-Fi and 5G applications.

The gain at 700 MHz, 2.38 GHz and 5.1 GHz center frequencies are about 8.2 dB, 6 dB and 6.2 dB. The Power Standing Wave Ratio (PSWR) for the generated antenna pattern is 1.21 as measured in the simulation. The return loss graph of configuration mode 3 is given in Fig. 12 and the comparison of return loss, gain and VSWR for various frequency are given in Table 2.

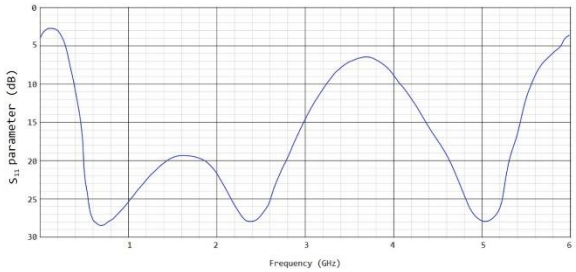

Fig. 12. Configuration mode 3 return loss graph.

The antenna has fabricated for our proposed method and also the radiation pattern of configuration mode 3 is given in the Fig. 13. The measured values of Return loss (RL), Gain and Voltage Standing Wave Ratio (VSWR) are listed in the Table 2.

Figure 14 shows the S11 parameter values by comparing the measured and simulated data for different frequencies.

Table 2: RL-Gain-VSWR graph

Frequency (GHz)	Return Loss (dB)	Gain (dB)	VSWR (dB)
0.5	4.8	-22	3.71
0.7	28.5	27	1.07
1	25.4	21	1.11
1.5	19.5	9	1.23
2	23.5	13.8	1.14
2.28	28	26	1.08
2.5	27	22	1.09
3	14.5	-1	1.46
3.5	7	-16	2.61
4	8.9	-12.1	2.11
4.5	17.5	5	1.31
5	27.9	25.7	1.09
5.5	12.4	-6.99	1.63
6	3.7	-22.8	4.76

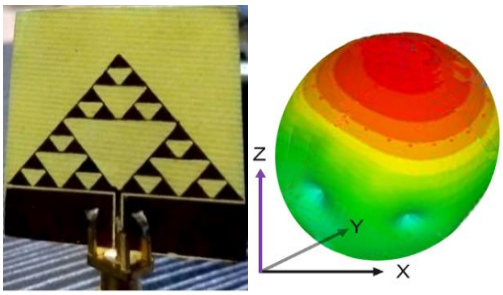

Fig. 13. Fabricated antenna and mode 3 radiation pattern.

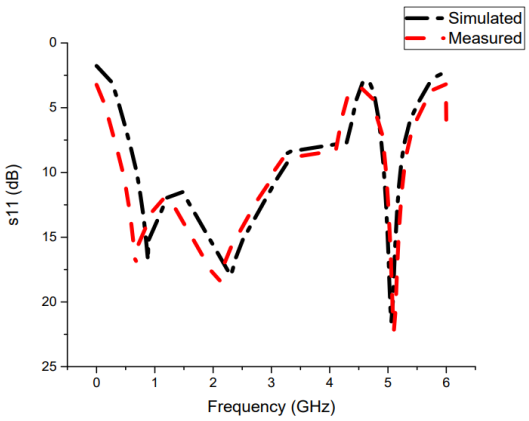

Fig. 14. S11 parameter measured vs simulated graph.

VII. CONCLUSION

A fractal image inspired antenna pattern is achieved with the help of ANN and the proposed reconfigurable antenna comprehends GSM, Bluetooth, Wi-Fi and 5G bands which is very suitable for wearable devices such as health wristbands. The reconfigurable property is achieved by presenting Nitinol based micro switching mechanism. The configuration mode 0 supports only GSM band with lesser bandwidth which has the less scope of applications. But Configuration mode 1 and 2 are supporting GSM + Wi-Fi applications and Wi-Fi + 5G applications respectively. Configuration mode 3 supports GSM, Bluetooth, Wi-Fi and 5G frequency bands with acceptable gain values. Many of the upcoming digital gadgets are having the communication capability in GSM, Wi-Fi and 5G bands. A wearable microstrip antenna that supports these bands will be very helpful for personal care electronic gadgets and wearable devices. Hence, the proposed antenna pattern may be recommended for the impending wearable electronic communication devices.

REFERENCES

[1] A. Shehab, A. Ismail, L. Osman, M. Elhoseny, and I. M. El-Henawy, "Quantified self using iot wearable devices," *Proceedings of the International Conference on Advanced Intelligent Systems and Informatics*, Springer, pp. 820-831, 2017.

[2] A. Y. I. Ashyap, Z. Z. Abidin, S. H. Dahlan, H. A. Majid, M. R. Kamarudin, and R. A. Abd-Alhameed, "Robust low-profile electromagnetic band-gap-based on textile wearable antennas for medical application," *International Workshop on Antenna Technology: Small Antennas, Innovative Structures, and Applications (iWAT)*, Athens, pp. 158-161, 2017.

[3] L. Wen, S. Gao, Q. Luo, Q. Yang, W. Hu, and Y. Yin, "A low-cost differentially driven dual-polarized patch antenna by using open-loop resonators," in *IEEE Transactions on Antennas and Propagation*, vol. 67, no. 4, pp. 2745-2750, Apr. 2019.

[4] M. Tang, X. Chen, M. Li, and R. W. Ziolkowski, "A bandwidth-enhanced, compact, single-feed, low-profile, multilayered, circularly polarized patch antenna," in *IEEE Antennas and Wireless Propagation Letters*, vol. 16, pp. 2258-2261, 2017.

[5] Y. Cai, K. Li, Y. Yin, S. Gao, W. Hu, and L. Zhao, "A low-profile frequency reconfigurable grid-slotted patch antenna," in *IEEE Access*, vol. 6, pp. 36305-36312, 2018.

[6] R. L. Haupt, "Optimizing the sidelobe level of a two-way antenna array pattern by thinning the receive aperture," 2018 *International Conference on Radar (RADAR)*, Brisbane, QLD, pp. 1-5, 2018.

[7] H. Li, Y. Jiang, Y. Ding, J. Tan, and J. Zhou, "Low-sidelobe pattern synthesis for sparse conformal arrays based on PSO-SOCP optimization," in *IEEE Access*, vol. 6, pp. 77429-77439, 2018.

[8] N. Gupta, J. Saxena, and K. S. Bhatia, "Optimized metamaterial-loaded fractal antenna using modified hybrid BF-PSO algorithm," in *Neural Computing and Applications*, Springer, pp. 1-18, 2019.

[9] R. N. Biswas, A. Saha, S. K. Mitra, and M. K. Naskar, "PSO-based antenna pattern synthesis: A

paradigm for secured data communications," in *Nature-Inspired Algorithms for Big Data Frameworks - IGI Global Disseminator of Knowledge, IGI-Global*, pp. 1-28, 2019.

[10] S. Bhatt, P. Mankodi, A. Desai, and R. Patel, "Analysis of ultra-wideband fractal antenna designs and their applications for wireless communication: A survey," *2017 International Conference on Inventive Systems and Control (ICISC)*, Coimbatore, pp. 1-6, 2017.

[11] N. K. Darimireddy, R. R. Reddy, and A. M. Prasad, "A miniaturized hexagonal-triangular fractal antenna for wide-band applications [Antenna Applications Corner]," in *IEEE Antennas and Propagation Magazine*, vol. 60, no. 2, pp. 104-110, Apr. 2018.

[12] Md. M. Hasan, M. R. I. Faruque, and M. T. Islam, "Dual band metamaterial antenna for LTE/Bluetooth/WiMAX system," in *Scientific Reports*, Springer, vol. 8, no. 1240, pp. 1-17, 2018.

[13] C. Mao, S. Gao, Y. Wang, Y. Liu, X. Yang, Z. Cheng, and Y. Geng, "Integrated dual-band filtering/duplexing antennas," in *IEEE Access*, vol. 6, pp. 8403-8411, 2018.

[14] Z. Zhao, J. Lai, B. Feng, and C. Sim, "A dual-polarized dual-band antenna with high gain for 2G/3G/LTE indoor communications," in *IEEE Access*, vol. 6, pp. 61623-61632, 2018.

[15] S. Gao, L. Ge, D. Zhang, and W. Qin, "Low-profile dual-band stacked microstrip monopolar patch antenna for WLAN and car-to-car communications," in *IEEE Access*, vol. 6, pp. 69575-69581, 2018.

[16] M. Elhabchi, M. N. Srifi, and R. Touahni, "A novel dual band hexagonal antenna for bluetooth and UWB applications with single band notched," in *Advanced Electromagnetics Journal*, vol. 7, no. 5, pp. 63-68, 2018.

[17] J. Zhang and Z. Shen, "Dual-band shared-aperture UHF/UWB RFID reader antenna of circular polarization," in *IEEE Transactions on Antennas and Propagation*, vol. 66, no. 8, pp. 3886-3893, Aug. 2018.

[18] N. K. Darimireddy, R. R. Reddy, and A. M. Prasad, "A miniaturized hexagonal-triangular fractal antenna for wide-band applications [Antenna Applications Corner]," in *IEEE Antennas and Propagation Magazine*, vol. 60, no. 2, pp. 104-110, Apr. 2018.

[19] M. Chetioui, A. Boudkhil, N. Benabdallah, and N. Benahmed, "A novel dualband coaxial-fed SIW cavity resonator antenna using ANN modeling," in *Journal of Engineering Science and Technology*, review 11, article 2, pp. 82-87, JESTR, 2018.

[20] E. E. Shin, D. A. Scheiman, and M. Lizcano, "Lightweight, durable, and multifunctional electrical insulation material systems for high voltage applications," 2018 *AIAA/IEEE Electric Aircraft Technologies Symposium (EATS)*, Cincinnati, OH, pp. 1-21, 2018.

A. Sivabalan working as an Assistant Professor in Chennai Institute of Technology. Received the B.E. degree in Electronics and Communication Engineering from Dhanalakshmi College of Engineering, Chennai Anna University, India, in 2009, received M.E. degree in Communication Systems from Sri Sairam Engineering College, Chennai, Anna University, Chennai, India, in 2012. Currently pursuing Ph.D. in "Design of reconfigurable antenna for medical applications". He had published two international Journals.

P. Jothilakshmi working as a Professor in the Department of Electronics and Communication Engineering, Sri Venkateswara College of Engineering, Chennai. Her research area is Microwave Antennas - Design and Analysis of a Class of Continuous Transverse Stub Array Antenna for Microwave Applications Anna University - Chennai-2015, M.E. (Communication Systems) – Mepco Schlenk Engineering College, Sivakasi- December 2000, B.E. (Electronics and Communication Engineering) – Thanthai Periyar Government Institute of Technology. She has published more than 100 research papers in international and national journals including IEEE conferences and SCI Indexed journals.